TU Delft

Delft University of Technology

Hardware in the Loop Emulation of Ship Propulsion Systems at Model Scale

Huijgens, L.J.G.

DOI
10.4233/uuid:24c5867a-6fbb-4e6a-9785-2c9362fada91

Publication date
2021

Document Version
Final published version

Citation (APA)
Huijgens, L. J. G. (2021). *Hardware in the Loop Emulation of Ship Propulsion Systems at Model Scale*. [Dissertation (TU Delft), Delft University of Technology]. TRAIL Research School. https://doi.org/10.4233/uuid:24c5867a-6fbb-4e6a-9785-2c9362fada91

Important note
To cite this publication, please use the final published version (if applicable).
Please check the document version above.

Copyright
Other than for strictly personal use, it is not permitted to download, forward or distribute the text or part of it, without the consent of the author(s) and/or copyright holder(s), unless the work is under an open content license such as Creative Commons.

Takedown policy
Please contact us and provide details if you believe this document breaches copyrights.
We will remove access to the work immediately and investigate your claim.

This work is downloaded from Delft University of Technology.
For technical reasons the number of authors shown on this cover page is limited to a maximum of 10.

Hardware in the Loop Emulation of Ship Propulsion Systems at Model Scale

Proefschrift

ter verkrijging van de graad van doctor
aan de Technische Universiteit Delft,
op gezag van de Rector Magnificus prof.dr.ir. T.H.J.J. van der Hagen,
voorzitter van het College voor Promoties,
in het openbaar te verdedigen op
donderdag 4 februari 2021 om 10:00 uur

door

Lodewijk Jozef Gerardus HUIJGENS

scheepsbouwkundig ingenieur
Technische Universiteit Delft
geboren te Vlissingen, Nederland

Dit proefschrift is goedgekeurd door de
promotor: prof.ir. J.J. Hopman
copromotor: dr.ir. A. Vrijdag

Samenstelling promotiecommissie:

Rector Magnificus	voorzitter
Prof.ir. J.J. Hopman	Technische Universiteit Delft, promotor
Dr.ir. A. Vrijdag	Technische Universiteit Delft, copromotor

Onafhankelijke leden:

Prof.dr.ir. T.J.C. van Terwisga	Technische Universiteit Delft
Prof.dr.ir. J.W. van Wingerden	Technische Universiteit Delft
Prof.dr. G. Theotokatos	University of Strathclyde
Prof.dr.ing. S. Steen	Norges Teknisk-Naturvitenskapelige Universitet
Prof.dr. M. Altosole	Università degli Studi di Napoli

Printed by Ridderprint

ISBN 978-94-6366-364-9

© 2021 L.J.G. Huijgens

All rights reserved. No part of this publication may be reproduced, stored in a retrieval system, or transmitted, in any form or by any means, electronic, mechanical, photocopying, recording or otherwise, without the prior written permission of the author.

An electronic version of this thesis is available at
`http://repository.tudelft.nl/`

Contents

Summary v

Samenvatting vii

1 Introduction 1
- 1.1 Predicting the Performance of Ships . . . 1
- 1.2 Hardware in the Loop in the Model Basin . . . 5
- 1.3 Scaling in the Ship Model Basin . . . 7
- 1.4 Research Goal and Scope . . . 11
- 1.5 Research Approach . . . 13
  - 1.5.1 Dissertation Structure . . . 13
  - 1.5.2 Visualising Shaft Dynamics . . . 15

2 Problem Description 17
- 2.1 Layout of the Scale Models . . . 18
  - 2.1.1 Ideal Scale Model: Diesel-Mechanical Propulsion System . . . 18
  - 2.1.2 Practical Scale Model: HIL Setup . . . 19
- 2.2 Non-linear Descriptions: Ideal and Practical Scale Models . . . 22
  - 2.2.1 Ideal Scale Model . . . 22
  - 2.2.2 Practical Scale Model . . . 26
- 2.3 Linear Descriptions: Ideal and Practical Scale Models . . . 28
  - 2.3.1 Ideal Scale Model . . . 28
  - 2.3.2 Practical Scale Model . . . 32
  - 2.3.3 Simplifications to the Practical Scale Model . . . 34
- 2.4 Verification of Linear Descriptions . . . 36
- 2.5 Scale Effects on Shaft Dynamics . . . 36
  - 2.5.1 Distortions by Electric Drive . . . 37
  - 2.5.2 Distortions by Different Shaft Friction . . . 38
  - 2.5.3 Distortions by Incorrect Moment of Inertia . . . 39
  - 2.5.4 Distortions by Hydrodynamic Scale Effects . . . 40
- 2.6 Criteria for Successful Dynamic Open Water Experiments . . . 42
  - 2.6.1 Added Value of Hardware in the Loop . . . 42
  - 2.6.2 Input and Output Signals . . . 43
  - 2.6.3 Criteria for Accurate Emulation of Shaft Dynamics . . . 44
- 2.7 Conclusion . . . 45

3 Tuning the Electric Drive of the Open Water Setup **47**
3.1 Approach . . . 48
3.2 Requirements on Current Controller Settings . . . 48
3.2.1 Poles and Zero of Ideal Scale Model . . . 49
3.2.2 Poles and Zero of Simplified Electric Loop . . . 49
3.2.3 Requirements on Poles and Zeros . . . 49
3.3 Discussion . . . 53
3.3.1 Influence of $K^*_{\mathrm{p,i}}$ and $K^*_{\mathrm{i,i}}$ on $\delta\omega^*/\delta\omega^*_{\mathrm{set}}$ . . . 55
3.3.2 Non-Linear Simulations . . . 57
3.4 Conclusion . . . 58

4 Correction of Propulsion Shaft Inertia **61**
4.1 Effect of Distorted Inertia on Shaft Dynamics . . . 62
4.2 Correcting the Moment of Inertia . . . 67
4.3 Numerical Correction of Inertia . . . 68
4.3.1 Shaft Speed Emulation . . . 68
4.3.2 Torque Emulation . . . 70
4.4 Implementation of the Numerical Inertia Correction . . . 72
4.4.1 Ideal and Uncorrected Scale Model . . . 72
4.4.2 Corrected Scale Model . . . 73
4.4.3 Influence of Parameters on Performance . . . 79
4.5 Conclusion . . . 84

5 Description and Preparation of the Experimental Setup **85**
5.1 Hardware Topology . . . 85
5.1.1 Hardware Components . . . 88
5.1.2 Supply and Communication Lines . . . 91
5.2 Software Modules . . . 92
5.3 Parameter Identification . . . 94
5.3.1 Friction Current . . . 97
5.3.2 Electric Motor Torque Constant . . . 99
5.3.3 Practical Moment of Inertia . . . 101
5.4 Conclusion . . . 103

6 Experimental Validation **107**
6.1 Approach to Validation . . . 107
6.2 Equilibrium Conditions . . . 109
6.3 Dynamic Model Scale Environment . . . 112
6.3.1 Environment: Ocean Wind Waves . . . 112
6.3.2 Relevant Frequency Range and Similarity Range . . . 117
6.4 Validation of Mathematical Descriptions . . . 117
6.4.1 Electric Loop . . . 118
6.4.2 Shaft Speed Loop . . . 123
6.5 Validation of the Numerical Inertia Correction . . . 129
6.5.1 Response on Speed Setting and Drive Torque . . . 129
6.5.2 Response to Waves . . . 137
6.6 Conclusion . . . 142

7 Case Study: Propeller Ventilation **145**
7.1 HIL Experiments on Propeller Ventilation 146
7.2 Added Value of the Inertia Correction 149
7.3 Conclusion 152

8 Conclusions and Recommendations **153**
8.1 Answers to Research Questions 153
8.2 Additional Conclusions 156
8.2.1 Validity of the Mathematical Descriptions 156
8.2.2 Performance of the Proposed Solutions for Dynamic Distortions 156
8.2.3 Scalability of the HIL Propulsion Drive 157
8.3 Recommendations 158
8.3.1 Regarding the HIL Setup 158
8.3.2 Further Research 159

A Linearised Response of Ideal and Practical Scale Models **161**

B Linearised Closed Loop Including Diesel Engine **167**

C Location of the Wave Probe During Experiments **169**

Acronyms and Abbreviations **171**

Nomenclature **173**

References **177**

Acknowledgements **185**

Curriculum Vitae **187**

Publications **189**

Summary

Requirements on ships are rapidly increasing. In particular, safety and environmental impact are under increasing scrutiny. At the same time, cost and profitability remain as important as they have ever been. These increasingly stringent constraints are beginning to pose problems during the design process. For example, the energy efficiency design index (EEDI) aims to reduce emissions of carbon dioxide by progressively limiting engine power installed on board. However, these reductions in propulsive power raise concerns about the ship's manoeuvrability in rough seas. Moreover, the expected introduction of novel power and propulsion systems based on, for example, fuel cell technology, further raises uncertainty regarding the performance of future ships and propulsion systems in dynamic environments. Considering these developments, detailed predictions of manoeuvrability and propulsion plant behaviour are becoming increasingly important in the ship design process.

Yet, present prediction methods are insufficient to evaluate manoeuvrability and behaviour of ship propulsion systems in complex, dynamic environments such as heavy seas. Fully numerical methods based on computational fluid dynamics (CFD) and first principles are inherently uncertain and compute-intensive. As such, these methods are presently unsuitable to assess the dynamic interaction between machinery and hydrodynamics over prolonged periods of time. As an alternative to numerical methods, experiments with scale model ships can be conducted. However, such experiments are subject to hydrodynamic scale effects: viscous friction, spray formation and propeller cavitation are not the same as at full scale. Moreover, these model ships are powered by considerably simplified propulsion systems, causing entirely different propulsion plant dynamics than at full scale. Ideally, scale model experiments would be conducted with, for example, a perfectly downscaled diesel engine, gearbox and propeller; in practice, however, this is generally not feasible. As such, existing prediction methods leave great uncertainty how future ship designs can simultaneously meet all requirements regarding operational performance, safety and compliance with environmental regulations.

A possible way to bridge this knowledge gap is by conducting hardware in the loop (HIL) experiments in the ship model basin. Such experiments combine numerical simulations with a physical test setup. During HIL experiments with free sailing ship models, the propulsion engine and other machinery are simulated by a computer. These simulations are then used to control an electric motor, powering the propeller of a physical scale model ship. As such, the complex interaction between engine, propeller, hull and environment can be physically reproduced, allowing to assess design choices early on in the ship design process.

However, HIL experiments in the model basin have their limitations, too. As is the case with traditional scale model tests, the flow of water around the hull and propeller is subject to hydrodynamic scale effects, resulting in distortions of forces acting on these components. In addition, despite being controlled by a simulation model of the ship propulsion system, the scale model's propulsion system is fundamentally different from its (downscaled) real counterpart. The scale model is powered by an electric drive, which may introduce additional, unwanted dynamic behaviour. At the same time, the geometry of the electric motor and shaft assembly is likely different from that of the simulated machinery, resulting in different moments of inertia and friction torques. These issues, resulting from dry mechanics and electrodynamics, are referred to as *mechanical scale effects*, and may considerably distort the dynamic behaviour of the scale model propulsion shaft.

The aim in this dissertation is to determine how individual scale effects distort the dynamic behaviour of the propulsion system, from (simulated) machinery to propeller, and subsequently, to investigate how these distortions can be corrected. These objectives are condensed in the following research question:

To what extent can hardware in the loop techniques be used to emulate ship propulsion system dynamics at model scale?

Hydrodynamic scale effects already received detailed attention in past research. Distortions inside the scale model's propulsion system, on the other hand, have remained largely unmentioned. This dissertation therefore concentrates on these mechanical scale effects. To avoid hydrodynamic scale effects as much as possible, the experimental setup is simplified: rather than free sailing ship models, open water experiments are considered in this dissertation. In open water experiments, the model hull is omitted, and the propeller operates in undisturbed, open water. As such, only limited hydrodynamic scale effects on propeller torque and thrust remain, which allows to concentrate on the mechanical scale effects.

As a first step, mathematical descriptions of the scale model propulsion train are derived. These descriptions allow to identify and predict scale effects using fully numerical simulations. Subsequently, the mathematical descriptions are used to formulate solutions for the expected mechanical scale effects. These mathematical descriptions and solutions are then validated by experiments in the towing tank of Delft University of Technology. It is demonstrated that if the proposed solutions for mechanical scale effects are applied, HIL open water experiments can indeed accurately emulate the dynamic behaviour of the full scale propulsion system. As a final step, additional experiments are conducted to illustrate the added value of HIL in the model basin. These experiments show that crucial aspects of the dynamic behaviour of the propulsion system are overlooked if HIL and the proposed corrections are not or only partly applied.

With the introduction of HIL in the ship model basin, a range of new research directions in the fields of marine engineering and hydrodynamics becomes available. Among other applications, HIL experiments allow to make detailed predictions of the performance of ship propulsion systems in realistic, complex environments. As such, HIL in the model basin could accelerate the acceptance and application of new, carbon neutral technologies in the marine industry.

Samenvatting

Eisen aan schepen worden steeds strenger. Veiligheid en impact op milieu en klimaat in het bijzonder krijgen steeds meer aandacht. Tegelijkertijd blijven kosten en rentabiliteit net zo belangrijk als voorheen. Deze verschillende, vaak tegengestelde eisen vormen in toenemende mate een probleem tijdens het ontwerp van schepen. Een voorbeeld hiervan is de energy efficiency design index (EEDI), die werd ingesteld om de uitstoot van CO_2 door de scheepvaart te beperken door een limiet te stellen op het geïnstalleerde motorvermogen. Een te klein motorvermogen kan echter voor onvoldoende manoeuvreerbaarheid zorgen in zwaar weer, wat op zijn beurt weer tot onveilige situaties leidt. Een andere piste naar een schone, klimaatneutrale scheepvaart zijn nieuwe technologieën zoals brandstofcellen. Ook voor deze technologieën geldt echter dat er twijfels zijn over hun toepasbaarheid aan boord van schepen. Door dergelijke onzekerheden is er een toenemende behoefte aan gedetailleerde voorspellingen van voortstuwinginstallaties en de manoeuvreerbaarheid van schepen, ook in complexe, dynamische omgevingen.

De huidige voorspellingsmethoden zijn echter ontoereikend om het gedrag van schepen en voorstuwingssytemen in zulke dynamische omgevingen te onderzoeken. Numerieke methoden zoals computational fluid dynamics (CFD) en simulaties gebaseerd op fysische wetten bevatten vaak aanzienlijke onzekerheden en kosten vaak veel rekenkracht. Deze methoden zijn dus vooralsnog ongeschikt voor het voorspellen van het dynamische interactie tussen machines en hydrodynamica gedurende een lange tijdsspanne. Een andere optie om deze interactie te onderzoeken is door middel van experimenten met schaalmodellen van schepen. Tijdens zulke experimenten treden echter schaaleffecten op: viskeuze rompweerstand, vorming van spatwater en cavitatie rond de propeller zijn bijvoorbeeld niet hetzelfde als op volle schaal. Daarnaast worden de schaalmodellen aangedreven door relatief eenvoudige voortstuwingssystemen die zich anders gedragen dan de systemen op volle schaal. Idealiter zouden proeven op schaal bijvoorbeeld met een perfect neergeschaalde dieselmotor, tandwielkast en propeller uitgevoerd worden; in de praktijk is dit om verschillende redenen niet haalbaar. Zowel fysieke experimenten met schaalmodellen als numerieke methoden zijn dus niet in staat om de onzekerheid met betrekking tot toekomstige scheepsvoortstuwingssystemen geheel weg te nemen.

Experimenten met hardware in the loop (HIL) bieden een mogelijke oplossing voor dit probleem. Zulke experimenten combineren numerieke simulaties met een fysieke testopstelling. Tijdens HIL-experimenten met vrijvarende modellen worden scheepsmotoren en andere machines gesimuleerd door een computer. Deze simulaties worden vervolgens gebruikt om een elektrische motor aan te sturen die op zijn beurt

de propeller van een fysiek schip op modelschaal aandrijft. Zo kan de complexe wisselwerking tussen motor, propeller, romp en omgeving fysiek nagebootst worden. De hieruitvolgende inzichten kunnen het ontwerpproces al in een vroege fase sturen.

Net als bij traditionele experimenten met schaalmodellen treden bij HIL-experimenten echter ook schaaleffecten op. Niet alleen de hydrodynamische krachten, maar ook de mechanische eigenschappen van de fysiek aanwezige, elektrische aandrijflijn van het schaalmodel kunnen aanzienlijk verschillen van de gesimuleerde aandrijflijn. Hierdoor kunnen gewichten, massatraagheden en wrijvingskrachten sterk afwijken, wat tot foutief geschaald dynamisch gedrag kan leiden. Daarnaast kunnen elektrische componenten in de aandrijving die op volle schaal afwezig zijn, verdere verstoringen veroorzaken. Deze verstoringen van elektrische en "droge" mechanische oorsprong worden hier onder de noemer *mechanische schaaleffecten* geplaatst.

Het doel in deze dissertatie is om vast te stellen hoe individuele schaaleffecten het dynamisch gedrag van de voortstuwingsinstalllatie vervormen, van (gesimuleerde) machinekamer tot propeller, en vervolgens te onderzoeken hoe deze vervormingen kunnen worden gecorrigeerd. Deze doelen zijn samengevat in de volgende onderzoeksvraag:

In welke mate kan hardware in the loop gebruikt worden om scheepsvoortstuwingssystemen te emuleren op modelschaal?

Aan hydrodynamische schaaleffecten werd in eerder onderzoek uitgebreid aandacht besteed; schaaleffecten op de aandrijflijn werden echter nog nauwelijks beschreven. Deze mechanische schaaleffecten vormen het onderwerp van deze dissertatie. Om hydrodynamische schaaleffecten te beperken wordt de testopstelling enigszins vereenvoudigd: in plaats van naar vrijvarende scheepsmodellen wordt in deze dissertatie gekeken naar openwaterproeven. Bij openwaterproeven wordt de scheepsromp weggelaten, waardoor de propeller zich door onverstoord, open water beweegt. Daardoor treden er slechts beperkte hydrodynamische schaaleffecten op rond de propeller en kan de aandacht gericht worden op de mechanische schaaleffecten.

Als een eerste stap naar het corrigeren van deze schaaleffecten worden wiskundige beschrijvingen van de aandrijflijn afgeleid. Met deze beschrijvingen kunnen schaaleffecten worden geïdentificeerd en voorspeld. Op basis van deze wiskundige beschrijvingen worden correcties voorgesteld voor de verwachte schaaleffecten. Ter validatie van de wiskundige beschrijvingen en voorgestelde correcties worden vervolgens proeven uitgevoerd in de sleeptank van de Technische Universiteit Delft. Zo wordt aangetoond dat HIL-experimenten inderdaad het dynamisch gedrag van scheepsvoortstuwingssystemen nauwkeurig kunnen nabootsen op schaal, als de voorgestelde correcties toegepast worden. Tenslotte volgen experimenten die de toegevoegde waarde van HIL in de sleeptank aantonen. Deze laatste reeks experimenten laat zien dat cruciale aspecten van de voortstuwingsdynamica over het hoofd worden gezien als HIL en de voorgestelde correcties niet of slechts gedeeltelijk toegepast worden.

De introductie van HIL in de sleeptank opent nieuwe mogelijkheden voor onderzoek in het gebied van scheepswerktuigkunde en hydrodynamica. HIL-experimenten kunnen bijvoorbeeld gebruikt worden om gedetailleerde voorspellingen te maken van de prestaties van scheepsvoortstuwingsinstallaties in complexe, realistische omgevingen. Door dergelijke toepassingen kan HIL bijdragen aan een snelle acceptatie en toepassing van nieuwe, klimaattneutrale technologie in de scheepvaart.

Chapter 1

Introduction*

1.1 Predicting the Performance of Ships

Since ancient times, ships have fulfilled a crucial role in trade and warfare. For example, merchant and naval fleets were instrumental in the expansion of the Roman empire around the beginning of the common era (Dorn and McClellan, 1999). Starting from the 16^{th} century, the increased competition between nations and desire for overseas territorial expansion spurred considerable technological advances in shipbuilding. Sponsored mostly by their governments and fired by curiosity, scientists from various disciplines started investigating the interactions between wind, water and ship; these first developments are described in great detail by Ferreiro (2007). In the late 17^{th} century, Christiaan Huygens described experiments in a towing tank similar to modern towing tank tests (Roach, 2008). Huygens demonstrated that the viscous resistance of an object travelling in a fluid has a square relation with the object's speed; his theories was later expanded and improved by Johan Bernoulli. Another significant step was made by Pierre Bouguer in the first half of the 18^{th} century, when he published his *Traité du navire*. As an important contribution, he introduced the metacentric height as a measure for a ship's stability; this parameter has retained its significance in naval architecture to this day. Similar efforts were conducted Leonhard Euler, who also made significant contributions to the understanding and quantification of ship stability. These are only some of the numerous bright minds who shaped the scientific field of hydrodynamics; the mentioned literature sources present more detailed accounts of the earliest developments in naval hydrodynamics.

In the 19^{th} century, the industrial revolution drove a next wave of scientific development in naval architecture. In the 1860s, systematic towing tank experiments allowed William Froude to formulate scaling laws for ship resistance which still form the basis of modern resistance predictions. In the 20^{th} century, too, developments in the field of naval architecture relied heavily on model scale experiments. Innovations such as the bulbous bow and the small waterline area twin hull (SWATH) were all tested in the model basin before being applied at full scale, as was demonstrated by, for example, Dallinga et al. (1988).

*This chapter is partially based on Huijgens et al. (2018).

As an expansion of experiments with towed models, the ship model can be fitted with a propulsion motor and propeller, allowing to conduct self-propulsion tests. These tests allow to determine required propulsive power and attainable speed, for instance as shown by Hooft (1969). Next to propulsive power and attainable speed, a ship's manoeuvrability is another fundamental aspect of a ship's performance. To assess manoeuvrability, self-propulsion tests were further developed into manoeuvrability tests, with a rudder assembly being added to provide steering capability. In calm water, the manoeuvrability of these scale model compares well to full scale reality, as Smitt (1971) and Hooft and Nienhuis (1994) demonstrated.

However, ship models and basins are simplified and miniaturised representations of full scale reality. As a consequence, the behaviour of the model does not completely correspond to that of the ship it represents, especially in dynamic environments. An important example of such a simplification is the lack of a realistic propulsion system at model scale. When sailing through waves, propeller load fluctuates due to waves and ship motions. At full scale, the ship's propulsion system can often not immediately respond to these fluctuations, resulting in fluctuating propeller speed and machinery load as simulations in this dissertation will demonstrate. These fluctuations may increase the diesel engine's fuel consumption, emissions and wear, while reducing the manoeuvrability of the ship. At model scale, however, the propeller is driven by an electric motor, which can respond much faster than the engines installed on board actual ships. As a result, the propeller speed is practically constant, meaning that dynamic interaction between environment, hull, propeller and machinery is virtually absent in model basin tests. In addition, miniaturisation leads to so-called *hydrodynamic scale effects*, mainly caused by incorrectly scaled viscosity. At model scale, the flow of water around hull and propeller is relatively viscous. As a result, torques and forces at model scale are relatively high and cannot simply be extrapolated to full scale.

At the same time, there has been an increasing interest in advanced ship performance predictions in recent years. Requirements on performance and environmental impact of new ship designs are becoming stricter, requiring increasingly detailed knowledge on practical performance already at early stages of the design process. Naval ships, for example, are subject to increasing manoeuvrability and seakeeping requirements such as the STANAG 4154 standard (Armaoglu et al., 2010). The interaction between the propulsion plant, propeller and environment is an important aspect when assessing whether new designs meet these requirements, as this interaction can play a crucial role for manoeuvrability in waves.

As another example, merchant ships are facing increasingly stringent environmental regulations. This, too, raises the need for more advanced performance predictions. A important development in this respect is the energy efficiency design index (EEDI), introduced by the International Maritime Organisation (IMO) to reduce the emissions of CO_2. In essence, the EEDI puts a gradual limit on the engine power installed in new ships. However, this imposed limit has sparked doubts whether future ships will still have sufficient propulsive power and propeller thrust to ensure safe navigation in adverse weather. The added resistance by waves and the resulting decrease in ship speed – assuming limited propulsive power – can be predicted well with experiments in the ship model basin and, to an increasing extent, with numerical methods (Kim et al., 2017). However, a great deal of uncertainty remains regarding the increased dy-

namic load on propulsion machinery and reduced manoeuvrability in adverse weather if propulsive power is reduced. Noting this potential side effect of the EEDI, Papanikolaou et al. (2015) concluded that general cargo ships, Ro-Ro ferries, bulk carriers and tankers are particularly vulnerable to navigational accidents related to reduced manoeuvrability in adverse conditions. Similar conclusions were drawn by Louzis et al. (2014), who mentioned grounding and collisions near ports as the most frequent type of accidents resulting from insufficient propulsive power and adverse weather.

Limiting the installed engine power is only one of several possibilities to abate emissions. As another option, novel propulsion technologies are considered to replace traditional diesel engines. Fuel cells, for example, are generally considered a key technology for carbon-neutral shipping. However, the dynamic interaction between load and drive is a cause for uncertainty also for these new technologies. As van Biert et al. (2016) noted, the load transient capabilities of fuel cell systems may be rather limited, potentially resulting in the same issues as the EEDI. Without demonstration of these new technologies in a realistic environment, doubts will inevitably remain regarding the practical applicability of new propulsion technologies, complicating the transition towards carbon-neutral ship propulsion.

Considering these developments, methods to predict propeller-engine interaction would provide a welcome extension to current performance prediction methods. Based on the model basin experiments described earlier, one could think of more advanced tests with scale model ships. However, model tests are not the only option: in the past decades, other methods to predict ship performance have seen considerable development, too. For example, computational fluid dynamics (CFD), a collective term for numerical simulation methods for fluid dynamics, play an increasingly important role in ship resistance predictions (Hunt and Zondervan, 2007). However, the computational cost and varying accuracy of these simulations still limit the applicability of CFD in assessments of manoeuvrability (Wang and Walters, 2012; Carrica et al., 2016). As a particular limitation, CFD analysis of propeller performance incorporates simplifications of free surface effects and viscous forces acting on the propeller blades (Krasilnikov, 2013). Exact prediction of flow requires an analytical solution of the highly complex Navier-Stokes differential equations. Since such a solution has not yet been found, approximations must be used such as the Reynolds-averaged Navier-Stokes equations (RaNS). While these approximations are not entirely accurate, they also require considerable computing power. As such, CFD is primarily suited for simulating hydrodynamics over a time range of at most seconds. This does not align with the need for advanced predictions of dynamic interaction between propulsion system and environment: transient behaviour between equilibrium points and dynamic behaviour in waves occurs occur in a time windows of several minutes. As such, CFD is currently not able to evaluate dynamic interaction between propeller and drive with sufficient detail, as was also pointed out by Shigunov et al. (2018).

As another option, one can obtain longer term, numerical predictions of propulsion plant behaviour using simulations based on first principles and regression. Regression-based prediction models are derived from measurements on model scale and full scale ships, the resistance prediction model presented by Holtrop and Mennen (1982) being a notable example. Schulten (2005) combined such regression models and first principles in a fully numerical model, predicting the interaction between the propulsion system, the ship and its environment. Using a similar approach, Calleya et al. (2015)

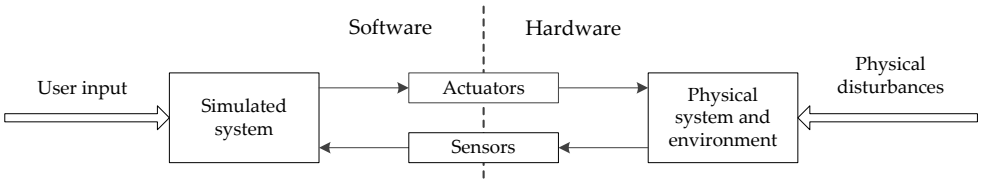


Figure 1.1: Generic diagram of a hardware in the loop setup in which the plant is partly simulated and partly included as hardware, operating in a physical (model scale) environment. Such a setup could be used to emulate interaction between the system and its environment if accurate simulation of all components is infeasible.

proposed a tool to assess the effectiveness of technologies to reduce carbon dioxide emissions by ships. Methods combining first principles and regression models produce reasonably accurate approximations of reality while requiring only limited computational power. However, these methods have a considerable inherent uncertainty, as was pointed out by Tillig et al. (2018). In some cases, this uncertainty may be too high to predict the performance of new technologies with sufficient accuracy. Moreover, these simulations can not be used to evaluate phenomena of which the physics are not yet completely understood, such as air entrainment between the propeller blades.

In general, the aforementioned methods can be divided into strictly hardware or software oriented methods: hardware model scale tests result in physical measurements, while CFD and other software-based methods result in numerical predictions. Both have their advantages, and combining physical models with numerical modules may, in some cases, offer the best of both worlds. In fact, such "hybrid" experiments have already been used for years in the automotive industry and other branches of industry. In these experiments, some components are included as hardware, while other parts of the system are simulated by a software module. This principle is often referred to as *hardware in the loop* (HIL). HIL experiments can be conducted for two reasons. As a first reason, the complexity of some physical phenomena may render them hard to simulate accurately or within a reasonable time frame, while other components can be simulated in an accurate and cost-effective manner. The interaction between propeller hydrodynamics and a ship's propulsion system is an example of such a case. Fig. 1.1 provides a schematic representation of such a HIL setup in a generic case. A second reason to conduct HIL experiments is to test the functioning of a finished product – for instance, a controller – in a simulated environment. In such a case, the schematic layout of the setup becomes different, as is shown in Fig. 1.2. There are numerous examples of both situations in various fields of engineering. Schreiber et al. (2016) described an HIL experiment assessing the dynamics of an automotive brake system design. In the field of power engineering, Li et al. (2006) used HIL to evaluate a new control algorithm for wind turbines. As an additional example, Roinila et al. (2019) demonstrated how a HIL setup can emulate electrical grids on board aircraft, concentrating on the frequency response of power distribution systems.

HIL has also been applied in the maritime field. Skjetne and Egeland (2006) conducted HIL tests for certification of a marine control system, while Johansen et al. (2005) used the same technique to conduct factory acceptance tests of a comparable system. In a similar fashion, Altosole et al. (2007) tested the propulsion control

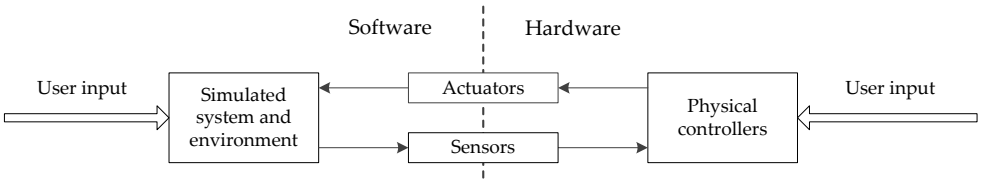


Figure 1.2: Generic diagram of a hardware in the loop setup in which the plant is partly simulated and partly included as hardware, and the environment is entirely simulated. Such a setup could be used to test controllers of a plant which is not yet completely produced.

system of aircraft carrier "Cavour", while Martelli and Figari (2017) described a related approach. Concentrating on electrodynamics, Nounou et al. (2018) conducted HIL tests on a scale model of the propulsion system of a naval ship. They emulated load and drive using two electric motors, controlled by simulation models of the ship, propeller and propulsion machinery. In these four cases, the ship and its environment were largely represented by numerical simulations, with only parts of the propulsion system being included as hardware. This allows to evaluate the response of individual components – mostly controllers – in a simplified, simulated environment. However, there is another way in which HIL can be used in the maritime field. Rather than to simplify and simulate the environment – the environment being the flow of water around hull and propellers –, one could use HIL to include it physically, and completely simulate the machinery instead. As will be shown, this approach has great potential to improve ship performance predictions.

1.2 Hardware in the Loop in the Model Basin

The flow of water around ship hulls and propellers is a highly complex matter and therefore hard to simulate. As such, the most accurate way to include this flow in an experiment is by including it physically. Machinery, on the other hand, can often be accurately simulated, so forces and moments exerted by this machinery can be emulated using simulators and actuators. An example of such a setup was presented by Ueland et al. (2018), who emulated forces from mooring lines and associated machinery on a scale model barge in a basin. They also discussed different sources of errors in their setup, noting the importance of sensor and simulation sample rates.

Similarly, HIL can be used to predict the interaction between propulsion system, hull, propeller and environment. Such experiments could comprise a self-propelled scale model ship in a water basin and a simulation model of the propulsion machinery, as is illustrated by Fig. 1.3. The simulation model controls the scale model's electric propulsion motor. As was demonstrated by Campora and Figari (2003) and Geertsma et al. (2017), ship propulsion system dynamics can be adequately simulated by a numerical model, so emulating realistic propulsion plant behaviour seems feasible. Noting this, Vrijdag (2016) gave an overview of the possibilities of a HIL experiment combining a physical hull and environment and a simulated engine room.

In fact, HIL experiments on ship propulsion performance have already been re-

ported. Ueno et al. (2017) conducted free-sailing model experiments with corrections for viscous friction, investigating the trajectory of a ship model during crash stops. They demonstrated the use of an air fan to overcome additional viscous friction at model scale. Following this, Suzuki et al. (2019) expanded the experiment by taking into account the torque limit of the ship's propulsion engine. As such, static performance limits were taken into account, although the dynamic behaviour of the propulsion system was not simulated. In addition to this, Suzuki et al. (2019) applied a real-time correction for hydrodynamic scale effects on rudder forces, as proposed and demonstrated earlier by Ueno et al. (2014); Ueno and Tsukada (2015); Ueno et al. (2017). They concluded that their setup allows to make reliable predictions of manoeuvrability in calm water and course keeping capabilities in regular waves. Similar experiments were conducted by Bassam et al. (2019), who installed battery power and independent sensors on board a model ship. As a notable advantage, this allowed them to leave the model basin and conduct experiments on a more spacious lake.

Still, the HIL experiments in the aforementioned publications do not provide full insight into the ship's performance, as they neglect the dynamic behaviour of the propulsion system. As such, complex, dynamic interactions between the environment and the propulsion system are neglected. In essence, this means that performance can be predicted only in calm water. In reality, however, perfectly calm seas are quite rare, and ocean going ships regularly face high seas. In such an environment, the ship's propulsion system experiences additional, dynamic loads, and manoeuvrability may be considerably reduced. To be able to predict additional load and reduced performance, more advanced HIL experiments are needed.

Such advanced experiments have already been demonstrated. As a notable example, Tanizawa et al. (2013a,b) conducted HIL experiments with a free sailing scale model ship, and reported oscillating motor torque and speed due to interaction between the simulated engine and real waves. As a next step, Kitagawa et al. (2014) included a thrust fan for dynamic correction for viscous friction. Kitagawa et al. (2015) subsequently introduced a correction on measured propeller torque to account for scale effects on wake fraction, corresponding to the performance prediction method by the International Towing Tank Conference, or ITTC (ITTC, 2014b). They then proceeded to predict average engine torque and speed in a range of wave fields. Later, Kitagawa et al. (2018) predicted dynamic behaviour of the diesel engine by showing time traces of torque, speed and power. They also expanded the diesel engine model by introducing a torque limiter in the governor.

These advanced HIL experiments could be the answer to the knowledge gap regarding dynamic performance of ship propulsion systems. While insights resulting from such experiments can be used to improve the safety and efficiency of new ships, HIL experiments may also accelerate the acceptance of new propulsion technologies with low or zero emissions. Yet, experiments in the model basin are subject to scale effects, potentially resulting in considerable differences with full scale reality and therefore limiting the validity of such experiments. Scale effects on hydrodynamics were already covered in detail in the publications mentioned earlier. However, there are additional, problematic scale effects that have received only limited attention in past literature.

Scale effects also occur inside the propulsion system. Due to different working

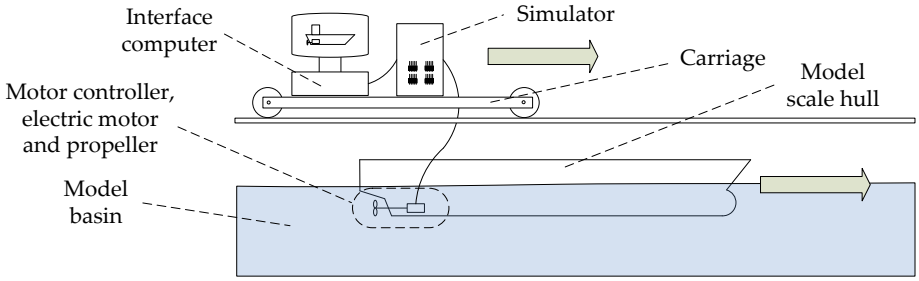


Figure 1.3: Schematic drawing of a HIL experiment with a free sailing scale model ship.

principles and geometries, the propulsion system in the scale model may behave entirely different than the downscaled, real propulsion system. For instance, the scale model is powered by an electric drive, while the actual ship may be powered by a diesel engine or any other kind of prime mover. Consequently, friction torques and moments of inertia likely scale incorrectly, in turn resulting in incorrect shaft accelerations even if load and drive torques are correctly scaled. As another consequence, the electric drive may introduce dynamic behaviour which is not present at full scale. Such scale effects, occurring inside the scale model propulsion system, have remained largely untouched by past literature. As such, it is still not entirely clear whether and how HIL experiments can be used to accurately emulate ship propulsion dynamics. To reduce this uncertainty, this dissertation aims to identify possible scale effects inside the model's propulsion system, and to develop and demonstrate solutions to these scale effects. As a first step towards a detailed problem description, Section 1.3 provides a brief description of scale effects during traditional ship model basin tests.

1.3 Scaling in the Ship Model Basin

Depending on the size of the model basin and hence, the available space for experiments, a geometric scale factor λ must be chosen. This factor is shown in Eq. (1.1), and expresses the relation between the length of the full scale ship, ranging up to several hundred meters, and the length of the scale model, which is usually in the order of several meters. Values for λ may vary considerably for different experiments: whereas Ueno et al. (2018) report experiments at a λ of 110, Pfitsch et al. (2016) conducted experiments at a λ of 20.

$$\lambda = \frac{L_{\mathrm{FS}}}{L_{\mathrm{MS}}} \tag{1.1}$$

For reasons of practicality, ship model experiments are usually conducted in fresh water with ship models that are made of a different material than the real ship. As a result, the density of the ship and environment changes, too. The change is expressed by density scale factor P.

$$P = \frac{\rho_{\mathrm{FS}}}{\rho_{\mathrm{MS}}} \tag{1.2}$$

Table 1.1: Scaling of mass and moment of inertia, assuming varying geometric scale ratio λ and density scale ratio P, from model to full scale.

	λ-power	P-power
Mass	3	1
Moment of inertia	5	1

Table 1.2: Scaling from model to full scale of static mechanisms, assuming that mass and moment of inertia are scaled as shown in Table 1.1.

	λ-power	P-power
Energy	4	1
Force	3	1
Torque	4	1

When the geometry and material density of the prototype and environment scale, mass and moment of inertia inevitably scale, too. The scale factor of these parameters can be expressed as a power of λ and P, as is shown in Table 1.1. Whereas mass and inertia should scale with λ in order to obtain correct model behaviour, effects resulting from changing densities are generally undesired. In some cases, these effects can be corrected by making physical changes to the model. For example, the material of the model hull generally has a relatively low density, resulting in a model which is too light. To counter this, the model is often fitted with ballast weights, restoring mass and moment of inertia of the hull to correct values. Other corrections, such as density corrections for hull resistance, can be made during post-processing of measurement data. If mass and moment of inertia are scaled correctly, static mechanisms, such as gravity-related potential energy, all scale with the same factor. Scale factors for such static mechanisms are given in Table 1.2.

Model basin experiments often involve a moving ship model and a dynamic environment, resulting in time dependent response of the model on its environment. This means that time must be scaled, too. Time scaling in turn implies scaling for time-dependent variables, such as speed, and therefore also of speed-dependent variables, such as different types of dynamic forces. This propagating dependency results in a complex relation between scaling of time, speed and force. As such, scaling of dynamics is more involved than for static parameters such as mass. To illustrate this, White (1998) distinguishes three kinds of *similarity*: geometric similarity, kinematic similarity and dynamic similarity.

Geometric similarity implies that the relative position of each particle is similar, meaning that the shapes of model and full scale objects are exactly the same (where relevant) while their size may be different. *Kinematic similarity* is maintained if the time derivative of all relative positions is similarly scaled. This becomes evident in the velocity vectors, which must all scale at the same ratio, while maintaining their directions. *Dynamic similarity* refers to the scaling of forces. Same as for the speed vectors, the force vectors must all scale in the same way. This implies that the ratios of all forces at model scale (including inertial, gravitational and viscous forces) are

the same as at full scale, at any time and location.

Ideally, model basin tests would be conducted at dynamic similarity. This would allow to extrapolate all forces by multiplication with the same force scaling factor, with no corrections being required to compensate for scale effects. Unfortunately, however, this is physically impossible. Different forces, such as the different components of hull resistance force, result from different physical mechanisms, such as viscous flow mechanisms and wave making mechanisms. These different mechanisms in turn scale differently with speed and thus, time. As such, dynamic similarity is impossible to achieve during most ship model basin experiments. One must choose which force mechanisms are to scale correctly and which mechanisms may become subject to scale effects. In essence, this means that one must choose a scale factor for time, taking into account the relative importance and predictability of different force mechanisms.

The subject of scaling in the ship model basin has been extensively covered in literature. A concise recapitulation of this subject is given here; more detailed accounts were given by, among others, Bertram (1999), Larsson et al. (2010) and Molland et al. (2011). A first option to scale time is by maintaining Froude similarity, as is often done during model basin tests with model ship hulls. Froude similarity implies that the Froude number, shown in Eq. (1.3), is kept the same at model scale and full scale by reducing the speed of the model scale hull. By maintaining Froude similarity, there is dynamic similarity of gravity forces and inertial forces. As a result, wave patterns generated by the ship's hull are correctly scaled. In the case of Froude similarity, this means that forces related to wave making resistance can be extrapolated from model scale to full scale by multiplying forces with a factor λ^3.

$$F_{\mathrm{n}} = \frac{v}{\sqrt{g \cdot L}} \tag{1.3}$$

Froude scaling implies that time intervals decrease in a square root relation with λ, as is shown in Eq. (1.4). In other words, reference time goes faster as the scale model becomes smaller.

$$\frac{\Delta t_{\mathrm{MS}}}{\Delta t_{\mathrm{FS}}} = \sqrt{\frac{L_{\mathrm{MS}}}{L_{\mathrm{FS}}}} = \lambda^{-0.5} \tag{1.4}$$

However, there is more to be scaled than gravity forces. The flow regime around both the scale model and full scale prototype must be the same, too, in order to obtain similar viscous forces. If Froude similarity is maintained, this is not the case: as water behaves relatively viscous at model scale, forces related to viscosity are often too high at model scale. In order to obtain correctly scaled viscous forces, one needs to maintain Reynolds similarity. The Reynolds number R_{n} describes the relation between inertial forces and viscous forces and is shown in Eq. (1.5).

$$R_{\mathrm{n}} = \frac{v \cdot L}{\nu} \tag{1.5}$$

Eq. (1.5) shows that in theory, one could simultaneously obtain Froude and Reynolds similarity by using a liquid with a kinematic viscosity much lower than that of water. Unfortunately, no such liquid exists. As an alternative, one could abandon Froude similarity and increase speed linearly with λ in order to maintain Reynolds similarity. This is completely impractical: no scale model hull or propeller would ever

be able to withstand the forces associated with such speeds. Moreover, a colossal model basin would be required. Given these issues, experiments with scale model ships are never conducted at Reynolds similarity.

Similarly to the Reynolds and Froude numbers, there are dimensionless numbers to quantify scaling of surface tension (Weber number W_{n}), cavitation (Euler number E_{n}) and a multitude of other forces. As with the Reynolds number, however, most of these numbers imply excessive speeds and forces. Therefore, experiments with scale model ships are usually conducted at Froude similarity. This inevitably results in scale effects on viscous friction, spray formation and cavitation. Yet, this is not necessarily problematic: scale effects on surface tension can be reduced to limited levels at practical speeds (Shiba, 1953), while distortions of viscous friction can be analytically corrected – as a notable example, the International Towing Tank Conference has formulated corrections for viscosity during bare hull tests (ITTC, 2011) and open water experiments with propellers (ITTC, 2014a). Another method to reduce viscous effects is to stimulate turbulence by increasing the roughness of the hull. Experiments concentrating on cavitation can be conducted in specialised basins with reduced air pressure, such as MARIN's depressurised wave basin in Ede, the Netherlands. In general, it can be concluded that scale effects related to hydrodynamic forces – from here on referred to as *hydrodynamic scale effects* – are surmountable for most practical applications.

Yet, hydrodynamic scale effects are not the only expected issue. Shaft dynamics also depend on the "dry" components inside the scale model – the term *shaft dynamics* here refers to the dynamic behaviour of load and drive torque and the resulting angular acceleration and speed of the propulsion shaft. As was mentioned earlier, scale models use electric propulsion drives, which respond much faster on load changes than does the real ship's propulsion system. As a result, scale model experiments may overestimate the performance in dynamic environments of the full scale propulsion system. HIL experiments offer the possibility to control the electric motor such that it behaves like a different kind of propulsion motor, as was demonstrated, for example, by Kitagawa et al. (2018).

However, applying HIL in the model basin is not as trivial as it may seem. The different mechanical properties and working principles of the propulsion systems at model and full scale may result in distortions of shaft dynamics (*dynamic distortions*). Although this subject has not received much attention in past research, it does have an importance influence on the accuracy of HIL model basin tests. The experiments reported by Tanizawa et al. (2013b), for example, seem to show a phase shift between simulated and measured shaft torque and speed. This distortion potentially limits the ability of their experiment to predict, among other issues, dynamic overloading of the propulsion engine. In general, four possible sources of dynamic distortions can be distinguished:

1. dynamic response of the scale model's electric motor and controller;
2. friction inside the scale model;
3. moment of inertia of the scale model's propulsion system;
4. hydrodynamic forces around the hull and propeller.

In Chapter 2, these issues will be described in detail. The aim of this dissertation is to address the first three issues in a scientifically substantiated way. As a first step in this direction, Section 1.4 formulates research questions and introduces the considered experimental setup.

1.4 Research Goal and Scope

The goal of this dissertation is to maximise dynamic similarity of HIL experiments in the model basin and full scale ship propulsion systems, resulting in a scientific substantiation of such experiments. The research goal can be condensed into the following main research question:

To what extent can hardware in the loop techniques be used to emulate ship propulsion system dynamics at model scale?

The main research question concentrates on distortions inside the propulsion system rather than hydrodynamics. As such, the flow around the hull is not of particular interest, and a scale model hull does not need to be included in the experiment. Considering this, the *dynamic open water experiment*, as introduced by Huijgens et al. (2018), is investigated here. Contrary to the free sailing HIL experiment shown in Fig. 1.3, the dynamic open water experiment does not include a scale model hull. Instead, the propeller operates in open water, as can be seen in Fig. 1.4. The propeller is powered by an electric motor which is housed in a submerged gondola. This gondola is mounted on a towing carriage which moves forward through the towing tank. The electric motor is controlled by a simulation computer which runs a numerical simulation of a real ship's propulsion system.

This HIL setup allows to evaluate a wide range of innovative propulsion systems. Yet, a proof of principle is easier to deliver with a relatively simple propulsion system. Considering this, a diesel-mechanical plant such as shown in Fig. 1.5 is considered in this dissertation.

To verify whether dynamic similarity of propulsion shaft dynamics is achieved, one can compare the shaft dynamics of the HIL setup with the shaft dynamics of the full scale prototype which it represents. When doing so, however, one must apply scale factors for geometry and time, complicating the comparison. To eliminate these scale factors from the comparison, the *ideal scale model* is introduced. The ideal scale model is a downscaled, virtual prototype, assuming that no scale effects occur. Comparing the dynamic behaviour of the ideal scale model to the response of the *practical scale model*, or *HIL scale model*, dynamic distortions can be identified.

To answer the main research question, results from HIL experiments will be compared to results from fully numerical simulations. Although these simulations may not exactly correspond to an existing full scale system, the comparison does allow to identify distortions in the dynamic behaviour of the HIL experiment.

It was indicated earlier that there are two main reasons for distortions of shaft dynamics during HIL experiments. First, hydrodynamic scale effects can be expected to affect propeller load torque. Second, the propulsion system at model scale may differ completely from the full scale system: rather than an ideal scale model of the full scale propulsion system, an electric drive is often used. This potentially results in

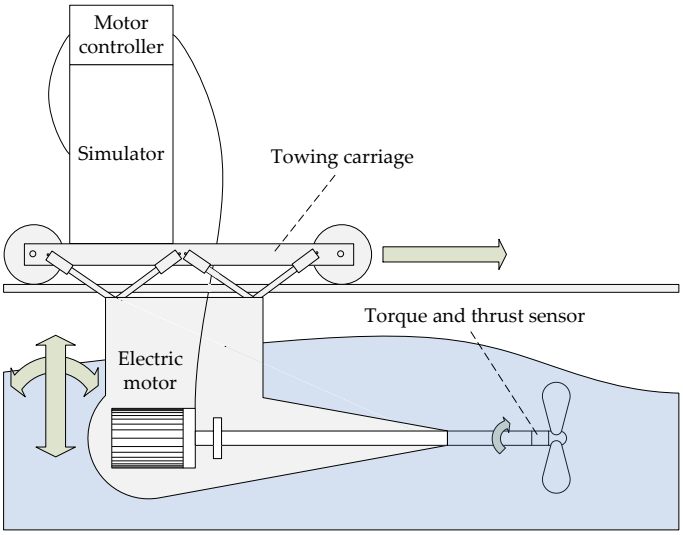


Figure 1.4: Schematic drawing of the considered dynamic open water experiment. The arrows indicate the degrees of freedom of the carriage, gondola and shaft.

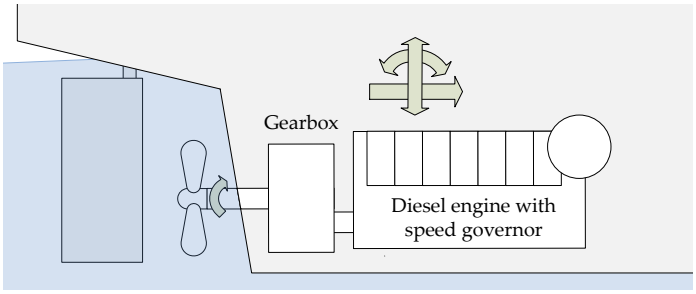


Figure 1.5: Schematic drawing of a diesel-mechanical ship propulsion system. This system represents the full scale situation in this dissertation; simulation models of the diesel engine and gearbox are run on the simulator shown in Fig. 1.4. The arrows indicate the degrees of freedom of the ship and shaft.

unwanted, additional electrodynamics and distorted friction and moment of inertia. These distortions will from here on be collectively referred to as *mechanical scale effects*. As was indicated before, hydrodynamic scale effects were already addressed in detail in past research. Moreover, their influence on the experiments considered here is rather limited, as will be shown later on. On the other hand, much less is known about mechanical scale effects. Considering this, the following research sub questions are formulated:

1. What is the added value of HIL when evaluating ship propulsion systems?
2. Which components are present in the scale model's propulsion system?
3. What are the dynamic properties of these components?
4. Which measures can be taken to avoid distortion of shaft dynamics by these components?
5. How can these measures be applied in dynamic open water experiments?

These questions are not necessarily answered in the same order as they are posed here. For example, an answer to the first answer is found by comparing the results from HIL experiments and traditional open water tests. Yet, to be able to conduct accurate HIL experiments, the other sub questions must be answered first. Therefore, the first sub question is answered only in Chapter 7.

Answers to the second and third sub questions follow from a detailed description and mathematical analysis of the HIL setup. This analysis is conducted in Chapter 2. Components relevant for shaft dynamics are identified, and mathematical descriptions of the scale model and full scale system are derived.

Using the mathematical descriptions derived in Chapter 2, methods to correct expected distortions of shaft dynamics are developed in Chapters 3 through 5. As such, the fourth question is answered. To answer the fifth sub question, these theoretical solutions are demonstrated in HIL experiments in the ship model basin of Delft University of Technology (TU Delft). These experiments are described in detail in Chapters 6 and 7. The approach to answering the research questions is explained in more detail in Section 1.5.

1.5 Research Approach

1.5.1 Dissertation Structure

In general, the approach in this dissertation is to first derive non-linear descriptions of the full scale propulsion system and its HIL equivalent at model scale. These non-linear descriptions are then linearised, which allows to evaluate shaft dynamics in the frequency domain and thus, investigate dynamic distortions related to scale effects. In addition, the linear descriptions are used to find solutions for such distortions. These solutions can then be demonstrated in linear and non-linear simulations, and finally, be applied in actual HIL experiments. This approach is visualised in Fig. 1.6.

In Chapter 2, a first step is made by deriving non-linear and linear descriptions of the ideal and practical scale models. As a second step, expected scale effects on

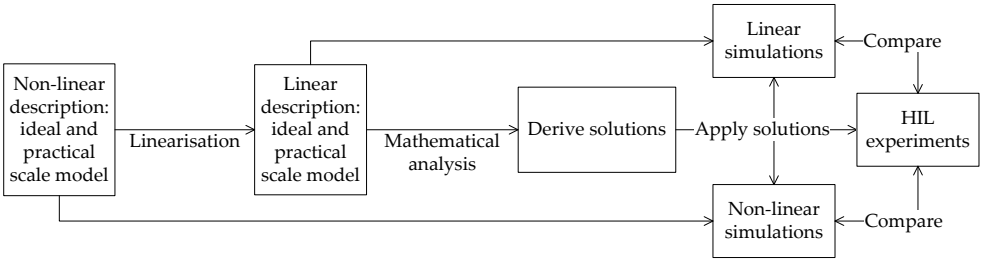


Figure 1.6: Graphic representation of the approach in this dissertation. Using non-linear and linear descriptions, scale effects can be evaluated in a simulated environment, and solutions can be derived. Finally, these solutions can be demonstrated in actual HIL experiments.

shaft dynamics are identified and evaluated using these mathematical descriptions. The third step is made in Chapters 3 and 4, in which methods to avoid distortions by electrodynamics and incorrect moments of inertia are presented. Chapter 5 subsequently introduces a method to compensate for friction torque as well as to identify important physical parameters of the HIL test setup.

With the theory and preparatory work described, Chapter 6 proceeds to the experimental phase of the research. Shaft dynamics resulting from HIL experiments are compared to simulated shaft dynamics. As such, it is verified that the mathematical descriptions indeed correspond to physical reality, and that the proposed corrections indeed reduce scale effects to an acceptable level.

In Chapter 7, additional measurements are presented, with the setup operating in a more complex environment. Propeller ventilation is a highly non-linear and difficult to model phenomenon, making it an interesting demonstration case. The final range of experiments therefore concentrates on the response of the emulated ship propulsion system and the traditional, constant-speed open water setup to the similar propeller ventilation events. Although these measurements cannot be easily compared to simulations, they do allow to demonstrate the added value of HIL experiments through qualitative analysis. Finally, Chapter 8 formulates conclusions and recommendations, exploring future applications of HIL in the ship model basin.

All measurement data presented in this dissertation were published in a dedicated folder on the 4TU.ResearchData repository (Huijgens, 2020). Every Figure containing measurement data is accompanied by a reference to the relevant data files. Data were recorded using the dSPACE ControlDesk and MATLAB software packages, as will be explained in Chapter 5. Data files have the MAT format (.mat). In addition to these data files, the repository contains MATLAB scripts that can assist with visualising the stored measurement data.

Before moving on to Chapter 2, it is useful to pay some more attention to the definition of shaft dynamics, and on the different ways in which these dynamics can be visualised. Section 1.5.2 elaborates on this subject, introducing and substantiating the approach in this dissertation.

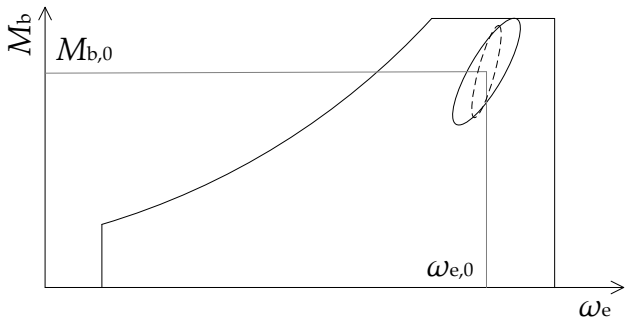


Figure 1.7: Examples of operating ellipses in the motor diagram, resulting from sinusoidal variations of engine speed setting $\omega_{e,set}$. The ellipses represent the dynamic load of a (simulated) diesel engine. The two ellipses correspond to different frequencies of speed setting fluctuations, the dashed ellipse resulting from the highest frequency.

1.5.2 Visualising Shaft Dynamics

Shaft dynamics can be visualised in several ways. A first option is to plot recorded data in time series. Such plots show signal states at every single time step, resulting in clear and intuitive representations of step changes and irregular occurrences such as propeller ventilation events.

As an alternative to time series, shaft dynamics can be visualised by plotting the simulated prime mover's operating ellipse. In such a representation, engine brake torque M_b is plotted versus engine speed ω_e. As such, the operating ellipse is the path described by the engine's operating point when the ship is sailing through regular waves; schematic examples of such ellipses are shown in Fig. 1.7. When drawn in the motor diagram, it shows which of the operating limits of the prime mover are first met as loads increase or fluctuate. Operating ellipses offer a quick and intuitive comparison of engine behaviour, especially to those with experience in the field of marine engineering. As a specific advantage over time plots, operating ellipses allow to more easily compare response on different input frequencies. While the size, shape and orientation of the ellipse may vary depending on the frequency, the ranges of torque and speed are more or less the same. This allows to plot operating ellipses corresponding to multiple input frequencies in a single, comprehensive figure.

Time domain plots and operating ellipses can clearly visualise shaft dynamics for a limited range of input frequencies. Sometimes, however, one wants to predict dynamic response on a wide range of input frequencies. For example, one may need to know at which frequencies dynamic similarity is achieved. For such cases, analysis in the frequency domain may be more suited, which means that response is evaluated with respect to frequency rather than time. Specifically, magnitudes and phases of a signal's response can be plotted in a Bode diagram as will be shown in Fig. 2.10. From a Bode diagram, one can easily see whether or not dynamic similarity is achieved. Two systems are dynamically similar if (1) the amplification (or gain) is the same, and (2) the phase between response and input signals is the same.

Although frequency domain analysis is a powerful tool to evaluate systems for a wide range of input frequencies, it is primarily suited to evaluate linearised, mathe-

matical descriptions of systems. Generating Bode plots from actual HIL experiments is considerably more involved. Since physical dynamics occur in the time domain rather than the frequency domain, response on each frequency has to be evaluated in a separate HIL experiment. As such, generating Bode diagrams from HIL experiments becomes rather laborious.

Depending on the type and purpose of the experiment or simulation, different methods for visualisation may be used in this dissertation. In general, Bode plots will be used mainly to present results from linear simulations, while results from HIL experiments will mostly be visualised using operating ellipses.

Chapter 2

Problem Description*

This Chapter mainly concentrates on answering the second and third research sub questions, as they were formulated in Section 1.4. These questions are the following:

- Which components are present in the scale model's propulsion system?
- What are the dynamic properties of these components?

To answer these questions, the HIL setup as well as the full scale propulsion system are analysed in detail. Using block diagrams, individual components in these systems and connections between these components are described. Based on these diagrams, mathematical descriptions are derived. These descriptions in turn allow to simulate the dynamic behaviour of the ideal scale model and the practical scale model, or HIL setup.

The practical scale model may be considerably different from the ideal scale model, potentially resulting in distorted shaft dynamics. These distortions will receive detailed attention in this Chapter, too. In Chapter 1, four possible sources of such distortions were already identified:

1. unwanted dynamic behaviour of the scale model's electric motor and controller;
2. friction specific to the scale model;
3. incorrectly scaled moment of inertia of the propulsion system;
4. hydrodynamic scale effects.

These issues become more clear if one compares the schematic drawings of the full scale and model scale propulsion systems, given in Figs. 2.1 and 2.2 respectively. As can be seen, the full scale system lacks an electric propulsion drive (or *closed electric loop*), while the three blocks representing friction, moment of inertia and propeller hydrodynamics may contain different parameters than in the practical scale model.

The dynamic performance of the electric drive depends on how fast the current controller of the electric motor can regulate motor current and hence, torque. As such

*This chapter is partially based on Huijgens et al. (2018).

a controller and electric motor are not present at full scale, they should not introduce any additional shaft dynamics at model scale. However, if the controller is not tuned properly, this may very well be the case, as will be shown further on in this Chapter. The second and third issues are related to the mechanical properties of the model propulsion system. Friction inside the full scale and model scale propulsion motors, bearings and shafting may not scale correctly because of different working principles. For the same reason, the mass moment of inertia of these components may scale incorrectly, too. As a result, the response on changing load or drive torque may not be the same. This can be solved by real-time correction of the simulated drive torque, as will be demonstrated in this dissertation. The last issue is related to differences in hydrodynamic forces acting on the model and full scale hull and propeller, mainly because of incorrectly scaled viscosity. This, too, may influence shaft dynamics.

In order to obtain correctly scaled shaft dynamics, these scale effects must be investigated in more detail and if necessary, corrected. As a first step in this direction, this Chapter presents mathematical descriptions of the ideal and practical model scale propulsion systems. These descriptions are then used to graphically illustrate the scale effects in a wide range of frequencies. In subsequent Chapters, the descriptions are used to mathematically analyse the mechanisms behind these scale effects and formulate solutions. As such, the descriptions derived in this Chapter fulfil a crucial role throughout the dissertation.

To obtain mathematical system descriptions, non-linear descriptions of propulsion system components are first formulated, while block diagrams are introduced to provide an overview of the considered systems in their entirety. Combining these non-linear descriptions with the block diagrams, non-linear simulation models can be developed, allowing to simulate shaft dynamics of the ideal and practical scale in the time domain. In addition, the non-linear descriptions and block diagrams are used to derive linearised transfer functions. Although these linear descriptions are a simplification of non-linear reality, they facilitate the analysis of shaft dynamics in the frequency domain, and allow to capture crucial aspects of system behaviour in a small set of parameters.

The solutions presented in Chapters 3 and 4 are mainly based on linear descriptions, too, as these descriptions are particularly convenient for mathematical analysis. In Chapter 6, it will be verified that the proposed solutions indeed result in correctly scaled shaft dynamics also for non-linear phenomena.

2.1 Layout of the Scale Models

2.1.1 Ideal Scale Model: Diesel-Mechanical Propulsion System

The full scale case considered in this dissertation is a refrigerated cargo ship with a service speed of 19 knots. As was mentioned in Section 1.4, the ship is powered by a constant speed diesel-mechanical propulsion system; a schematic drawing of this system was shown in Fig. 1.5. The prime mover is a four stroke diesel engine with a nominal brake power of 8336 kW, which drives a Wageningen C4-40 propeller with a diameter of 4.2 m through a gearbox. Although this configuration does not exactly

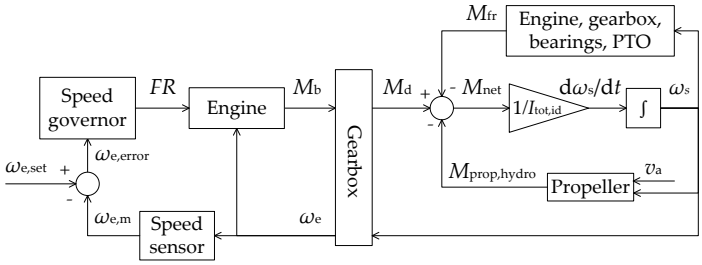


Figure 2.1: Block diagram of the ideal scale model from speed setting to shaft speed. The ideal scale model is the full scale propulsion system, scaled down without any distortions.

match a known full scale equivalent, it combines readily available simulation models and an available, well-documented scale model propeller in a realistic reference case.

The diesel engine runs at a constant speed $n_{e,nom}$. Engine speed is regulated by a PI controller, as is common in modern merchant ships (Bondarenko and Kashiwagi, 2010). The gearbox reduces engine speed by a factor of 3.4965, resulting in a propeller shaft speed n_s. The Wageningen C4-40 propeller belongs to a series of controllable pitch propellers developed by Maritiem Research Instituut Nederland (MARIN); the Wageningen C series is described in detail by Dang et al. (2013). The propeller used in this dissertation has a design P/D ratio of 1.0. The actual P/D ratio is fixed at 1.3 throughout the experiments, which means that the C4-40 is essentially used as a fixed pitch propeller here.

The main parameters of the full scale propulsion system and the corresponding ideal scale model are given in Table 2.1 – the parameters will be explained in more detail in Section 2.2. Fig. 2.1 presents a block diagram of this system. It can be noted that the equilibrium torque and fuel rack setting, given in Table 2.1, are relatively low. This is because a part of the propulsion engine's power is reserved for a power take-off (PTO) such as a shaft generator. To simplify linearisations and simulation models, PTO loads are not included in this dissertation.

If one would be able to scale down this diesel-mechanical system while avoiding scale effects, one would obtain the ideal scale model. This ideal scale model would be dynamically similar to the full scale propulsion system, and is therefore considered the reference case. As Froude similarity is maintained, parameters and variables are scaled from ideal model scale to full model scale according to Table 2.2.

In addition to the parameters of the ship, the environmental conditions are relevant, too. These conditions are the same for the full scale ship and the ideal scale model, and are given in Table 2.3. The water density at full scale is taken at 1000 kg/m^3 to facilitate comparison with experimental measurements.

2.1.2 Practical Scale Model: HIL Setup

Unfortunately, ideal scale models are practically infeasible in the case of ship propulsion systems. A miniaturised diesel engine would introduce a multitude of additional scale effects, for example, related to combustion dynamics, as well as practical issues

Table 2.1: Main parameters and equilibrium values of the full scale (FS) and ideal model scale (id. MS) propulsion systems. The geometric scale factor λ equals 17.9; time is scaled according to Froude's law. The propeller is a Wageningen C4-40 with a design P/D ratio of 1.0. The parameters and variables given here are described in detail in Section 2.2.

	Symbol	Unit	FS	id. MS
Nom. eng. power	$P_{\mathrm{b,nom}}$	[W]	8336×10^3	343.5
Eq. eng. power	$P_{\mathrm{b},0}$	[W]	6926×10^3	285.5
Nom. eng. torque	$M_{\mathrm{b,nom}}$	[Nm]	159.2×10^3	1.551
Eq. eng. torque	$M_{\mathrm{b},0}$	[Nm]	132.3×10^3	1.289
Nom. eng. speed	$n_{\mathrm{e,nom}}$	[rpm]	500	2115
Eq. eng. speed	$n_{\mathrm{e},0}$	[rpm]	500	2115
Min. eng. speed	$n_{\mathrm{e,min}}$	[rpm]	200	846.2
Nom. eng. speed	$n_{\mathrm{e,max}}$	[rpm]	500	2115
Norm. eq. eng speed	$n_{\mathrm{e},0}^{=}$	[−]	1	1
Governor static gain	$K_{\mathrm{p},\omega}$	[−]	1	1
Governor int. gain	$K_{\mathrm{i},\omega}$	[−]	0.5	2.12
Min. FR setting	FR_{min}	[mm]	10	10
Max. FR setting	FR_{max}	[mm]	40	40
Eq. FR setting	FR_0	[mm]	34.93	34.93
Norm. eq. FR setting	$FR_0^{=}$	[−]	0.831	0.831
Eng. derivative	g	[−]	−0.25	−0.25
Gearbox reduction	i_{gb}	[−]	3.4965	3.4965
Eq. prop. torque	$M_{\mathrm{prop,hydro},0}$	[Nm]	462.5×10^3	4.505
Eq. prop. thrust	$T_{\mathrm{prop},0}$	[N]	572.8×10^3	99.87
Eq. prop. speed	$n_{\mathrm{s},0}$	[rpm]	143	605
Mech. inertia	I_{mech}	[kgm^2]	54.58×10^3	0.029 70
Prop. P/D ratio	P/D	[−]	1.3	1.3
Prop. diameter	D	[m]	4.199	0.2346
Prop. advance speed	v_{a}	[m/s]	7.33	1.73
Ship speed	v_{s}	[m/s]	9.77	2.31

such as spatial requirements. As an alternative, a hardware in the loop (HIL) setup is considered in this dissertation; Fig. 1.4 shows a schematic drawing of such a setup.

In the full scale system considered in this thesis, drive torque is developed by a diesel engine. In the HIL setup, on the other hand, drive torque is simulated by a numerical model of the prime mover, running on a simulation computer. The computer communicates the simulated drive torque to an electric motor (in this case a permanent magnet synchronous machine, or PMSM) via a motor drive. The PMSM then exerts torque on the propeller shaft on which a scale model propeller is mounted. The balance of load and drive torque results in dynamic response of shaft speed. The shaft speed is measured and subsequently fed back to the simulation computer. Using the measured shaft speed and the simulated prime mover torque from the previous time step, the diesel engine simulation model calculates a new torque, after which the loop is reiterated.

Table 2.2: Scaling factors from ideal model scale to full scale of parameters and variables. The densities of materials inside and around the ideal scale model are the same as at full scale. Time is scaled maintaining Froude similarity.

	λ-power
Distance	1
Energy	4
Force	3
Linear speed	0.5
Mass	3
Moment of inertia	5
Power	3.5
Rotative speed	−0.5
Time	0.5
Torque	4

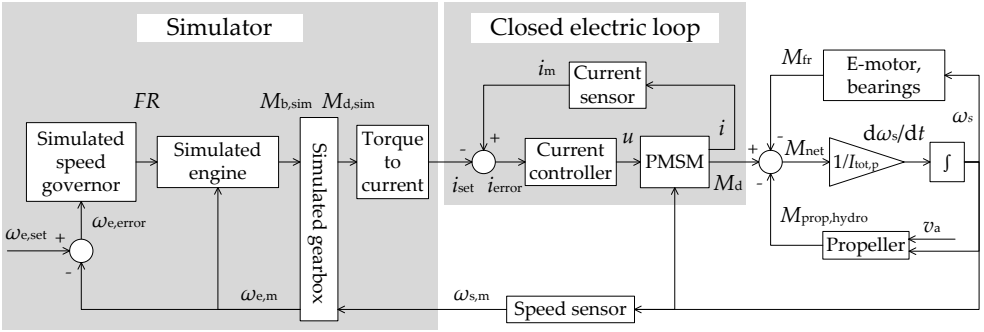


Figure 2.2: Block diagram of the practical scale model's propulsion system from speed setting to shaft speed.

Table 2.3: Parameters of the environment in which the full scale ship and ideal scale model are operating.

	Symbol	Unit	
Gravity constant	g	[N/kg]	9.81
Water density	ρ_{H2O}	[kg/m^3]	1000
Water kinematic viscosity	ν	[m^2/s]	1.17×10^{-6}

Table 2.4: Parameters of the electric drive, powering the practical scale model. Detailed descriptions of these parameters and variables are given in Section 2.2.

	Symbol	Unit	Value
Torque constant	k_{t}	[Nm/A]	0.55
Back EMF constant	k_{e}	[Vs/rad]	0.55
Terminal resistance	R	[Ω]	0.555
Terminal inductance	L	[H]	3.6×10^{-3}
Max. terminal voltage	$u_{\max}$	[V]	400

Parameters of the electric drive are given in Table 2.4. Equilibrium values of the practical scale model must be identified during actual experiments and are thus not yet given here. The mentioned parameters will be explained further in Section 2.2. The practical scale model is represented by the block diagram shown in Fig. 2.2.

The diesel engine is simulated as a fuel injection map which determines brake torque as a function of engine speed and fuel rack setting, as was proposed by Vrijdag and Stapersma (2017). Dynamic behaviour of the turbocharger is neglected, which means that delays in available air for combustion are not taken into account. A considerable, stepwise increase of injected fuel may cause the air-to-fuel ratio to drop to a level where not all fuel is burnt, temporarily limiting engine torque. In practice, however, this dynamic limit is usually accounted for by limiters in the speed governor (Vrijdag and Stapersma, 2017). Here, it is assumed that the settings of the speed governor result in a sufficiently smooth response of the fuel rack setting on disturbances, rendering a model based on a fuel injection map sufficient to assess shaft dynamics. This approach results in a simpler simulation model, requiring less numerical power during HIL experiments while also facilitating linearisation.

2.2 Non-linear Descriptions: Ideal and Practical Scale Models

2.2.1 Ideal Scale Model

In this Section, non-linear mathematical descriptions of the components in Fig. 2.1 are introduced. By connecting the inputs and outputs of these mathematical descriptions, one obtains a non-linear simulation model of the ideal propulsion system. A full scale validation of the behaviour of the diesel engine and gearbox is outside the scope

of this dissertation. It is assumed that the non-linear descriptions of these components, as derived in this Section, are accurate representations of the diesel-mechanical propulsion system.

The general equation for propulsion shaft dynamics is given in Eq. (2.1). In brief, the combination of drive torque, friction torque and propeller load torque results in a shaft acceleration inversely proportional to the moment of inertia of the system.

$$I_{\mathrm{tot,id}}(t) \cdot \frac{\mathrm{d}\omega(t)}{\mathrm{d}t} = M_{\mathrm{d}}(t) - M_{\mathrm{fr}}(t) - M_{\mathrm{prop,hydro}}(t) \tag{2.1}$$

In the non-linear description, drive torque M_{d} equals the brake torque M_{b} of the diesel engine, multiplied by the gearbox box reduction ratio i_{gb}. This relation is expressed by Eq. (2.2).

$$M_{\mathrm{d}}(t) = M_{\mathrm{b}}(t) \cdot i_{\mathrm{gb}} \tag{2.2}$$

Shaft speed is converted by the same gearbox reduction factor, though in the opposite direction. The diesel engine is represented by a fuel rack map, which maps engine brake torque M_{b} as a function of engine speed n_{e} (in rpm) and fuel rack setting FR (in mm). Such a fuel rack map is mathematically described by Eq. (2.3) and visualised by Fig. 2.3. Parameter g in Eq. (2.3) equals the engine derivative.

$$M_{\mathrm{b}}(t) = \left(\frac{FR(t) - FR_{\mathrm{min}}}{FR_{\mathrm{nom}} - FR_{\mathrm{min}}} + g \cdot \frac{n_{\mathrm{e}}(t) - n_{\mathrm{e,nom}}}{n_{\mathrm{e,nom}} - n_{\mathrm{e,min}}} \right) \cdot M_{\mathrm{b,nom}} \tag{2.3}$$

Dynamic behaviour of the turbocharger is neglected, which means that delays in available air for combustion are not taken into account. In reality, a considerable, stepwise increase of injected fuel may cause the air-to-fuel ratio to drop to a level where not all fuel is burnt, temporarily limiting engine torque. In practice, however, this dynamic limit is usually accounted for by limiters in the speed governor (Vrijdag and Stapersma, 2017). Here, it is assumed that the settings of the speed governor result in a sufficiently smooth response of the fuel rack setting on disturbances, rendering a model based on a fuel injection map sufficient to assess shaft dynamics. As a key benefit, such a model can be linearised more easily, as will prove useful in the Sections to follow. Moreover, improving existing prime mover simulation models is outside the scope of this paper; no further attention is paid here to the validity of the diesel engine model. On the load side of the propulsion shaft, one can distinguish friction torque M_{fr} and hydrodynamic propeller load torque $M_{\mathrm{prop,hydro}}$. Friction torque of the diesel-mechanical propulsion system is a subject in the field of tribology, which is outside the scope of this dissertation. Considering this, friction inside the engine, gearbox and bearings of the ideal scale model is not considered, as is the case for torque absorbed by PTO machinery such as shaft generators.

Propeller load torque is described by Eq. (2.4), in line with Kuiper (1992). Torque coefficient K_{Q} is a function of advance ratio J, which in turn is a function of shaft speed ω_{s}, propeller advance speed v_{a} and propeller diameter D; this relation is written out in Eq. (2.5). Interaction between the hull and propeller is outside the scope of this dissertation, which implies that the propeller operates in open water. Relative rotative efficiency η_{r} of the propeller is therefore taken as 1, and not further included in the mathematical descriptions.

$$M_{\mathrm{prop,hydro}}(t) = \rho \cdot \left(\frac{\omega_{\mathrm{s}}(t)}{2\pi} \right)^2 \cdot D^5 \cdot K_{\mathrm{Q}}(J(t)) \tag{2.4}$$

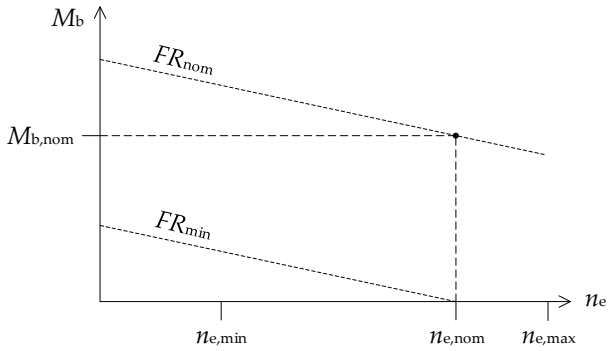


Figure 2.3: Visualisation of a fuel rack map as used to model the diesel engine in this dissertation.

$$J(t) = \frac{2\pi \cdot v_a(t)}{D \cdot \omega_s(t)} \tag{2.5}$$

The acceleration of the shaft is also a function of the moment of inertia of the drive train. The total moment of inertia, $I_{tot,id}$, is the sum inertia of the diesel engine, gearbox and shaft ($I_{mech,id}$), inertia of the propeller ($I_{prop,id}$), and inertia of the water entrained between the propeller blades (I_{H2O}). Values for $I_{mech,id}$ and $I_{prop,id}$ can be obtained from manufacturers. On the other hand, entrained mass and the resulting added inertia are a much more complicated hydrodynamic phenomenon. Considering its complex nature, added inertia is not yet considered in this Chapter. This subject will receive further attention in Chapter 4.

To control the speed of the propulsion system, a PI controller (or PI governor) is introduced. Before giving a mathematical description of this controller, some attention is paid to the input and output signals. One could directly supply measured and set shaft speed, expressed in rpm, to the speed controller, and define the output as a fuel rack setting in mm. In practice, however, the input and output signals – measured shaft speed n_e and fuel rack setting FR – are often scaled between minimum and nominal values for n_e, and between minimum and maximum values for FR. Scaling to standardised shaft speed $n_e^=$ and from standardised fuel rack setting $FR^=$ is described by Eqs. (2.6) and (2.7), and illustrated by Figs. 2.4 and 2.5. As such, governor settings for diesel engines become more or less standardised. Eq. (2.8) shows how the PI controller calculates a standardised fuel rack command from measured and set standardised shaft speeds.

$$n_e^= = \begin{cases} 0, & \text{if } n_e \leq n_{e,min} \\ \frac{n_e - n_{e,min}}{n_{e,nom} - n_{e,min}}, & \text{otherwise} \end{cases} \tag{2.6}$$

$$FR = \begin{cases} FR_{min}, & \text{if } FR^= < 0 \\ FR_{min} + FR^= \cdot (FR_{max} - FR_{min}), & \text{if } 0 \leq FR^= \leq 1 \\ FR_{max}, & \text{otherwise} \end{cases} \tag{2.7}$$

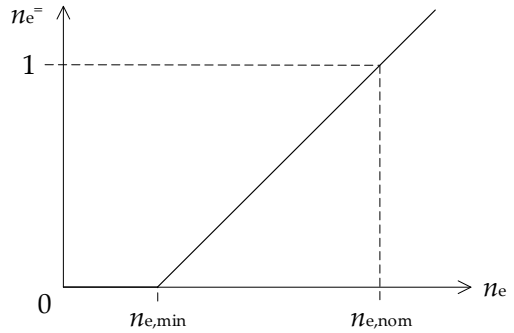


Figure 2.4: Scaling of engine speed governor input, measured shaft speed, as is commonly done in shaft speed governors of marine diesel engines.

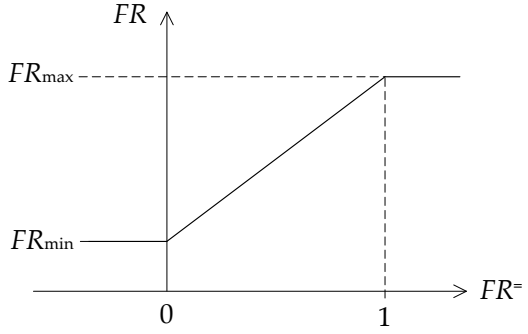


Figure 2.5: Scaling of engine speed governor output, fuel rack setting, as is commonly done in shaft speed governors of marine diesel engines.

$$FR^{=}(t) = K_{\mathrm{p},\omega} \cdot \left(n^{=}_{\mathrm{e,set}}(t) - n^{=}_{\mathrm{e}}(t)\right) + K_{\mathrm{i},\omega} \cdot \int_0^t \left(n^{=}_{\mathrm{e,set}}(t) - n^{=}_{\mathrm{e}}(t)\right) \mathrm{d}t$$

$$= K_{\mathrm{p},\omega} \cdot n^{=}_{\mathrm{e,error}}(t) + K_{\mathrm{i},\omega} \cdot \int_0^t n^{=}_{\mathrm{e,error}}(t)\mathrm{d}t \tag{2.8}$$

Eq. (2.8) shows that the PI controller has a static gain term and a time-dependent integration term. When conducting scale model experiments, time scaling must be taken into account for all time-dependent phenomena, including operations inside the shaft speed controller. This means that, while $K_{\mathrm{p},\omega}$ does not require scaling from full scale to model scale, $K_{\mathrm{i},\omega}$ does. Eq. (2.9) shows how shaft speed controller settings are scaled from full scale to model scale, assuming Froude time scaling.

$$K_{\mathrm{p},\omega,\mathrm{MS}} = K_{\mathrm{p},\omega,\mathrm{FS}} \tag{2.9a}$$

$$K_{\mathrm{i},\omega,\mathrm{MS}} = K_{\mathrm{i},\omega,\mathrm{FS}} \cdot \lambda^{0.5} \tag{2.9b}$$

Although the shaft speed sensor is displayed as a separate component in Fig. 2.1, it is assumed in this dissertation that it does not introduce any additional propulsion shaft dynamics. Therefore, it is not separately included in the non-linear description. With all components of the ideal scale model now described, Section 2.2.2 proceeds to present non-linear descriptions for the practical scale model.

2.2.2 Practical Scale Model

Before proceeding to non-linear descriptions of individual components, differences between the practical and ideal scale models are identified by comparing the block diagrams in Fig. 2.1 and Fig. 2.2. First, the governor, engine and gearbox are no longer physically present, but included as simulations. Second, an additional subsystem is introduced: the closed electric loop. This loop represents the electric propulsion drive, which is to emulate the ideal propulsion system. Third, friction, moment of inertia and hydrodynamic propeller load are physically present in the practical scale model, but may not be the same is for the ideal scale model.

The first difference, simulating rather than physically including the diesel-mechanical propulsion system, will not receive further attention in this dissertation. As was mentioned in Section 2.2.1, validating the simulation model of the diesel-mechanical propulsion system is outside the scope of this dissertation. It is assumed that the non-linear descriptions and resulting simulation models are accurate, and that simulating rather than physically including components does not affect the dynamic behaviour of the propulsion shaft.

On the other hand, the two remaining differences may have a considerable effect on propulsion shaft dynamics. In previous Sections, dynamic behaviour of the electric propulsion drive was already mentioned as a possible source of dynamic distortions. In addition, changes in friction torque, moment of inertia and hydrodynamic propeller load were identified as relevant for shaft dynamics, too. In essence, the practical scale model is an expansion of the ideal scale model: a number of components are added, while the physical properties of components also present in the ideal scale model may be different. Only properties of components that are simulated in the practical scale

model remain identical. Considering this, a non-linear description of the electric loop is introduced, following which the effect of different physical properties is evaluated.

As the central component in the electric loop, the electric motor is described first. Permanent magnet synchronous machines (PMSM) are particularly suited for the HIL setup's electric propulsion system because of their compactness, and because their torque can be controlled relatively easily. Drive torque of these machines is proportional to winding current by torque constant k_t, which is referred to as the motor torque constant. This relation is expressed by Eq. (2.10).

$$M_\mathrm{d}(t) = k_\mathrm{t} \cdot i(t) \tag{2.10}$$

The relation between voltage, speed and current of the PMSM is described by Eq. (2.11). Terminal voltage u has a maximum value u_max.

$$L \cdot \frac{\mathrm{d}i\,(t)}{\mathrm{d}t} = -k_\mathrm{e} \cdot \omega\,(t) - R \cdot i\,(t) + u\,(t) \tag{2.11}$$

R and L are the terminal resistance and inductance of the electric motor, respectively. Using the the law of conservation of energy, one could show that torque constant k_t and back EMF constant k_e have practically equal values. Both variables will therefore be represented by k_t from here on.

The aim of the dynamic open water experiment is to emulate drive torque of the ideal propulsion system, which means that torque and therefore winding current of the electric motor must be precisely controlled. To this end, a PI controller for current is introduced. The current controller regulates voltage based on the difference between the measured current and the current set point; Eq. (2.12) gives a mathematical description of this operation.

$$\begin{aligned} u(t) &= K_\mathrm{p,i} \cdot (i_\mathrm{set}(t) - i_\mathrm{m}(t)) + K_\mathrm{i,i} \cdot \int_0^t (i_\mathrm{set}(t) - i_\mathrm{m}(t))\,\mathrm{d}t \\ &= K_\mathrm{p,i} \cdot i_\mathrm{error}(t) + K_\mathrm{i,i} \cdot \int_0^t i_\mathrm{error}(t)\mathrm{d}t \end{aligned} \tag{2.12}$$

Often, the current controller and sensor are integrated into the motor drive which also commutates the motor. Since motor drives contain proven, off-the-shelf technology, it is assumed that commutation and current measurement is done sufficiently fast to avoid dynamic distortions. This means that the current sensor block, shown in Fig. 2.2, is not further considered.

The physical components in the HIL setup, located on the right in Fig. 2.2, are governed by the same equations as in the ideal scale model. However, parameters in these equations such as moments of inertia and friction coefficients may have different values. This, too, results in dynamic distortions, as will be demonstrated in Section 2.5 using linear descriptions. These linear descriptions are derived in Section 2.3.

2.3 Linear Descriptions: Ideal and Practical Scale Models

2.3.1 Ideal Scale Model

Linear descriptions provide an effective means to analyse dynamic systems in the frequency domain. For this reason, the non-linear descriptions from Section 2.2 are linearised, with some additional simplifications being introduced as well.

A first simplification is made to the prime mover model. As was mentioned earlier, this dissertation concentrates on dynamic distortions introduced by hardware components, such as the additional electric loop, rather than the accuracy of the diesel engine's simulation model. Therefore, the prime mover is modelled as a static gain in the linear descriptions.

Second, the total moment of inertia of the shaft, gearbox, propeller and entrained water, $I_{\text{tot,id}}$, is assumed to be constant, which means that changes in entrained water mass in the propeller are neglected in the linear descriptions.

Third, it is assumed that the (simulated) gearbox does not introduce additional dynamic behaviour. The gearbox and reduction ratio are therefore eliminated from the linear descriptions. This means that there is no longer distinction between propeller and engine speed, and shaft speed can be referred to by ω without subscripts e or s.

Before proceeding to the linear descriptions, some attention is paid to notation first. Stapersma and Vrijdag (2017) proposed a linear description of torque of a controllable pitch propeller operating behind a ship. In their linearisation, they used operator δ to signify a small excursion from the equilibrium value, and superscript * to indicate a value normalised with respect to the equilibrium condition. This notation is assumed here, too. As an example, Eq. (2.13) illustrates how shaft speed ω relates to normalised shaft speed excursion $\delta\omega^*$.

$$\delta\omega^* = \frac{\delta\omega}{\omega_0} = \frac{\omega - \omega_0}{\omega_0} \tag{2.13}$$

Using this notation and the aforementioned simplifications, the non-linear descriptions given in Section 2.2.1 are linearised. The general, non-linear equation for shaft dynamics, given in Eq. (2.1), can be linearised as shown in Eq. (2.14). As a minor modification, friction torque M_{fr} is no longer included.

$$\tau_\omega \cdot \frac{\mathrm{d}\omega^*(t)}{\mathrm{d}t} = \delta M_{\text{d}}^*(t) - \delta M_{\text{prop,hydro}}^*(t) \tag{2.14}$$

Shaft speed time constant τ_ω was introduced by Stapersma and Vrijdag (2017), and is determined from equilibrium shaft speed ω_0, moment of inertia I and equilibrium drive torque $M_{\text{d,0}}$ as shown in Eq. (2.15).

$$\tau_\omega = \frac{I \cdot \omega_0}{M_{\text{d,0}}} \tag{2.15}$$

As was mentioned earlier, the prime mover is modelled as a static gain for the linearisation in this Section, while the gearbox ratio is eliminated. In essence, this means that

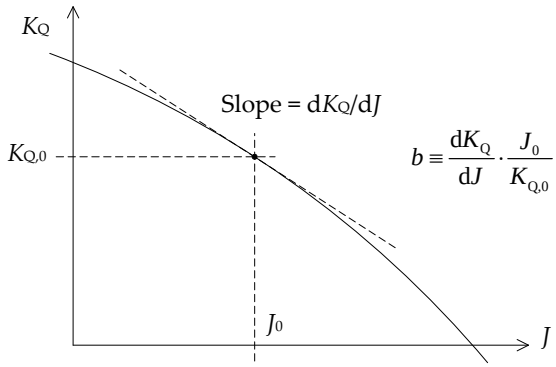


Figure 2.6: Determining propeller derivative b for a given equilibrium point in the open water propeller performance diagram.

the normalised fuel rack setting equals normalised torque without time delay, which implies that the output of the current controller function C_ω equals drive torque M_d. Considering this, no further attention is paid to the relation between FR and M_d for the time being. Propeller torque $M_\mathrm{prop,hydro}$, on the other hand, does require some further explanation. Stapersma and Vrijdag (2017) linearised the non-linear propeller load torque, as given in Eq. (2.4), to the form given in Eq. (2.16).

$$\delta M^*_\mathrm{prop,hydro}(t) = (2-b) \cdot \delta\omega^*(t) + b \cdot \delta v^*_\mathrm{a}(t) \tag{2.16}$$

This linearisation of propeller load torque will be used here, too. Propeller derivative b expresses the change of normalised torque coefficient δK^*_Q with changing normalised advance ratio δJ^*. Fig. 2.6 illustrates how b can be determined for a given equilibrium point in the open water propeller diagram. The equation for linearised propelled load torque, Eq. (2.16), can be substituted in the equation for linearised shaft dynamics, Eq. (2.14), resulting in Eq. (2.17).

$$\tau_\omega \cdot \frac{\mathrm{d}\omega^*(t)}{\mathrm{d}t} = \delta M^*_\mathrm{d}(t) - (2-b) \cdot \delta\omega^*(t) - b \cdot \delta v^*_\mathrm{a}(t) \tag{2.17}$$

After Laplace transform and some reordering, Eq. (2.17) can be written as shown in Eq. (2.18).

$$\delta\omega^*(s) = \frac{\frac{1}{2-b}}{\frac{\tau_\omega}{2-b} \cdot s + 1} \cdot \delta M^*_\mathrm{d}(s) + \frac{\frac{-b}{2-b}}{\frac{\tau_\omega}{2-b} \cdot s + 1} \cdot \delta v^*_\mathrm{a}(s) \tag{2.18}$$

In the non-linear description in Section 2.2.1, engine torque depends on the fuel rack position and shaft speed according to a fuel rack map. In order to keep the linear description as simple and generic as possible, this fuel rack map will not be taken into account in this Chapter. Later, when comparing linear simulations with actual HIL measurements, the fuel rack map will be included. From Eq. (2.18), two normalised Laplace transfer functions can be derived: one for shaft speed response on drive torque, and one for shaft speed response on advance speed. These are given

in Eq. (2.19).

$$S_1^*(s) = \frac{\delta\omega_1^*(s)}{\delta M_\mathrm{d}^*(s)} = \frac{\frac{1}{2-b}}{\frac{\tau_\omega}{2-b}\cdot s+1} \tag{2.19a}$$

$$S_2^*(s) = \frac{\delta\omega_2^*(s)}{\delta v_\mathrm{a}^*(s)} = \frac{\frac{-b}{2-b}}{\frac{\tau_\omega}{2-b}\cdot s+1} \tag{2.19b}$$

Next, the shaft speed controller described in Eq. (2.8) is linearised. Non-linear limits of the input and output signals are not included in the linear description. This means that the behaviour of the linear model is valid only for shaft speeds and fuel rack settings within their respective minimum and maximum values. Second, controller settings $K_\mathrm{p,i}$ and $K_\mathrm{i,i}$ need to be converted from their standardised, non-linear values before they can be used in the linear descriptions. The conversion factor depends on the nominal and equilibrium values as well as minimum and maximum values for the standardised governor settings.

In general, the conversion factor for controller settings in different reference conditions depends on the equilibrium values of the process variables, as shown in Eq. (2.20). x is the variable to be controlled, while y is the output variable of the controller.

$$K_\mathrm{converted} = \frac{x_0}{x_{0,\mathrm{converted}}}\cdot K\cdot\frac{y_{0,\mathrm{converted}}}{y_0} \tag{2.20}$$

The aim here is to convert shaft speed controller settings for the non-linear ideal scale model to settings for a linear model, based on the notation given in Eq. (2.13). Consequently, the variables x and y in Eq. (2.20) are engine speed and torque, respectively. In the specific case of the shaft speed controller described in Section 2.2.1, engine speed and torque are scaled between minimum and maximum values. These ranges must be taken into account in the conversion of controller settings, as is shown in Eq. (2.21).

$$K_\mathrm{scaled} = \frac{x_0}{(x_\mathrm{max}-x_\mathrm{min})\cdot x_{0,\mathrm{converted}}}\cdot K\cdot\frac{(y_\mathrm{max}-y_\mathrm{min})\cdot y_{0,\mathrm{converted}}}{y_0} \tag{2.21}$$

Moreover, deviations from the equilibrium are expressed in fractions of one in the linear description, implying that equilibrium values $x_{0,\mathrm{converted}}$ and $y_{0,\mathrm{converted}}$ are equal to one. Taking this into account as well as the scaling ranges, Eq. (2.22) shows how the standardised, non-linear speed controller settings can be converted for use in the linear descriptions.

$$K_\omega^* = \frac{n_\mathrm{e,0}}{n_\mathrm{e,nom}-n_\mathrm{e,min}}\cdot K_\omega\cdot\frac{M_\mathrm{b,nom}-M_\mathrm{b,min}}{M_\mathrm{b,0}} \tag{2.22}$$

Using these scaled settings, the shaft speed controller described in Eq. (2.8) can be linearised. The resulting Laplace transfer function is given in Eq. (2.23).

$$C_\omega(s) = K_{\mathrm{p},\omega}^* + K_{\mathrm{i},\omega}^*\cdot\frac{1}{s} \tag{2.23}$$

Table 2.5 gives values for the parameters of the linearised ideal scale model, corresponding to the values in Table 2.1. For reasons of simplicity, the added hydrodynamic

Table 2.5: Parameters and equilibrium values of the linearised ideal scale model.

	Symbol	Unit	Value
Eq. drive torque	$M_{\mathrm{d},0}$	[Nm]	4.505
Eq. shaft speed	ω_0	[rad/s]	63.36
Moment of inertia	I_{tot}	[kgm^2]	0.0297
Prop. derivative	b	[−]	−0.643
Shaft time constant	τ_ω	[s]	0.4177
Norm. governor static gain	$K^*_{\mathrm{p},\omega}$	[−]	2.01
Norm. governor integral gain	$K^*_{\mathrm{i},\omega}$	[s^{-1}]	4.25

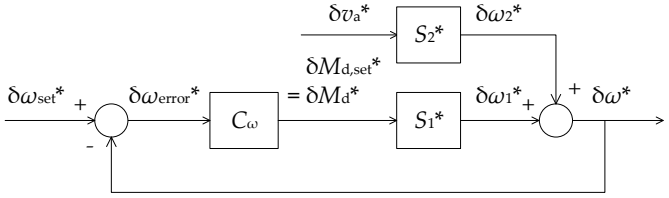


Figure 2.7: Graphical representation of the linearised ideal scale model.

inertia I_{H2O} is not included in the simulations in this Chapter, implying that I_{tot} equals I_{mech}.

Fig. 2.7 gives a visual representation of the linearised ideal scale model, with each block representing one of the Laplace transfer functions derived in this Section. The corresponding Laplace transfer function for response of shaft speed on set speed, $\delta\omega^*/\delta\omega^*_{\mathrm{set}}$, is given in Eq. (2.24).

$$\begin{aligned}\frac{\delta\omega^*(s)}{\delta\omega^*_{\mathrm{set}}(s)} &= \frac{C_\omega(s)\cdot S_1^*(s)}{1+C_\omega(s)\cdot S_1^*(s)} \\ &= \frac{\frac{K^*_{\mathrm{p},\omega}}{K^*_{\mathrm{i},\omega}}\cdot s+1}{\frac{\tau_\omega}{K^*_{\mathrm{i},\omega}}\cdot s^2+\frac{(2-b)+K^*_{\mathrm{p},\omega}}{K^*_{\mathrm{i},\omega}}\cdot s+1}\end{aligned} \tag{2.24}$$

The Laplace transfer function given in Eq. (2.24) represents the response of shaft speed on speed setting of the ideal scale model. It has one zero and two poles, which determine how gain and phase evolve as the input frequency increases. At very low frequencies, the gain is practically equal to 1 and the phase is practically equal to 0, as the propulsion system can easily follow the set point. However, as the frequency of the set speed fluctuations increases, the gain asymptotically decreases to 0 and the phase to -90 degrees, as the propulsion system can no longer attain the set speed and starts to lag behind.

As a next step, Section 2.3.2 derives the linear description of the practical scale model, which later on allows to compare the response of the ideal and practical scale models in Section 2.5.

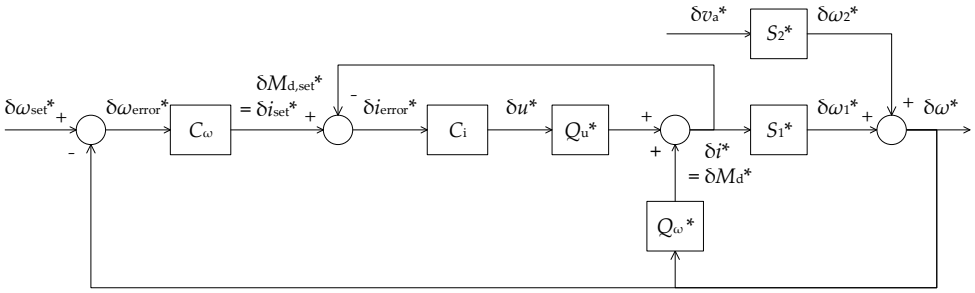


Figure 2.8: Graphical representation of the linearised practical scale model or HIL setup.

2.3.2 Practical Scale Model

As was stated earlier, the practical scale model is essentially an ideal scale model with an added electric propulsion system and different parameters for several physical components. Considering this, the linearised, ideal scale model is expanded with descriptions of the components of the electric drive in order to obtain a linear description of the practical scale model. Comparison of Figs. 2.7 and 2.8 shows where blocks (or transfer functions) are to be added.

Fig. 2.8 introduces three new transfer functions: Q_{u}^*, Q_{ω}^* and C_{i}. The first two describe the response of motor winding current on voltage and shaft speed, respectively, while the third represents the current controller. First, the response of motor current on speed and voltage is linearised.

After reordering and normalising, the relation between voltage, speed and current of the PMSM given in Eq. (2.11) can be written as shown in Eq. (2.25).

$$\delta u^*(t) = \frac{\delta\omega^*(t)}{1 + \frac{i_0 \cdot R}{\omega_0 \cdot k_{\mathrm{t}}}} + \frac{\delta i^*(t)}{1 + \frac{k_{\mathrm{t}} \cdot \omega_0}{i_0 \cdot R}} + \frac{\frac{L}{R} \cdot \frac{\mathrm{d}i^*(t)}{\mathrm{d}t}}{1 + \frac{k_{\mathrm{t}} \cdot \omega_0}{i_0 \cdot R}} \tag{2.25}$$

Laplace transform of Eq. (2.25) results in Eq. (2.26).

$$\delta u^*(s) = \frac{1}{1 + \frac{i_0 \cdot R}{\omega_0 \cdot k_{\mathrm{t}}}} \cdot \delta\omega^*(s) + \frac{\frac{L}{R} \cdot s + 1}{1 + \frac{k_{\mathrm{t}} \cdot \omega_0}{i_0 \cdot R}} \cdot \delta i^*(s) \tag{2.26}$$

Rearranging Eq. (2.26) to isolate normalised current increment δi^* yields Eq. (2.27).

$$\delta i^*(s) = \frac{1 + \frac{k_{\mathrm{t}} \cdot \omega_0}{i_0 \cdot R}}{\frac{L}{R} \cdot s + 1} \cdot \delta u^*(s) - \frac{\frac{k_{\mathrm{t}} \cdot \omega_0}{i_0 \cdot R}}{\frac{L}{R} \cdot s + 1} \cdot \delta\omega^*(s) \tag{2.27}$$

Eq. (2.27) shows that there are two input signals that cause response of current i and hence, drive torque M_{d}: terminal voltage u and shaft speed ω. These responses can be represented by two separate transfer functions, Q_{u}^* and Q_{ω}^*, which are given in

Table 2.6: Equilibrium values of the electric propulsion system in the conditions described by Table 2.5.

	Symbol	Unit	Value
Equilibrium voltage	u_0	[V]	39.40
Equilibrium current	i_0	[A]	8.19

Eq. (2.28).

$$Q_{\mathrm{u}}^{*}(s) = \frac{\delta i^{*}(s)}{\delta u^{*}(s)} = \frac{1 + \frac{k_{\mathrm{t}} \cdot \omega_0}{i_0 \cdot R}}{\frac{L}{R} \cdot s + 1} = \frac{\frac{u_0}{i_0 \cdot R}}{\frac{L}{R} \cdot s + 1} \tag{2.28a}$$

$$Q_{\omega}^{*}(s) = \frac{\delta i^{*}(s)}{\delta \omega^{*}(s)} = -\frac{\frac{k_{\mathrm{t}} \cdot \omega_0}{i_0 \cdot R}}{\frac{L}{R} \cdot s + 1} \tag{2.28b}$$

Current and voltage corresponding to the equilibrium point considered in this Chapter are given in Table 2.6. With the relation between current, voltage and speed now described by transfer functions Q_{u}^{*} and Q_{ω}^{*}, the mathematical description of the current controller given in Eq. (2.12) can be linearised. Recalling that the controller settings can be converted according to Eq. (2.20), Eq. (2.29) gives the Laplace transfer function of the linearised current controller.

$$C_{\mathrm{i}}(s) = K_{\mathrm{p,i}}^{*} + K_{\mathrm{i,i}}^{*} \cdot \frac{1}{s} \tag{2.29}$$

Using the transfer functions derived in this Section and the block diagram given in Fig. 2.8, the dynamic behaviour of $\delta\omega^{*}/\delta\omega_{\mathrm{set}}^{*}$ of the HIL setup can be derived. The resulting transfer function is shown in Eq. (2.30).

$$\frac{\delta\omega^{*}(s)}{\delta\omega_{\mathrm{set}}^{*}(s)} = \frac{C_{\omega}(s) \cdot S_1^{*}(s) \cdot \frac{C_{\mathrm{i}}(s) \cdot Q_{\mathrm{u}}^{*}(s)}{1 + C_{\mathrm{i}}(s) \cdot Q_{\mathrm{u}}^{*}(s)}}{1 + \left(C_{\omega}(s) \cdot C_{\mathrm{i}}(s) \cdot Q_{\mathrm{u}}^{*}(s) - Q_{\omega}^{*}(s)\right) \cdot \frac{S_1^{*}(s)}{1 + C_{\mathrm{i}}(s) \cdot Q_{\mathrm{u}}^{*}(s)}} \tag{2.30}$$

The Laplace transfer function given in Eq. (2.30) represents the response of shaft speed on speed setting of the practical scale model. Dynamic similarity of shaft dynamics is achieved until a given frequency if the gain and phase of Eq. (2.30) equals the gain and phase of Eq. (2.24) until that given frequency. In other words, the shape of the Bode diagram must be the same. However, in contrast to Eq. (2.24), Eq. (2.30) has two zeros and four poles. This means that, even if the locations of two poles and one zero are the same for the ideal and practical scale model (which is not self-evident), the shape of the Bode diagram may still be different because of influence by the additional two poles and zero.

Section 2.5 demonstrates how different pole and zero locations or interference by additional poles and zeros can distort shaft dynamics. First, however, Section 2.3.3 introduces an additional simplification to the practical scale model, facilitating the mathematical analysis in Chapter 3. Furthermore, Section 2.4 compares shaft dynamics predicted by the linear and non-linear descriptions, demonstrating that the linear descriptions are valid representations of non-linear reality.

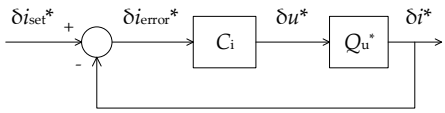


Figure 2.9: Graphical representation of the linearised, simplified electric loop, corresponding to Eq. (2.32).

2.3.3 Simplifications to the Practical Scale Model

In Chapter 3, tuning guidance for the current controller is derived by mathematical analysis. This involves analytical determination of the poles of Eqs. (2.24) and (2.30), which means that the zeros of the denominators must be determined. However, the denominator of Eq. (2.30) is a fourth order polynomial, rendering analytical determination of the poles rather involved. Considering this, a simplification to the linear description of the practical scale model is introduced.

The practical scale model represented by Fig. 2.8 is essentially the ideal scale model with an additional, interlinked electric loop. This also becomes apparent when writing out the transfer function for the response of current i on current set point i_{set}, as is done in Eq. (2.31).

$$\frac{\delta i^*(s)}{\delta i^*_{\mathrm{set}}(s)} = \frac{C_{\mathrm{i}}(s) \cdot Q^*_{\mathrm{u}}(s)}{1 + C_{\mathrm{i}}(s) \cdot Q^*_{\mathrm{u}}(s) - S^*_1(s) \cdot Q^*_{\omega}(s)} \tag{2.31}$$

Eq. (2.31) contains a term related to the electric loop, $C_{\mathrm{i}} \cdot Q^*_{\mathrm{u}}$, and a term related to the shaft speed loop, $S^*_1 \cdot Q^*_{\omega}$, showing the link between these two loops. However, the electric loop can be regarded as independent from the shaft speed loop if one assumes that shaft speed responds much slower than current on a new current set point (and thus, voltage). This assumption implies that ω remains virtually constant during the short time it takes for i to move to a new equilibrium, allowing to neglect the term $S^*_1 \cdot Q^*_{\omega}$. The block diagram of the resulting, simplified electric system with current controller is shown in Fig. (2.9). The corresponding Laplace transfer function for controlled current behaviour is given in Eq. (2.32).

$$\begin{aligned} \frac{\delta i^*(s)}{\delta i^*_{\mathrm{set}}(s)} &= \frac{C_{\mathrm{i}}(s) \cdot Q^*_{\mathrm{u}}(s)}{1 + C_{\mathrm{i}}(s) \cdot Q^*_{\mathrm{u}}(s)} \\ &= \frac{\frac{K^*_{\mathrm{p,i}}}{K^*_{\mathrm{i,i}}} \cdot s + 1}{\frac{L}{R \cdot K^*_{\mathrm{i,i}} \cdot \frac{u_0}{i_0 \cdot R}} \cdot s^2 + \frac{1 + K^*_{\mathrm{p,i}} \cdot \frac{u_0}{i_0 \cdot R}}{K^*_{\mathrm{i,i}} \cdot \frac{u_0}{i_0 \cdot R}} \cdot s + 1} \end{aligned} \tag{2.32}$$

The denominator of Eq. (2.32) is a second order polynomial, which means that analytical determination of the poles of the transfer function is much easier than for Eq. (2.30). This will prove helpful in Chapter 3, which relies on mathematical analysis of poles and zeros for tuning of the current controller. In this Chapter, however, this simplification is not yet necessary and will therefore not be used.

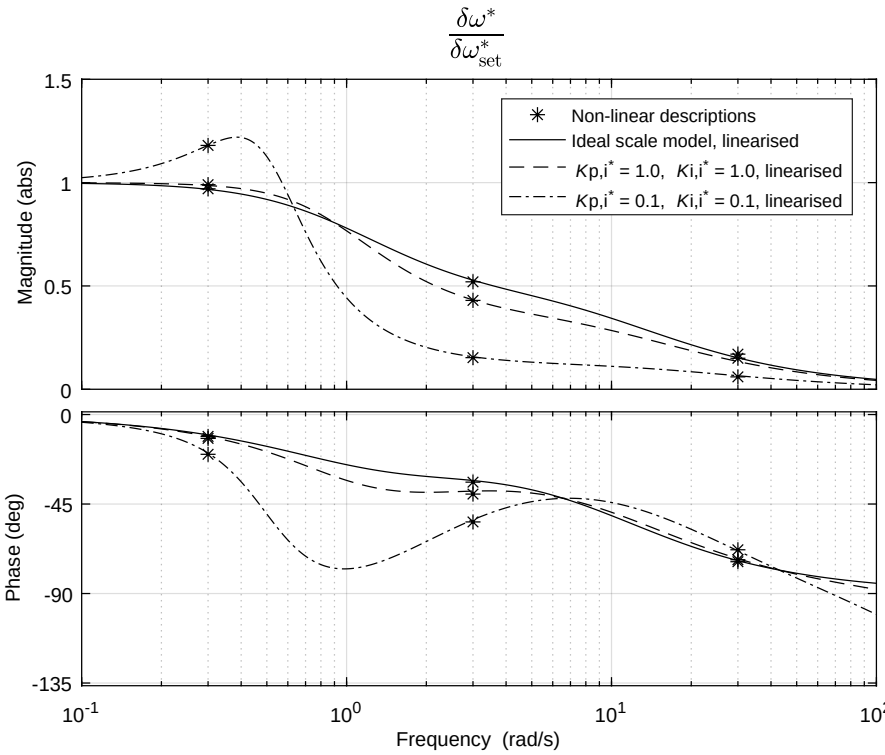


Figure 2.10: Bode diagram of $\delta\omega^*/\delta\omega^*_{\mathrm{set}}$ for the ideal scale model and HIL scale models with different current controller settings. Lines represent the response predicted by the linear descriptions derived in Section 2.3. Asterisks represent response predicted by the non-linear descriptions introduced in Section 2.2. Equilibrium values and controller settings are given in Tables 2.5 and 2.6. The amplitude of the sinusoidal ω_{set} signal in the non-linear simulations is 10% of ω_0.

2.4 Verification of Linear Descriptions

One could argue that linearising the considered propulsion system and HIL setup leads to considerable inaccuracies as all non-linear relations are simplified. However, this is not necessarily an issue. As long as variables remain near their equilibrium values, the linearisation error is limited, rendering linear descriptions sufficiently accurate to assess dynamic behaviour around the considered equilibrium.

To check whether this is also the case for the linear descriptions of the considered propulsion system and HIL setup, response of shaft speed on speed setting is simulated using both non-linear and linear descriptions. The results are shown in Fig. 2.10. One can conclude that linearisation errors are negligible if speed oscillations with a small amplitude – at least up to 10% of equilibrium speed – are considered: linear and non-linear simulations predict practically the same shaft speed response. Considering this, the linear descriptions will be relied upon to assess dynamic behaviour throughout this dissertation, supplemented by non-linear descriptions and actual HIL measurements.

2.5 Scale Effects on Shaft Dynamics

Causes of the expected dynamic distortions can be found by comparing the block diagrams shown in Figs. 2.1 and 2.2. A first conspicuous difference is the additional electric system in the practical scale model. As was indicated before, this additional system introduces additional, undesired dynamics, possibly influencing the behaviour of the scale model. Proper tuning of the electric propulsion system is therefore crucial.

Second, shaft friction is not the same for the ideal and practical scale model. The practical scale model is powered by an electric motor rather than a diesel engine, and lacks most of the ancillary equipment found in the ideal scale model. In fact, as was indicated before, friction torque inside the ideal scale model is neglected altogether in this dissertation. As a result, friction torque likely does not scale correctly. This, too, may influence shaft dynamics, and compensation for friction in the scale model shafting may be required.

Third, the moment of inertia is likely different due to differences in geometry between the ideal and practical propulsion systems. If the practical scale model has a smaller moment of inertia, shaft speed responds faster to changes in torque than it ideally should. This, too, requires compensation, either by physically adjusting the drive train or by applying a correction to the drive torque.

While mentioning these three scale effects, Section 1.3 excluded hydrodynamic scale effects from the research scope. To support this choice, Section 2.5.4 evaluates the influence on shaft dynamics of increased equilibrium torque due to viscous scale effects.

The linear descriptions derived in Sections 2.3.1 and 2.3.2 allow to visualise possible distortions of shaft dynamics around an equilibrium. As an illustration of what can go wrong during dynamic open water experiments, Sections 2.5.1 through 2.5.3 show Bode diagrams of linearised shaft dynamics with interference from the electric drive, incorrect friction, incorrect moment of inertia and hydrodynamic scale effects on propeller load. The reference case is the ideal scale model with the parameters given in Table 2.5.

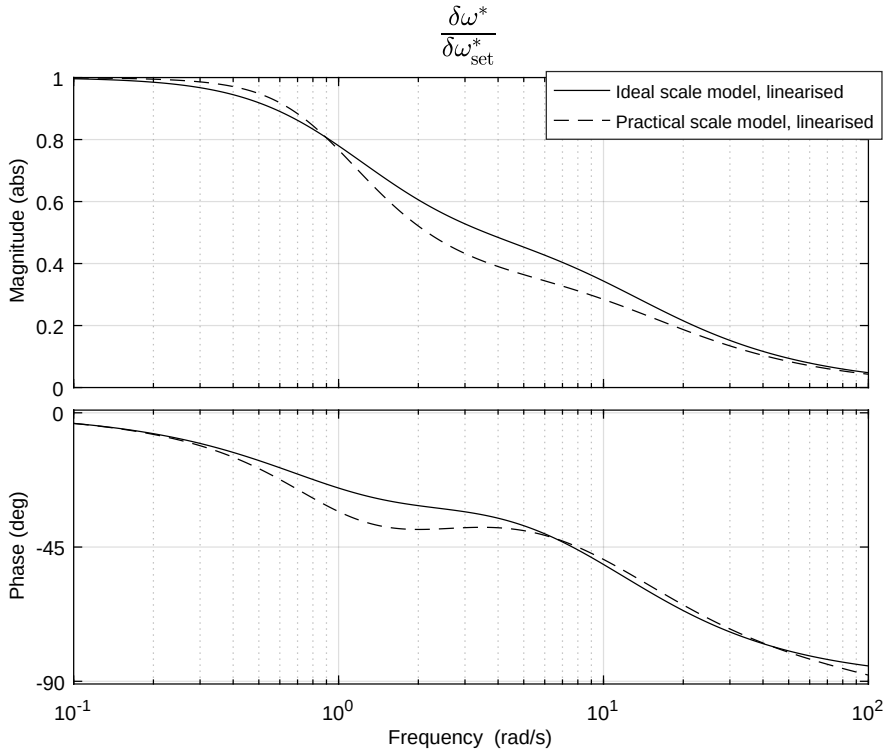


Figure 2.11: Bode diagram of linearised response of shaft speed $\delta\omega^*$ on set speed $\delta\omega^*_{\text{set}}$ with distortions due to an improperly tuned current controller. Parameters and equilibrium values are given in Tables 2.5 and 2.6; current controller settings $K^*_{\text{p,i}}$ and $K^*_{\text{p,i}}$ are both set to 1 for the practical scale model.

2.5.1 Distortions by Electric Drive

To correctly emulate torque of the prime mover, the torque command from the simulator must be converted into physical drive torque sufficiently fast. The torque of the electric motor in the HIL setup is proportional to the current in the motor windings, so fast torque response is achieved by fast control of winding current.

In order to achieve sufficiently fast current control, the proportional and integral gains of the current controller, $K^*_{\text{p,i}}$ and $K^*_{\text{i,i}}$, must be properly tuned. The significance of these settings will be explained in Chapter 3. As a first indication of the importance of proper current controller tuning, Fig. 2.11 shows the effect of choosing arbitrary controller settings.

Fig. 2.11 presents a Bode diagram with shaft speed response on speed setting both for the ideal scale model and a practical scale model with an electric drive. Mechanical parameters for the practical scale model are given in Table 2.5, while the additional electric drive has the equilibrium values given in Table 2.6. At this

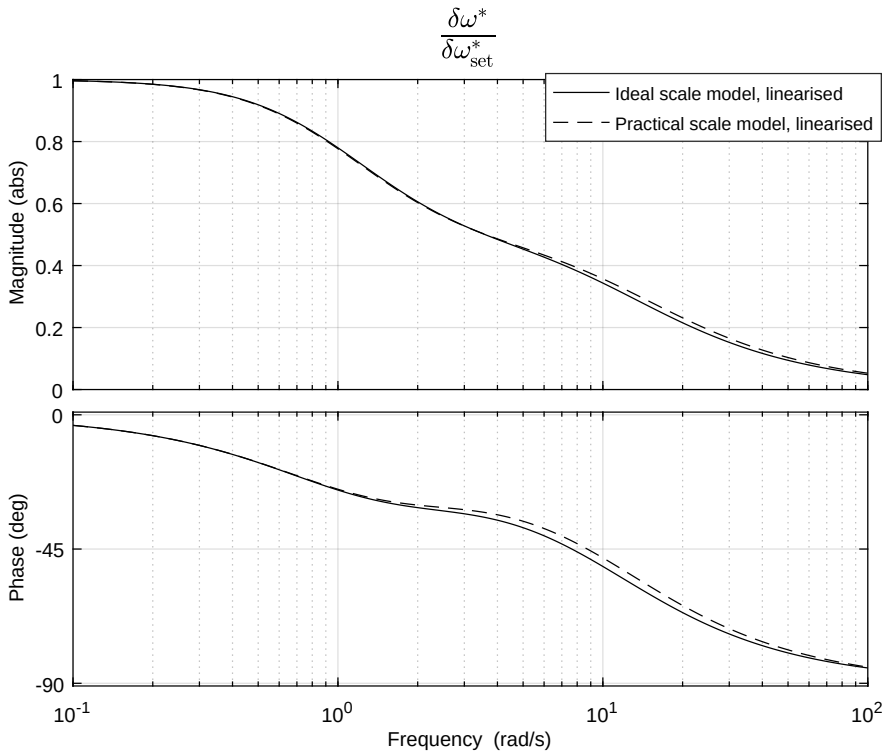


Figure 2.12: Bode diagram of linearised response of shaft speed $\delta\omega^*$ on set speed $\delta\omega^*_{\mathrm{set}}$ with distortions due to increased friction inside the practical scale model. Response is shown of the ideal scale model and a practical scale model with an equilibrium torque increased by 10% compared to the ideal equilibrium value. Apart from the equilibrium torque of the practical scale model, parameters for both scale models are given in Table 2.5.

point, no guidance is available for tuning the electric drive of a dynamic open water setup, and both $K^*_{\mathrm{p,i}}$ and $K^*_{\mathrm{i,i}}$ are arbitrarily set to a value of 1. As can be seen in Fig. 2.11, these settings result in considerable distortions of shaft dynamics already at low frequencies, as becomes evident in the differences in gain and phase between the ideal and practical scale model. This demonstrates that proper current controller settings are an absolute requirement for dynamic similarity. The current controller settings will receive detailed attention in Chapter 3, resulting in tuning guidance for the current controller.

2.5.2 Distortions by Different Shaft Friction

Another relevant variable for shaft dynamics is the equilibrium drive torque. This, too, can be illustrated using linear simulations. In Fig. 2.12, the shaft dynamics

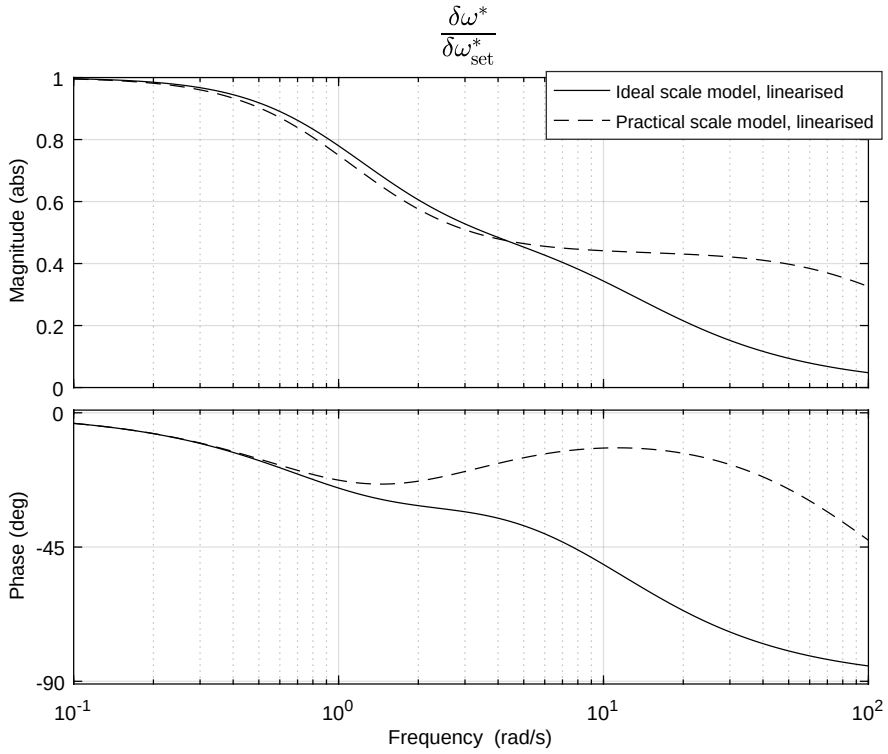


Figure 2.13: Bode diagram of linearised response of shaft speed $\delta\omega^*$ on set speed $\delta\omega^*_{\mathrm{set}}$ with distortions due to incorrect moment of inertia. Response is shown of the ideal scale model and a practical scale model with a moment of inertia which is 9.8% of the ideal inertia. Apart from the moment of inertia of the practical scale model, parameters for both scale models are given in Table 2.5.

are shown for the ideal scale model and a practical scale model which has the same properties, though with an equilibrium torque $M_{\mathrm{d},0}$ which is increased by 10% to 4.956 Nm due to friction in the model drive. As can be seen, this too results in distorted shaft dynamics, although the effect is more limited than for scale effects. In Chapter 5, a method is proposed to compensate for model scale friction.

2.5.3 Distortions by Incorrect Moment of Inertia

An incorrectly scaled moment of inertia of the propulsion systems may result in dynamic distortions, too. Fig. 2.13 illustrates this by comparing shaft speed response of the ideal scale model and a practical scale model which has a considerably smaller moment of inertia. Whereas the ideal moment of inertia $I_{\mathrm{tot,id}}$ equals 0.0297 kgm^2, practical inertia $I_{\mathrm{tot,p}}$ is 0.0029 kgm^2, or only 9.8% of the ideal value. As will be shown later on, the latter value corresponds to the actual HIL setup considered in this

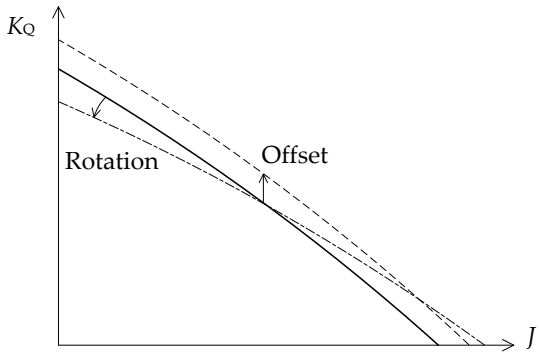


Figure 2.14: Generic open water diagram in which K_Q is plotted as a function of advance ratio J. Due to hydrodynamic scale effects, the K_Q function can be offset or rotated. A similar drawing can be made for scale effects on propeller thrust constant K_T.

dissertation. Apart from a different moment of inertia, parameters and equilibrium values are the same. Again, shaft dynamics appear to be distorted, this time to a considerable extent. Chapter 4 elaborates on these distortions, resulting in a method to compensate for incorrect moment of inertia.

2.5.4 Distortions by Hydrodynamic Scale Effects

Load torque of a propeller depends, among other things, on the physical properties of the fluid in which the propeller operates. Not all of these physical properties can be scaled: viscosity and pressure, for example, are often not correct at model scale. This results in scale effects on propeller torque.

Distortions of propeller torque can be categorised into static and dynamic distortions. Static distortions are scale effects on the torque and thrust constants in the open water diagram; these constants express non-dimensional propeller torque and thrust at static equilibrium conditions. Fig. 2.14 shows a generic open water diagram, with K_Q plotted as a function of advance ratio J. Due to hydrodynamic scale effects, the K_Q function can be offset or rotated.

In the past, multiple efforts have been made to predict viscous scale effects on open water propeller torque. As a notable example, Kuiper (1992) developed a regression model to estimate static scale effects on torque and thrust constants for the Wageningen B propeller series, predicting an offset of K_Q and K_T. A very similar correction has been adopted for propeller open water experiments and self-propulsion tests by the International Towing Tank Conference (ITTC, 2014a). Although this model is subject to discussion (Brown et al., 2014; Helma, 2015), especially for non-conventional propeller designs, this correction is still the standard for open water propeller experiments. As such, it is considered a good starting point for predicting static scale effects on open water propeller performance. Kuiper's regression model predicts that in the case described in this dissertation, open water propeller torque for the practical scale model may be 1 to 2% higher than for the ideal scale model.

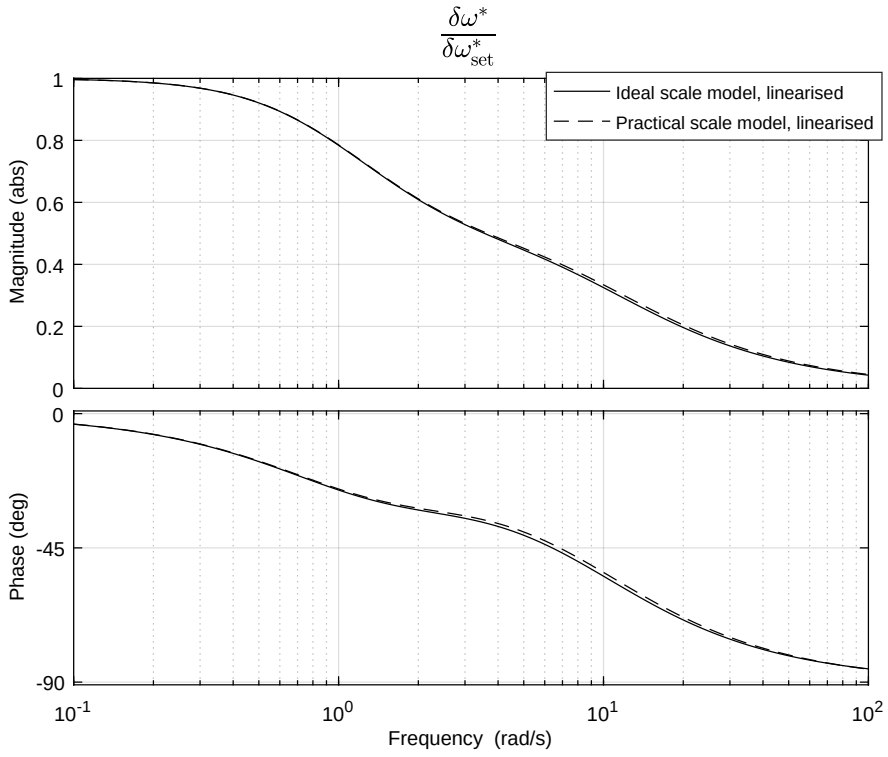


Figure 2.15: Bode diagram of linearised response of shaft speed $\delta\omega^*$ on set speed $\delta\omega^*_{\mathrm{set}}$ with distortions of propeller performance due to viscous scale effects. Response is shown of the ideal scale model and a practical scale model with an equilibrium torque constant K_{Q} which is 5% higher than its ideal value. As a result of this, the equilibrium drive torque $M_{\mathrm{d},0}$ increases by 5%, too. This increase is higher than the effect predicted by Kuiper (1992), resulting in a conservative estimate of distortions by viscous scale effects. Apart from propeller equilibrium torque of the practical scale model, parameters for both scale models are given in Table 2.5.

Propeller thrust, on the other hand, is somewhat lower for the practical scale model. To be on the conservative side, Fig. 2.15 shows the response of the linearised scale model, assuming a 5% increase in equilibrium torque. One can conclude that the resulting effect on shaft dynamics is rather limited.

Apart from static distortions, one can also expect dynamics distortions of propeller torque and thrust. Interactions between the propeller and appendages, such as struts and rudders, may trigger vortex shedding around the propeller. In turn, this causes fluctuations of propeller torque and thrust, with a possible effect on shaft dynamics. However, different viscosity and vapour pressures between full scale and model scale situations may result in different vortex behaviour. Noting this, Krasilnikov et al. (2015) compared CFD simulations and scale model experiments with podded propellers, paying attention to scale effects on propeller-pod interaction and resulting vortex behaviour. They concluded that scale effects on factors which are a result of propeller-pod interaction, such as relative rotative efficiency η_r and wake fraction w, are very limited. Although Krasilnikov et al. indicate that these factors do not completely characterise the complex interaction between propeller and pod, their limited variation with scale does indicate that such dynamic distortions are of a limited magnitude. In addition, Bertram (1999) stated that scale effects on vortex shedding and flow separation are sufficiently small to allow accurate manoeuvrability experiments with scale model ships. From this, one can conclude that scale effects on dynamic propeller performance are very limited, at least in the frequency range relevant for ships with displacement hulls.

In conclusion, the reported magnitude of static and dynamic distortions of propeller performance and their effect on shaft dynamics is rather limited. In addition, this subject is a highly complex matter, justifying a separate research project. Scale effects on propeller performance are therefore not further considered in this dissertation.

These first illustrations of dynamic distortions in the frequency domain raise the question which distortions are still acceptable, or differently put, when sufficient dynamic similarity is achieved. To answer this question, criteria for accurate dynamic open water experiments are formulated in Section 2.6.

2.6 Criteria for Successful Dynamic Open Water Experiments

2.6.1 Added Value of Hardware in the Loop

As a first step towards criteria for dynamic open water experiments, some attention must be paid to the usefulness of hardware in the loop experiments in general. Earlier, it was indicated that the added value of HIL lies in the dynamic interaction between the simulated components and connected hardware. This implies that HIL has added value only in the frequency range where both the simulation model and hardware show dynamic behaviour. Thus, depending on the frequency of the considered disturbance input, HIL may not always be necessary to evaluate a system's response. In this respect, three frequency ranges can be distinguished:

1. low frequencies, at which the hardware shows static response on input;

2. medium frequencies, at which the hardware shows dynamic response on input;

3. high frequencies, at which the hardware no longer responds on input.

In the low frequency range, disturbance input fluctuates so slowly that the system has ample time to respond. As a consequence, there is practically no phase delay, and the gain does not change with frequency. This range is located in the left hand side of the Bode diagram. Considering the ideal scale model in Fig. 2.10 as an example, the gain is 1 for frequencies below 0.2 rad/s, while the phase delay is close to zero. Response of the propulsion plant in this frequency range is practically static, and dynamic interaction between simulated and hardware subsystems hardly occurs. In other words, HIL is not required to emulate dynamic interaction between load and drive.

In the medium frequency range, on the other hand, dynamic response of the hardware is observed. In Fig. 2.10, the gain and phase of the ideal scale model start to vary as the disturbance frequency exceeds 0.2 rad/s. From this point, gain and phase clearly start to become dependent on the dynamic properties of the propulsion plant, and complex, dynamic interaction may occur between simulated and physical subsystems. In this frequency range, HIL does have added value, especially if complex phenomena such as hydrodynamics are involved. The frequency interval in which the hardware responds on disturbances is from here on referred to as the *responsive frequency range*.

At some point, however, the response of the propeller shaft starts to diminish to negligible levels. In Fig. 2.10, this point is reached around 80 rad/s: from there on, the gain is less than 5% of its steady state value. This means that above this frequency, input disturbances no longer cause noticeable fluctuations of shaft speed. Simulated components inside the simulation model may still show response; for these dynamics, however, the physical behaviour of the shaft and its environment is no longer relevant. In other words, these dynamics can be entirely simulated, without the need for a HIL setup.

In conclusion, the responsive frequency range for HIL experiments is determined by the response of physical output signals, or more colloquially, hardware response. At frequencies which no longer trigger hardware response, dynamic similarity of the hardware becomes irrelevant.

The Bode diagrams presented so far showed the response of speed to speed setting. However, there are more signals that can be used to evaluate dynamic similarity. The block diagrams in Figs. 2.7 and 2.8 show two input signals, while there are signals other than shaft speed which could be considered as output, such as drive torque. Section 2.6.2 elaborates on the different input and output signals of the ship propulsion system, identifying the most efficient way to evaluate the performance of the HIL setup considered in this dissertation.

2.6.2 Input and Output Signals

In the analysis conducted in this Chapter, shaft dynamics are described by the response of actual shaft speed on set shaft speed, or $\delta\omega^*/\delta\omega^*_{\mathrm{set}}$. However, as can be seen in the block diagrams in Figs. 2.7 and 2.8, advance speed v_{a} presents an additional input, while drive torque M_{d} can be considered as an output, too.

In Section 2.6.1, it was indicated that to assess the dynamic performance of a HIL setup, physical output signals are relevant. In the case of the dynamic open water setup, this means that shaft speed ω is a relevant output, as it is a physical signal. Drive torque M_d, on the other hand, is a simulated variable, and may respond on frequencies much higher than relevant for interaction between load and drive. Moreover, Appendix A shows that the response of shaft speed on speed setting $\delta\omega^*/\delta\omega^*_\mathrm{set}$ is representative also for other input and output signals. The transfer functions of the different combinations of inputs and outputs all have the same denominator, indicating that the response of these transfer functions is similar. By comparing the Bode diagrams given in Appendix A, one indeed finds that as long as dynamic similarity is achieved for $\delta\omega^*/\delta\omega^*_\mathrm{set}$, this is also the case for all other input and output signals.

At the same time, shaft speed setting ω_set can be controlled with more ease and precision during HIL experiments than advance speed v_a. Whereas the shaft speed setting can be adjusted by simply turning a knob, advance speed is the result of a combination of carriage speed, hexapod motions and water motions. Not all of these can always be precisely known, let alone controlled. Considering this, $\delta\omega^*/\delta\omega^*_\mathrm{set}$ is considered as determinant for dynamic similarity of model scale and full scale shaft dynamics in this dissertation. Section 2.6.3 proceeds to formulate criteria to the gain and phase of $\delta\omega^*/\delta\omega^*_\mathrm{set}$ of the ideal and practical scale models, defining when a dynamic open water experiment accurately emulates shaft dynamics.

2.6.3 Criteria for Accurate Emulation of Shaft Dynamics

Ideally, the response of the propeller shaft on all input disturbances would be exactly equal for the ideal and practical scale model. In practice, scale effects introduce distortions of shaft dynamics, and the aim in this dissertation is to derive methods to avoid or correct these distortions.

To assess the performance of the formulated solutions, the response of shaft speed on speed setting for the ideal and practical scale models will be compared. In first instance, this is done using frequency domain analysis of linear descriptions, as this allows to assess shaft dynamics over a wide range of frequencies using only simulations. At a later stage, the performance of the scale models is assessed by comparing actual HIL experiments to non-linear simulations in the time domain.

Criteria for dynamic similarity in a Bode diagram can be expressed in mathematical terms. In this dissertation, similarity of shaft dynamics is considered to be achieved if the gain of the practical scale model does not differ from the ideal gain by more than 5% of the ideal DC gain, and the phase does not differ by more than 10 degrees. These criteria are expressed by Eq. (2.33).

$$\left|\frac{G_\mathrm{id} - G_\mathrm{p}}{G_\mathrm{id,DC}}\right| \leq 0.05 \tag{2.33a}$$

$$|\varphi_\mathrm{id} - \varphi_\mathrm{p}| \leq 10 \text{ deg.} \tag{2.33b}$$

These criteria are based on observations from linear and non-linear simulations under varying conditions; for example, different regular wave types and at different equilibrium points were evaluated. If the criteria given in Eq. (2.33) are met, dynamic distortions are practically invisible in phase plots and time traces. The frequency interval in which these criteria are met, is from here on referred to as the *similarity*

range. Ideally, the similarity range would cover the entire responsive frequency range. In practice, however, it may not always be possible and necessary to achieve this level of similarity. Properties of sensors and other experimental equipment likely impose limits on the similarity range. At the same time, it may be unnecessary to accurately emulate all disturbances in the responsive frequency range, as relevant disturbances are expected only at relatively low frequencies. Ocean waves, for example, tend to carry less energy as their frequency increases, so experiments focusing on interaction between waves and the propulsion system do not require high-frequency interaction to be emulated with high precision. For brevity, the frequency interval in which all relevant disturbances occur is from here on referred to as the *relevant frequency range*. HIL experiments can be considered accurate if the similarity range covers either the relevant frequency range or the responsive frequency range. Fig. 2.16 shows how the responsive frequency range, similarity range and relevant frequency range are related to each other in a generic HIL experiment.

The criteria formulated for the Bode diagrams are also valid in the time domain. However, gain and phase of response can not always be derived as easily from time domain representations. Therefore, the analysis of results in the time domain will in some cases be of a more qualitative nature.

2.7 Conclusion

The main aim of this Chapter was to give detailed descriptions of the ideal and practical scale models, including mathematical descriptions. These mathematical descriptions were subsequently used to illustrate scale effects expected during dynamic open water experiments. In addition, criteria regarding the performance of the HIL setup were introduced.

In the next Chapters, the mathematical descriptions will continue to play an important role, as they will be used to derive methods to correct distortions of shaft dynamics. Moreover, the mathematical descriptions are crucial to assess the accuracy of emulated shaft dynamics: as the ideal scale does not physically exist, ideal shaft dynamics must be estimated using simulations based on mathematical descriptions of the ideal scale model. In brief, this Chapter has laid the mathematical foundations for the Chapters to come.

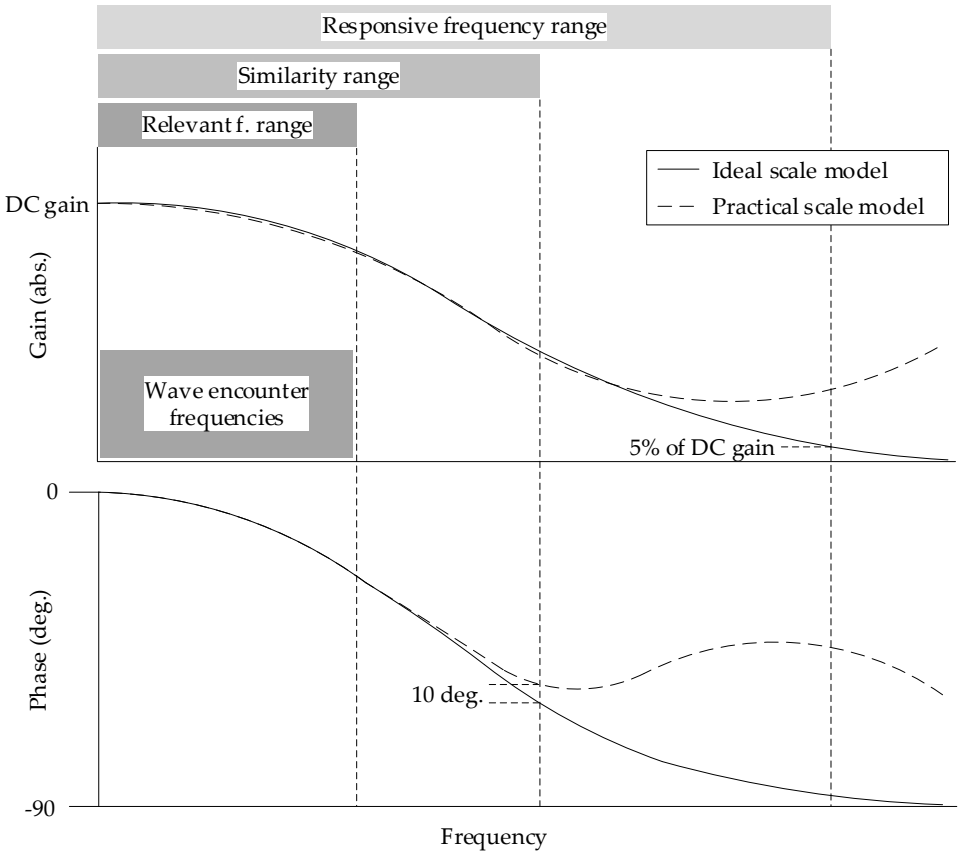


Figure 2.16: Schematic Bode diagram of a HIL experiment concentrating on the interaction between waves and the propulsion system. To accurately emulate relevant dynamics, the similarity range must completely cover either the relevant frequency range or the responsive frequency range.

Chapter 3

Tuning the Electric Drive of the Open Water Setup

With mathematical descriptions of the ideal and practical scale models and their respective components derived in Chapter 2, the fourth research sub question can be addressed. This question was formulated as follows:

– Which measures can be taken to avoid distortion of shaft dynamics by these components?

In this Chapter, a first part of the answer to this question is formulated by analysing the dynamic response of the electric drive. Through mathematical analysis, recommended settings for the current controller in the drive are derived, eliminating unwanted shaft dynamics caused by the current control loop.

In Chapter 2, it was stated that the similarity range should completely cover either the relevant frequency range or the responsive frequency range – these three ranges were visualised in Fig. 2.16. As the expected disturbances and their frequencies were not yet discussed, the relevant frequency range is not known at this stage. The responsive frequency range, on the other hand, depends on the properties of the ideal scale model propulsion system. These properties were laid out in detail in Chapter 2, and the responsive frequency range can be derived from the Bode diagrams in said Chapter. Considering this, the aim in this Chapter is to ensure that the similarity range covers the responsive frequency range.

As was also indicated earlier, the HIL setup contains an additional propulsion system, consisting of an electric motor and current controller. This additional system may introduce unwanted dynamics. To avoid such dynamics, the electric propulsion system must be properly tuned. Using the linear system descriptions given in Chapter 2, settings for the current controller are derived in this Chapter, ensuring that the electric propulsion system does not distort relevant propulsion shaft dynamics. These settings are derived using the poles and zeros of the transfer function for shaft dynamics. The obtained controller settings will be verified using numerical simulations. In Chapter 6, these simulations will be compared to actual HIL measurements.

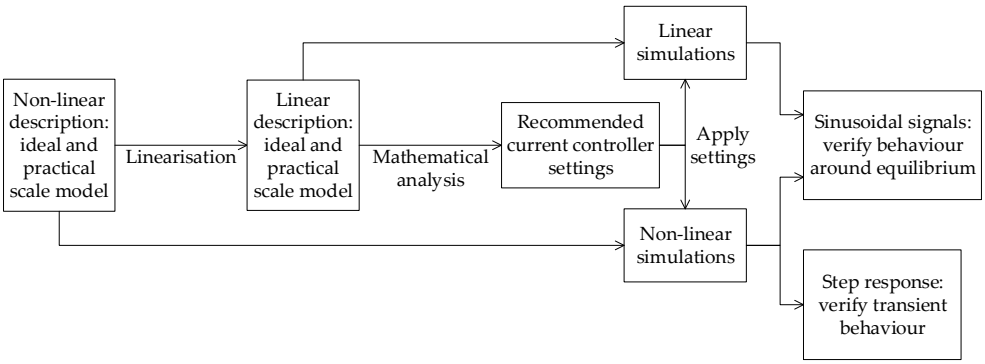


Figure 3.1: Graphic representation of the approach in this Chapter. From the non-linear and linear descriptions derived in Chapter 2, recommended current controller settings are derived. As a verification, these settings are subsequently applied in non-linear and linear simulation models.

3.1 Approach

Fig. 3.1 gives an overview of the approach to deriving current controller settings. In Chapter 2, non-linear and linear system descriptions were derived, which constitute the first two blocks in Fig. 3.1. This Chapter proceeds to analyse these descriptions, resulting in settings for the electric drive's current controller that ensure that the closed current loop does not introduce dynamic distortions in the responsive frequency range. According to the criteria formulated in Section 2.6.3, this means that the gain and phase error of the practical scale model's response must be less than 5% and 10 degrees, respectively, as long as the gain of the ideal scale model's response is more than 5% of its steady state value.

The dynamic response of a linearised system is determined by the locations of the system's poles and zeros. Thus, to be able to analytically derive controller settings, the pole and zero locations of the linearised transfer functions for the shaft speed loop and electric loop must be known. The pole and zero locations are determined by a range of physical properties. By expressing the relation between these properties and pole and zero locations, requirements on the setup and hence, current controller settings can be derived. As a final step in this Chapter, it is verified that these settings indeed result in negligible dynamic distortion by the electric drive. This verification is done using linear and non-linear simulations.

3.2 Requirements on Current Controller Settings

As a first step to deriving guidelines for current controller tuning, the poles and zeros of the relevant transfer functions are given in Sections 3.2.1 and 3.2.2. Following this, requirements are formulated to the location of these poles and zeros, and current controller settings $K_{\mathrm{p,i}}^{*}$ and $K_{\mathrm{i,i}}^{*}$ are derived such that these requirements are met. This is done in Section 3.2.3.

3.2.1 Poles and Zero of Ideal Scale Model

The ideal scale model represents a perfectly downscaled version of the full scale diesel-mechanical propulsion system. The poles and zero of this system are referred to as *mechanical poles and zeros*. Their equations follow from the transfer function for ideal response of shaft speed on speed setting $\delta\omega^*/\delta\omega^*_{\text{set}}$, given in Eq. (2.24). Mathematical expressions for the mechanical poles are given in Eq. (3.1).

$$s_{n,\omega} = \frac{-\frac{(2-b)+K^*_{\text{p},\omega}}{K^*_{\text{i},\omega}} \pm \sqrt{\left(\frac{(2-b)+K^*_{\text{p},\omega}}{K^*_{\text{i},\omega}}\right)^2 - 4 \cdot \frac{\tau_\omega}{K^*_{\text{i},\omega}}}}{2 \cdot \frac{\tau_\omega}{K^*_{\text{i},\omega}}} \tag{3.1}$$

The transfer function for the closed shaft speed loop has one mechanical zero, which is expressed by Eq. (3.2).

$$z_\omega = -\frac{K^*_{\text{i},\omega}}{K^*_{\text{p},\omega}} \tag{3.2}$$

These poles and zero define the dynamic behaviour of the linearised ideal closed shaft speed loop, which must ideally be replicated without distortions by the HIL setup. In Section 3.2.3, the expressions for the mechanical poles and zero will be used to derive current controller settings such that dynamic distortions by the electric drive are avoided.

3.2.2 Poles and Zero of Simplified Electric Loop

In analogy with the mechanical poles and zero, the electric propulsion system has *electric poles and zeros*, which follow from the transfer function for response of current on set current $\delta i^*/\delta i^*_{\text{set}}$ of the simplified electric loop, given in Eq. (2.32). Expressions for the electric poles are given in Eq. (3.3).

$$s_{n,\text{i}} = \frac{-\frac{1+K^*_{\text{p,i}} \cdot \frac{u_0}{i_0 \cdot R}}{K^*_{\text{i,i}} \cdot \frac{u_0}{i_0 \cdot R}} \pm \sqrt{\left(\frac{1+K^*_{\text{p,i}} \cdot \frac{u_0}{i_0 \cdot R}}{K^*_{\text{i,i}} \cdot \frac{u_0}{i_0 \cdot R}}\right)^2 - 4 \cdot \frac{L}{R \cdot K^*_{\text{i,i}} \cdot \frac{u_0}{i_0 \cdot R}}}}{2 \cdot \frac{L}{R \cdot K^*_{\text{i,i}} \cdot \frac{u_0}{i_0 \cdot R}}} \tag{3.3}$$

The transfer function for the simplified electric loop has one electric zero, which is expressed by Eq. (3.4).

$$z_\text{i} = -\frac{K^*_{\text{i,i}}}{K^*_{\text{p,i}}} \tag{3.4}$$

As the locations of poles and zeros define the dynamic behaviour of the linearised systems, the following sections use Eqs. (3.1) through (3.4) to tune the current controller of the electric drive.

3.2.3 Requirements on Poles and Zeros

The ideal scale model has two poles and one zero, whose locations determine the dynamic behaviour of the ship's propulsion plant. The HIL setup combines the ideal scale model and the electric loop, resulting in a system with four poles and two

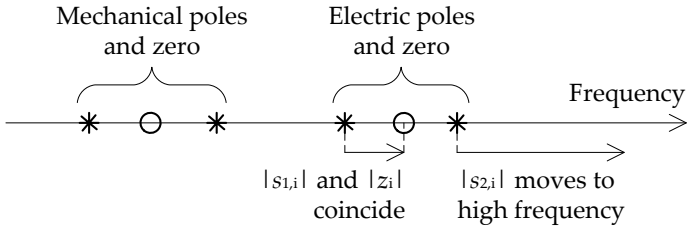


Figure 3.2: To avoid dynamic distortion, the electric poles and zero must be cancelled out and moved away from the mechanical poles and zero.

zeros. The two additional poles and zero of the electric loop are unwanted, and their influence on the dynamic behaviour of the ideal scale model must be reduced such that the similarity range completely covers the responsive frequency range. As is illustrated by Fig. 3.2, this can be achieved by meeting the following two requirements:

1. The slow electric pole $s_{1,\mathrm{i}}$ must coincide with electric zero z_{i}. As such, they cancel out each other's influence.

2. There must be sufficient distance between the fast electric pole $s_{2,\mathrm{i}}$ and the fast mechanical pole $s_{2,\omega}$, ensuring that no distortion of gain and phase occurs in the responsive frequency range.

To determine the minimum distance between the fast electric and mechanical poles, the effect of poles and zeros on gain and phase is visualised. Fig. 3.3 shows the Bode diagram of two first order systems, one of which has a pole at 1 rad/s and the other a zero at the same frequency. The respective transfer functions are given in Eqs. (3.5a) and (3.5b). From Fig. 3.3, one can conclude that the effect on phase of poles and zeros becomes visible two decades before the pole and zero frequencies. A minimum distance of two decades between the fast mechanical electric pole and fast electric pole is therefore recommended.

$$H_1(s) = \frac{1}{1 \cdot s + 1} \tag{3.5a}$$

$$H_2(s) = 1 \cdot s + 1 \tag{3.5b}$$

Thus, the two requirements formulated earlier can be expressed as in Eq. (3.6).

$$s_{1,\mathrm{i}} = z_{\mathrm{i}} \tag{3.6a}$$

$$|s_{2,\mathrm{i}}| \geq 1\mathrm{E}2 \cdot |s_{2,\omega}| \tag{3.6b}$$

These two requirements can be written out in two equations, which means that constraints can be set on two parameters. Preferably, these parameters can be easily changed. This is only true for current controller settings $K^*_{\mathrm{p,i}}$ and $K^*_{\mathrm{i,i}}$. The other parameters are either defined by the chosen test case ($K^*_{\mathrm{p},\omega}$, $K^*_{\mathrm{i},\omega}$, τ_ω, u_0, i_0 and b) or fixed by the scale model hardware (L and R). Considering this, the requirements on pole and zero locations are rewritten as requirements on $K^*_{\mathrm{p,i}}$ and $K^*_{\mathrm{i,i}}$.

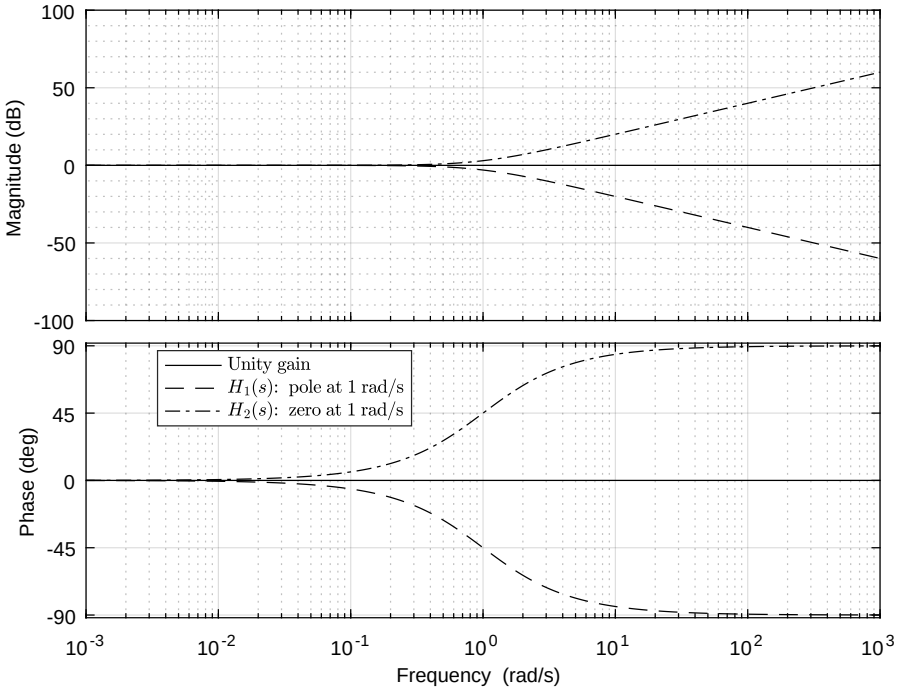


Figure 3.3: Bode diagram with two first order systems, one of which has a pole at 1 rad/s and the other a zero at 1 rad/s. For reference, a static unity gain with zero phase is also plotted. For both first order systems, the phase starts to show distortions at a frequency of 10^{-2} rad/s, or two decades before the pole and zero frequencies.

Requirement on $s_{1,\mathrm{i}}$ and z_{i}

Recalling the equations for electric poles and zero given in Eqs. (3.3) and (3.4), the requirement stated in Eq. (3.6a) can be rewritten as shown in Eq. (3.7).

$$-\frac{K^*_{\mathrm{i,i}}}{K^*_{\mathrm{p,i}}} = \frac{-\frac{1+K^*_{\mathrm{p,i}}\cdot\frac{u_0}{i_0\cdot R}}{K^*_{\mathrm{i,i}}\cdot\frac{u_0}{i_0\cdot R}} + \sqrt{\left(\frac{1+K^*_{\mathrm{p,i}}\cdot\frac{u_0}{i_0\cdot R}}{K^*_{\mathrm{i,i}}\cdot\frac{u_0}{i_0\cdot R}}\right)^2 - 4\cdot\frac{L}{R\cdot K^*_{\mathrm{i,i}}\cdot\frac{u_0}{i_0\cdot R}}}}{2\cdot\frac{L}{R\cdot K^*_{\mathrm{i,i}}\cdot\frac{u_0}{i_0\cdot R}}} \tag{3.7}$$

Considering that $K^*_{\mathrm{p,i}}$ and $K^*_{\mathrm{i,i}}$ are the only controllable variables in Eq. (3.7), the equation is developed into the requirement on $K^*_{\mathrm{i,i}}$ shown in Eq. (3.8).

$$K^*_{\mathrm{i,i}} = \frac{R}{L}\cdot K^*_{\mathrm{p,i}} \tag{3.8}$$

The ratio L/R equals the electric time constant τ_{el} of the open electric loop, describing the response time of uncontrolled current on voltage. The ratio $K^*_{\mathrm{p,i}}/K^*_{\mathrm{i,i}}$ equals

the integration time of the current controller τ_i, describing the response time of the controller's integrator. Eq. (3.8) implies that these time constants should be the same. The intuitive explanation for this is that the current controller, including its integrator, must be able to react as fast as does current.

Requirement on $s_{2,\mathrm{i}}$ and $s_{2,\omega}$

The requirement given by Eq. (3.6b) can be rewritten using the equations for the high mechanical and electric poles given in Eq. (3.1) and (3.3), respectively. This results in the relation given in Eq. (3.9).

$$\frac{-\frac{1+K^*_{\mathrm{p,i}}\cdot\frac{u_0}{i_0\cdot R}}{K^*_{\mathrm{i,i}}\cdot\frac{u_0}{i_0\cdot R}} - \sqrt{\left(\frac{1+K^*_{\mathrm{p,i}}\cdot\frac{u_0}{i_0\cdot R}}{K^*_{\mathrm{i,i}}\cdot\frac{u_0}{i_0\cdot R}}\right)^2 - 4\cdot\frac{L}{R\cdot K^*_{\mathrm{i,i}}\cdot\frac{u_0}{i_0\cdot R}}}}{2\cdot\frac{L}{R\cdot K^*_{\mathrm{i,i}}\cdot\frac{u_0}{i_0\cdot R}}} \geq 1\mathrm{E}2\cdot\frac{-\frac{(2-b)+K^*_{\mathrm{p},\omega}}{K^*_{\mathrm{i},\omega}} - \sqrt{\left(\frac{(2-b)+K^*_{\mathrm{p},\omega}}{K^*_{\mathrm{i},\omega}}\right)^2 - 4\cdot\frac{\tau_\omega}{K^*_{\mathrm{i},\omega}}}}{2\cdot\frac{\tau_\omega}{K^*_{\mathrm{i},\omega}}} \tag{3.9}$$

The right hand side of Eq. (3.9) contains the exact formula for $s_{2,\omega}$ and can be simplified. In a practical case, such as presented by Tables 2.5 and 2.6, the term $4\cdot\frac{\tau_\omega}{K^*_{\mathrm{i},\omega}}$ is considerably smaller than the term $\left(\frac{(2-b)+K^*_{\mathrm{p},\omega}}{K^*_{\mathrm{i},\omega}}\right)^2$. This means that $s_{2,\omega}$ can be approximated as shown in Eq. (3.10), resulting in a slightly higher estimation of the pole frequency.

$$s_{2,\omega} \approx -\frac{(2-b)+K^*_{\mathrm{p},\omega}}{\tau_\omega} \tag{3.10}$$

This approximation of $s_{2,\omega}$ results in a conservative and simpler relation, shown in Eq. (3.11).

$$\frac{-\frac{1+K^*_{\mathrm{p,i}}\cdot\frac{u_0}{i_0\cdot R}}{K^*_{\mathrm{i,i}}\cdot\frac{u_0}{i_0\cdot R}} - \sqrt{\left(\frac{1+K^*_{\mathrm{p,i}}\cdot\frac{u_0}{i_0\cdot R}}{K^*_{\mathrm{i,i}}\cdot\frac{u_0}{i_0\cdot R}}\right)^2 - 4\cdot\frac{L}{R\cdot K^*_{\mathrm{i,i}}\cdot\frac{u_0}{i_0\cdot R}}}}{2\cdot\frac{L}{R\cdot K^*_{\mathrm{i,i}}\cdot\frac{u_0}{i_0\cdot R}}} \geq 1\mathrm{E}2\cdot\frac{(2-b)+K^*_{\mathrm{p},\omega}}{\tau_\omega} \tag{3.11}$$

Assuming that the requirement on $K^*_{\mathrm{i,i}}$ given in Eq. (3.8) is satisfied, Eq. (3.11) can be developed into a requirement on $K^*_{\mathrm{p,i}}$ shown in Eq. (3.12).

$$K^*_{\mathrm{p,i}} \geq -\frac{\frac{1\mathrm{E}2\cdot\left((2-b)+K^*_{\mathrm{p},\omega}\right)}{R\cdot\tau_\omega}\cdot L^2\cdot\frac{u_0}{i_0\cdot R} - L}{\frac{R\cdot\tau_\omega}{1\mathrm{E}2\cdot\left((2-b)+K^*_{\mathrm{p},\omega}\right)} - \frac{u_0}{i_0\cdot R}\cdot L} \tag{3.12}$$

Eq. (3.12) can be simplified. The left hand side of Eq. (3.11) equals $s_{2,\mathrm{i}}$, which can be approximated, too. Assuming the values given in Tables 2.5 and 2.6, the term $4\cdot\frac{L}{R\cdot K^*_{\mathrm{i,i}}\cdot\frac{u_0}{i_0\cdot R}}$ is considerably smaller than the term $\left(\frac{1+K^*_{\mathrm{p,i}}\cdot\frac{u_0}{i_0\cdot R}}{K^*_{\mathrm{i,i}}\cdot\frac{u_0}{i_0\cdot R}}\right)^2$. As a result, $s_{2,\mathrm{i}}$

can be approximated by Eq. (3.13).

$$s_{2,\mathrm{i}} \approx -\frac{R \cdot \left(1 + K^*_{\mathrm{p,i}} \cdot \frac{u_0}{i_0 \cdot R}\right)}{L} \tag{3.13}$$

As this approximation results in a higher estimated pole frequency, it could lead to a too relaxed requirement on $K^*_{\mathrm{p,i}}$. Assuming, for the time being, that this is not the case, one can rewrite Eq. (3.11) as Eq. (3.14).

$$\frac{R \cdot \left(1 + \frac{u_0}{i_0 \cdot R} \cdot K^*_{\mathrm{p,i}}\right)}{L} \geq 1\mathrm{E}2 \cdot \frac{(2-b) + K^*_{\mathrm{p},\omega}}{\tau_\omega} \tag{3.14}$$

The relation given in Eq. (3.14) can in turn be developed into the requirement shown in Eq. (3.15).

$$K^*_{\mathrm{p,i}} \geq 1\mathrm{E}2 \cdot \frac{L \cdot i_0 \cdot \left((2-b) + K^*_{\mathrm{p},\omega}\right)}{\tau_\omega \cdot u_0} - \frac{i_0 \cdot R}{u_0} \tag{3.15}$$

Equilibrium values for u_0, i_0 and τ_ω can be obtained using the non-linear system equations given in Chapter 2. Linear simulations indicate that the requirement given in Eq. (3.15) results in practically the same current controller settings and dynamic behaviour as does the requirement shown in Eq. (3.12). In other words, both Eq. (3.12) and (3.15) can be used to determine the minimum setting for $K^*_{\mathrm{p,i}}$, although Eq. (3.15) may be more convenient.

As a first verification of these current controller settings, Fig. 3.4 shows a Bode diagram with linearised response of shaft speed on speed setting $\delta\omega^*/\delta\omega^*_{\mathrm{set}}$ for different scale models. The corresponding transfer functions are given in Eqs. (2.24) and (2.30). Because the systems are linearised, the results are valid for small, sinusoidal variations around the equilibrium point. Two practical scale models with differently tuned electric drives are shown, with the response of the ideal scale model also plotted for reference. One electric drive is tuned with a pole margin of two decades, according to the recommended settings, while the other is tuned with a pole margin of one decade. This margin becomes apparent in the locations of the poles, which are plotted as well. It appears that the recommended current controller settings indeed result in negligible dynamic distortion in the responsive frequency range, while this is not the case if a pole margin of only one decade is attained.

With recommended settings for $K^*_{\mathrm{p,i}}$ and $K^*_{\mathrm{i,i}}$ now known, the effect of these settings on the dynamic behaviour of the HIL setup is discussed in detail in Section 3.3.

3.3 Discussion

As is shown in Fig. 3.1, the final step in this Chapter is to verify that the recommended current controller settings indeed result in negligible distortions by the electric drive. This was already partially verified in Fig. 3.4, which showed that linear simulations in the frequency domain predict negligible dynamic distortions with the recommended current controller settings. In this Section, this verification is elaborated. First, the effects of individual current controller settings on shaft dynamics are investigated in Section 3.3.1. In specific, the effects of $K^*_{\mathrm{p,i}}$ and $K^*_{\mathrm{i,i}}$ on gain and phase of shaft

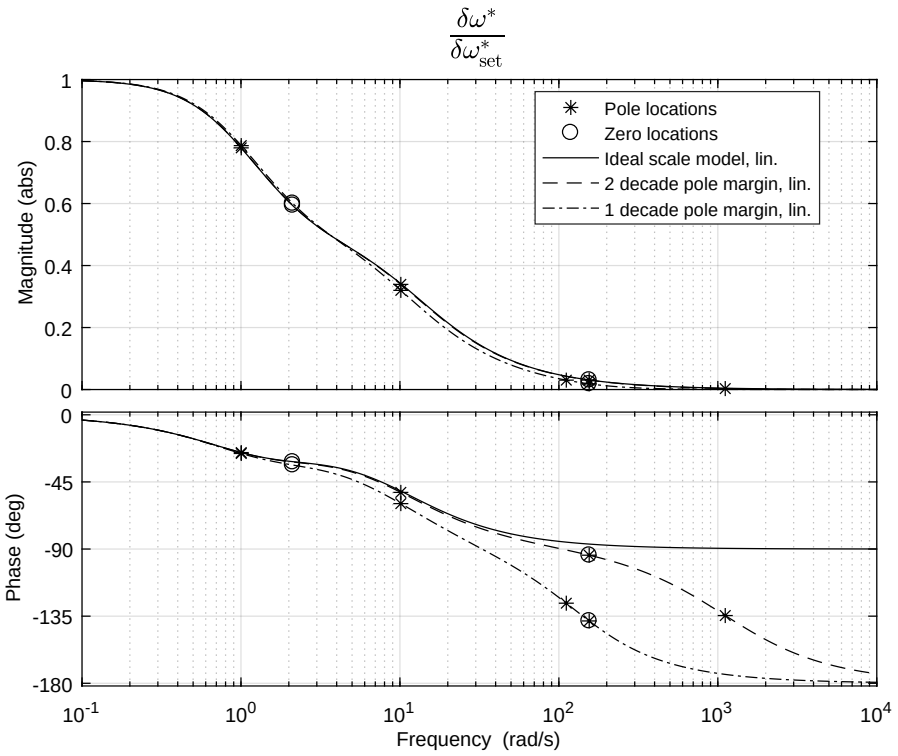


Figure 3.4: Bode diagram with response of $\delta\omega^*/\delta\omega^*_{\mathrm{set}}$ for the ideal scale model and two practical scale models with differently tuned current controllers. For both practical scale models, poles and zeros are plotted: four poles and two zeros can be distinguished per system. On the left hand side of the diagram, one mechanical zero and two mechanical poles are visible, while one electric zero and two electric poles are located on the right hand side, per system. The first practical scale model is tuned with a two decade pole margin, with $K^*_{\mathrm{p,i}}$ set to 0.83 and $K^*_{\mathrm{i,i}}$ set to 128.61. As can be seen, this results in negligible dynamic distortion in the responsive frequency range. The other practical scale model is tuned with a pole margin of one decade, with $K^*_{\mathrm{p,i}}$ set to 0.08 and $K^*_{\mathrm{i,i}}$ set to 12.86. In that case, considerable dynamic distortion does occur in the responsive frequency range.

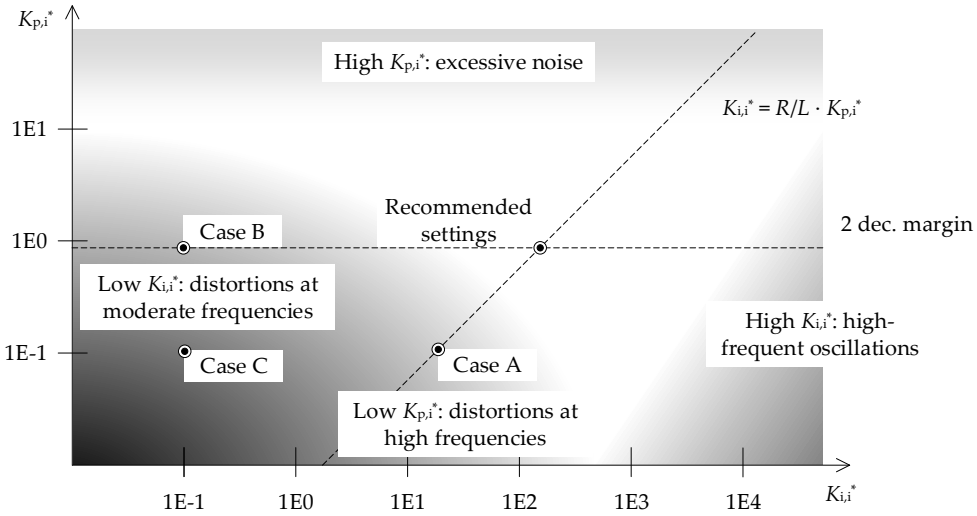


Figure 3.5: Influence of different settings for $K_{\mathrm{p,i}}^*$ and $K_{\mathrm{i,i}}^*$ on shaft speed response $\delta\omega^*/\delta\omega_{\mathrm{set}}^*$ of the HIL setup considered in this dissertation. In dark colored areas, audible noise and dynamic distortions occur.

speed response on speed setting $\delta\omega^*/\delta\omega_{\mathrm{set}}^*$ are evaluated using linear simulations. Following this, the influence of current controller settings is investigated using non-linear simulations in Section 3.3.2. By plotting operating ellipses, the consequences of improper settings can be made more clear, while also demonstrating that the recommended settings are valid also for non-linear loads.

3.3.1 Influence of $K_{\mathrm{p,i}}^*$ and $K_{\mathrm{i,i}}^*$ on $\delta\omega^*/\delta\omega_{\mathrm{set}}^*$

The requirements on $K_{\mathrm{p,i}}^*$ and $K_{\mathrm{i,i}}^*$ are visualised in Fig. 3.5. Horizontal lines represent the requirement on $K_{\mathrm{p,i}}^*$; a setting corresponding to two decades is shown. The requirement on $K_{\mathrm{i,i}}^*$ is represented by the diagonal line.

Fig. 3.4 shows that the recommended current controller settings result in negligible dynamic distortions in the responsive frequency range, at least for small variations around an equilibrium. Taking these recommended settings as a starting point, linear simulations of the response with reduced $K_{\mathrm{p,i}}^*$ and $K_{\mathrm{i,i}}^*$ are conducted. In addition to these recommended settings, Fig. 3.5 presents three differently tuned setups: cases A, B and C. The Bode diagrams corresponding to these four cases are shown in Fig. 3.6. Evaluating the effect on the Bode diagram provides insight into how these settings are related to dynamic distortions. As the largest distortions result from low values for $K_{\mathrm{p,i}}^*$ and $K_{\mathrm{i,i}}^*$, these will first be considered in detail. At the end of this Section, the effect of settings higher than recommended will be briefly discussed.

In case A, $K_{\mathrm{p,i}}^*$ is reduced to 0.1, while the value for $K_{\mathrm{i,i}}^*$ is kept as recommended. Fig. 3.6 shows that this has an effect on behaviour at high frequencies: the dashed line becomes visible in the right hand side of the Bode diagram. Effects on the gain are limited; the phase, however, becomes considerably different from the phase of the

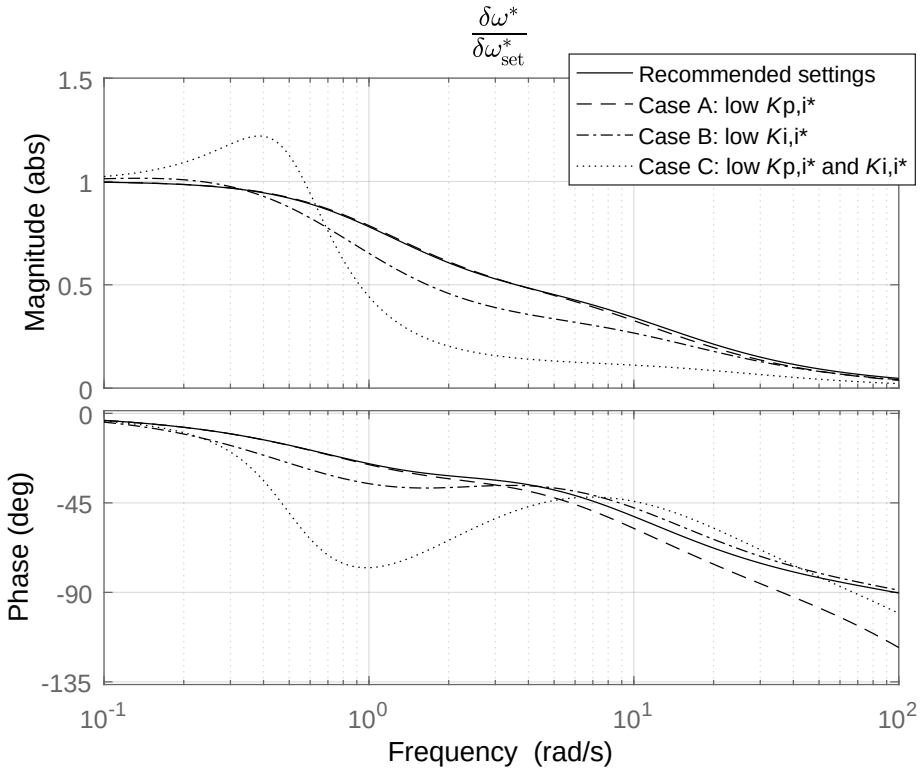


Figure 3.6: Bode diagrams of $\delta\omega^*/\delta\omega^*_{\text{set}}$ for the linearised ideal scale model and linearised scale models with different current controller settings, corresponding to the cases shown in Fig. 3.5.

ideal scale model as the frequency increases.

In case B, on the other hand, $K^*_{\mathrm{i,i}}$ is reduced to 0.1, while the value for $K^*_{\mathrm{p,i}}$ is kept as recommended. This has a minor effect at moderate frequencies: in the gain plot in Fig. 3.6, the dash-dot line becomes visible around a frequency of 10 radians per second, again coinciding with the solid line of the recommended settings as the frequency increases. There is an intuitive explanation for the different frequency dependency of $K^*_{\mathrm{p,i}}$ and $K^*_{\mathrm{i,i}}$. The static gain component of a PI controller immediately responds on input signals, while the integrator gain component needs time to build up an output signal. As a result, the integrator component responds mainly at low to moderate frequencies, with the static component becoming more dominant as frequency increases.

Case C represents the HIL setup with $K^*_{\mathrm{p,i}}$ and $K^*_{\mathrm{i,i}}$ both set to 0.1. In that case, gain and phase are completely different from those of the ideal scale model, indicating that the HIL setup does not at all represent the ideal scale model.

Fig. 3.5 suggests that there are also practical upper limits on $K^*_{\mathrm{p,i}}$ and $K^*_{\mathrm{i,i}}$. On one hand, increasing $K^*_{\mathrm{p,i}}$ generally results in better response at high frequencies. However, a very high setting for $K^*_{\mathrm{p,i}}$ causes the controller to respond very quickly on current errors. During trials with the actual HIL setup, considerable noise was observed if values for $K^*_{\mathrm{p,i}}$ were increased to an order of magnitude above its recommended value. This noise is expected to be related to peaks in controller output and therefore, voltage supplied to the motor. It cannot be excluded that these peaks cause damage to the electric drive. $K^*_{\mathrm{p,i}}$ can therefore not be increased infinitely.

On the other hand, if $K^*_{\mathrm{i,i}}$ is much higher than recommended, the integrating component of the PI current controller will change much faster than does current. For example, after a step increase of set speed, rapid integration of the error signal will result in considerable overshoot of current and hence, torque. This in turn causes high-frequency oscillations of shaft speed. In general, however, the effects from high $K^*_{\mathrm{p,i}}$ and $K^*_{\mathrm{i,i}}$ are less pronounced than the effects from low $K^*_{\mathrm{p,i}}$ and $K^*_{\mathrm{i,i}}$, and will therefore not be further considered here.

To further illustrate the practical consequences of incorrect current controller settings, Section 3.3.2 compares non-linear simulations of the ideal scale model and the practical scale model with different current controller settings.

3.3.2 Non-Linear Simulations

Fig. 3.7 shows three operating ellipses, corresponding to HIL scale models with different current controller settings. As Chapter 1 mentions, operating ellipses are particularly relevant to marine engineers as they present fluctuations of prime mover torque and speed in a single graph. When plotted in the motor diagram, operating ellipses give clear indication where operating limits are approached or even exceeded. Whereas the previous simulations considered fluctuations of control input $\delta\omega^*_{\mathrm{set}}$, the operating ellipses in Fig. 3.7 follow from sinusoidal variations of disturbance input δv^*_{a} and a constant speed setting.

Ellipses are plotted for the ideal scale model, for a practical scale model with recommended current controller settings and for a practical scale model with the same, low settings as in Case C introduced earlier. In addition, a torque limit is plotted at 110% of equilibrium torque. The ellipse corresponding to the practical setup with

recommended settings exactly coincides with the ellipse of the ideal scale model, indicating that no dynamic distortions occur. For Case C, on the other hand, the ellipse is considerably smaller, remaining below the torque limit. This demonstrates that incorrect current controller settings may cause overestimation of the propulsion system's dynamic capabilities.

3.4 Conclusion

HIL experiments on ship propulsion systems rely on electric drives to develop simulated torque. As was shown in Fig. 2.10, this drive may introduce additional, unwanted dynamic behaviour if it is not properly tuned. To avoid such distortions, Section 3.2 introduced requirements on the settings of the current controller in the drive. Following this, simulations were conducted to show that by using recommended current controller settings, this unwanted influence is indeed avoided. This is an important condition during HIL experiments: Fig. 3.7 compared the simulated operating ellipses resulting from different current controller settings, indicating that improper controller settings may result in erroneous assessments of a ship's dynamic capabilities.

However, the current controller settings derived here are not the only correct solution. Fig. 3.5 presented three cases in which the settings deviated from the recommendations with different degrees. The Bode plots corresponding to these cases were shown in Fig. 3.6, and it appeared that the current controller settings have a considerable margin before dynamic distortion becomes problematic. Furthermore, Eqs. (3.8) and (3.15) showed that the requirements on current controller settings have a linear relation with system parameters. As a consequence, one does not need highly accurate estimations of system parameters to obtain useful values for $K^*_{\mathrm{p,i}}$ and $K^*_{\mathrm{i,i}}$.

The wide margin for $K^*_{\mathrm{p,i}}$ and $K^*_{\mathrm{i,i}}$ also implies that there are other ways to properly tune the current controller of the electric motor in a HIL experiment. If one is willing to invest some time, trial and error will eventually result acceptable settings, too. As another option, some motor drives offer the possibility of automatic controller tuning. However, these methods depend on availability of time or automated tuning algorithms, and the resulting settings can be hard to substantiate. The rules derived here, on the other hand, provide a fast, mathematically substantiated and robust way to tune the current controller at once, requiring only estimates of a few mechanical and electrical parameters.

Using the recommended settings, one can use an electric propulsion system to physically replicate a simulated prime mover while avoiding dynamic distortion by electric components in the responsive frequency range. This issue being solved, the next scale effect can be addressed in Chapter 4: incorrect moment of inertia.

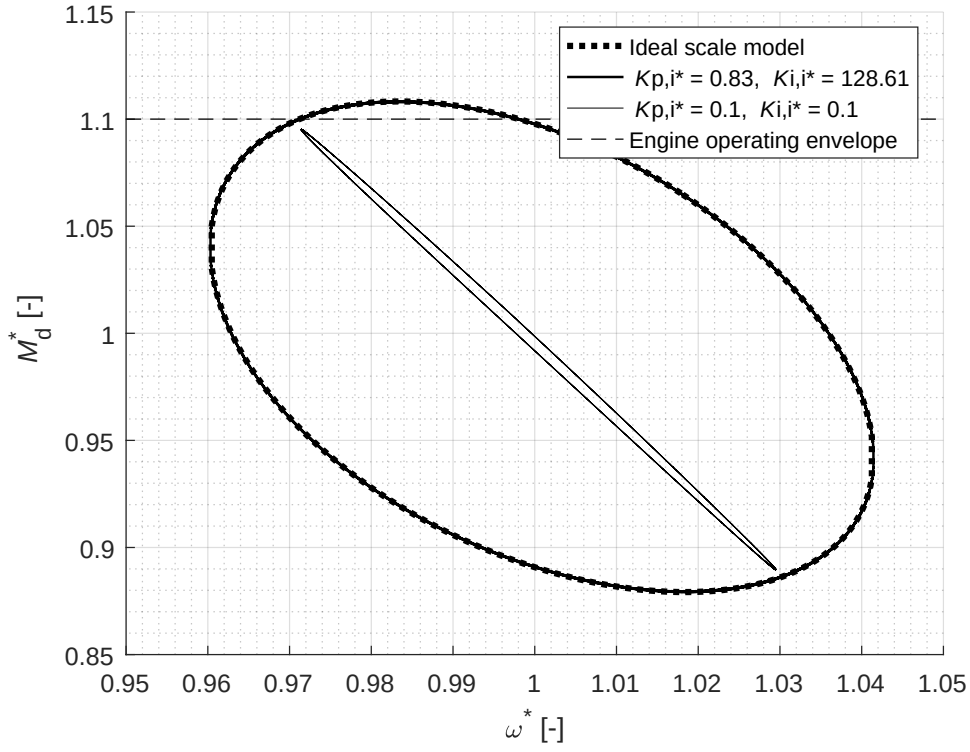


Figure 3.7: Non-linear simulations of operating ellipses for the ideal scale model and practical scale models with varying current controller settings. At 110% of equilibrium torque, an upper limit of the operating envelope is drawn, representing the maximum continuous torque of the simulated engine. Note that this limit is an arbitrary example and does not reflect the parameters given in Table 2.1. The propeller is moving through regular waves with an equilibrium advance speed of 1.73 m/s. The waves are modelled as sinusoidal fluctuations of axial homogeneous propeller inflow velocity around the equilibrium advance speed. The wave encounter frequency equals 1 rad/s; the oscillation amplitude of the propeller inflow is 0.433 m/s, or 25% of the equilibrium inflow speed. The ellipse of the practical setup with recommended settings completely coincides with the ellipse of the ideal scale model. The other practical scale model has the same, low settings for $K^*_{p,i}$ and $K^*_{i,i}$ as in case C, introduced earlier in this Chapter. As can be seen, these settings result in a smaller operating ellipse.

Chapter 4

Numerical Correction of Propulsion Shaft Inertia

Chapter 3 partially answered the fourth research sub question by deriving settings for the current controller, such that dynamic distortions by the electric drive are avoided. A second aspect to the problem of dynamic distortions is the incorrect scaling of moment of inertia. This subject is addressed in this Chapter, further answering the fourth research sub question. For the sake of completeness, the fourth research sub question can be recapitulated as follows:

– Which measures can be taken to avoid distortion of shaft dynamics by these [electrical and mechanical] components [in the HIL setup]?

In Section 2.5.3, the effects on incorrectly scaled moment of inertia of the propulsion system were illustrated. Fig. 2.13 showed that, if the inertia is not correct, shaft dynamics may be entirely different, especially as frequencies increase. Hence, to maintain dynamic similarity of the ideal and practical scale models, the moment of inertia of the propulsion system must be scaled correctly, too. Yet, the ship and scale model are usually powered by different kinds of propulsion systems: whereas the real ship is powered by, for example, a diesel-mechanical propulsion system, the scale model has an electric drive. These systems have entirely different geometries, and therefore, different moments of inertia.

Eq. (4.1) shows that drive torque M_d, load torque M_l and total moment of inertia of the propulsion system I_tot result in an angular acceleration $\mathrm{d}\omega/\mathrm{d}t$. Distorted inertia therefore leads to distorted shaft dynamics even if load and drive torque are properly scaled.

$$\frac{\mathrm{d}\omega}{\mathrm{d}t} = \frac{M_\mathrm{d} - M_\mathrm{l}}{I_\mathrm{tot}} \tag{4.1}$$

Thus, a correction for inertia may be necessary to avoid dynamic distortions during HIL open water experiments. Based on the mathematical descriptions given in Chapter 2, different methods will be analysed here to correct moment of inertia. The most promising method will be described in detail, providing guidance to applying a correction for inertia in practice.

4.1 Effect of Distorted Inertia on Shaft Dynamics

Paying attention to the different components of the moment of inertia, the shaft dynamics of the ideal scale model can be mathematically expressed as in Eq. (4.2). I_{d}, I_{prop} and I_{H2O} refer to the moments of inertia of the propulsion motor and shafting, propeller and added mass, respectively. I_{d} and I_{prop} are determined by the geometry and material density of the drive and propeller, which are constant. I_{H2O}, on the other hand, depends on the water entrained between the propeller blades, which may change with advance speed, propeller speed, propeller pitch and number blades.

$$(I_{\mathrm{d,id}} + I_{\mathrm{prop,id}} + I_{\mathrm{H2O,id}}) \cdot \frac{\mathrm{d}\omega\,(t)}{\mathrm{d}t} = M_{\mathrm{d}}\,(t) - M_{\mathrm{fr,id}}(t) - M_{\mathrm{prop,hydro}}\,(t) \tag{4.2}$$

In previous Chapters, distortions of propeller load torque $M_{\mathrm{prop,hydro}}$ and electric motor drive torque M_{d} were discussed. The former were dismissed because of their negligible effects on dynamic behaviour, while the latter could be reduced to acceptable levels by properly tuning the current controller. To avoid unnecessary complexity of the simulation models, friction torque inside the downscaled diesel-mechanical propulsion system, $M_{\mathrm{fr,id}}$, is not considered any further. Yet, as was indicated earlier, correctly scaled torque terms are not sufficient to obtain dynamic similarity; Eq. (4.2) shows that the moment of inertia must scale correctly, too. As the geometries and materials of the full scale and model scale propulsion systems are not the same, this is not self-evident. In the practical scale model, shaft dynamics are governed by Eq. (4.3).

$$(I_{\mathrm{d,p}} + I_{\mathrm{prop,p}} + I_{\mathrm{H2O,p}}) \cdot \frac{\mathrm{d}\omega\,(t)}{\mathrm{d}t} = M_{\mathrm{d}}\,(t) - M_{\mathrm{fr,p}}\,(t) - M_{\mathrm{prop,hydro}}\,(t) \tag{4.3}$$

Note that the subscript has changed for the inertia terms, with p denoting the practical scale model. Distortions resulting from model friction torque $M_{\mathrm{fr,p}}$ will be covered in Chapter 5, and are neglected in this Chapter. As will be shown later on, distortions of I_{d} and I_{prop} and their effects on dynamic behaviour may be considerable. For brevity, the sum of solid inertia components I_{d} and I_{prop} is from here on referred to as the mechanical moment of inertia I_{mech}.

The inertia of the entrained water I_{H2O} can be subject to distortions as well. Such distortions would be mainly the result of viscous scale effects on flow around the propeller blades. However, as was mentioned in Section 2.5.4, viscous these effects are rather limited compared to the other scale effects considered in this dissertation. At the same time, entrained moment of inertia constitutes a highly complex hydrodynamic subject, and efforts to formulate a definitive estimation method for this parameter have so far remained inconclusive. Often, the estimation methods proposed by, among others, Lewis and Auslaender (1960), Burrill and Robson (1962) and Schwanecke (1963) are relied upon, although their applicability on modern propellers is disputed (Krüger and Abels, 2017). In brief, the subject of entrained inertia justifies a research project on its own. Considering the complexity of this subject and the limited magnitude of the associated scale effects, no further attention is paid to scale effects on entrained inertia. From here on, I_{H2O} is estimated according to Burrill and Robson (1962). As Table 4.1 shows, this implies that $I_{\mathrm{H2O,id}}$ is equal to $I_{\mathrm{H2O,p}}$. Considering this, both ideal and practical added inertia are referred to as I_{H2O}.

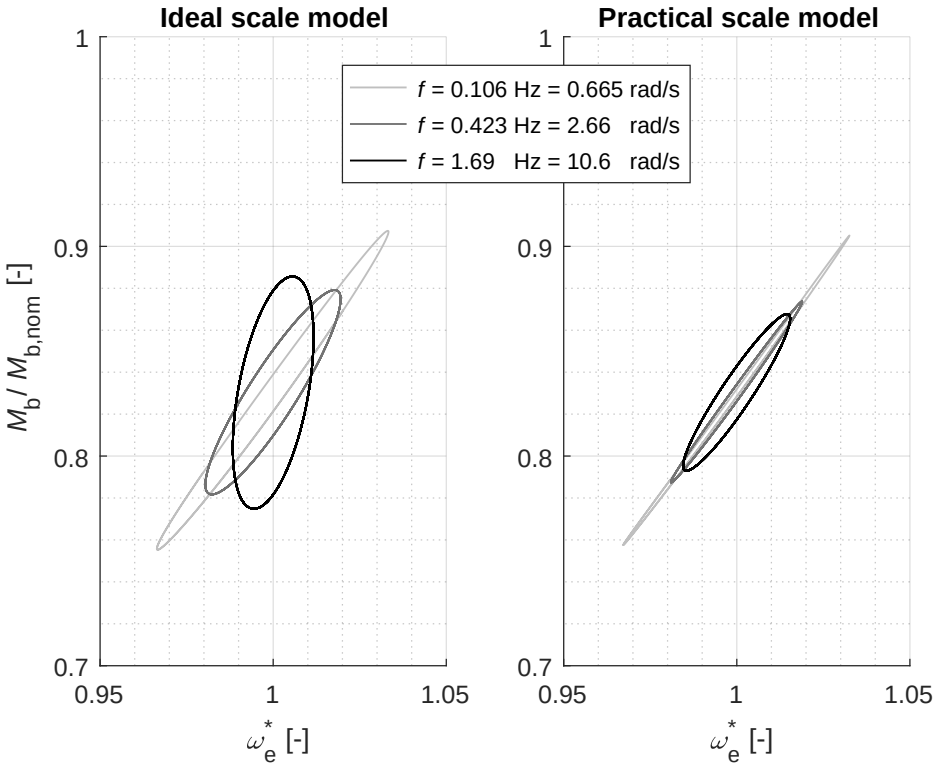


Figure 4.1: Non-linear simulations of operating ellipses for the ideal and practical scale model. Engine speed setting is varied sinusoidally with an amplitude of 20 rpm around an equilibrium of 500 rpm (with rpm values in full scale equivalents), at three different frequencies. The mechanical moment of inertia of the practical scale model, $I_{\mathrm{mech,p}}$, is 9.8% of the ideal inertia $I_{\mathrm{mech,id}}$. The estimated added moments of inertia I_{H2O} are the same. The moments of inertia are listed in Table 4.1. Other parameters for these simulations are the same as in previous Chapters and were given in Table 2.1.

Table 4.1: Moments of inertia of the ideal and practical scale model propulsion systems. These values correspond to the downscaled diesel-mechanical propulsion system and the actual HIL setup used to emulate this propulsion system. The moment of inertia of the HIL setup is considerably smaller because of lighter propeller material, a more compact propulsion motor and the absence of gear reduction.

	Symbol	Unit	Ideal	Practical
Drive moment of inertia	I_{d}	[kgm^2]	0.027 80	0.002 26
Prop. moment of inertia	I_{prop}	[kgm^2]	0.001 90	0.000 64
Mech. moment of inertia	I_{mech}	[kgm^2]	0.029 70	0.002 90
Added inertia	I_{H2O}	[kgm^2]	0.003 68	0.003 68
Total moment of inertia	I_{tot}	[kgm^2]	0.033 38	0.006 58

The distortions caused by an incorrect moment of inertia can be illustrated using non-linear time domain simulations. Fig. 4.1 shows operating ellipses of the ideal scale model and a corresponding practical scale model with incorrect model scale inertia. Engine speed setting $\omega_{\mathrm{e,set}}$ was varied at three different frequencies. Although no helmsman would in practice apply such changes to the shaft speed setting, other disturbances may very well occur at the considered frequencies. Regular waves, for example, may induce variations of advance speed at the simulated frequencies. At the same time, speed setting and advance speed are similar from a control engineering perspective, as is argued in Chapter 2 and Appendix A. Parameters for the ideal scale model are given in Chapter 2, Table 2.1. The practical scale model has the same parameters and equilibrium values as in previous simulations. As an addition compared to simulations in previous Chapters, added inertia I_{H2O} is now taken into account, too. The moments of inertia and their components are listed in Table 4.1.

Interestingly, Table 4.1 shows a substantial difference between ideal and practical moment of inertia: $I_{\mathrm{mech,p}}$ is only 9.8% of $I_{\mathrm{mech,id}}$. This has several reasons. First, the ship's propeller is made of a nickel-aluminium-bronze (NAB) alloy, while the scale model propeller is made of aluminium. The specific mass of aluminium is approximately three times lower than that of NAB, resulting in a much lower moment of inertia for the aluminium propeller. In addition, the electric propulsion motor of the practical scale model has a relatively low moment of inertia, as it has a more compact construction than the diesel engine installed in the ideal scale model. Moreover, in the diesel-mechanical propulsion system, the engine is connected to the propeller through a gearbox with a reduction factor i_{gb}. This has a considerable effect on the moment of inertia of the combined system. In this dissertation, the moment of inertia is expressed with respect to propeller rotation, which implies that the inertia of the components on the engine side of the gearbox must be multiplied with a factor $(i_{\mathrm{gb}})^2$. As the practical scale model has no gearbox, its moment of inertia is considerably lower than that of the ideal scale model.

In case of complete dynamic similarity, the operating ellipses of the ideal and practical scale models are the same at all frequencies. Fig. 4.1 shows that incorrect inertia hinders similarity: sizes, shapes and orientations of the ellipses differ considerably. For example, at a frequency of 1.69 Hz (corresponding to 0.4 Hz at full scale),

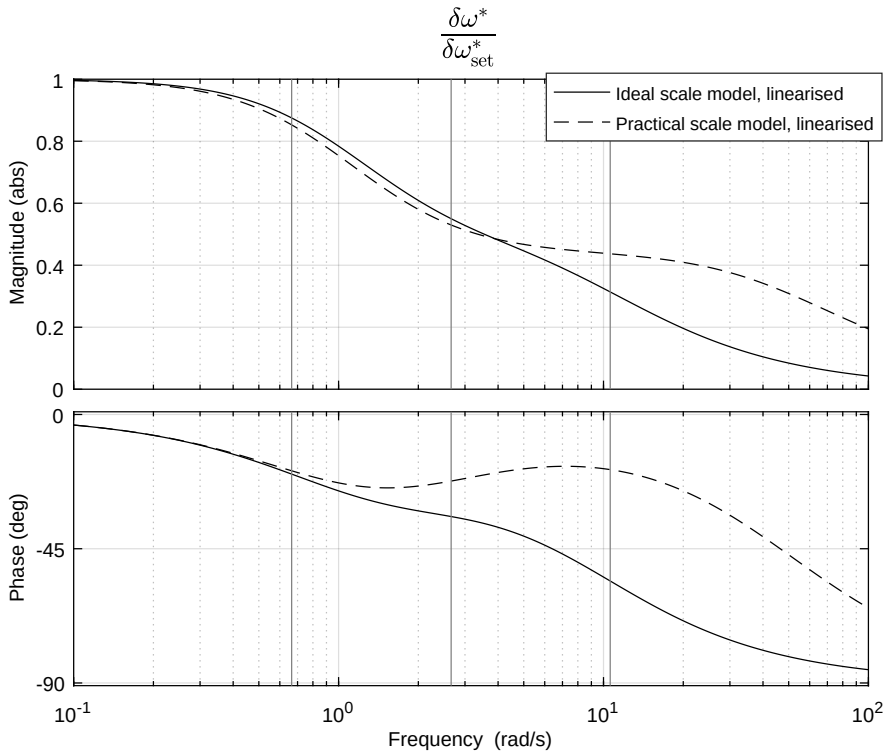


Figure 4.2: Effect of incorrectly scaled moment of inertia on $\delta\omega^*/\delta\omega^*_{\text{set}}$. The corresponding transfer function is given in Appendix A, Eq. (A.1a). Parameters for these simulations are the same as in previous Chapters and were given in Table 2.5. Moments of inertia are given in Table 4.1. Verticals are drawn at the frequencies shown in Fig. 4.1.

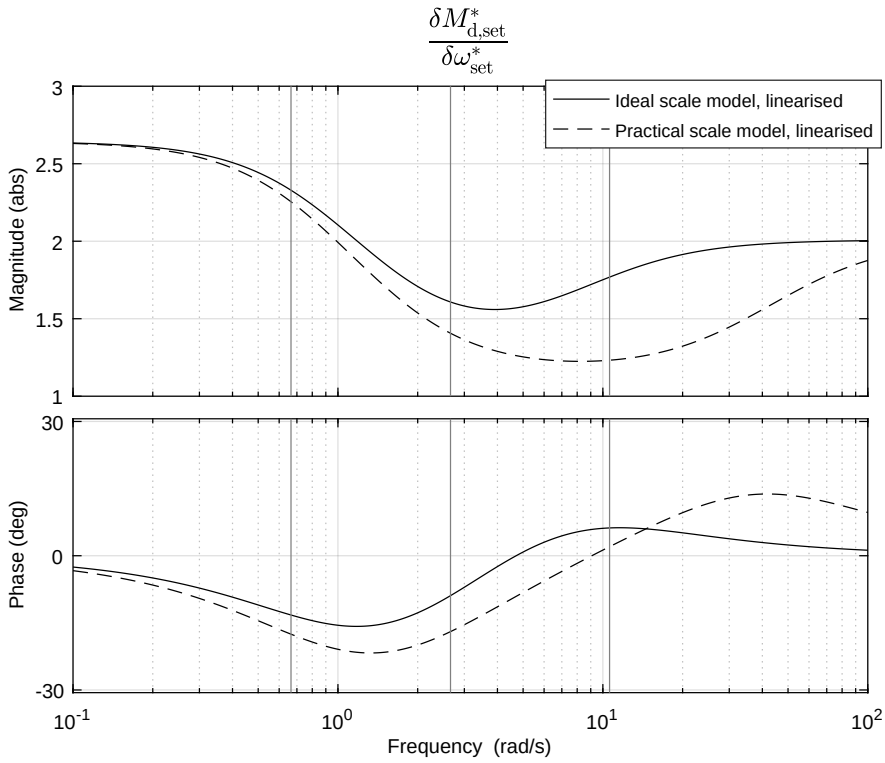


Figure 4.3: Effect of incorrectly scaled moment of inertia on $\delta M^*_{\mathrm{d,set}}/\delta\omega^*_{\mathrm{set}}$. The corresponding transfer function is given in Appendix A, Eq. (A.2a). Parameters for these simulations are the same as in previous Chapters and were given in Table 2.5. Moments of inertia are given in Table 4.1. Verticals are drawn at the frequencies shown in Fig. 4.1.

torque oscillations of the practical model are considerably smaller than for the ideal scale model, while the speed oscillations are visibly larger. As was the case with an improperly tuned current controller, these distortions may in some cases lead to false conclusions regarding the dynamic performance of a ship's propulsion system.

A close examination of the ellipses in Fig. 4.1 shows that there is a complex relation between the response of the propulsion system and disturbance frequency. For example, the torque oscillations of the ideal scale model are the largest at the lowest frequency, becoming smaller as the frequency increases to around 0.4 Hz. However, at 1.69 Hz, the oscillations become larger again. Similarly, the magnitude of the distortions has a rather complex relation with frequency. These frequency dependencies become more clear in Bode plots.

Figs. 4.2 and 4.3 show the linearised response of shaft speed $\delta\omega^*$ and drive torque $\delta M^*_{\mathrm{d,set}}$ on shaft speed setting $\delta\omega^*_{\mathrm{set}}$. Note that simulated brake torque M_{b} and simulated drive torque $M_{\mathrm{d,set}}$ are separated only by a simulated gearbox with a fixed reduction factor, and therefore have the same dynamic response. Close inspection of the Bode diagrams reveals the same relation between torque, shaft speed and input frequency as seen in Fig. 4.1. Moreover, it becomes clear that dynamic distortions become substantial in the responsive frequency range, indicating that a correction of the practical scale model's inertia is necessary. Different approaches to such corrections are explored in Section 4.2.

4.2 Correcting the Moment of Inertia

The moments of inertia of the propulsion drive and propeller are subject to mechanical scale effects. To avoid distorted shaft dynamics, a correction must be applied, as will be demonstrated in this Section. As a first step, Eq. (4.4) gives a mathematical expression for the required correction of inertia, starting from the differential equation for the practical scale model. As was indicated earlier, friction torque $M_{\mathrm{fr,p}}$ is neglected here; a method to compensate friction torque inside the practical scale model will be introduced in Chapter 5.

$$(I_{\mathrm{d,p}} + I_{\mathrm{prop,p}} + I_{\mathrm{H2O}} + I_{\mathrm{c}}) \cdot \frac{\mathrm{d}\omega\,(t)}{\mathrm{d}t} = M_{\mathrm{d}}\,(t) - M_{\mathrm{prop,hydro}}\,(t) \tag{4.4}$$

I_{c} is referred to as the *inertia correction*, required to correct the practical scale model inertia to its ideal value. To achieve dynamic similarity, the left hand side of the differential equation for the corrected practical scale model, given in by Eq. (4.4), must be equal to the left hand side of the differential equation for the ideal scale model, given in Eq. (4.2). This requirement is written out in Eq. (4.5).

$$(I_{\mathrm{d,p}} + I_{\mathrm{prop,p}} + I_{\mathrm{H2O}} + I_{\mathrm{c}}) \cdot \frac{\mathrm{d}\omega\,(t)}{\mathrm{d}t} = (I_{\mathrm{d,id}} + I_{\mathrm{prop,id}} + I_{\mathrm{H2O}}) \cdot \frac{\mathrm{d}\omega\,(t)}{\mathrm{d}t} \tag{4.5}$$

Eq. (4.5) can be developed into Eq. (4.6), isolating I_{c}.

$$\begin{aligned} I_{\mathrm{c}} &= I_{\mathrm{d,id}} + I_{\mathrm{prop,id}} - I_{\mathrm{d,p}} - I_{\mathrm{prop,p}} \\ &= I_{\mathrm{mech,id}} - I_{\mathrm{mech,p}} \end{aligned} \tag{4.6}$$

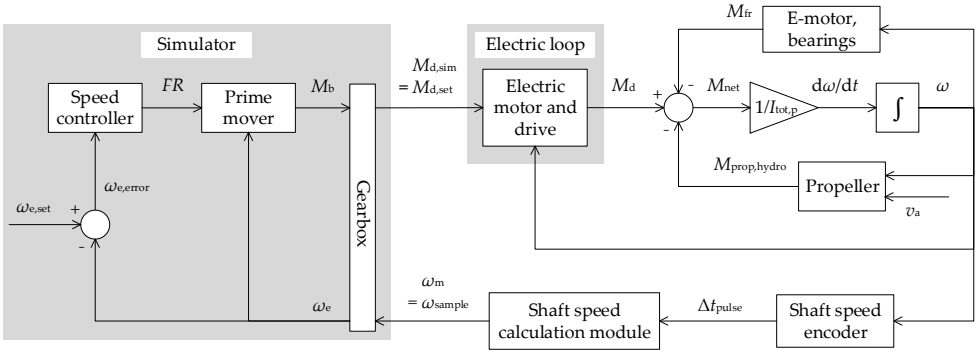


Figure 4.4: Block diagram of the practical dynamic open water test, assuming no corrections for scale effects on moment of inertia are applied.

As was mentioned earlier, the moment of inertia of the entrained water, I_{H2O}, is assumed to scale correctly. I_{c} can be positive or negative, a positive value indicating that the practical moment of inertia is too small.

There are three different methods to put this mathematical correction into physical practice. As a first option, one could physically change the moment of inertia, for example by means of an additional flywheel. This flywheel would have a moment of inertia equal to I_{c}. However, physical modifications of the setup are impractical for several reasons. First, a physical flywheel can only increase the scale model's moment of inertia. Removing material is generally not an option, which means that physical corrections are not possible if the inertia of the practical scale model is too large. Second, in order to avoid disturbance of the flow around the propeller, the additional flywheel would need to be mounted inside the streamlined body that also contains the electric motor. This may however be complicated by spatial restrictions inside the streamlined body as well as limited accessibility. As a another disadvantage, mounting and exchanging flywheels may become impractical and time consuming if one wants to evaluate a range of different propulsion systems with varying moments of inertia. Therefore, a different, more versatile approach to correcting inertia is investigated in Section 4.3.

4.3 Numerical Correction of Inertia

There are two ways to introduce a numerical inertia correction: by emulating a corrected shaft speed, or by emulating a corrected drive torque. Sections 4.3.1 and 4.3.2 describe and compare both approaches, resulting in one approach to be chosen for application in the HIL experiments later on. As a starting point, a block diagram of the uncorrected practical scale model is given in Fig. 4.4.

4.3.1 Shaft Speed Emulation

A first approach to emulating ship propulsion systems is by emulating shaft speed, as was demonstrated by Tanizawa et al. (2013a). In their setup, shaft acceleration is

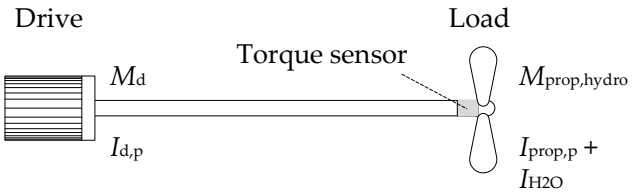


Figure 4.5: Schematic representation of the open water setup with torque sensor.

calculated each simulation step, based on measured propeller torque, simulated drive torque and the inertia of the simulated (ideal) propulsion system. The acceleration is then integrated, resulting in a simulated shaft speed. This shaft speed is communicated to the motor drive as a motor speed set point. The motor drive finally controls the electric motor to run at the simulated speed by controlling motor torque. As such, the practical inertia is overruled by the simulated, ideal inertia, implicitly correcting shaft dynamics. Although Tanizawa et al. (2013a) and Kitagawa et al. (2018) presented promising results, several remarks can be made on this approach.

Emulating shaft speed requires an additional shaft speed loop, which in turn also introduces another possible source of dynamic distortions. More importantly, however, shaft speed emulation relies on measured propeller load torque. This potentially introduces dynamic distortions, as the physical properties and working principles of the torque sensor limit its dynamic performance.

As an example, Fig. 4.5 gives a schematic representation of the torque sensor as commonly used during open water experiments. The sensor is a cylindrical extension of the shaft with reduced torsional stiffness, mounted in front of the propeller. Torque exerted on both ends of the sensor results in a torsion deflection. Using a Wheatstone bridge, this deflection is converted into a voltage signal, which is in turn converted into a digital torque signal.

Each conversion step is a possible source of measurement noise, non-linearities and quantisation errors. In the conversion from torque to deflection, the first distortions may already occur. As the relation between torque and deflection is non-linear, the torque measurement may contain non-linearity errors. Although these errors may be considered negligible in the design range of the sensor, they increase as the limits of this range are approached. In addition to this, there may be cross-coupling effects. Torque and thrust are often measured by the same sensor. Deflections caused by thrust may influence the torque measurement and vice versa. These errors can be determined during calibration and corrected in real-time; however, this assumes that the error remains constant.

Moreover, torque sensors are highly susceptible to damage and wear. Even minor plastic deformations caused by small impacts may result in considerable differences in measured torque, since torque is determined from minute elastic deformations. For similar reasons, protracted use and storage may affect the elasticity of the material and conductance of electrical components. Although the torque sensor can be periodically calibrated to account for this, measurement errors resulting from deformations may not always be detected.

Furthermore, the intentionally reduced stiffness of the sensor results in a reduced

eigen frequency of the shaft assembly. Near this eigen frequency, dynamic amplification of deformation may occur, and the amplitude and phase of measured torque does not correspond to the actual propeller load. Depending on the geometry of the sensor and the moment of inertia of the propeller, this eigen frequency may be below 20 Hz, with deformations occurring already at lower frequencies. This, too, can cause considerable distortions in the responsive and relevant frequency ranges. As such, the reduced eigen frequency of the shaft assembly potentially sets a problematic lower limit to the similarity range.

The torsional deflection results in a voltage differential. This is an analog signal, while the simulation model requires digital input. In the conversion from analog to digital, quantisation errors may occur, depending on the resolution of the signal converter.

Finally, the measured torque signal contains noise. The noise level may need to be reduced before the measured torque signal can be used in a realtime, numerical simulation model. Therefore, the signal likely needs to be filtered, causing further distortions of gain and phase especially at higher frequencies. Indeed, the time traces of engine speed presented by Tanizawa et al. (2013a) show a phase shift between fully numerical simulations and HIL measurements, possibly owing to filtering.

Considering the limitations of the torque sensor, shaft speed emulation may not be the most suitable method to reproduce shaft dynamics. Section 4.3.2 therefore considers torque emulation as an alternative approach.

4.3.2 Torque Emulation

In HIL experiments with torque emulation, the electric motor is controlled to develop a simulated torque rather than a simulated shaft speed. This way, shaft acceleration occurs physically by interaction between load and drive torque. Shaft dynamics occur in a more natural way than with speed emulation, since torque emulation involves one less control loop. Moreover, as the torque sensor is not part of the loop, distortions originating from this sensor are avoided. Contrary to speed emulation, however, torque emulation does not implicitly contain a correction for moment of inertia. Thus, if no correction for incorrectly scaled moment of inertia is applied, torque emulation results in distorted shaft dynamics. Following from the analysis in Section 4.2, these distortions can be corrected by an additional term, as is shown in Eq. (4.7).

$$(I_{\mathrm{d,p}} + I_{\mathrm{prop,p}} + I_{\mathrm{H2O}}) \cdot \frac{\mathrm{d}\omega\,(t)}{\mathrm{d}t} = M_{\mathrm{d}}\,(t) - I_{\mathrm{c}} \cdot \frac{\mathrm{d}\omega\,(t)}{\mathrm{d}t} - M_{\mathrm{prop,hydro}}\,(t) \tag{4.7}$$

The correction term on the right hand side of Eq. (4.7) is referred to as the torque correction $M_{\mathrm{d,corr}}$, shown separately in Eq. (4.8). The correction term consists of shaft acceleration $\mathrm{d}\omega/\mathrm{d}t$ and an inertia correction I_{c}, which could be considered a "virtual flywheel".

$$M_{\mathrm{d,corr}}\,(t) = I_{\mathrm{c}} \cdot \frac{\mathrm{d}\omega\,(t)}{\mathrm{d}t} \tag{4.8}$$

Eq. (4.8) shows that to determine $M_{\mathrm{d,corr}}$, the required inertia correction I_{c} and the actual shaft acceleration $\mathrm{d}\omega/\mathrm{d}t$ must be known. The former was written out in Eq. (4.6) and is a constant. The latter, on the other hand, varies constantly, and

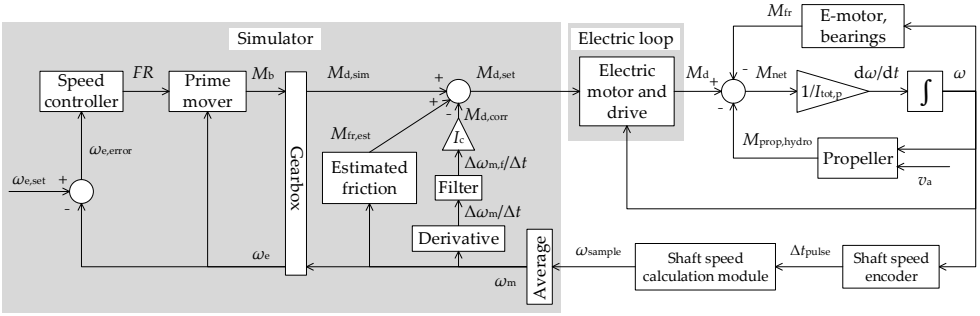


Figure 4.6: Block diagram of the practical dynamic open water test. Scale effects on the moment of inertia of the drive train are corrected using measured shaft speed. A correction for shaft friction torque of the practical scale model is also included; this correction will be described in Section 5.3.1.

must therefore be determined in realtime. However, accurate determination of shaft acceleration poses a considerable challenge.

Fig. 4.6 shows how the numerical inertia correction is applied in a HIL open water experiment. Apart from the inertia correction, an additional correction is included for friction torque inside the scale model drive train. This correction will receive further attention in Section 5.3.1.

The block diagram in Fig. 4.6 allows to explain the working principles of the numerical inertia correction step by step. Starting on the right hand side of the diagram, the shaft speed encoder emits a fixed number of pulses per shaft revolution, resulting in a pulse interval $\Delta t_{\mathrm{pulse}}$ inversely proportional to shaft speed ω. The shaft speed calculation and conversion modules measure this pulse interval, and calculate shaft speed sample ω_{sample} upon reception of a new pulse. Following this, ω_{sample} is averaged over a given time interval. This block average of sampled shaft speed is referred to as measured shaft speed ω_{m}. The reason for this averaging operation will be given in Section 4.4.

From measured shaft speed ω_{m}, the discrete derivative of the measured shaft speed, $\Delta\omega_{\mathrm{m}}/\Delta t$, is calculated. As will be explained in Section 4.4.2, this discrete derivative is a particularly noisy signal. Hence, as a next step, an infinite impulse response (IIR) filter is applied, resulting in a filtered derivative of the measured shaft speed, $\Delta\omega_{\mathrm{m,f}}/\Delta t$. Finally, the filtered derivative is multiplied with inertia correction I_{c}, given in Eq. (4.6). The thus obtained $M_{\mathrm{d,corr}}$ is added to the simulated drive torque $M_{\mathrm{d,sim}}$, resulting in realtime, numerical correction of moment of inertia by means of a correction of drive torque.

Ideally, this correction would be implemented continuously, ensuring a smooth correction of inertial torque. In practice, however, the HIL setup is a discrete system: corrections are calculated and applied in steps. As the frequency of input and disturbance signals increases, the time delays between these steps cause increasing distortions of the gain and phase of the corrected shaft response. In addition, the IIR filter also introduces unwanted distortion of gain and phase. These distortions increase with frequency, setting a limit to the frequency at which the numerical inertia correction is still sufficiently accurate.

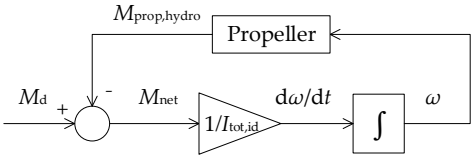


Figure 4.7: Block diagram of the ideal scale model, from drive torque to shaft speed. Propeller advance speed v_a is not considered in this Section and is therefore not included in this diagram.

In Section 4.4, the numerical inertia correction including discrete effects is analysed in detail, allowing to quantify distortions due to discretisation. It will be shown that the proposed numerical inertia correction is practically feasible, provided that close attention is paid to sample rates, IIR filter settings and the properties of the shaft speed encoder.

4.4 Implementation of the Numerical Inertia Correction

A crucial aspect in the performance of the numerical inertia correction is the frequency up to which it accurately corrects shaft dynamics. To be able to determine this frequency, this Section compares mathematical descriptions of the ideal scale model, the practical scale model without numerical inertia correction (*uncorrected scale model*) and the practical scale model with correction (*corrected scale model*). As in Chapters 2 and 3, this comparison will be based on linear descriptions as this allows analysis in the frequency domain. In addition to analysing the performance of the numerical inertia correction, a detailed description is given of how measured shaft speed is processed to obtain a correction torque. This description can be used as a guidance when applying the numerical inertia correction in future HIL setups.

4.4.1 Ideal and Uncorrected Scale Model

Fig. 4.7 shows a block diagram of the ideal scale model, from drive torque to shaft speed. Since the simulated prime mover and the performance of the electric drive are not of interest here, these are not included in the block diagrams and mathematical derivations in this Chapter. Following the analysis conducted in Chapter 2, the response of shaft speed on torque for the ideal scale model can be linearised to the form shown in Eq. (4.9).

$$\frac{\delta\omega^*}{\delta M_d^*}(s) = \frac{\frac{1}{2-b}}{\frac{I_{d,id}+I_{prop,id}+I_{H2O}}{2-b} \cdot s + 1} \tag{4.9}$$

As was explained in Chapter 2, variable b is the propeller torque derivative introduced by Stapersma and Vrijdag (2017). In the practical, uncorrected scale model, some of the inertia terms are subject to scale effects. This situation is represented by the block diagram shown in Fig. 4.8. In addition to different inertia terms, the diagram

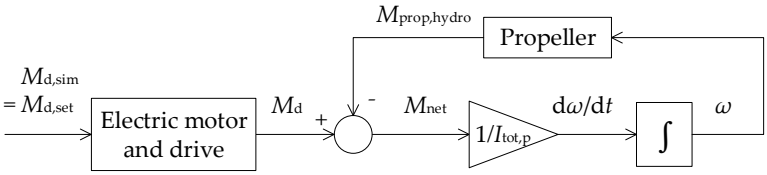


Figure 4.8: Block diagram of the HIL scale model with incorrect moment of inertia, or uncorrected scale model, from drive torque to shaft speed.

includes an electric motor and drive. Chapter 3 presented a method to avoid unwanted dynamic distortions by these components. The transfer function corresponding to the block diagram in Fig. 4.8, assuming no distortions by the electric motor and drive, is given in Eq. (4.10).

$$\frac{\delta\omega^*}{\delta M^*_{\text{d,sim}}}(s) = \frac{\delta\omega}{\delta M_{\text{d}}}(s) = \frac{\frac{1}{2-b}}{\frac{I_{\text{d,p}}+I_{\text{prop,p}}+I_{\text{H2O}}}{2-b} \cdot s + 1} \tag{4.10}$$

As was explained earlier, scale effects on the moments of inertia result in distorted shaft dynamics. Sections 4.4.2 and 4.4.3 analyse how and to which extent the numerical inertia correction can correct this distortion.

4.4.2 Corrected Scale Model

Fig. 4.9 shows a block diagram of the HIL setup with the proposed numerical inertia correction. Six operations are performed on sampled shaft speed ω_{sample} to calculate and apply correction torque $M_{\text{d,corr}}$:

1. sampling of shaft speed by the shaft speed calculation module;
2. averaging of shaft speed samples over a given time interval;
3. discrete differentiation of averaged shaft speed;
4. discrete filtering of the derivative;
5. multiplication of the filtered derivative with I_{c};
6. communicating $M_{\text{d,corr}}$ to the motor drive.

First, these six operations are visualised and explained in detail. Following this, a mathematical description of the practical scale model with numerical inertia correction is derived, including these operations. Predictions of linearised response using these mathematical descriptions are then compared in Section 4.4.3, allowing to assess the performance of the numerical inertia correction.

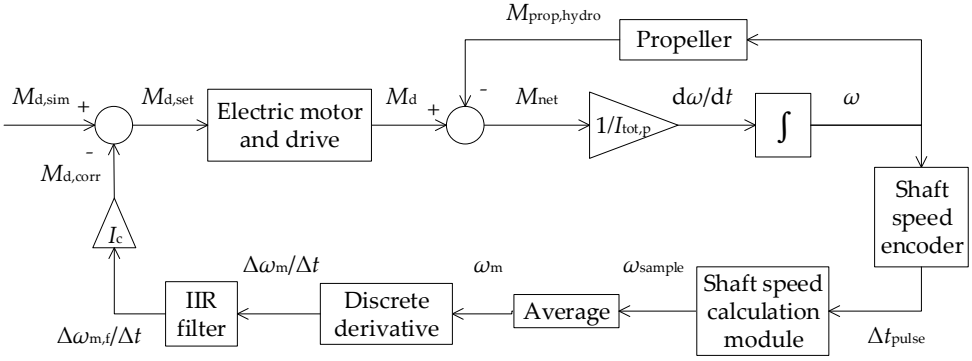


Figure 4.9: Block diagram of the HIL scale model with numerical inertia correction, or corrected scale model, from drive torque to shaft speed.

Numerical Operations in the Correction Algorithm

Fig. 4.10 visualises four of the six steps listed earlier, from shaft speed sampling to the filtered discrete derivative. First, shaft speed is measured by the shaft speed calculation module at a sample frequency f_{sample}. Second, the shaft speed samples are recorded by the simulation computer and averaged over a loop interval Δt_{loop} – the significance of this interval will be explained in more detail later on in this Section. Third, the discrete derivative of the measured shaft speed signal ω_{m} is calculated as shown in Eq. (4.11).

$$\frac{\Delta\omega_{\text{m}}}{\Delta t}(n) = \frac{\omega_{\text{m}}(n) - \omega_{\text{m}}(n-1)}{\Delta t} \tag{4.11}$$

Fourth, the calculated discrete derivative passes a discrete filter. Filtering is necessary as the discrete derivative of a signal is generally much noisier than the source signal. This can be illustrated with a simple example. If the measured values of any constant shaft speed ω have a standard deviation $\sigma_{\omega,m}$, the standard deviation of its discrete derivative is determined as shown in Eq. (4.12).

$$\begin{aligned}\sigma_{\omega,\Delta} &= \frac{\sqrt{{\sigma_{\omega,\text{m}}}^2 + {\sigma_{\omega,\text{m}}}^2}}{\Delta t} \\ &= \sqrt{2} \cdot f_{\text{loop}} \cdot \sigma_{\omega,\text{m}}\end{aligned} \tag{4.12}$$

It appears that $\sigma_{\omega,\Delta}$ is considerably greater than $\sigma_{\omega,\text{m}}$. One can conclude that in general, the noise level of a discrete derivative is considerably higher than the noise level of its source signal, especially at high sample rates. If the discrete derivative of measured shaft speed is used as input for the inertia correction, the amplified noise may cause erratic simulation behaviour. Noise spikes may exceed the operation envelope of the simulated propulsion system, causing unrealistic response and possibly triggering numerical errors. To avoid this, an infinite impulse response (IIR) filter is introduced. The mathematical description of this filter will be given further on in this Section; for a detailed elaboration on IIR filters and other discrete filters, reference is made to Balmer (1998).

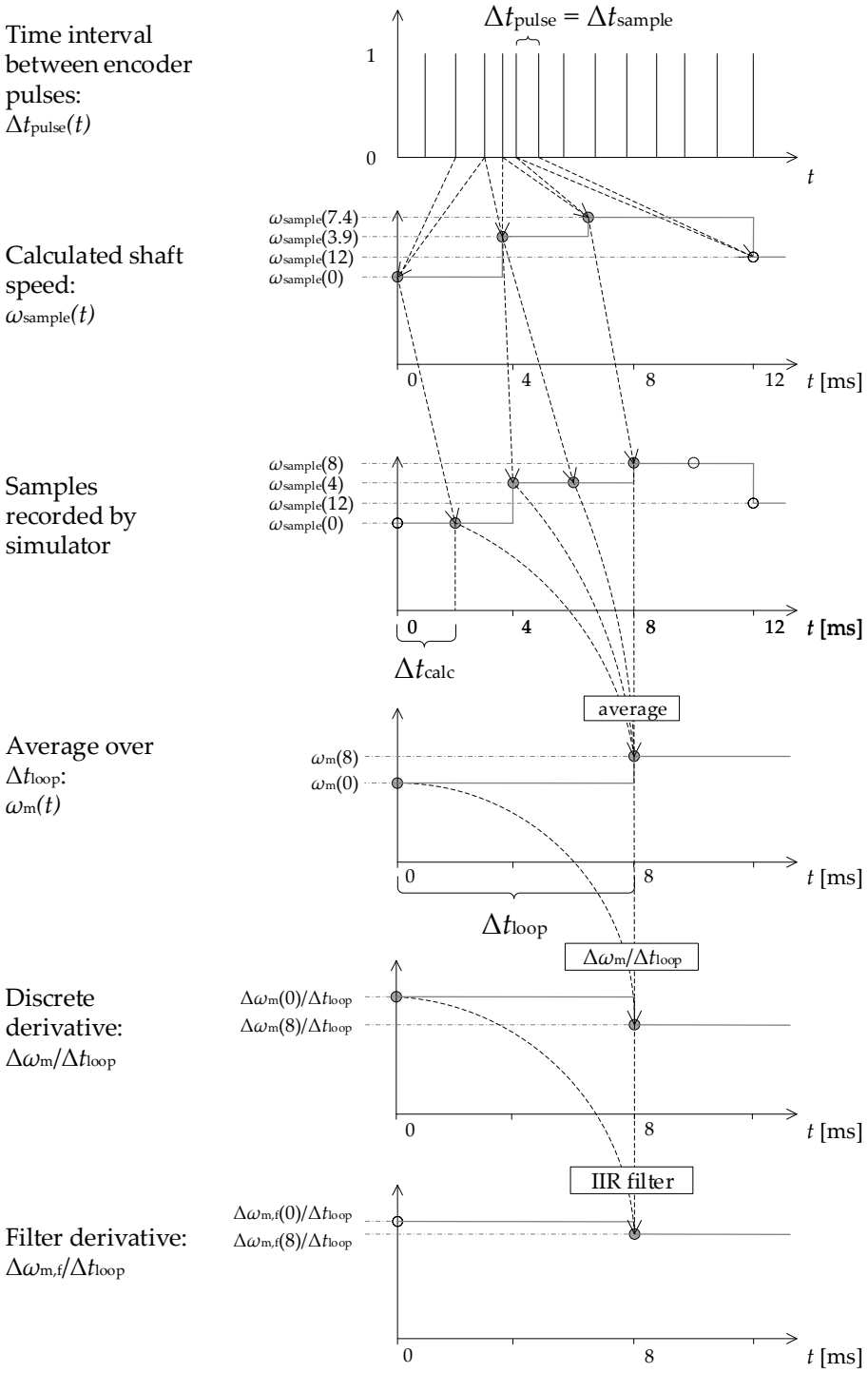


Figure 4.10: Processing of shaft speed samples to filtered discrete derivatives. Note that $\Delta t_{\mathrm{pulse}}$ and thus, $\Delta t_{\mathrm{sample}}$ are inversely proportional to shaft speed.

Finally, the filtered discrete derivative of shaft speed is multiplied by the inertia correction factor I_c. As this is a static factor, this final step does not introduce additional dynamics, and is therefore not included in Fig. 4.10.

The aforementioned operations occur at different frequencies, which are the inverses of the different step sizes shown in Fig. 4.10. Three frequencies can be distinguished:

1. shaft speed sample frequency f_{sample}, corresponding to Δt_{sample};
2. simulator calculation frequency f_{calc}, corresponding to Δt_{calc};
3. drive command frequency f_{command}, corresponding to Δt_{loop}.

f_{sample} indicates how many times per second the shaft speed is calculated by the shaft speed calculation module. This is done each time the module receives a pulse from the shaft speed encoder, implying that f_{sample} increases with shaft speed. f_{calc} expresses the frequency at which the simulator can sample and process measurement data. f_{command} indicates the frequency at which commands from the simulator can be received and executed by the motor drive. For a simulation loop to be completed, the measured shaft speed must be communicated to the simulator, which in turn passes on a torque set point to the motor drive. The motor drive must then execute the torque command and return feedback to the simulator. In addition, the shaft speed must be measured and fed back to the simulator. Only if all these successive actions have taken place, a loop iteration is completed, so the simulation loop as a whole can be executed only at the lowest of the three mentioned frequencies. This lowest, limiting frequency is from here on referred to as the loop frequency f_{loop}, corresponding to a loop step size Δt_{loop}. For the sake of brevity, Δt_{loop} is also referred to as Δt.

In the HIL setup considered in this dissertation, drive command frequency f_{command} is the lowest frequency in the loop, which means that f_{loop} equals f_{command}. Shaft speed is sampled at a higher frequency, so per loop iteration, multiple shaft speed samples are available. One could choose to use only the most recent sample to calculate the next torque set point. However, this would mean that a part of the shaft speed samples are lost. Instead, to make the best possible use of the sensor data, all shaft speed samples received between two subsequent torque set points are averaged. Compared to using only the most recent sample, this approach results in a shaft speed signal with a lower noise level and a higher resolution. Note that, to be able to calculate this average, calculation frequency f_{calc} of the simulator must be equal to or higher than sample frequency f_{sample}.

The time steps shown in Fig. 4.10 serve only as an illustration and do not correspond to the HIL experiments described in this dissertation. In the actual HIL setup, the shaft speed encoder emits 720 pulses per shaft revolution, while the shaft may rotate at speeds up to 1000 rpm. This results in 12000 pulses per second. As the shaft speed calculation module calculates a new shaft speed sample upon reception of each pulse, this results in values for f_{sample} up to 12 kHz. The simulator has a dSPACE DS1006 processor board, allowing for a f_{calc} of 20 kHz. Commands are passed from the simulator to the motor drive through a CAN bus at a f_{command} of 5 kHz. Thus, the loop frequency f_{loop} equals 5 kHz, corresponding to a Δt_{loop} or Δt of 0.002 s.

As a next step, linear descriptions are derived of the practical scale model including the aforementioned numerical operations. Later on, these are used to analyse the

Table 4.2: Frequencies for the example case illustrated by Fig. 4.10 and the actual HIL setup in this dissertation.

	Fig. 4.10	Actual setup	
f_{sample}	0.25	$\leq$12	kHz
f_{calc}	1	20	kHz
f_{command}	0.125	5	kHz
f_{loop}	0.125	5	kHz

dynamics of the practical scale model including numerical inertia correction, and check up to which frequency the practical scale model behaves the same as the ideal scale model.

Linear Description of the Applied Correction Algorithm

The discrete operations described before influence the accuracy of the numerical inertia correction. To be able to predict the performance of the correction including these discrete operations, z transforms of the correction are derived. The fundamental time step of these z transforms is the loop frequency t_{loop}, which is also referred to as Δt. This step size corresponds to the frequency at which the simulation computer sends current set points to the motor drive. Note that calculations inside the simulation computer are conducted at a higher frequency.

To arrive at a z transform of the inertia correction, the numerical operations introduced before are described in the discrete domain. As was explained earlier, the first numerical operation inside the simulator is the averaging of shaft speed samples over a time interval with length Δt. This means that a new measured shaft speed ω_{m} follows not not only from the most recent shaft speed sample ω_{sample}. Instead, it is the average of the most recent and older samples, as also becomes apparent in the transition from the third to the fourth stage shown in Fig. 4.10. Consequently, measured shaft speed ω_{m} slightly lags behind actual shaft speed ω. This lag can be conservatively approximated by a step delay with length Δt, as is shown in Eq. (4.13).

$$\omega_{\text{m}}(n) = \omega(n-1) \tag{4.13}$$

As a next step, the discrete derivative is calculated from this averaged shaft speed. This introduces an additional delay, as the discrete derivative depends on the difference between values for ω_{m} in the current and previous loop step. Eq. (4.14) gives the difference equation of the averaging operation, conservatively approximated by Eq. (4.13), combined with discrete differentiation as introduced by Eq. (4.11).

$$\frac{\Delta\omega_{\text{m}}}{\Delta t}(n) = \frac{\delta\omega(n-1) - \delta\omega(n-2)}{\Delta t} \tag{4.14}$$

Note that Δ indicates the difference between two measured values, while δ indicates the difference between a variable and its equilibrium value. Eq. (4.14) can be transformed to the z domain as shown in Eq. (4.15).

$$\frac{\Delta\omega_{\text{m}}}{\Delta t}(z) = \frac{\delta\omega(z) \cdot \left(z^{-1} - z^{-2}\right)}{\Delta t} \tag{4.15}$$

Eq. (4.15) describes the first three steps given in the beginning of Section 4.4.2. The fourth step introduces the IIR filter with the aim of reducing the noise level. The IIR filter maps output as a weighted sum of the current measurement and the previous filtered value. Eq. (4.16) gives the difference equation of the filter, applied on measured shaft speed ω_{m}.

$$\omega_{\mathrm{m,f}}(n) = a_0 \cdot \omega_{\mathrm{m}}(n) + (1 - a_0) \cdot \omega_{\mathrm{m,f}}(n-1) \tag{4.16}$$

Filter coefficient a_0 can have values between 0 and 1, with lower values indicating more filtering. A suitable value can be found through trial and error and depends on the noise level of the measured shaft speed signal. Noisy signals can be made more smooth by decreasing a_0; however, this comes at the cost of decreased signal responsiveness. This trade-off will be covered in detail in Section 4.4.3. Eq. (4.17) gives the z transform of the difference equation given in Eq. (4.16).

$$F(z) = \frac{\omega_{\mathrm{m,f}}}{\omega_{\mathrm{m}}}(z) = \frac{a_0}{1 - (1 - a_0) \cdot z^{-1}} \tag{4.17}$$

A mathematical description of the filtered discrete derivative is obtained by multiplying the discrete differentiation given in Eq. (4.15) and the filtering operation given in Eq. (4.17). The resulting z transform of the filtered discrete derivative is given by Eq. (4.18).

$$\frac{\Delta\omega_{\mathrm{m,f}}}{\Delta t}(z) = \frac{\delta\omega(z) \cdot \left(z^{-1} - z^{-2}\right)}{\Delta t} \cdot \frac{a_0}{1 - (1 - a_0) \cdot z^{-1}} \tag{4.18}$$

As a fifth step, the filtered discrete derivative is multiplied by inertia correction I_{c}, yielding torque correction $M_{\mathrm{d,corr}}$. The resulting z transform from measured speed to torque correction is shown in Eq. (4.19).

$$M_{\mathrm{d,corr}}(z) = \frac{\delta\omega(z) \cdot \left(z^{-1} - z^{-2}\right)}{\Delta t} \cdot \frac{a_0}{1 - (1 - a_0) \cdot z^{-1}} \cdot I_{\mathrm{c}} \tag{4.19}$$

The final step in the correction algorithm is to communicate this correction torque to the motor drive. This is done at the end of every time step. As the motor drive executes commands in less than a millisecond, this operation does not introduce noticeable delays.

In this Chapter, the performance of the numerical inertia correction algorithm is assessed using the open loop response of shaft speed on simulated drive torque, or $\delta\omega/\delta M_{\mathrm{d,sim}}$. To obtain this transfer function, the correction algorithm given in Eq. (4.19) is combined with the z transform of the uncorrected scale model. Departing from the Laplace transfer function given in Eq. (4.10), the difference equation of the uncorrected scale model can be written as in Eq. (4.20).

$$\delta\omega(n) = \frac{\Delta t}{I_{\mathrm{tot,p}}} \cdot \left(\delta M_{\mathrm{d,sim}}(n) - (2 - b) \cdot \delta\omega(n)\right) + \delta\omega(n-1) \tag{4.20}$$

Eq. (4.20) can in turn be transformed to the z domain, yielding the z transform of the uncorrected scale model shown in Eq. (4.21).

$$\delta\omega(z) = \frac{\Delta t}{I_{\mathrm{tot,p}}} \cdot \delta M_{\mathrm{d,sim}}(z) - (2 - b) \cdot \frac{\Delta t}{I_{\mathrm{tot,p}}} \cdot \delta\omega(z) + \delta\omega(z) \cdot z^{-1} \tag{4.21}$$

The z transform of $M_{\mathrm{d,corr}}$ given in Eq. (4.19) can now be inserted into Eq. (4.21), in line with Fig. 4.9. Without writing out $M_{\mathrm{d,corr}}$ for the time being, this results in Eq. (4.22).

$$\delta\omega\,(z) = \frac{\Delta t}{I_{\mathrm{tot,p}}} \cdot \big(\delta M_{\mathrm{d,sim}}\,(z) - M_{\mathrm{d,corr}}\,(z)\,\big) - (2-b) \cdot \frac{\Delta t}{I_{\mathrm{tot,p}}} \cdot \delta\omega\,(z) + \delta\omega\,(z) \cdot z^{-1} \quad (4.22)$$

After writing out $M_{\mathrm{d,corr}}$ and rearranging, one finally obtains the z transform of the practical scale model including the inertia correction algorithm, as given in Eq. (4.23). According to the requirements formulated in Section 2.6.3, the gain and phase predicted by Eq. (4.23) must be the same as for the ideal system, described by Eq. (4.9), in the complete relevant frequency range or in the complete responsive frequency range. To check whether this requirement can be fulfilled in practice, Section 4.4.3 elaborates on the effect of varying Δt, a_0 and I_{c} on the similarity range of a practical scale model with the proposed numerical inertia correction.

$$\begin{aligned}\frac{\delta\omega}{\delta M_{\mathrm{d,sim}}}\,(z) = \frac{\Delta t - \Delta t \cdot (1-a_0) \cdot z^{-1}}{I_{\mathrm{tot,p}} + (2-b) \cdot \Delta t} \\ + \big((a_0-2) \cdot I_{\mathrm{tot,p}} + (a_0-1) \cdot (2-b) \cdot \Delta t + a_0 \cdot I_{\mathrm{c}}\big) \cdot z^{-1} \\ + \big(\,(1-a_0) \cdot I_{\mathrm{tot,p}} - a_0 \cdot I_{\mathrm{c}}\big) \cdot z^{-2}\end{aligned} \quad (4.23)$$

4.4.3 Influence of Parameters on Performance

The ideal scale model has a range of parameters and equilibrium values which determine its dynamic response on disturbances and input signals. As was explained in Section 4.4.2, the corrected practical scale model contains additional components to correct for scale effects on inertia, and therefore has additional parameters influencing its dynamic response. These parameters determine the performance of the numerical inertia correction – performance is defined here as the extent to which the similarity range covers the responsive or relevant frequency range. Three parameters are particularly relevant in this respect: loop frequency f_{loop}, IIR filter setting a_0 and inertia correction I_{c}. These parameters may vary depending on the test setup hardware and the simulated propulsion system. For example, by using more powerful simulation processors or a faster acting motor drive, one can increase the calculation and command frequencies, and thus, f_{loop}. On the other hand, the properties of the shaft speed encoder influence the noise level of the signal and thus, the optimal setting for a_0. I_{c} depends on the moment of inertia of the scale model drive, but also on the inertia of the simulated propulsion system. As such, I_{c} may take a wide range of values, both positive and negative.

Thus, by making informed choices concerning hardware, one can maximise the similarity range. Still, even the best possible shaft speed sensors and the most powerful processors cannot guarantee that the responsive frequency range of every imaginable propulsion system can be covered. It is therefore recommended to check the frequency response of the numerical inertia correction before conducting HIL experiments.

To demonstrate how the frequency response can be checked as well as to investigate the influence of the three aforementioned parameters on the performance of the numerical inertia correction, linear simulations are conducted in which these parameters are varied systematically. The resulting Bode diagrams are found in Figs. 4.11

Table 4.3: Combinations of f_{loop}, a_0 and I_{c} for which linear simulations of the numerical inertia correction were conducted.

	f_{loop} [kHz]	a_0 [−]	I_{c} [kgm^2]
Case I	5	0.01	0.0268
Case II	1	0.01	0.0268
Case III	5	0.002	0.0268
Case IV	5	0.01	−0.0268

through 4.13, which show the response of shaft speed ω on drive torque setting $M_{\text{d,set}}$. Transfer functions for the ideal and corrected scale models were given in Eqs. (4.9) and (4.23), respectively. The parameters and equilibrium values for the ideal scale model were given in Table 2.5. These parameters and equilibrium values are also valid for the corrected scale model, apart from the mechanical moment of inertia $I_{\text{mech,p}}$, which is 0.0029 kgm^2. For reasons of simplicity, added inertia I_{H2O} is not taken into account. The combinations of f_{loop}, a_0 and I_{c} evaluated in this Section are listed in Table 4.3. Case I corresponds to the actual HIL experiments described in following Chapters, while Cases II, III and IV have changes to individual parameters, negatively affecting similarity.

Fig. 4.11 shows that f_{loop} has a considerable influence on the performance of the correction. For Case I, the phase error exceeds 10 degrees at a frequency of approximately 12 rad/s, or 1.9 Hz. This frequency therefore marks the upper limit of the similarity range. As will be described in Chapter 6, this is sufficient to emulate the considered propulsion system at full speed in a fully developed wave spectrum. In Case II, the loop frequency is reduced from 5 to 1 kHz. As a result, the maximum allowed phase error occurs at a lower frequency, around 3.4 rad/s, or 0.54 Hz. In addition to this, the maximum allowed gain error occurs at 2 rad/s, or 0.32 Hz. This trend is not surprising: if the loop is iterated at a lower frequency, delays become relatively larger, decreasing the accuracy of the correction. It can be concluded that an increased loop frequency improves the performance of the numerical inertia correction, assuming that all other parameters remain the same.

The same conclusion can be drawn regarding a_0: Fig. 4.12 shows that the effect of a lower a_0 is very similar to the effect of a lower f_{loop}. This, too, is not unexpected: a lower value for a_0 implies that new measurements have a lower weight in the filtered value, or in other words, that more filtering is applied. While reducing noise, this also slows down the dynamic response of the correction, reducing its effect at high frequencies.

From Fig. 4.13, an interesting conclusion can be drawn regarding the effect of I_{c}. If the sign of I_{c} is changed, so does the sign of the gain and phase errors. The frequency at which these errors exceed their acceptable limits, however, remains practically the same. This implies that in a properly tuned HIL setup, the numerical correction works equally well in both directions.

In addition to this, an important reservation must be made regarding the closed loop performance of the inertia correction algorithm. Under some circumstances, the correction algorithm introduces a positive feedback if applied in a closed shaft speed loop. If I_{c} is negative, or if the phase angle between simulated drive torque and shaft

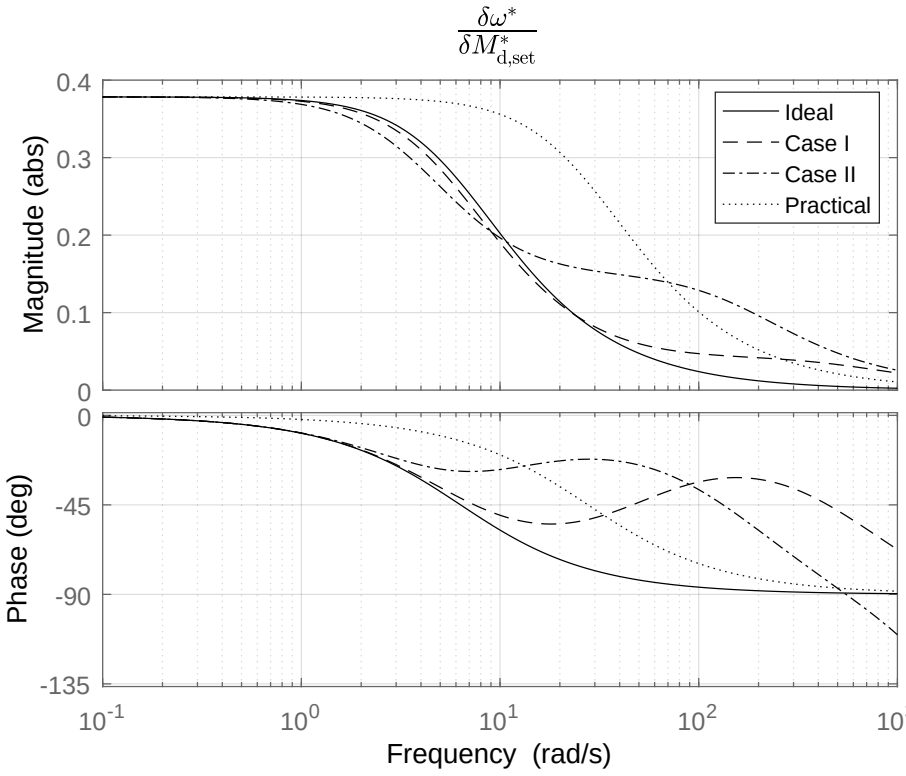


Figure 4.11: Response of $\delta\omega/\delta M_{\mathrm{d}}$ for the practical scale model with numerical inertia correction at a varying loop frequency f_{loop}, compared to ideal and uncorrected scale model behaviour. f_{loop} is 5 kHz and 1 kHz for Case I and II, respectively.

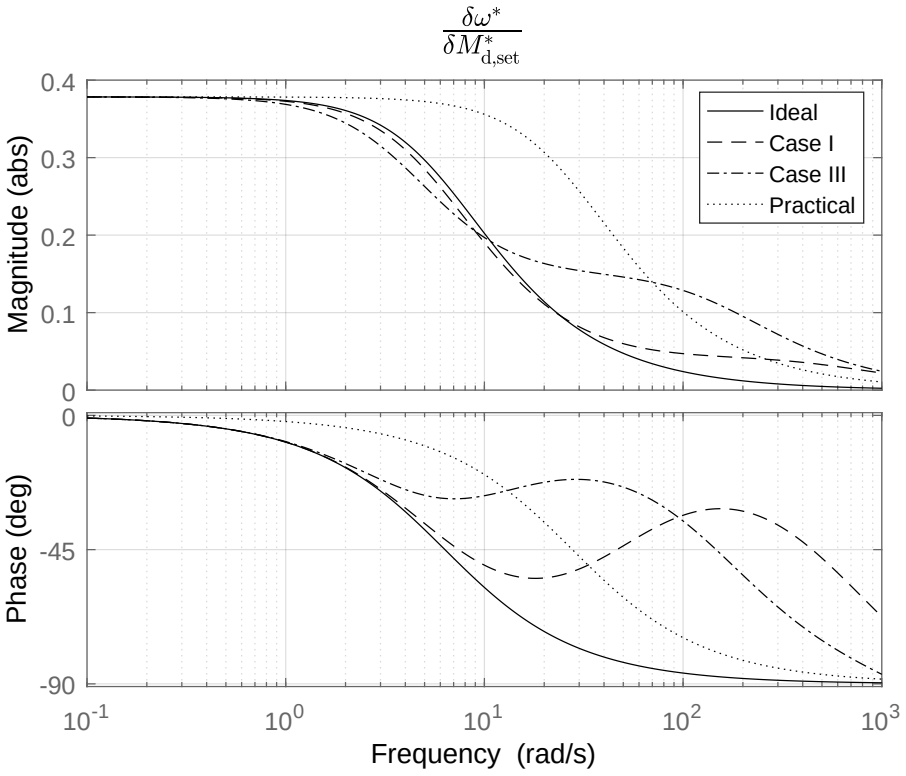


Figure 4.12: Response of $\delta\omega/\delta M_{\mathrm{d}}$ for the practical scale model with numerical inertia correction at a varying IIR filter setting a_0, compared to ideal and uncorrected scale model behaviour. a_0 is 0.01 and 0.002 for Case I and III, respectively.

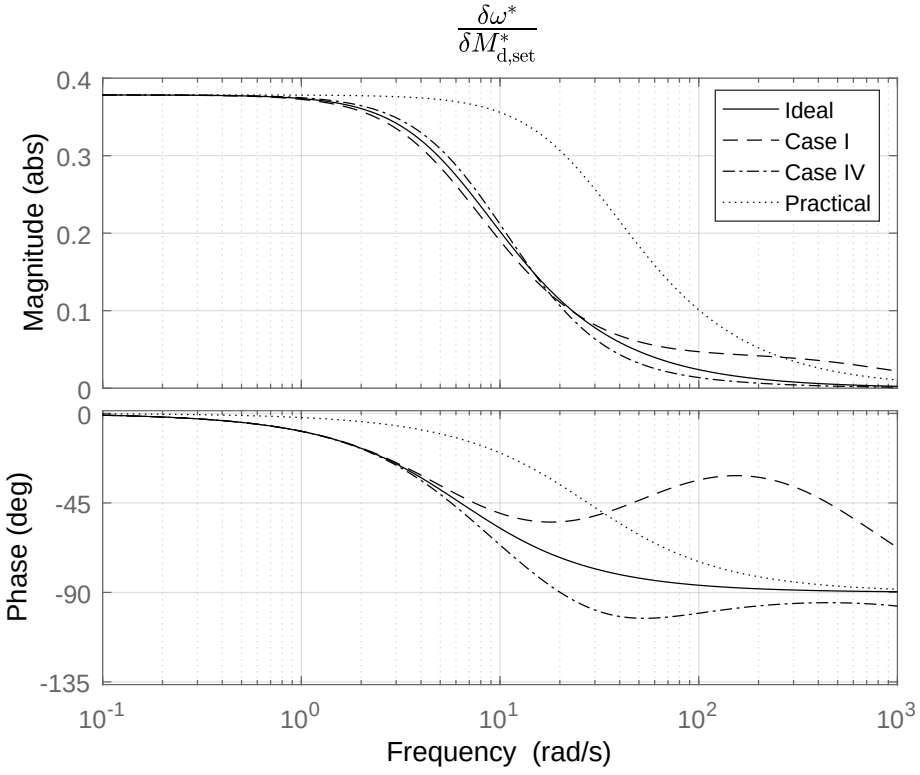


Figure 4.13: Response of $\delta\omega/\delta M_{\mathrm{d}}$ for the practical scale model with numerical inertia correction at a varying inertia correction I_{c}, compared to ideal and uncorrected scale model behaviour. I_{c} is 0.0268 kgm^2 and -0.0268 kgm^2 for Case I and IV, respectively.

speed equals 180 degrees, the calculated torque correction is in phase with shaft speed. Depending on the magnitude of I_c, this may result in a positive feedback loop. This positive feedback can be avoided by increasing filter coefficient a_0; however, as was shown earlier, increasing a_0 also increases dynamic distortions at high frequencies. Considering that the gain and phase of the torque correction depends on the scale model hardware and simulated machinery, it is advisable to find a new, optimal setting for a_0 each time the hardware or parameters inside the simulation model are changed: the minimum a_0 for a given configuration of hardware and simulations may be too low or overly conservative for another configuration.

4.5 Conclusion

This Chapter covered the issue of incorrectly scaled moment of inertia in the HIL setup. Differential equations and linear descriptions were used to illustrate how an incorrectly scaled moment of inertia distorts shaft dynamics. Subsequently, these linear descriptions were used to derive a numerical correction for these distortions. Given a set of equilibrium values and settings, these linear descriptions can also be used to determine the similarity range of a HIL setup with a numerical inertia correction.

In Section 4.4.3, the influence of f_{loop}, a_0 and I_c on the performance of the inertia correction algorithm was investigated. It was shown that if f_{loop} and a_0 are decreased, the performance of the numerical inertia correction deteriorates. Thus, one would aim to keep f_{loop} and a_0 as high as possible. However, there parameters have practical upper limits.

f_{loop} is limited by the capabilities of the simulation processors and motor drive, which implies that possibilities to increase this frequency are limited once the hardware is installed. a_0, on the other hand, can be easily adjusted during experiments; however, there is a crucial trade-off. Whilst resulting in smoother measurements and emulated dynamics, lower values for a_0 also reduce the frequency at which the dynamic distortions caused by the IIR filter become unacceptable. By trial and error, one can find a setting sufficiently low to reduce noise to an acceptable limit, yet sufficiently high to ensure that the similarity range still spans the entire relevant frequency range.

A final remark can be made regarding the practical feasibility of the numerical inertia correction. Simulation computers and motor drives that are able to meet the stated requirements are commercially available, rendering the proposed numerical inertia correction applicable in practice. Moreover, it is important to realise that the dynamic open water experiment is in essence an expansion of the traditional open water experiment, as was explained in Chapter 1. The hardware for traditional open water experiments is highly specialised: worldwide, only a few parties have the knowledge to design and manufacture this scientific equipment. After having gone through the effort of designing or purchasing a state-of-the-art open water setup, it is only a relatively small step to expand it to an even more advanced dynamic open water setup. In this light, Chapter 5 contains a detailed description of the necessary preparations for such experiments.

Chapter 5

Description and Preparation of the Experimental Setup

The tuning guidance and inertia corrections proposed in Chapters 3 and 4 will be demonstrated during HIL open water experiments. This requires a functional HIL setup, which will be introduced in this Chapter. Hardware and software components will be individually described as well as the way in which they are interlinked. In addition, a method to identify unknown hardware parameters is introduced, resulting in estimates for motor torque constant k_t, moment of inertia $I_\mathrm{mech,p}$ and friction torque M_fr. As such, the fourth and fifth research sub questions are addressed:

- Which measures can be taken to avoid distortion of shaft dynamics by these components?
- How can these measures be applied in the dynamic open water test?

By introducing a compensation for friction torque, the associated dynamic distortions are avoided, too. Adding this compensation to the solutions for distortions by the electric drive and incorrectly scaled inertia, derived in the previous two Chapters, the fourth research sub question is entirely answered. Furthermore, by giving an account of the preparations for HIL experiments, this Chapter partly answers the fifth research sub question.

5.1 Hardware Topology

Fig. 5.1 gives a schematic overview of the hardware components in the HIL open water setup, including supply and communication lines. Before moving on to a detailed description of these components and their connections, the functional layout of the setup is briefly described. The power and pressurised air supply lines are relatively straightforward; specifications for these subsystems are given in Section 5.1.2. The remaining hardware components and connections between these components are more elaborate, and deserve a more detailed introduction. These components and connections can be divided into two categories: a simulation feedback loop and a passive

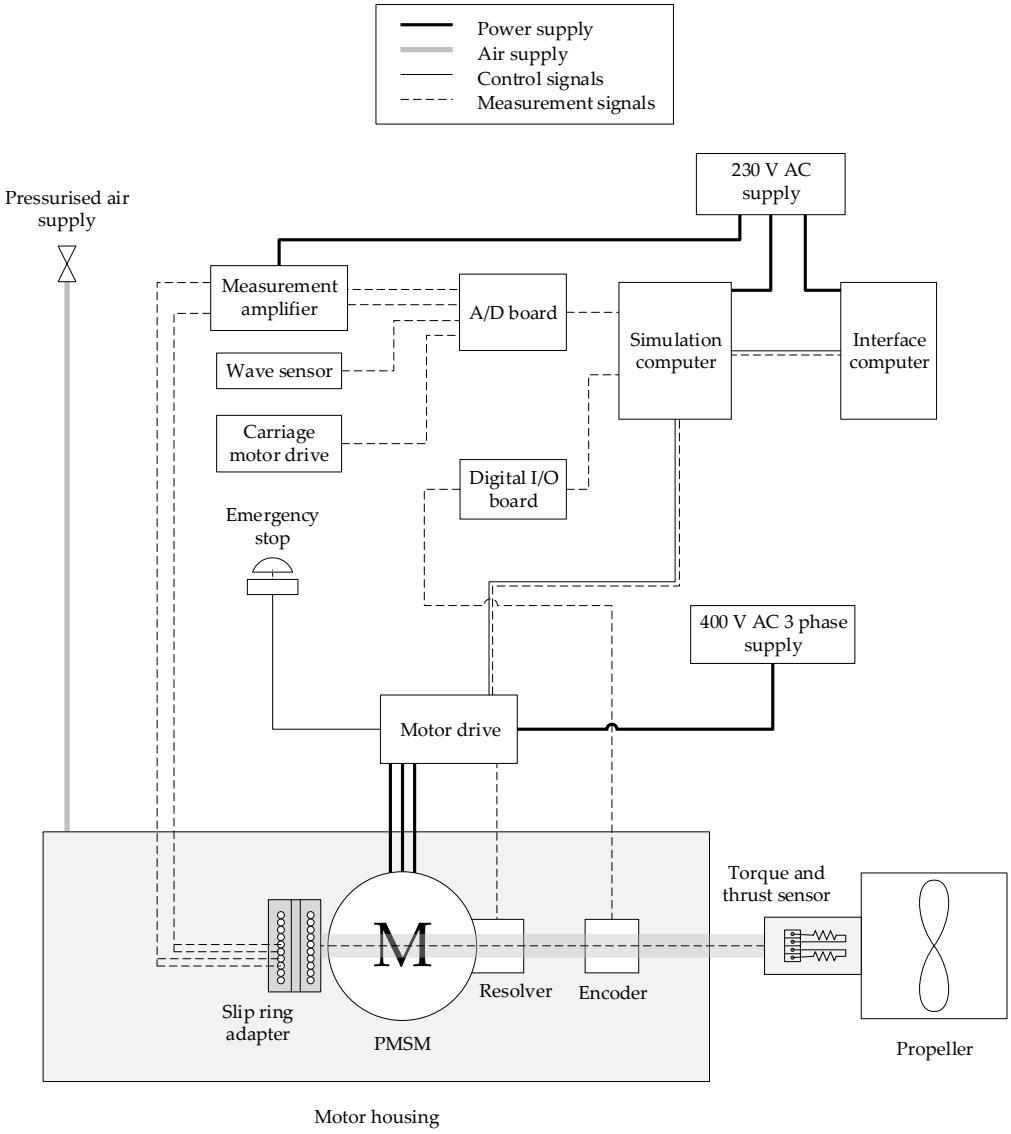


Figure 5.1: Hardware components, supply lines, control lines and measurement lines in the HIL open water test setup.

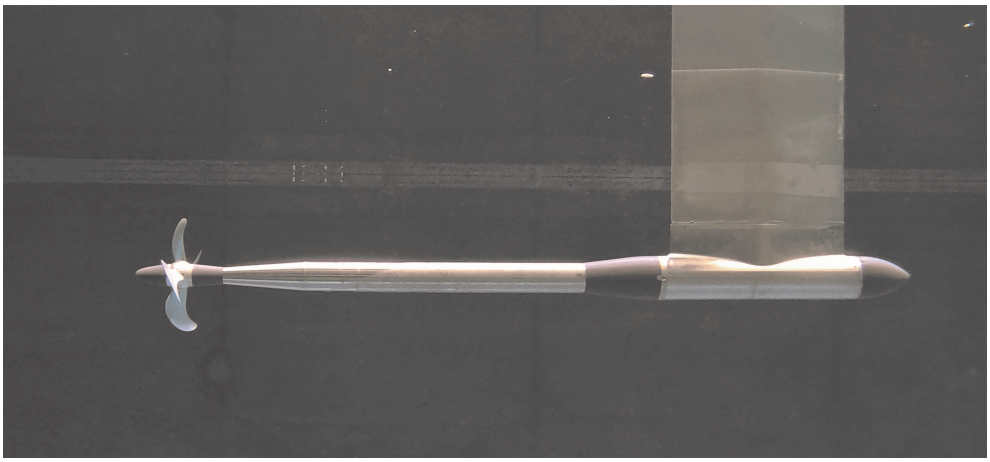


Figure 5.2: Submerged section of the HIL open water test setup. During open water experiments, the setup moves in the direction of the propeller, minimising the disturbance of propeller inflow by the shaft, motor housing and strut. The length over all is approximately 1.4 m.

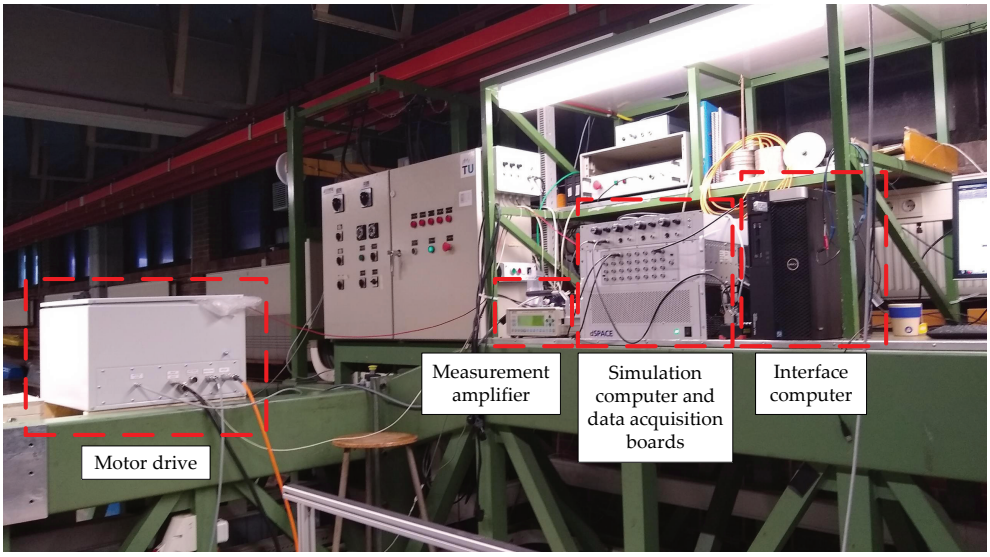


Figure 5.3: Motor drive, measurement amplifier, data acquisition boards, simulation computer and interface computer mounted on the towing tank carriage.

measurement system. As the name implies, the former is a feedback loop which uses measurement signals to simulate machinery, calculate corrections and control motor torque. The passive measurement system, on the other hand, measures and stores signals that are not used as input for simulations or corrections in realtime, but may be relevant for analysis a posteriori.

To describe the simulation feedback loop, the simulation computer (or simulator) and interface computer are taken as a starting point. The simulator calculates engine torque and thus, gearbox output torque based on measured speed and fuel rack setting. Any corrections for friction and moment of inertia are subsequently added to this torque, resulting in a drive torque setting $M_{\mathrm{d,set}}$. Simulated and measured variables are communicated to the interface computer, where they can be read out by the operator. The interface computer also allows to control the simulator, for example to initialise communication of the simulator with the motor drive, or to change the speed setting.

Drive torque setting $M_{\mathrm{d,set}}$ is converted to a current set point i_{set} in the simulator. i_{set} is subsequently communicated to the motor drive. The motor drive then regulates current and thus, motor torque. The balance between motor drive torque and propeller load torque results in acceleration and thus, speed of the shaft. The encoder mounted on the shaft emits pulses with a frequency that is proportional to the shaft speed. The pulse frequency is measured in the digital I/O board and passed on to the simulator, which uses this frequency to calculate measured shaft speed and simulate the engine operating point. In addition, the resolver measures the position of the rotor, and communicates this position to the motor drive for commutation.

With that, the simulation feedback loop is complete. Signals in the passive measurement system, on the other hand, are not used as feedback during the HIL experiment but stored for analysis afterwards. This category contains analog measurement signals from the torque and thrust sensor, wave sensor and carriage motor drive. These analog signals are converted to digital signals in the A/D board and subsequently recorded on the simulation computer.

The following Section will expand on this broad overview of the HIL setup. Section 5.1.1 contains an introduction of the individual components, followed by a detailed description of how these components are physically connected in Section 5.1.2.

5.1.1 Hardware Components

The HIL setup consists of both custom built and commercial off-the-shelf components. The torque and thrust sensor (*QT sensor*), propeller and gondola enclosing the electric motor are designed, manufactured and assembled by Maritiem Research Instituut Nederland (MARIN). In addition to this, the setup contains the following off-the-shelf components:

- Shaft speed sensor: Zettlex INC-6-75 incremental encoder, 7200 pulses per revolution, ABZ quadrature signal
- Simulation processor board: dSPACE DS1006, 4 cores, AMD Opteron 2.80 GHz
- Interface computer: commercially available desktop computer
- Digital I/O board: dSPACE DS4004

- A/D board: dSPACE DS2003
- CAN interface board: dSPACE DS4302
- Measurement amplifier: Peekels Instruments PICAS
- Motor drive: Kollmorgen S724
- Electric motor: PMSM with a maximum continuous torque of 8.82 Nm – in consultation with MARIN, it has been decided not to make public further technical details

The components manufactured by MARIN have the following properties:

- QT sensor: MARIN 232S; torque measurement range: -14 to 14 Nm; thrust measurement range: -340 to 340 N
- Propeller: Wageningen C4-40; design P/D ratio: 1.0; actual P/D ratio: 1.3; diameter: 0.2346 m

The shaft speed encoder emits two traces, A and B, with 7200 pulses per revolution (ppr) each. A reference trace Z with one pulse per rotation is available to determine angle. At a shaft speed of 600 rpm, this results in a pulse frequency of 72 kHz per trace, or one pulse every 13.8 μs. The time between these pulses is measured by the digital I/O board in increments of 50 ns. As a result, the measurement traces have a resolution of only 276 increments. At the same time, the simulation computer is not able to accept and process measurement at this rate. Considering these limitations, an additional converter is introduced which only passes on every tenth pulse to the digital I/O board. This means that the I/O boards receives 720 pulses per rotation. As such, a shaft speed of 600 rpm is measured with a frequency of 7.2 kHz and a resolution of 2760 increments. This measured shaft speed corresponds to ω_{sample} as it was shown in Fig. 4.10 in the previous Chapter. As a disadvantage of this approach, the angle of rotation relative to the Z pulse can no longer be determined, as the pulses can not be counted individually. Yet, as this functionality is not required for the proposed dynamic open water experiments, this limitation is accepted.

Based on the shaft speed calculated from the encoder pulse frequency, the simulation computer calculates a new drive torque which must then be communicated to the motor drive. Communication between the simulation computer and the motor drive occurs through a CAN bus link, as will be explained later on. The simulation computer communicates a current set point to the motor drive which uses these set points to commutate the PMSM. In addition, the drive sends a response message containing the measured motor current. As an extra check of the shaft speed encoder signal, the drive also sends a message containing the shaft speed as it is measured by the resolver.

The electric motor is mounted inside the watertight, gondola-shaped casing shown in Fig. 5.2. The QT sensor and propeller are mounted on the other end of the propeller shaft. The gondola is suspended underneath a hexapod frame, which in turn is mounted on the towing carriage. Fig. 5.4 shows how the gondola is fixed to the hexapod. The carriage can advance at a speed of maximum 7 m/s through a model basin which has a length of 142 m, a width of 4.22 m and a maximum depth

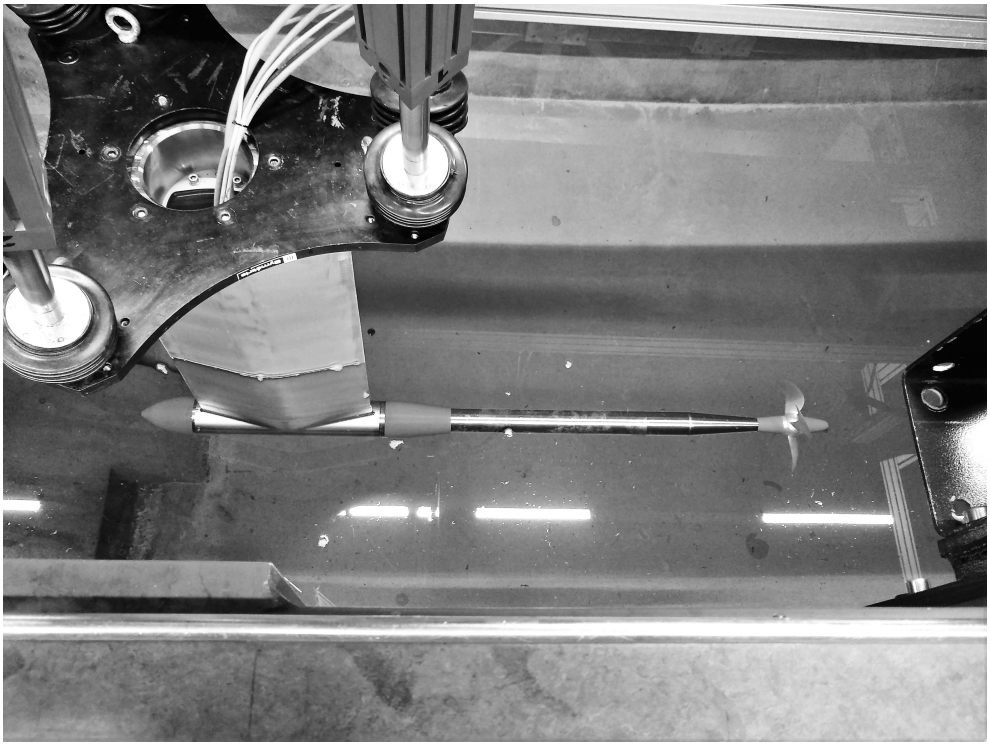


Figure 5.4: The gondola mounted underneath the hexapod frame. The hexapod allows to move the gondola relative to the carriage with six degrees of freedom, providing easy access to the propeller. After each day of experiments, the aluminium propeller was removed to minimise galvanic corrosion.

of 2.50 m. During the HIL experiments, the water level was 2.13 m with variations up to 1 cm.

5.1.2 Supply and Communication Lines

As was indicated in Fig. 5.1, the supply and communication lines can be divided into four categories:

1. pressurised air supply;
2. power supply;
3. measurement lines;
4. control lines.

The first category is limited to a pressurised air supply line. Through a reduction valve, a pressure of 0.2 bar above atmospheric pressure is maintained inside the watertight gondola. This minor overpressure avoids water from entering the gondola in case of leakage, thus avoiding damage to electrical components.

Second, the motor drive, simulation and interface computers and measurement amplifier require power supply. The motor drive, which commutates the PMSM, requires a 400 V 3-phase supply. The safety switches on the motor drive require a 5 V DC signal; this signal is converted from the 400 V AC supply. The measurement amplifier, simulation computer and interface computer each depend on a 230 V AC supply.

The third category comprises the measurement lines. These signals can be digital or analog, with the measured shaft speed being an example of a digital signal. The shaft speed encoder already received attention in previous Sections. As was indicated, the A and B pulse traces are processed by a separate hardware unit which only passes on every tenth pulse of each trace. The DS4004 digital I/O board uses the resulting traces to determine shaft speed, which is then passed on to the simulation model.

The wave sensor, carriage motor drive and QT sensor emit analog voltage signals. The voltage signal from the wave sensor is proportional to the measured water level at the location of the propeller, while the towing carriage emits a voltage signal proportional to its speed. The QT sensor emits two signals proportional to measured propeller torque and thrust. The wave sensor and carriage motor drive are directly connected to the DS2003 A/D board, which converts analog voltage into 16-bit digital signals. The signals from the QT sensor, on the other hand, first pass a measurement amplifier which amplifies the otherwise minute voltage differentials expressing torque and thrust. Upon reception by the simulation computer, these voltage differentials are converted into measured torque and thrust using conversion factors supplied by MARIN.

The fourth and final category consists of control signals. The simulation computer simulates drive torque $M_{\mathrm{d,set}}$, which must subsequently be passed on to the motor drive. The simulation computer and motor drive communicate through a CAN bus link, using the CANopen protocol. This protocol and the way it is implemented in the considered HIL setup will receive more attention in Section 5.2. In addition, the interface computer can be connected with the motor drive through a RS232 bus link,

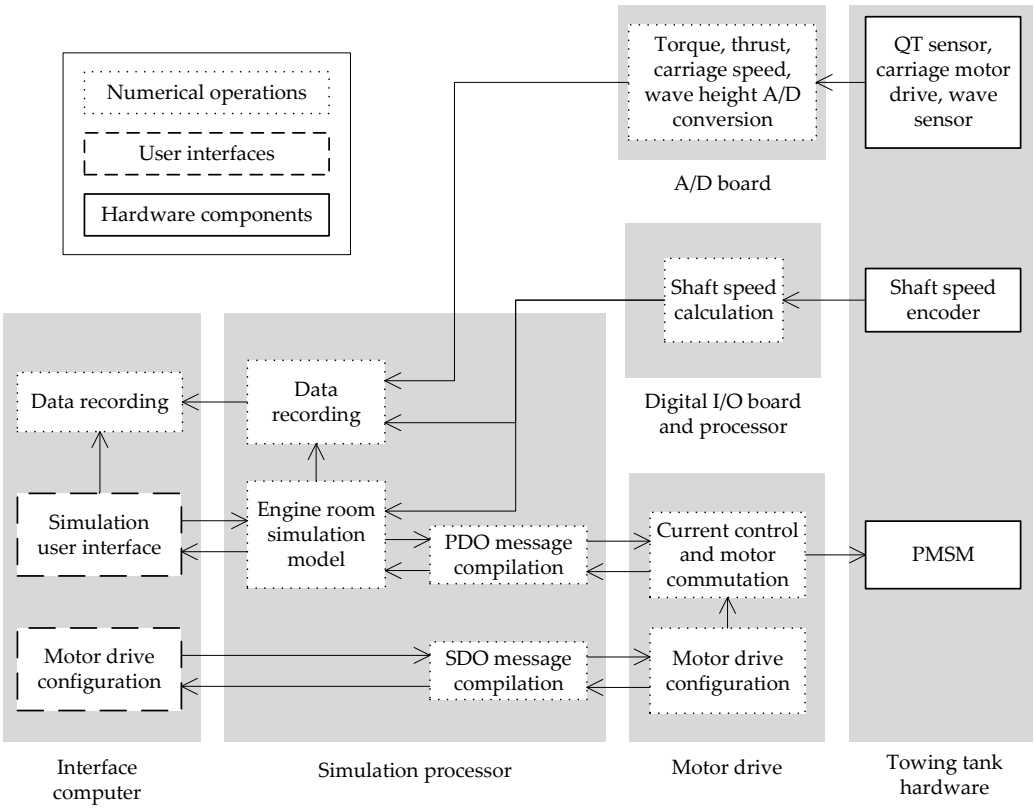


Figure 5.5: Hardware and software components in the HIL open water setup and their interconnections.

allowing to set parameters such as the CAN bus baud rate and current controller gains. The interface computer is linked to the simulation computer by an optical wire, allowing the user to upload new simulation models to the simulation computer, and to monitor and control the HIL experiment in real time. During experiments, the experimenter can send new set points to the simulator, while the simulator sends simulated and measured values back to the interface computer.

The physical connections described in this Section on themselves are not sufficient for communication between the hardware components. To obtain a functional loop, the simulation computer and motor drive must be configured to compile and interpret command and feedback messages. This subject receives more attention in Section 5.2.

5.2 Software Modules

Fig. 5.5 presents an overview of the different software modules including their connections with other software and hardware components. The software modules can be divided into seven subsystems:

1. a module to configure communication between simulator and motor drive;
2. the engine room simulation, including corrections for inertia and friction;
3. PDO and SDO message compilers;
4. current control and motor commutation;
5. a module to calculate shaft speed from encoder pulses;
6. A/D conversion of analog sensor signals;
7. a module for data recording.

Before experiments can be conducted, the motor drive must be initialised. This is done using the module for communication configuration. Initialisation includes switching on the drive and enabling the power stage, but also setting the frequency, content and format of the messages that will be exchanged. For example, the drive can be set to operate in current control, speed control or position control mode. The chosen configuration as well as the format of the command messages must be specified before the drive's power stage is enabled.

The engine room simulation model is based on the non-linear description given in Section 2.2. Using the measured shaft speed and simulated PI governor output, the simulation model calculates drive torque of the ideal scale model. To this simulated drive torque, a correction torque for moment of inertia is added as was described in Chapter 4. In addition, a correction is added for friction inside the practical scale model; this correction will receive further attention in Section 5.3. The sum of the simulated drive torque and corrections is converted to a current, which is subsequently sent as a command to the motor drive. These operations are performed on one of the four 2.8 GHz processors on the DS1006 processor board.

Configuration information, current set points and drive feedback are communicated through a high-speed CAN bus which allows for a bit speed of up to 1 Mbit/s. The motor drive uses the CANopen higher-layer protocol, which means that information to be sent to the drive must be compiled into service data objects (SDO) and process data objects (PDO). Conversely, messages received from the drive must be decompiled. SDO and PDO messages are different in format, size and purpose. SDO messages are typically used to transfer configuration information, and provide a relatively simple way to communicate set points and feedback. However, SDO messages are relatively large, limiting the frequency at which they can be exchanged. PDO messages, on the other hand, require more elaborate configuration of the motor drive, but are comparably short. As such, they allow to exchange set points and feedback at higher frequencies than do SDO messages. In the described HIL experiments, set points and feedback are therefore transferred using PDO messages as 16-bit signed integers. Per second, up to 5000 of these messages can be reliably sent to and from the motor drive, resulting in a loop frequency of 5 kHz as mentioned in Section 4.4.2. Instructions for CAN communication and examples of SDO and PDO communication for the S724 motor drive are provided in the CAN bus manual by Kollmorgen (Kollmorgen, 2016).

Current set points received by the motor drive are passed on to the current controller inside the drive. The current controller regulates output voltage based on the

current set point and measured current, as was described in detail in Chapter 3. The drive commutates the output voltage to the motor based on the rotor position measured by the resolver. The commutated output voltage is a pulse-width modulated signal (PWM) with a switching frequency of 8 kHz. Detailed specifications of the S724 motor drive are provided in the drive manual (Kollmorgen, 2015).

The calculation of shaft speed was covered in detail in Section 5.1.1 and earlier in Chapter 4. As an additional, practical remark, the processor mentioned next to the digital I/O board in Fig. 5.5 is in fact one of the four 2.8 GHz processors on the DS1006 processor board. This processor is dedicated to averaging the frequency measurements received from the DS4004 digital I/O board, and calculating a shaft speed by dividing this frequency by 720 – recall that 720 is the number of pulses received by the digital I/O board per shaft revolution. As was indicated in Chapter 4, the processor can execute these operations at a calculation frequency f_{calc} of 20 kHz.

Propeller torque and thrust, wave height and carriage speed are measured as analog voltages; propeller torque and thrust signals are amplified by a PICAS measurement amplifier. Analog voltage signals are converted into 16-bit digital values by the DS2003 A/D board. Analog measurements are not used as feedback input for the simulation model, but are recorded and can be visually monitored in realtime on the interface computer.

All measured and simulated data is collected by the simulation processor. From here, the data is transferred to the interface computer which stores all data in a single file after each measurement run. Measurement data are stored unfiltered; where necessary, measurement data are filtered and downsampled afterwards. Table 5.1 lists relevant variables recorded during experiments and their notation in this dissertation.

5.3 Parameter Identification

The corrections proposed in previous Chapters aim to modify the behaviour of the practical scale model such that it emulates the ideal scale model. For this, the parameters that govern the practical and ideal dynamics must be known. Whereas the parameters of the ideal scale model are to be chosen by the experimenter, parameters for the practical scale model follow from the available hardware. For example, the moments of inertia provided by manufacturers of the scale model propeller and electric motor may not be entirely correct, or even entirely absent. This is not necessarily an issue: some parameters do not need to be known exactly, and rough estimates and data supplied by manufacturers may often be sufficient. To tune the current controller, for instance, indications of winding resistance and inductance are sufficient since the tuning guidance contains a considerable margin for errors. However, other parameters such as the practical moment of inertia must be known with more precision. In such cases, parameters must be identified by measurements.

To point out which parameters are important in this respect, the governing equation for shaft dynamics of the uncorrected HIL setup is recapitulated in Eq. (5.1).

$$\begin{aligned}(I_{\text{mech,p}} + I_{\text{H2O}}) \cdot \frac{\mathrm{d}\omega\,(t)}{\mathrm{d}t} &= M_{\text{d}}(t) - M_{\text{fr}}(t) - M_{\text{prop,hydro}}\,(t) \\ &= k_{\text{t}} \cdot i\,(t) - M_{\text{fr}}(t) - M_{\text{prop,hydro}}\,(t) \end{aligned} \tag{5.1}$$

Table 5.1: Variables stored during HIL experiments and their notation in this dissertation if applicable. Data are unfiltered and stored in double-precision floating point format. The first eight variables are constants and settings which are mostly static, and are stored only upon change. Other variables are sampled at 1 kHz.

Variable name	Notation
Estimated motor k_t, filtered	$k_\mathrm{t,est}$
Loop frequency	f_loop
Ideal mechanical inertia	$I_\mathrm{mech,id}$
Practical mechanical inertia	$I_\mathrm{mech,p}$
Shaft speed IIR filter coefficient	a_0
Speed governor K_i	$K_{\mathrm{i},\omega}$
Speed governor K_p	$K_{\mathrm{p},\omega}$
Set engine speed (FS)	n_set
Simulated engine torque, normalised	$M_\mathrm{b}/M_\mathrm{b,nom}$
Simulated engine speed, normalised	$n_\mathrm{e}/n_\mathrm{e,nom}$
Simulated gearbox torque	$M_\mathrm{d,sim}$
Sim. gearbox torque, corrected	$M_\mathrm{d,set}$
Set current	i_set
Current	i_m
Current without estimated friction	$i_\mathrm{m} - i_\mathrm{fr,est}$
Shaft speed (resolver)	
Shaft speed (encoder)	ω_m
Shaft acceleration, filtered	$\mathrm{d}\omega_\mathrm{m,f}/\mathrm{d}t_\mathrm{loop}$
Propeller torque	$M_\mathrm{prop,m}$
Propeller trust	$T_\mathrm{prop,m}$
Carriage speed	$v_\mathrm{a,m}$
Propeller Reynolds number	R_n
Propeller Weber number	W_n
Propeller advance ratio	J
Wave height	ζ_m

The left hand side of Eq. (5.1) shows the combined moments of inertia of the electric motor, shaft, propeller and other rotating mechanical components, $I_\mathrm{mech,p}$, and the inertia components of entrained mass, I_H2O. I_H2O is assumed to scale correctly, as was indicated in Chapter 2. $I_\mathrm{mech,p}$, on the other hand, may considerably differ from the ideal mechanical moment of inertia and must therefore be identified and corrected.

On the right hand side of Eq. (5.1), $k_\mathrm{t} \cdot i(t)$ represents the torque developed by the electric motor. Chapter 3 described how the current controller can be tuned such that current responds sufficiently fast. Since the proposed settings result in a considerable margin, the parameters supplied by the motor manufacturer are sufficiently accurate for tuning of the current controller. However, to accurately control drive torque M_d, motor torque constant k_t must be known, too. Although this parameter is supplied by the manufacturer, this value must be experimentally verified, since any errors in k_t result in proportional errors in M_d.

The second term on the right hand side, M_fr, refers to the friction torque of the

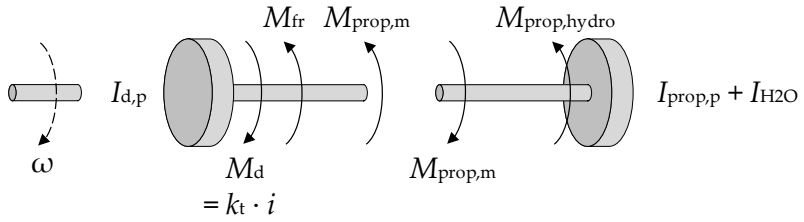


Figure 5.6: Visual representation of the torque components in Eq. (5.1). The torque sensor is located at the cut-through of the shaft. The absolute values of total torque on both ends of the torque sensor are equal, assuming that the torque sensor is a rigid body – an assumption which holds at low frequencies, as was discussed earlier. Measured propeller torque $M_{\mathrm{prop,m}}$, winding current i and shaft speed ω can be directly measured during experiments; the other variables and parameters shown can only be derived indirectly.

practical scale model. This torque is different from the ideal friction torque – in this dissertation, ideal friction torque is not simulated. Hence, practical friction torque must be compensated for in order to avoid distortion of shaft dynamics. Before it can be compensated, however, the friction torque must be known.

As the third term on the right hand side of Eq. (5.1), hydrodynamic propeller load torque $M_{\mathrm{prop,hydro}}$ is subject to viscous scale effects. However, Chapter 2 indicated that because of their limited effect on shaft dynamics and high complexity, viscous scale effects are outside the scope of this dissertation. As such, these scale effects receive no further attention here, even though a correction could be added to the simulated torque once a suitable model of viscous scale effects would be known.

This leaves the following parameters to be identified:

1. friction torque M_{fr};
2. motor torque constant k_{t};
3. mechanical moment of inertia $I_{\mathrm{mech,p}}$, which is the sum of the practical drive inertia $I_{\mathrm{d,p}}$ and propeller inertia $I_{\mathrm{prop,p}}$.

As a first step, Fig. 5.6 visualises the equation of motion given in Eq. (5.1). Of the shown variables and parameters, only $M_{\mathrm{prop,m}}$, i and ω can be directly measured. Located between the propulsion shaft and the propeller, the torque sensor essentially represents an equals sign: absolute values for total torque are the same on both sides of the sensor.

Fig. 5.6 shows that the torque measured by the QT sensor, $M_{\mathrm{prop,m}}$, is a combination of drive torque, friction torque and acceleration torque on the drive side. Equally, it is a combination of hydrodynamic propeller load torque and acceleration torque on the load side. As such, the QT sensor does not allow to identify these torque components individually. Moreover, as was indicated earlier, the QT sensor is preferably not used to conduct dynamic measurements, while some steps in the parameter identification do require such dynamic measurements.

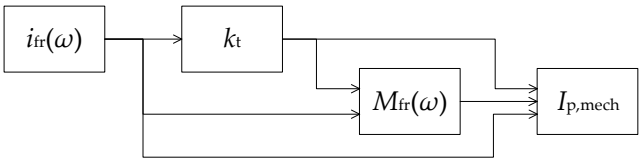


Figure 5.7: Stepwise approach to parameter identification in this Chapter. First, friction current i_{fr} is identified. Second, using estimated i_{fr}, motor torque constant k_{t} can be determined. From i_{fr} and k_{t}, friction torque M_{fr} can be calculated without additional measurements. As a final step, the combined moment of inertia of the electric motor, shaft assembly and propeller, $I_{\mathrm{mech,p}}$, can be identified.

Considering this, a stepwise approach to parameter identification is adopted and shown in Fig. 5.7. The three successive steps in this approach are described in detail in Sections 5.3.1 through 5.3.3.

5.3.1 Friction Current

As a first identification step, friction torque is considered. At constant speed, friction torque equals the difference between motor drive torque and propeller load torque. A logical approach would thus be to make steady state measurements of load and drive torque. However, motor torque cannot be directly measured, as torque constant k_{t}, which expresses the relation between drive torque and motor winding current, is not yet known at this point. However, Eq. (2.10) showed that torque is proportional to current, which implies that a given friction torque M_{fr} corresponds to a given friction current i_{fr}, as is shown in Eq. (5.2).

$$M_{\mathrm{fr}} = k_{\mathrm{t}} \cdot i_{\mathrm{fr}} \tag{5.2}$$

Considering this, motor winding current is measured without propeller load at various speeds, resulting in a regression model for friction current in function of shaft speed. Friction current is determined both outside the towing tank, in air, and submerged, with the propeller dismounted. Friction is slightly greater when the shaft is submerged, since the water around the shaft causes additional viscous friction. As will be shown later on, dry friction current must be known for inertia identification, while submerged friction current is relevant during HIL open water experiments.

The measurements necessary for these friction regression models are obtained by imposing a slow, sinusoidal variation of shaft speed around an equilibrium. This results in a range of quasi-static current measurements to which a polynomial can be fitted. Here, the regression polynomial has the form shown in Eq. (5.3), with c and e being free variables.

$$i_{\mathrm{fr,est}} = c_0 + \sum_{j=1}^{3} c_j \cdot \omega^{e_j} \tag{5.3}$$

This approach can be illustrated with measurement data. Fig. 5.8 shows shows current measurements on a submerged shaft without propeller and without streamlined fairings. The speed of the shaft is varied between 50 and 1000 rpm in positive direction. Polynomial regression on these measurements results in a polynomial fit with

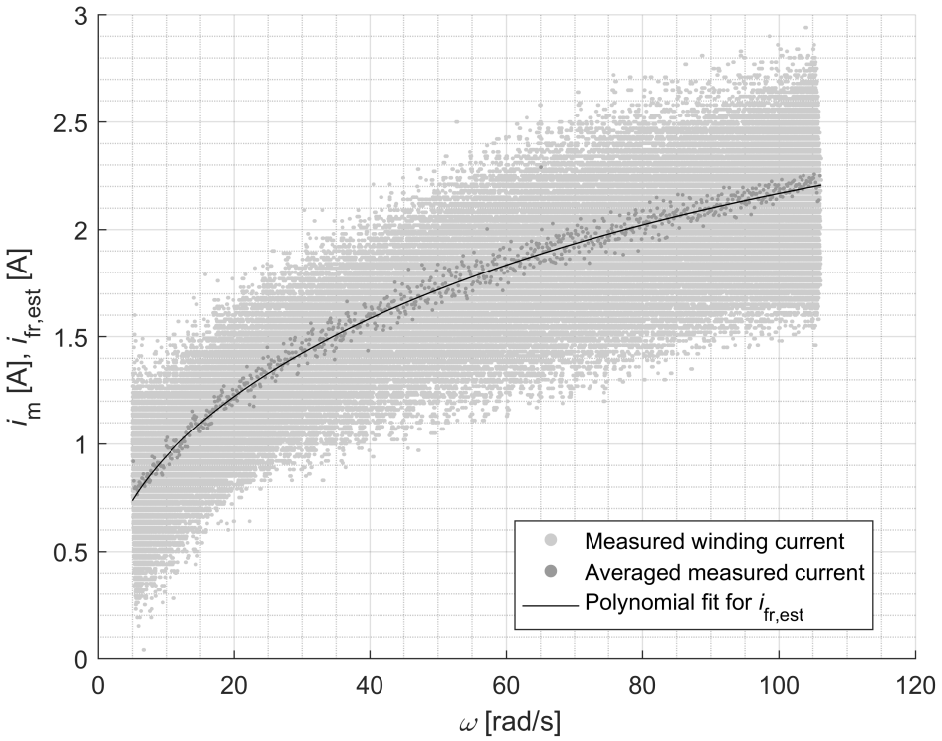


Figure 5.8: Polynomial regression of measured friction current at speeds between 50 and 1000 rpm. In the shown measurement run, the shaft was submerged with the propeller, streamline caps and fairing dismounted. The polynomial fit has an R^2 of 0.986; Table 5.2 shows the corresponding coefficients. This Figure is based on the data in *cal_085.mat*, stored in the measurement data repository (Huijgens, 2020).

an R^2 of 0.986, indicating that the fit adequately describes friction current. The corresponding coefficients are given in Table 5.2. Based on similar coefficients, a real-time correction for friction was introduced during the experiments described in this dissertation.

As the shaft is almost entirely covered and supported by a watertight casing, only a small part of the shaft is exposed to the surrounding water. Friction current therefore mostly results from friction inside the bearings and electric motor. During calibration, it was observed that friction torque slightly varies in function of time. These variations occurred mostly during the first 30 seconds of operation, possibly as a result of changing bearing temperatures. For this reason, the shaft was rotated at intermediate speeds for about one minute prior to each experiment and calibration run. Furthermore, friction was calibrated twice per day; this did not indicate significant changes in the friction model coefficients on the longer term.

Table 5.2: Polynomial regression coefficients for friction current resulting from the measurements shown in Fig. 5.8. These coefficients were obtained with a submerged shaft and with the propeller, streamline caps and fairing dismounted. The polynomial assumes the format given by Eq. (5.3).

j	c	e
0	0.162	
1	0.261	0.406
2	0.0242	0.772
3	−0.001 36	1.30

5.3.2 Electric Motor Torque Constant

With friction current estimated and compensated for, motor torque constant k_t can be determined. k_t expresses the ratio between motor drive torque and motor winding current, as is shown in Eq. (5.4)

$$k_\mathrm{t} = \frac{M_\mathrm{d}}{i} \tag{5.4}$$

Taking this relation into account, the equation of motion given in Eq. (5.1) is rearranged to the form shown in Eq. (5.5).

$$k_\mathrm{t} = \frac{\left(I_\mathrm{mech,p} + I_\mathrm{H2O}\right) \cdot \frac{\mathrm{d}\omega(t)}{\mathrm{d}t} + M_\mathrm{fr}\left(t\right) + M_\mathrm{prop,hydro}\left(t\right)}{i\left(t\right)} \tag{5.5}$$

In the case of constant shaft speed, the acceleration terms can be omitted. Eq. (5.5) can then be simplified to the form shown in Eq. (5.6).

$$k_\mathrm{t} = \frac{M_\mathrm{fr}\left(t\right) + M_\mathrm{prop,hydro}\left(t\right)}{i\left(t\right)} \tag{5.6}$$

Fig. 5.6 shows that in a static case, the hydrodynamic propeller torque $M_\mathrm{prop,hydro}$ equals measured propeller torque $M_\mathrm{prop,m}$. Eq. (5.6) can therefore be rewritten as shown in Eq. (5.7).

$$k_\mathrm{t} = \frac{M_\mathrm{fr}\left(t\right) + M_\mathrm{prop,m}\left(t\right)}{i\left(t\right)} \tag{5.7}$$

Furthermore, M_fr equals $k_\mathrm{t} \cdot i_\mathrm{fr}$ as was shown in Eq. (5.2). Thus, Eq. (5.7) can be developed into Eq. (5.8).

$$k_\mathrm{t} = \frac{M_\mathrm{prop,m}\left(t\right)}{i\left(t\right) - i_\mathrm{fr}\left(t\right)} \tag{5.8}$$

It is assumed that the measured winding current and estimated friction current are accurate estimates of the actual winding current and friction current. Although no systematic measurement campaign was conducted, the consistency of observations in varying environments over the course of several weeks support this assumption. Thus, k_t can be estimated by measuring propeller torque at a constant speed ω_0, and comparing this torque to measured current i_m minus estimated friction current $i_\mathrm{fr,est}$.

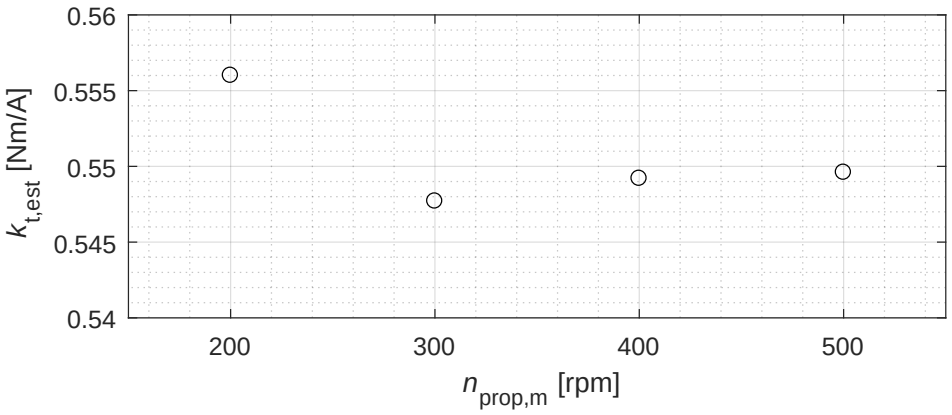


Figure 5.9: Estimated motor torque constant at different shaft speeds in bollard pull condition. Corresponding equilibrium values for torque and corrected current are given in Table 5.3. This Figure is based on the data in *cal_091.mat*, stored in the measurement data repository (Huijgens, 2020).

Table 5.3: Estimated motor torque constant k_t and relevant equilibrium values at different shaft speeds in bollard pull condition.

$n_{prop,m}$ [rpm]	$i_m - i_{fr,est}$ [A]	$M_{prop,m}$ [Nm]	$k_{t,est}$ [Nm/A]
200	1.49	0.830	0.556
300	3.38	1.85	0.548
400	6.03	3.31	0.549
500	9.66	5.31	0.550

This step is expressed by Eq. (5.9).

$$k_{t,est} = \frac{M_{prop,m}(t)}{i_m(t) - i_{fr,est}(t)} \tag{5.9}$$

Fig. 5.9 presents measurements of propeller torque and corrected winding current, resulting in an estimated value of k_t for the HIL setup in this dissertation. The measurement run shown was conducted in bollard pull condition, which means that the propeller is rotating but not moving forward. Table 5.3 lists the estimated torque constants as well as relevant equilibrium values. As can be seen, k_t is consistently estimated at 0.55 Nm/A for a range of different torques and speeds. At the same time, one can conclude that at a shaft speed of 200 rpm, the estimate becomes slightly higher. At very low speeds, friction torque becomes harder to estimate, while the measured propeller load torque becomes comparatively small. Moreover, the torque sensor becomes less accurate as torque decreases to low values, possibly introducing errors in measured propeller torque. These combined effects result in less accurate estimates of k_t at low speed and torque.

Interestingly, the estimated k_t of 0.55 Nm/A is 3.8% higher than the value provided

by the manufacturer, which is 0.53 Nm/A. There are multiple possible causes for this difference:

1. the motor manufacturer's specification of k_t is off;
2. current is not correctly measured and converted inside the drive;
3. friction current is estimated too high;
4. torque is in fact smaller than measured by the QT sensor;
5. a combination of the above.

Checking the first two points requires information only readily available to the manufacturers of the motor and drive; tolerances for the motor torque constant and detailed specifications of the current sensor in the Kollmorgen drive are not publicly available. The effort of obtaining this information is not made here. The third point, however, could be checked by repeating the k_t identification with different settings for the friction current compensation. It was found that its effect on measured k_t is very limited unless obvious under- or overcompensation is applied.

The fourth point is a plausible option, too, and presents some possibilities for simple checks. Measurements showed that the tip of the QT sensor is 0.75 mm off centre, indicating a minor plastic deformation. As a result, there may be an error in measured torque. This conjecture could have been further investigated by calibration measurements, which were not conducted due to time constraints. However, a similar offset in measured torque was observed during the open water experiments described in Chapter 6, causing further attention to be paid to this potential issue in Section 6.2. For reasons of consistency, the measured values for propeller torque and k_t are assumed to be correct throughout this dissertation.

Depending on the permanent magnet material, the motor torque constant may vary in function of temperature. In this case, the electric motor contains Neodymium Iron Boron (NdFeB) magnets. NdFeB magnets experience considerable demagnetisation as their temperature increases. As a result, the k_t of motors using NdFeB magnets decreases by approximately 0.12% per K temperature increase of the magnet material. During prolonged motor operation at high load, temperatures may increase by more than 100 K, causing a considerable decrease of k_t. With this in mind, k_t was identified multiple times before and after experiments. These measurements did not show significant changes in k_t, likely because of the relatively short durations of experiments – usually less than two minutes – and effective cooling by the water surrounding the gondola.

Any remaining error in estimated k_t results in a proportional error in emulated equilibrium torque. As was shown in Section 2.5.4, changes in equilibrium torque of several percent only have a negligible effect on emulated shaft dynamics. Consequently, minor errors in estimated k_t are not a cause for concern during HIL open water experiments.

5.3.3 Practical Moment of Inertia

With friction current and the motor torque constant now estimated, only $I_\mathrm{mech,p}$ remains to be identified – note that I_H2O does not need to be identified as the limited

scale effects on this inertia term are neglected here. The approach to identification of $I_{\mathrm{mech,p}}$ can be explained by simplifying Eq. (5.1), as was done in the previous Section. If the propeller is emerged from the water, hydrodynamic propeller load $M_{\mathrm{prop,hydro}}$ and added inertia term I_{H2O} disappear – the load torque and entrained inertia in air are sufficiently small to be dismissed here. Furthermore, the friction torque M_{fr} can be compensated for, as was demonstrated in Section 5.3.1. If this is done accurately, the equation of motion given in Eq. (5.1) can be simplified and rewritten to the form given in Eq. (5.10).

$$\frac{\mathrm{d}\omega\left(t\right)}{\mathrm{d}t} = \frac{M_{\mathrm{d}}\left(t\right)}{I_{\mathrm{mech,p}}} \tag{5.10}$$

Eq. (5.10) shows that in the described conditions, $I_{\mathrm{mech,p}}$ can be easily calculated if drive torque M_{d} and shaft acceleration $\mathrm{d}\omega/\mathrm{d}t$ are known. Drive torque is controlled and therefore known. Shaft acceleration, on the other hand, cannot be directly measured: it can be obtained by numerical differentiation of measured shaft speed. However, numerical differentiation introduces some additional issues, as was discussed in Chapter 4. Considering this, $I_{\mathrm{mech,p}}$ is determined based on measured shaft speed rather than calculated acceleration.

This approach requires additional analysis of Eq. (5.10) as the relation between shaft speed, torque and inertia is not yet described. As in earlier Chapters, shaft dynamics are analysed in the Laplace domain. As a first step, Eq. (5.11) gives the Laplace transform of Eq. (5.10).

$$s \cdot \omega\left(s\right) = \frac{M_{\mathrm{d}}\left(s\right)}{I_{\mathrm{mech,p}}} \tag{5.11}$$

To identify $I_{\mathrm{mech,p}}$, drive torque is varied sinusoidally with frequency ω_{osc} and amplitude $|M_{\mathrm{d}}|$. This allows to impose considerable changes on drive torque without causing excessive shaft speeds. The sinusoidal torque signal can be represented in the time domain as shown in Eq. (5.12).

$$M_{\mathrm{d}}\left(t\right) = |M_{\mathrm{d}}| \cdot \sin\left(\omega_{\mathrm{osc}} \cdot t\right) \tag{5.12}$$

Laplace transformation of Eq. (5.12) yields Eq. (5.13).

$$M_{\mathrm{d}}\left(s\right) = |M_{\mathrm{d}}| \cdot \frac{\omega_{\mathrm{osc}}}{s^2 + \omega_{\mathrm{osc}}^2} \tag{5.13}$$

Combining Eqs. (5.11) and (5.13) results in the Laplace transform shown in Eq. (5.14).

$$\omega\left(s\right) = \frac{|M_{\mathrm{d}}| \cdot \omega_{\mathrm{osc}}}{I_{\mathrm{mech,p}}} \cdot \frac{1}{s \cdot \left(s^2 + {\omega_{\mathrm{osc}}}^2\right)} \tag{5.14}$$

Transforming Eq. (5.14) back to the time domain, one obtains Eq. (5.15).

$$\omega\left(t\right) = \frac{|M_{\mathrm{d}}|}{I_{\mathrm{mech,p}} \cdot \omega_{\mathrm{osc}}} \cdot \left(1 - \cos\left(\omega_{\mathrm{osc}} \cdot t\right)\right) \tag{5.15}$$

The amplitude of this sinusoidal shaft speed is expressed in Eq. (5.16).

$$|\omega| = \frac{|M_{\mathrm{d}}|}{I_{\mathrm{mech,p}} \cdot \omega_{\mathrm{osc}}} \tag{5.16}$$

Hence, $I_{\mathrm{mech,p}}$ can be calculated from the amplitudes of measured shaft speed and drive torque as shown in Eq. (5.17).

$$I_{\mathrm{mech,p}} = \frac{|M_{\mathrm{d}}|}{|\omega| \cdot \omega_{\mathrm{osc}}} \tag{5.17}$$

This approach was used to identify $I_{\mathrm{mech,p}}$ of the HIL open water test setup. Before inertia identification measurements were conducted, friction current was carefully measured at a wide range of speeds, including very low and negative speeds. With some additional, manual fine-tuning, the influence of friction on inertia measurements could be reduced to a negligible level.

Fig. 5.10 shows identified $I_{\mathrm{mech,p}}$ and $I_{\mathrm{d,p}}$ at different sinusoidal torque amplitudes A_{M} and frequencies f_{osc} around an equilibrium of 0 Nm. For the calculated propeller inertia, a value supplied by MARIN was used. The inertia of the motor and shaft assembly, on the other hand, was calculated from drawings and material densities. The calculated shaft inertia includes minor simplifications; for example, the geometry of the slip ring is not taken into account. For both $I_{\mathrm{mech,p}}$ and $I_{\mathrm{d,p}}$, one can observe a converging trend towards the calculated values as A_{M} increases and f_{osc} decreases. This is mainly due to the limited accuracy of the friction correction at low speeds.

At shaft speeds below 50 rpm, friction becomes difficult to predict. As a consequence, friction at low speeds is not entirely compensated. This in turn results in a lower amplitude of shaft speed oscillations and thus, overestimation of inertia. As the amplitude of the oscillating torque increases, or as the frequency decreases, the amplitude of the shaft speed oscillations increases. This means that relatively less time is spent at low speeds, limiting the effect of inaccurate friction compensation at low speeds.

Thus, inertia identification measurements are ideally conducted with large torque amplitudes at low frequencies, resulting in large speed oscillations. However, these speed oscillations must remain within the safe motor speed range. For this reason, torque amplitude A_{M} was limited to 2 Nm at an oscillation frequency f_{osc} of 1 Hz. Due to the linear relations in Eq. (5.17), these settings are equivalent to a torque amplitude of 6 Nm and an oscillation frequency of 3 Hz. The data points for 3 Hz in Fig. 5.10 indicate that at such settings, the estimated inertia has converged to a value with practically no distortions by unwanted friction. Table 5.4 compares the moments of inertia identified during inertia measurements to a priori calculations. Although these calculated values do not provide an absolute reference, they do indicate that the identified values are in line with expectations.

With respect to the required accuracy of the measured inertia, it is important to note that $I_{\mathrm{mech,p}}$ is about 9.8% of the ideal inertia $I_{\mathrm{mech,id}}$. Consequently, an error of 10% in estimated $I_{\mathrm{mech,p}}$ corresponds to an error of only 0.98% in emulated moment of inertia. The effects of an error in identified inertia with such small a magnitude are practically invisible in the responsive frequency range, as is shown in Fig. 5.11.

5.4 Conclusion

Sections 5.1 and 5.2 described the hardware and software components in the HIL open water setup and the way in which these components were linked to obtain a

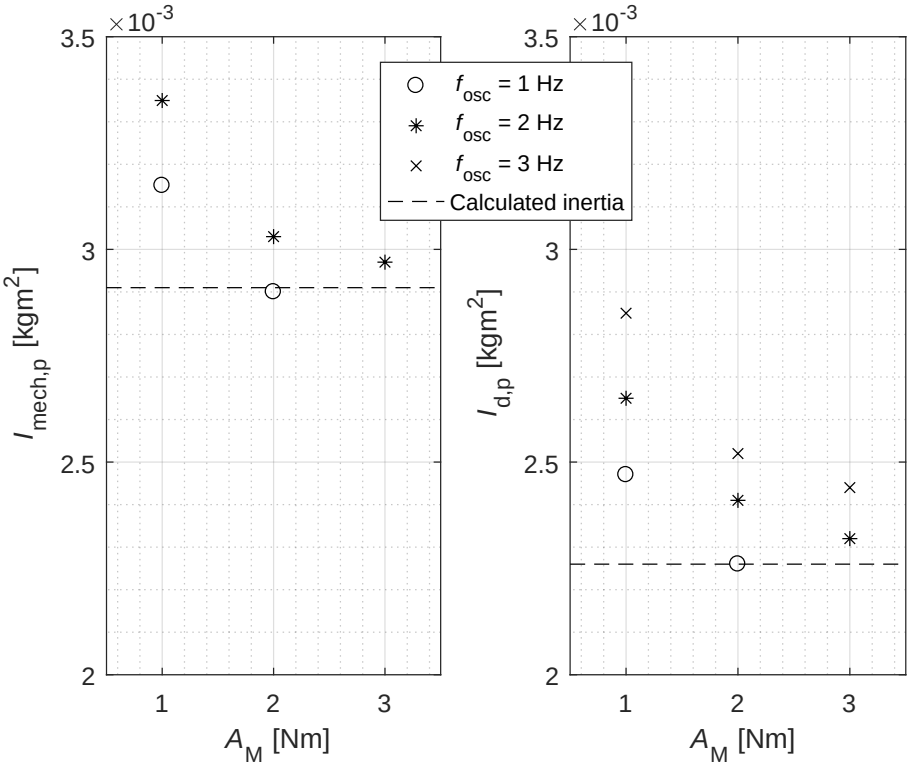


Figure 5.10: $I_{\mathrm{mech,p}}$ and $I_{\mathrm{d,p}}$ identified at different sinusoidal torque amplitudes A_{M} and frequencies f_{osc} around an equilibrium of 0 Nm. Experiments at 1 Hz and 2 Nm yield the most accurate results as these settings result in relatively little near-zero shaft speeds. At speeds below 50 rpm, friction becomes difficult to predict and is not entirely compensated, resulting in an overestimated moment of inertia. The measurements in these Figures result from repeated visual observations of time traces during experiments; no MAT-files with measurement data were stored.

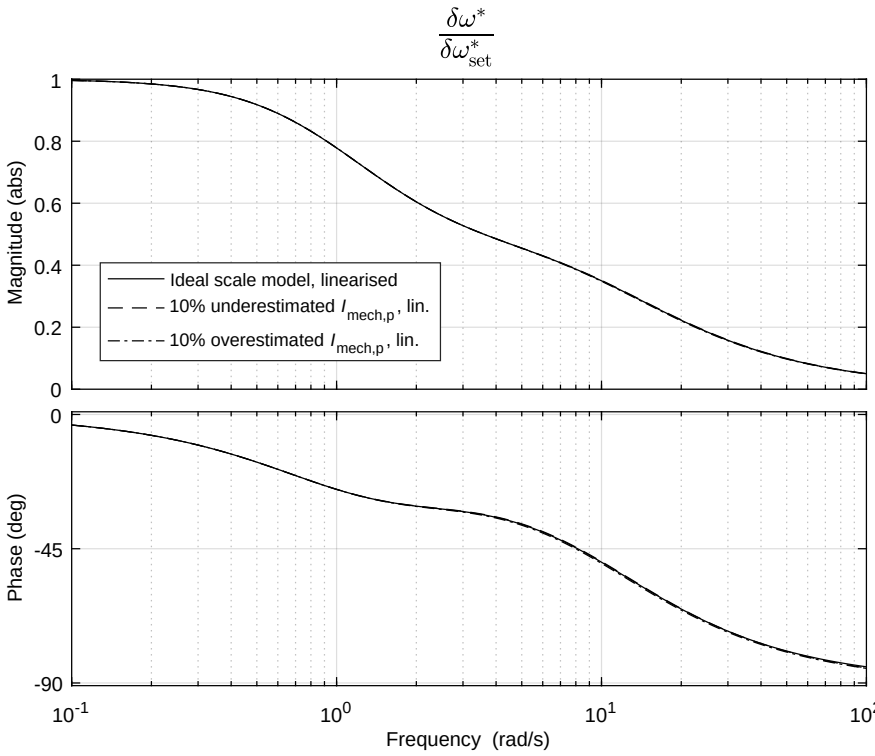


Figure 5.11: Linear simulations of shaft speed response on speed setting of the ideal scale model and ideal scale models with different inertias. The differences in inertia correspond to a 10% error in estimated moment inertia of propeller and shaft, or $I_{\mathrm{mech,p}}$. The inertia of water entrained between the propeller blades, or I_{H2O}, is not included in these simulations.

Table 5.4: Calculated and identified moments of inertia of the HIL setup without entrained water. These values were identified with drive torque oscillating at 1 Hz with an amplitude of 1 Nm around an equilibrium of 0 Nm. $I_{\mathrm{d,p}}$ equals the inertia of the electric motor and shaft assembly, while $I_{\mathrm{mech,p}}$ also includes the inertia of the propeller. The calculated variables are based on drawings and data supplied by MARIN. $I_{\mathrm{d,p}}$ and $I_{\mathrm{mech,p}}$ were identified individually; subtracting $I_{\mathrm{mech,p}}$ from $I_{\mathrm{d,p}}$ allows to identify $I_{\mathrm{prop,p}}$.

	Calculated	Identified	
$I_{\mathrm{d,p}}$	0.002 33	0.002 26	kgm^2
$I_{\mathrm{mech,p}}$	0.002 91	0.002 90	kgm^2
$I_{\mathrm{prop,p}}$	0.000 58	0.000 64	kgm^2

functional loop. These descriptions showed how the HIL experiments described in earlier Chapters can be conducted in practice.

Following this, Section 5.3 introduced methods to identify shaft friction current i_{fr}, motor torque constant k_{t} and mechanical moment of inertia $I_{\mathrm{mech,p}}$. By comparing estimations with expected values, it was shown that these methods yield useful results. The parameters obtained through these methods will be used in Chapter 6 to demonstrate that HIL experiments in the model basin indeed allow accurate prediction of ship propulsion system dynamics.

Yet, the identification methods described here are not the only possible approach to parameter identification. Here, different parameters are identified individually and sequentially. For the first proof of principle delivered in this dissertation, this sequential approach is suitable as it provides insight into inaccuracies of identification measurements and sensitivities of individual parameters. For future applications, other methods may allow to identify these parameters faster and easier. For example, input signals containing white noise or chirps could be used to simultaneously identify friction torque, torque constants and moments of inertia. Such advanced identification strategies are outside the scope of this dissertation.

Chapter 6

Experimental Validation

In previous Chapters, scale effects on shaft dynamics were identified, and methods to correct for these scale effects were introduced. Following this, the aim in this Chapter is to answer the fifth research sub question. In Chapter 1, this question was formulated as follows:

– How can these measures be applied in dynamic open water experiments?

The preparations for HIL open water experiments were described in Chapter 5. By describing and analysing HIL experiments conducted in the towing tank at TU Delft, this Chapter proves that such HIL experiments indeed are accurate representations of full scale reality. By delivering this proof, the fifth research sub question is answered.

6.1 Approach to Validation

In Chapter 1, the HIL open water test was introduced, and the issue of scale effects was brought up. This resulted in the question whether whether HIL techniques can be used to accurately emulate ship propulsion dynamics, despite these scale effects. As was indicated in Section 1.5, this question is answered in five steps:

1. deriving mathematical descriptions;
2. identifying and illustrating scale effects;
3. formulating solutions for these scale effects;
4. validating mathematical descriptions;
5. validating proposed solutions for scale effects.

The first three steps were taken in Chapters 2 through 4. First, non-linear descriptions of the ideal and practical scale models were developed in Section 2.2 and subsequently linearised in Section 2.3. As a second step, these linear descriptions allowed to illustrate expected scale effects on shaft dynamics in Section 2.5. The third step was to derive solutions to account for these scale effects; this was done in Chapters 3 through 5.

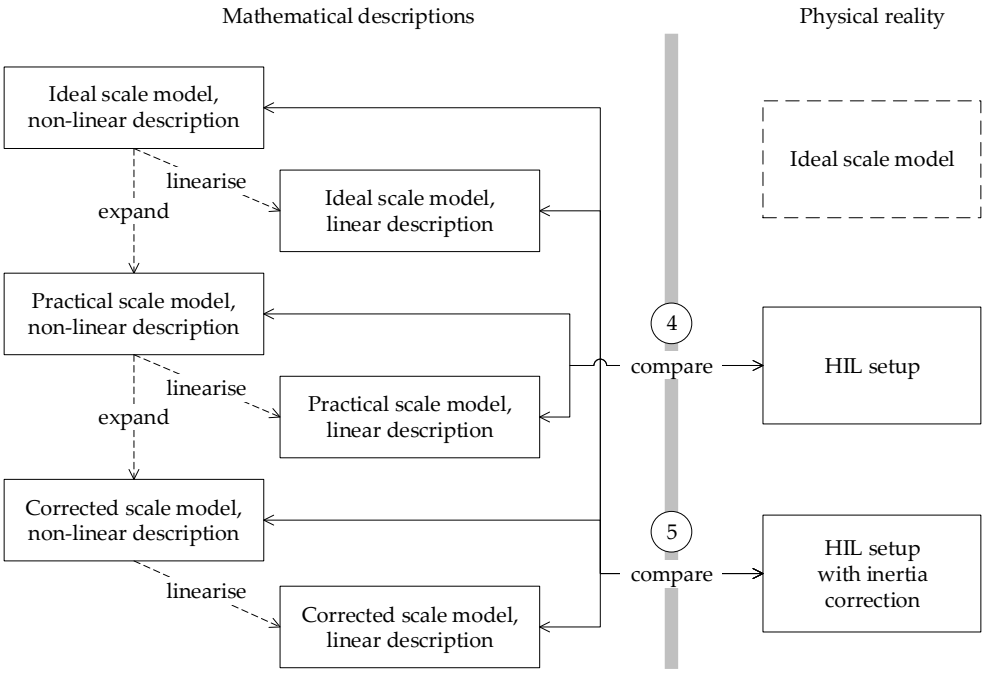


Figure 6.1: Approach to validating mathematical descriptions and proposed solutions for scale effects, using numerical simulations and HIL experiments. In this Chapter, steps 4 and 5 are described. To validate the mathematical descriptions, non-linear and linear simulations of the practical scale model are compared to HIL measurements without numerical inertia correction. Next, the performance of the proposed corrections is verified by comparing simulations of the corrected scale model and ideal scale model to HIL measurements with the proposed corrections applied. Note that the ideal scale model has a dashed edge as it does not actually exist.

Steps four and five are pointed out in Fig. 6.1 and covered in this Chapter. In the fourth step, simulations of the practical scale model are compared to actual HIL measurements without corrections, thus demonstrating that the mathematical descriptions of the shaft speed loop and electric loop are indeed valid descriptions of physical reality. This validation is done in Section 6.4. As the practical scale model is in fact a modified and extended version of the ideal scale model, this also serves as a validation of the ideal scale model. Finally, as a fifth step, the numerical inertia correction is demonstrated in HIL experiments and compared to simulations in Section 6.5. Note that the friction correction is applied by default and not validated separately, as it does not introduce noteworthy dynamic distortions.

HIL experiments are conducted with the setup introduced in Chapter 5. A first set of measurement runs is conducted in static, nominal conditions, allowing to identify equilibrium values. These equilibrium values are used in the linear models that are run in parallel with the dynamic open water experiments. In addition, the measurements are compared with the equilibrium values simulated in Chapter 2.

Dynamic experiments are conducted in various environments. The first series of dynamic experiments is conducted in calm water, and dynamic response is enforced by introducing sinusoidal variations and step changes into the torque and speed setting of the simulated engine. The resulting response with and without the proposed corrections is compared to simulations of the ideal and practical scale models. This allows to validate the mathematical descriptions introduced in Chapter 2 and to demonstrate that the numerical inertia correction performs as predicted.

The second series of experiments in this Chapter corresponds to a more realistic environment, introducing waves rather than enforced fluctuations in drive torque and speed setting. In this dissertation, an ocean with fully developed wind waves as described by Pierson and Moskowitz (1964) is considered. These waves can be reproduced at model scale in the towing tank, as will be described in more detail in Section 6.3. As a first step, however, measurements in static, nominal conditions are described and analysed in Section 6.2.

6.2 Equilibrium Conditions

Before conducting dynamic open water experiments, equilibrium values are determined in static open water experiments. The equilibrium values thus obtained serve as input for the linear simulations conducted in this Chapter. Furthermore, these values can be compared to the simulated equilibrium values given in Chapter 2, indicating how simulated equilibrium points relate to physical reality.

A first static run is conducted at a carriage speed of 1.73 m/s and a propeller speed of 605 rpm, consistent with the conditions given in Table 2.1. The propeller hub immersion depth equals 0.418 m, which corresponds to a hub immersion ratio of 1.78 – the immersion ratio here expresses the ratio between immersion depth and propeller diameter. At 1.78, the immersion ratio is comfortably higher than the minimum of 1.5 recommended by the ITTC to avoid surface interaction (ITTC, 2014a). As Table 6.1 shows, the measured and simulated equilibrium values are not entirely equal. The largest deviation is observed for current, which is measured to be 24.4% higher than predicted by simulations. This is primarily due to the fact that friction torque, which constitutes approximately 17% of total drive torque, is not simulated. At the same time, friction torque can be identified and corrected, as was shown in Section 5.3.1. Thus, this difference between simulated and measured equilibrium current is not an issue.

Smaller deviations are observed for measured propeller torque and thrust. Measured torque is 4.3% higher than simulated torque. This is not entirely unexpected: the Wageningen C regression model used for simulations was based on measurements at higher Reynolds numbers. As a consequence, the simulations in Chapter 2 assume lower viscous friction of the propeller blades. Based on the viscous friction correction proposed by Kuiper (1992), the different Reynolds number would account for a 0.1% to 0.2% difference in torque. The remaining difference may be explained by a measurement error. Interestingly, the approximately 4% difference between simulated and measured propeller torque aligns with the observation made during the identification of motor torque constant k_t in Section 5.3.2. The measured k_t was found to be 3.8% higher than the value provided by the motor manufacturer. In Section 5.3.2, it was concluded that this deviation is possibly due to a 3.8% error in measured propeller

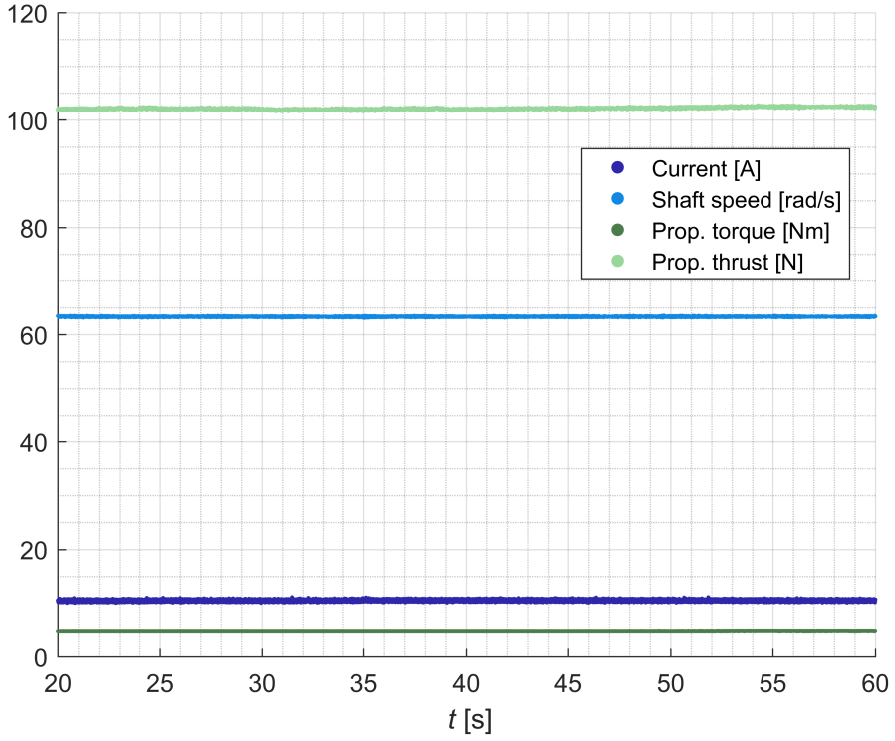


Figure 6.2: Static measurement run conducted at at a carriage speed of 1.73 m/s and a propeller speed of 605 rpm. The measured equilibrium values are given in Table 6.1 and will be used for linear simulations throughout this Chapter. This Figure is based on the data in *exp_173.mat*, stored in the measurement data repository (Huijgens, 2020). These equilibrium values were confirmed by later measurements stored in *exp_221.mat*.

Table 6.1: Comparison of equilibrium values obtained through non-linear simulations and measurements shown in Fig. 6.2. These values result from closed loop experiments with a full scale equivalent engine speed setting of 500 rpm, which corresponds to a model scale propeller speed of 605 rpm. The measured equilibrium values are valid for all HIL experiments in this dissertation unless mentioned otherwise.

	Symbol	Unit	Simulated	Measured
Eq. prop. torque	$M_{\text{prop,hydro,0}}$	[Nm]	4.505	4.7
Eq. prop. thrust	$T_{\text{prop,0}}$	[N]	99.87	102.4
Eq. winding current	i_0	[A]	8.19	10.3
Eq. prop. speed	$n_{\text{s,0}}$	[rpm]	605	605
Prop. advance speed	v_{a}	[m/s]	1.73	1.73

Table 6.2: Equilibrium conditions for open loop bollard pull experiments. These equilibrium values are valid for all open loop HIL experiments in this dissertation unless mentioned otherwise. The friction correction introduced in Section 5.3.1 is applied, resulting in a measured propeller torque $M_{\text{prop,hydro,0}}$ which is practically equal to the simulated drive torque $M_{\text{d,sim,0}}$.

	Symbol	Unit	Measured
Eq. sim. drive torque	$M_{\text{d,sim,0}}$	[Nm]	4.0
Eq. prop. torque	$M_{\text{prop,hydro,0}}$	[Nm]	4.0
Eq. prop. thrust	$T_{\text{prop,0}}$	[N]	94.6
Eq. winding current	i_0	[A]	9.00
Eq. prop. speed	$n_{\text{s,0}}$	[rpm]	438
Prop. advance speed	v_{a}	[m/s]	0.00

torque caused by a plastic deformation of the QT sensor. As another possibility, the non-linear simulation model of the propeller may be not entirely accurate. The geometry of the propeller used during HIL experiments may not be exactly the same as the geometry of the propeller used to derive the regression model, while the implementation of this regression model as a lookup table may introduce additional inaccuracies.

In any case, differences in equilibrium torque in the observed order of magnitude only have a very limited effect on shaft dynamics, as was illustrated by Fig. 2.15. Moreover, measurements by the QT sensor are not used as feedback for the simulation model. Considering that this dissertation concentrates on dynamic behaviour, these potential static measurement errors are not analysed in detail here.

In addition to experiments with a propeller advance speed of 1.73 m/s, a number of experiments are conducted in bollard pull condition. In bollard pull, the propeller rotates but does not move in axial direction; in other words, propeller advance speed and thus towing carriage speed equals zero. As a particular advantage, experiments in bollard pull condition require considerably less time than experiments with a moving towing tank carriage. In specific, open loop response of the shaft speed loop is verified in bollard pull at the equilibrium conditions given in Table 6.2.

6.3 Dynamic Model Scale Environment

With equilibrium conditions now known, the dynamic model scale environment can be described. This is a crucial step towards successful HIL experiments, as the dynamic environment determines the frequencies of the expected disturbances, and thus, the relevant frequency range. As was indicated in Chapter 2, the HIL setup must be able to accurately emulate dynamic response in the relevant frequency range, and the relevant frequency range depends on the considered environment.

The dynamic model scale environment is analysed in two stages. First, Section 6.3.1 introduces the full scale environment and corresponding model scale environment. Next, Section 6.3.2 condenses the analysis in Section 6.3.1 to a relevant frequency range, and compares this range to the similarity range of the HIL setup, taking into account the findings from Chapters 3 and 4. As such, it can be verified whether the HIL setup is able to accurately emulate shaft dynamics in the model scale environment.

6.3.1 Environment: Ocean Wind Waves

The environment considered in this dissertation is an ocean with fully developed deep water wind waves, as described by Pierson and Moskowitz (1964). Fully developed waves are in equilibrium with the wind, meaning that a longer fetch does not further increase wave heights. Although wave fields are often not fully developed in practice, the Pierson-Moskowitz spectrum suffices as an approximation of ocean wave patterns for demonstrative experiments. A detailed account on wave theory is outside the scope of this dissertation, so no further attention is paid to other wave spectra. Rather than reproducing entire wave spectra, regular waves are generated based on significant wave heights and modal frequencies corresponding to different wind speeds.

Since the considered ocean waves are generated by wind at full scale, properties of these waves such as frequency, height and energy are related to wind speed. Here, wind speed is defined as the average speed 10 meter above the surface and referred to as U_{10}, in correspondence with the well known Beaufort scale for wind speed. The energy present in a wave system can be expressed as a function of wave frequency ω by wave variance spectrum S. The integral of S to ω equals the wave height variance $\left\langle \zeta^2 \right\rangle$, which is directly proportional to the average potential and kinetic energy present in the wave system per square meter. The Pierson-Moskowitz wave variance spectrum $S(\omega)$ of a wave field resulting from a given U_{10} can be calculated as shown in Eq. (6.1).

$$S(\omega) = \frac{8.1 \cdot 10^{-3} \cdot g^2}{\omega^5} \cdot \exp\left(-0.64 \cdot \left(\frac{g}{\omega \cdot U_{10}}\right)^4\right) \tag{6.1}$$

Fig. 6.3 shows the wave variance spectra for a range of winds speeds, calculated according to Eq. (6.1). As a reference, the Beaufort scale is included in Table 6.3, allowing to intuitively relate wind speeds to sea conditions. It can be seen that the wave variance and thus, wave amplitude rapidly diminishes as the wind speed decreases. This confirms the intuitive expectation that waves generated by weak winds cause only minor fluctuations of propeller load. Moreover, waves generated at lower wind speeds have a higher frequency, implying a faster decay of orbital motions with increasing depth. Although not visible in Fig. 6.3, this effect further reduces

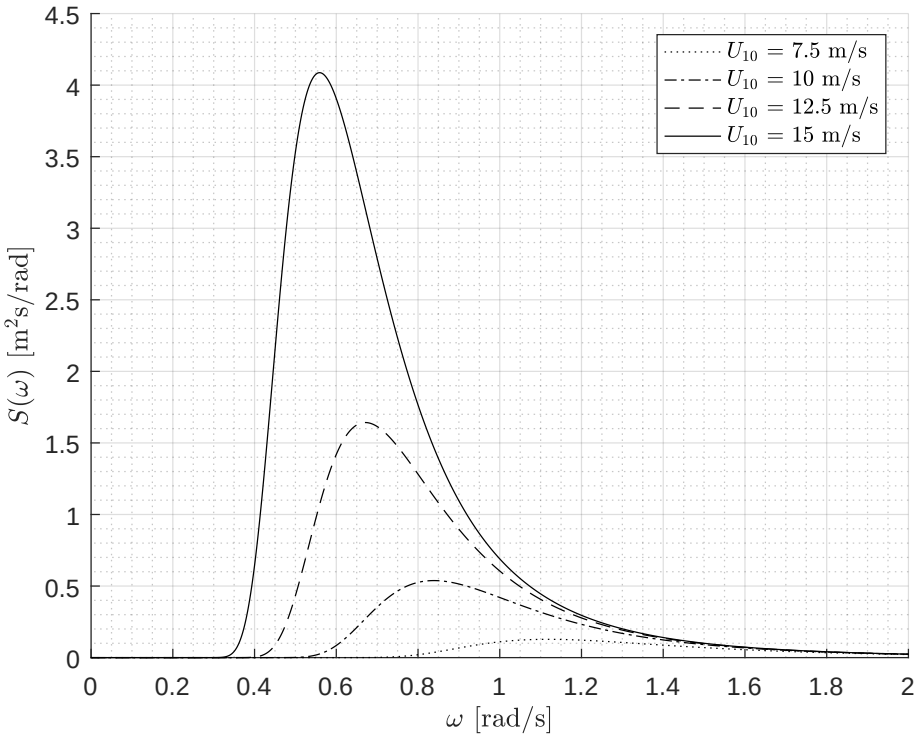


Figure 6.3: Wave variance spectrum $S(\omega)$ at full scale calculated in accordance with Eq. (6.1) for wind speeds between 7.5 and 15 m/s, with g equal to 9.81 m/s^2. The spectral density and thus, energy carried by the waves rapidly diminishes with decreasing wind speeds.

Table 6.3: Modern Beaufort wind scale. Wind speeds are averages 10 meter above the surface. Note that the Beaufort number is not a scientific unit. In this dissertation, the Beaufort scale only serves as an intuitive reference for sea conditions.

Beaufort number (Bft)	Description	U_{10} [m/s]
0	Calm	< 0.2
1	Light air	0.2 to 1.5
2	Light breeze	1.6 to 3.3
3	Gentle breeze	3.4 to 5.4
4	Moderate breeze	5.5 to 7.9
5	Fresh breeze	8.0 to 10.7
6	Strong breeze	10.8 to 13.8
7	Near gale	13.9 to 17.1
8	Gale	17.2 to 20.7
9	Strong gale	20.8 to 24.4
10	Storm	24.5 to 28.4
11	Violent storm	28.5 to 32.6
12	Hurricane force	> 32.7

Table 6.4: Wind speeds assumed for HIL experiments in this Chapter, along with the resulting significant wave heights $H_{1/3}$ and modal frequencies ω_p according to the Pierson-Moskowitz wave spectrum. Values are converted from full scale to model scale maintaining Froude similarity, with a geometric scale factor of 17.9.

		Full scale		Model scale	
U_{10} [m/s]	Bft	$H_{1/3}$ [m]	ω_p [rad/s]	$H_{1/3}$ [m]	ω_p [rad/s]
7.5	4	1.26	1.18	0.07	5.0
8.5	5	1.62	1.04	0.09	4.4
9.5	5	2.02	0.93	0.11	3.9
10.5	5	2.47	0.84	0.14	3.6
11.5	6	2.97	0.77	0.17	3.3

the relative importance of weak wind waves for interaction between environment and machinery.

In addition, the capabilities of the wave generator and towing tank put a limit on the waves that can be reproduced at model scale. In the towing tank at the TU Delft, waves are generated by hydraulically powered oscillating bulkheads. The frequency and amplitude of these oscillations are limited, setting upper and lower limits to wave amplitudes and frequencies. Moreover, when generating deep water waves, amplitudes are limited by the water level of the towing tank: in order to avoid deformation of waves due to interaction with the bottom of the tank, the water level in the towing tank must be at least half the wave length. Taking into account these limits and the relative small amount of wave energy at wind speeds below 7.5 m/s, five types of regular waves corresponding to the wind speeds in Table 6.4 are generated during HIL experiments in this Chapter.

The wave spectrum described by Eq. (6.1) and illustrated by Fig. 6.3 is valid for a fixed point in the wave field. The ship, however, moves through the wave field, compressing or decompressing the wave field encountered by the propeller depending on the ship's speed and course. The frequency at which the propeller encounters waves is referred to as the wave encounter frequency ω_E. As Eq. (6.2) shows, the wave encounter frequency is a function of the actual wave frequency ω, the ship's course μ relative to the waves and the ship's speed v_s relative to the water.

$$\omega_\mathrm{E} = \omega_\mathrm{p} + \frac{v_\mathrm{s} \cdot \cos(\mu) \cdot \omega_\mathrm{p}^2}{g} \tag{6.2}$$

During the experiments in this Chapter, the heading relative to the waves, or μ, equals 0, indicating that the ship is sailing in head seas. In addition to the ship's speed and course, the interaction between waves and the ship's hull considerably influences the wave encounter frequency in practice. Wave forces on the hull excite ship motions in six degrees of freedom, inducing additional fluctuations of propeller inflow. At the same time, these waves forces and ship motions cause added hull resistance, often resulting in a reduced speed in rough seas and thus, reduced encounter frequency. However, including the interaction between wave forces on the hull and ship motions would considerably complicate the HIL experiments without adding information relevant for validation. Thus, ship motions are not emulated here, while the advance speed remains the same irrespective of the wave field. For cases in which ship motions and added resistance are relevant, HIL experiments with free sailing models are more suited. The propulsion system of such free sailing models can be based on the open water HIL setup described in this dissertation.

In analogy with the encounter frequency, the ship's course and speed also has an effect on the wave variance spectrum S. The variance spectrum encountered by the propeller, referred to as the encounter variance spectrum S_E, can be obtained from the static variance spectrum S as shown in Eq. (6.3).

$$\begin{aligned} S_\mathrm{E}\left(\omega_\mathrm{E}\right) &= S_\mathrm{E}\left(\omega_\mathrm{p} + \frac{v_\mathrm{s} \cdot \cos(\mu) \cdot \omega_\mathrm{p}^2}{g}\right) \\ &= \frac{S\left(\omega_\mathrm{p}\right)}{\left|1 + \frac{2 \cdot \omega_\mathrm{p} \cdot v_\mathrm{s} \cdot \cos(\mu)}{g}\right|} \end{aligned} \tag{6.3}$$

Because of the law of conservation of energy, wave energy is concentrated at higher frequencies in the encounter variance spectrum S_E than in the actual variance spectrum S when sailing in head seas. This is illustrated by Fig. 6.4, which shows that the peaks of the encounter variance spectra are located at higher frequencies than for comparable wind speeds in Fig. 6.3. Describing the environment encountered by the propeller, wave encounter spectra are the key to determining the relevant frequency range for HIL open water experiments in this dissertation. In Section 6.3.2, the relevant frequency range is determined and compared to the expected similarity range of the HIL setup.

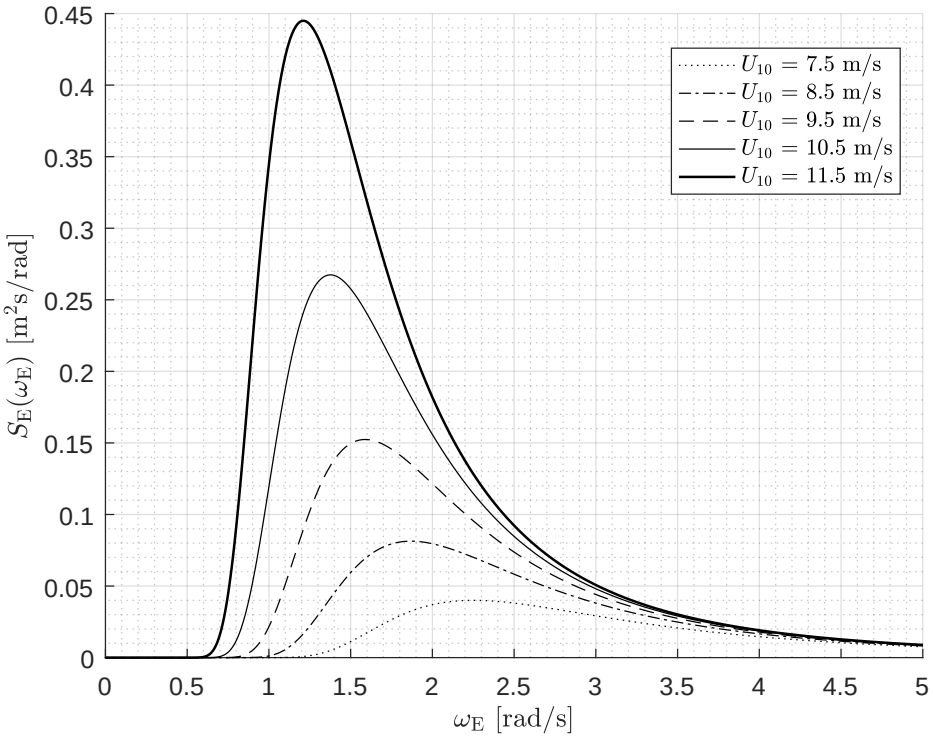


Figure 6.4: Encounter wave variance spectrum $S_{\mathrm{E}}(\omega_{\mathrm{E}})$ at full scale, calculated in accordance with Eq. (6.3) for the wind speeds given in Table 6.4. v_{s} equals 9.77 m/s, while μ equals 0. When sailing in head seas, wave energy is concentrated at higher frequencies in the encounter variance spectrum than in the static variance spectrum.

6.3.2 Relevant Frequency Range and Similarity Range

The relevant frequency range is the frequency interval in which environmental disturbances are expected. In theory, this interval extends to the high frequencies associated with capillary waves. In practice, however, the energy carried by such high-frequent disturbances is negligible compared to waves with lower frequencies. Fig. 6.4 shows that for the considered wind speeds, most of the wave energy is carried by waves with encounter frequencies below 3 rad/s.

The frequency limit of 3 rad/s is expressed at full scale; for Froude scaled experiments with a λ of 17.9, the frequency limit becomes 12.7 rad/s. Thus, the relevant frequency range extends up to 12.7 rad/s for the HIL experiments in this dissertation. Note that for different cases, the wave encounter spectrum would look different. A different wave spectrum, ship speed or ship course would cause energy peaks at lower or higher frequencies. This means that the relevant frequency limit of 3 rad/s is not automatically valid for all HIL experiments. The example described here serves to illustrate how this limit can be determined for HIL experiments in the model basin, and to demonstrate that HIL can indeed be used to emulate propulsion dynamics in realistic environments. The experiments in this Chapter assume a ship sailing at full speed in head waves, resulting in high wave encounter frequencies. As such, the reported experiments demonstrate that similarity can be achieved for most practical cases at the same scale.

The relevant frequency range must fall within the similarity range, which equals the frequency interval at which the HIL setup can accurately emulate shaft dynamics. In Chapters 3 and 4, the effects of the motor current controller settings and inertia correction on the similarity range were discussed. In Section 3.2.3, it was shown that given the properties and equilibrium values of the considered HIL setup, the motor current controller can be tuned to avoid distortions by the electric drive at frequencies below 100 rad/s. The numerical inertia correction, on the other hand, imposes a considerably lower frequency limit. Based on the equilibrium values given in Table 6.1 and the moments of inertia in Table 5.4, the linear description given in Section 4.4.3 predicts accurate correction of inertia up to a frequency of 13 rad/s. Considering this, the similarity range of the considered HIL setup extends up to about 13 rad/s at model scale, or about 3.1 rad/s at full scale.

The upper limit of the similarity range of 3.1 rad/s is slightly higher than the relevant frequency limit of 3 rad/s. It can thus be concluded that the requirements regarding dynamic similarity, introduced in Chapter 2, are met during the HIL experiments in this dissertation. Yet, even if these requirements had not entirely been met, this would not necessarily have been problematic. The similarity and relevant frequency ranges should be regarded as indicative rather than exact, as they were introduced to raise awareness regarding the practical limits of dynamic open water experiments.

6.4 Validation of Mathematical Descriptions

Fig. 6.1 showed that first, the non-linear and linear descriptions are validated, followed by validation of the numerical inertia correction. This Section concentrates on the first step, comparing simulations based on the non-linear and linear descriptions with

actual HIL measurements.

The practical scale model was introduced in Chapter 2. In essence, this scale model consists of two control loops: the electric loop and the shaft speed loop. Both loops will be analysed here, starting with the electric loop. The response of current on current setting is measured and compared to simulations based on the mathematical description given in Section 6.4.1. Following this, the mathematical description of the shaft speed loop is validated in Section 6.4.2, paying attention to both open loop and closed loop response.

Up to this point, linear simulations of the closed shaft speed loop were based on the transfer functions given in Appendix A. These transfer functions do not take into account the diesel engine model introduced in Section 2.2.1. This simplification allowed for a convenient, generic and yet sufficiently accurate prediction of shaft dynamics up to this point. However, the HIL experiments do include the diesel engine model. Thus, in order to make a correct comparison between linear simulations and HIL measurements, linear descriptions including the diesel engine model are used from here on. These linear descriptions are given in Appendix B.

6.4.1 Electric Loop

A set of experiments was conducted to investigate whether the response of current i on current set point i_{set} corresponds with the mathematical descriptions derived in Sections 2.2.2 and 2.3.2. The original plan was to systematically vary current controller settings, allowing to compare the observed trends in dynamics with predictions by simulations. However, this was not possible, as the range of the current controller settings in the motor drive is limited by the manufacturer, prohibiting the use of deliberately low settings for $K_{\text{p,i}}$ and $K_{\text{i,i}}$. Still, a range of current controller settings were tried, which uncovered a number of issues with the electric drive.

One of these issues was the unexpected acoustic noise produced by the motor when using the settings for $K_{\text{p,i}}$ and $K_{\text{i,i}}$ following from the guidance in Chapter 3. This noise is possibly caused by resonance between mechanical components and electromotive forces which depend on the settings of the current controller. Such resonances are reported to occur in PMSM and BLDC motors especially if commutation occurs through PWM signals (Brackley and Pollock, 2000). The noise of the electric motor in the HIL setup was first noticed by engineers at MARIN. Since experiments at MARIN regularly involve sound measurements, the current controller settings were adjusted until audible noise no longer occurred. This resulted in the settings given in Table 6.5. The linear simulations of shaft speed response shown in Fig. 6.5 suggest that these settings should not cause dynamic distortions in the responsive frequency range. This is in line with expectations: the settings chosen by MARIN are higher than the minimum settings recommended by the guidance in Chapter 3 and given in Table 6.5, and therefore on the safe side.

To verify that the electric loop indeed acts as fast as predicted, the response of current i on current setting i_{set} was measured in bollard pull conditions and compared to linear simulations. The current setting was oscillated with an amplitude of 0.9 A – corresponding to a torque amplitude of 0.5 Nm – around an equilibrium current of 7.3 A – corresponding to an equilibrium torque set point of 4 Nm. Note that these conditions are slightly different from the conditions described in Table 6.2, as

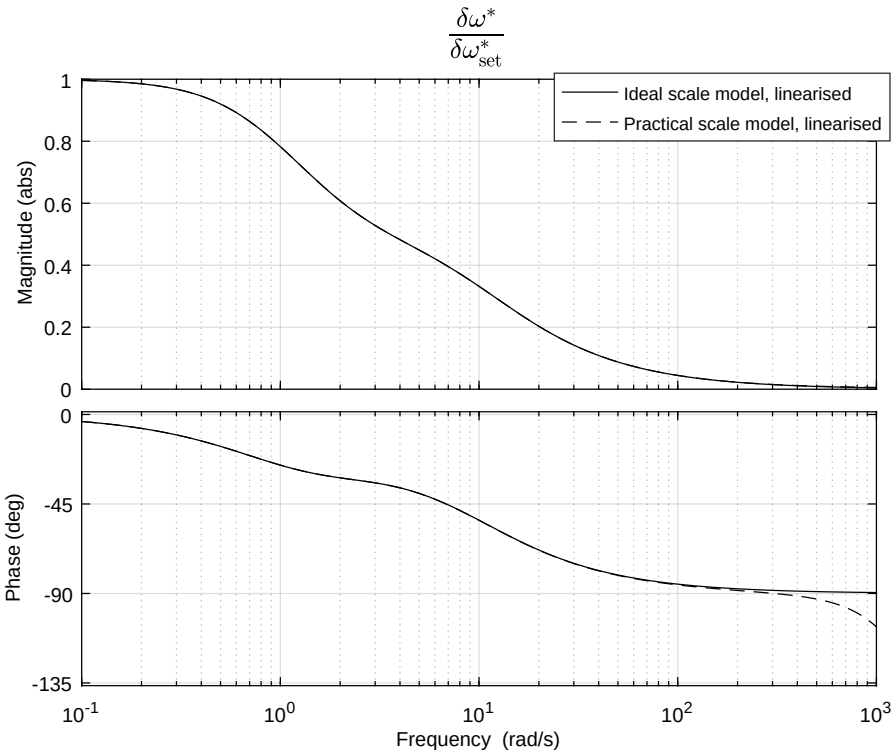


Figure 6.5: Linear simulations of the ideal and practical response of shaft speed ω on speed setting ω_{set}. The corresponding transfer functions were given in Eq. (2.24) and Eq. (2.30). The current controller has the actual settings given in Table 6.5. Based on these simulations, no dynamic distortions are expected in the responsive frequency range.

Table 6.5: Minimum settings of the current controller recommended in Chapter 3, and current controller settings that were actually used during HIL experiments in this dissertation. The minimum settings are based on the equilibrium values given in Table 6.1. Both absolute settings and normalised settings (with asterisk) are given.

	Minimum	Actual
$K_{\mathrm{p,i}}$	3.7	6.3
$K_{\mathrm{i,i}}$	574.2	8689.7
$K^*_{\mathrm{p,i}}$	0.9	1.6
$K^*_{\mathrm{i,i}}$	145.8	2206.3

the friction correction was not applied for measurements on current response. As an example, Fig. 6.6 shows the time trace of measured current response at a frequency of 10 Hz, or 62.8 rad/s.

These measurements uncovered another serious issue. In Fig. 6.7, linear simulations and measurements are compared in a Bode diagram. As the current loop is in fact an unwanted, additional dynamic system, dynamic similarity can be achieved as long as the gain of this additional system remains 1 and the phase remains 0 degrees. Apparently, dynamic distortions occur at much lower frequencies than predicted by linear simulations: the phase exceeds 5 degrees already at a frequency around 10 rad/s, while the trends with increasing frequency are different, too.

A possible explanation for the difference between measurements and simulations could be that the mathematical descriptions of the electric motor and control loop, on which the simulations are based, are incorrect. However, the descriptions derived in Chapter 2 are in line with literature. Among other examples, Martinez-Alvarado et al. (2014) reported the use of a PMSM motor to power a small scale air thruster, basing their mathematical descriptions on the same fundamental equations as those used in this dissertation. Although the extensiveness of PMSM models varies from source to source, these differences in implementation cannot explain the substantial discrepancy between measured and simulated current response.

As a more likely hypothesis, there may be an additional, dynamic system in or around the HIL setup, unaccounted for in the mathematical description. Three possible sources were considered:

1. dynamic response of line filters;
2. dynamics and discrete effects inside the motor drive;
3. dynamic response of the power supply.

Between the 380 V power supply, motor drive and motor, line filters are installed with the aim of damping high-frequent noise. Although the resulting additional inductance is taken into account in the calculation of the motor's R and L, measurements were conducted to check that these filters do not introduce additional, unexpected delays. These measurements indicated that this was indeed not the case.

As a second possible source of distortions, the dynamics inside the motor drive are not exactly known. For example, it is assumed that the current sensor inside the drive

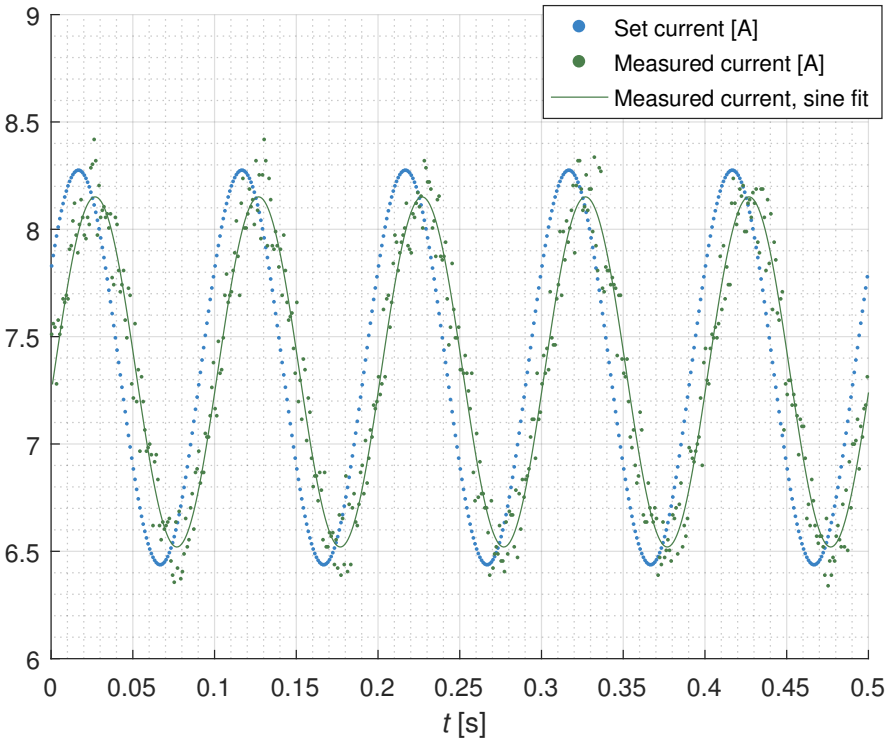


Figure 6.6: Response of current i on set current i_{set} at a frequency of 10 Hz, or 62.8 rad/s. At this frequency, the dynamic gain equals 0.89, while the phase delay equals 35 degrees. As can be seen in Fig. 6.7, linear simulations predict virtually no distortion at this frequency. This Figure is based on the data in *exp_179.mat*, stored in the measurement data repository (Huijgens, 2020).

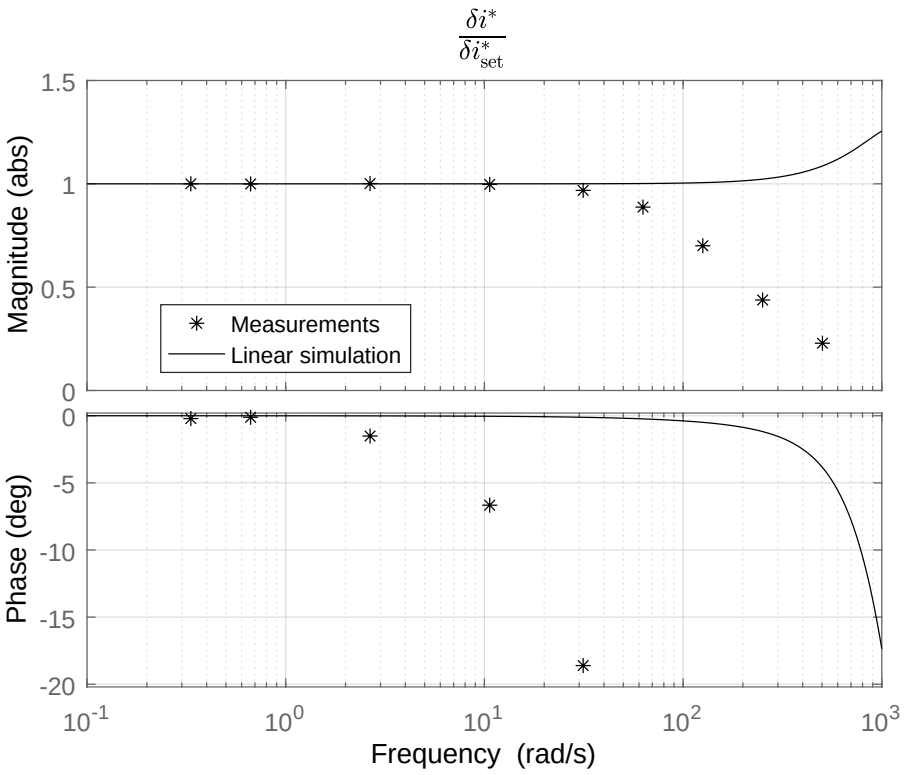


Figure 6.7: Simulated and measured response of current i on current setting i_{set}. The corresponding transfer function was given in Eq. (2.31). The current controller has the actual settings given in Table 6.5. Exact dynamic similarity can be achieved as long as the gain remains 1 and the phase remains 0 degrees. Considering this, these measurements indicate that dynamic distortions occur at far lower frequencies than predicted by linear simulations. Moreover, the trends in gain and phase are considerably different with increasing phase. This Figure is based on the data in *exp_-174.mat, exp_175.mat, exp_176.mat, exp_177.mat, exp_178.mat, exp_179.mat, exp_-180.mat, exp_181.mat* and *exp_182.mat*, stored in the measurement data repository (Huijgens, 2020).

is able to measure current within microseconds. It could not be verified whether or not this is actually the case. The sensor is located inside the motor drive, rendering it inaccessible for calibration. Although independent measurements on the current through the motor supply cables did not reveal any errors in current measurements by the drive, this component could not be entirely excluded as a source for distortions. Other than the current sensor, the motor drive contains multiple components relevant for dynamic response. The control loop, for example, is a discrete system operating at a given frequency. The operations inside this control loop could not monitored, leaving some uncertainty regarding possible discrete effects. As is the case with the current sensor, limited accessibility prevented calibration measurements on components and subsystems inside the motor drive.

As a third possible source of distortions, the 380 V supply rail introduces additional dynamics. So far, it has been assumed that these dynamics occur only at very high frequencies, and can therefore be neglected. However, this assumption may not be valid under all circumstances, and the grid may not be able to follow up on high-frequent load fluctuations. As a result, high-frequent load peaks could lead to drops in supply voltage. Due to time and material constraints, no measurements were conducted to check this hypothesis; additional measurements on the supply rail of the towing tank at the TU Delft are recommended for future measurement campaigns.

In conclusion, an explanation for the relatively slow response of the electric loop could not be found through measurements. The model basin was not available for HIL experiments indefinitely, while there were systems to be analysed other than the electric loop. At the same time, the unexpectedly large electric time constant does not pose an insurmountable problem. As is shown in Section 6.5, the requirement regarding dynamic similarity stated in Eq. (2.33) can still be satisfied. In any case, this unexpected distortion demonstrates that the dynamics of the electric drive are not always negligible during model basin experiments. Especially if HIL is applied, it is advisable to check the response of current in the complete relevant frequency range prior to conducting experiments.

6.4.2 Shaft Speed Loop

Open Loop Response

Following the analysis of current response, the mathematical description of the shaft speed loop is validated. First, the open loop response of shaft speed ω on set drive torque $M_{\mathrm{d,set}}$ is considered; the corresponding linear description was given in Eq. (2.19a). To validate this linear description, the response of shaft speed of the uncorrected scale model is measured in the towing tank and compared to linear simulations. Open loop response is measured in bollard pull conditions at the equilibrium values given in Table 6.2. Drive torque is varied with an amplitude of 0.5 Nm around an equilibrium torque of 4 Nm. The resulting measurements and simulations are compared in Fig. 6.8.

Fig. 6.8 shows measurements of uncorrected open loop response at five speed setting fluctuation frequencies between 0.33 rad/s (0.05 Hz) and 21.26 rad/s (3.38 Hz). Measurements with applied numerical inertia correction are shown as well; these will receive detailed attention in Section 6.5 and are not yet considered here. Up to 2.66 rad/s, errors in gain and phase are negligible. At 10.63 and 21.26 rad/s, the phase

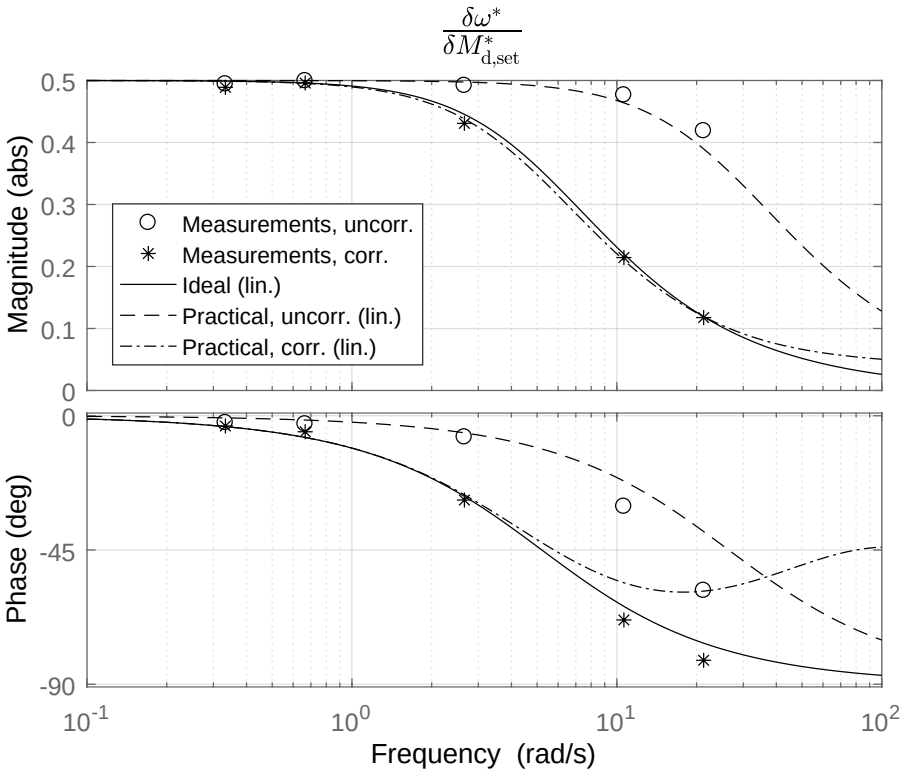


Figure 6.8: Simulated and measured open loop response of shaft speed ω on set drive torque $M_{\mathrm{d,set}}$. In addition to the linearised ideal and uncorrected response, the response with inertia correction algorithm is shown. The electric loop is not included in the linear simulations, explaining most of the differences between predicted and measured phase. The transfer function for uncorrected open loop response is given in Eq. (2.19a), while the transfer function for corrected open loop response is given in Eq. (4.23). This Figure is based on the data in *exp_189.mat, exp_190.mat, exp_191.mat, exp_192.mat, exp_193.mat* (without inertia correction) and *exp_195.mat, exp_196.mat, exp_197.mat, exp_198.mat, exp_199.mat* (with inertia correction), stored in the measurement data repository (Huijgens, 2020).

error increases to 8 and 20 degrees, respectively. This error is mostly caused by the slow response of the electric loop: Fig. 6.7 shows phase errors of 7 and 15 degrees at the same frequencies. Yet, after accounting for the error introduced by the electric loop, a phase error still remains. This error is likely due to inaccuracies in the estimated inertia of the water entrained by the propeller blades. As was indicated earlier, no conclusive estimation model is available for added inertia. Moreover, the added inertia may depend on the oscillation frequency, further complicating the estimation of added inertia in this particular case. At the same time, the error in predicted shaft dynamics resulting from incorrectly estimated added inertia is rather limited, with phase errors below 5 degrees in the relevant frequency range. Thus, without paying detailed attention to the exact value of I_{H2O}, it can be concluded that the linear description of open loop shaft speed response is valid for the practical scale model.

The ideal shaft speed loop is essentially equal to the practical uncorrected shaft speed loop, although with different values for inertia and equilibrium torque. As such, the validation of the mathematical description of the practical shaft speed loop is also a validation of the mathematical description of the ideal shaft speed loop.

Closed Loop Response

As a next step in the validation of the linear descriptions, closed loop response is analysed. The dynamic behaviour of the uncorrected, closed shaft speed loop can be simulated using the non-linear and linear descriptions given in Chapter 2. First, non-linear simulations and measurements of closed loop step response are visually compared in Fig. 6.9. As can be seen, non-linear simulations and measurements predict practically the same response of engine speed.

In addition to the predicted step response of shaft speed, Fig. 6.9 shows a vibration in measured speed with a frequency of approximately 10 Hz. This frequency equals the propeller shaft rotation frequency. This renders an eccentricity due to a minor plastic deformation of the QT sensor, as was observed in Section 5.3.2, a possible cause for this vibration. Apart from being visible in time traces, this vibration did not cause issues during experiments and post-processing.

However, this visual comparison in insufficient as a validation. A more quantitative comparison is made by comparing measurements with linear simulations in Bode diagrams in Fig. 6.11. These measurements are conducted at the conditions described in Table 6.1. The speed setting is sinusoidally varied with an amplitude of 20 rpm around an equilibrium of 500 rpm – engine speed is expressed in full scale equivalent speed here. As an example, a time trace of set speed and measured speed is shown in Fig. 6.10.

In Fig. 6.11, closed loop response without inertia correction is measured at 0.67, 2.66 and 10.63 rad/s. Again, one can conclude that the linear description is sufficiently accurate: at all three frequencies, the errors of gain and phase remain within the criteria given in Eq. (2.33).

Interestingly, the phase error at 10.63 rad/s is considerably smaller for closed loop response than for open loop response, which was shown in Fig. 6.8. The phase error introduced by the electric loop is practically absent. This effect can be attributed to the shaft speed PI controller, which has a considerable influence on shaft dynamics. As such, it reduces the influence of distortions by the electric loop and added inertia.

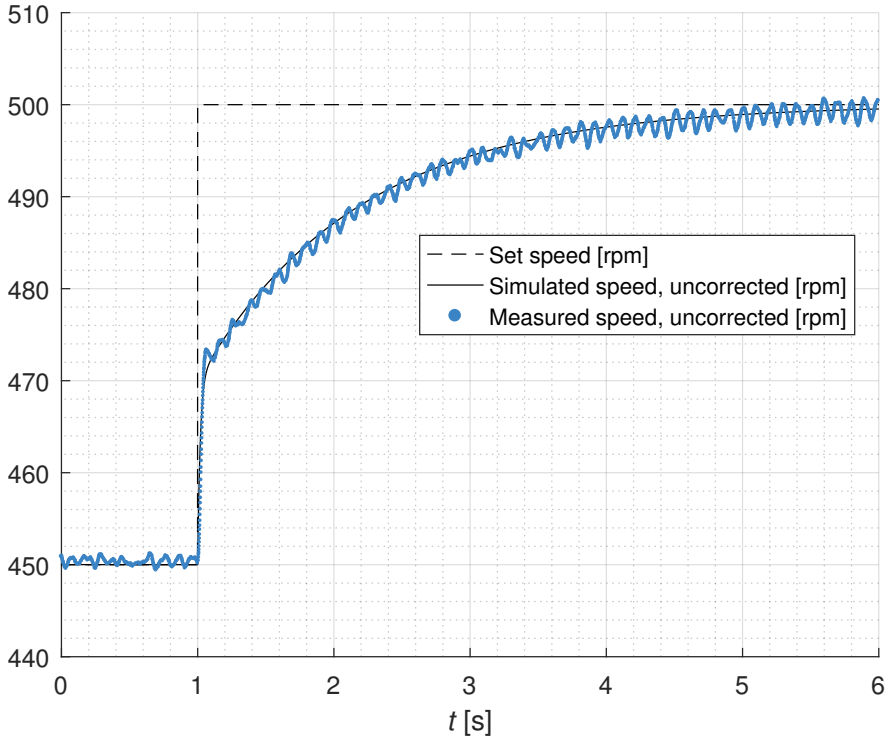


Figure 6.9: Simulated and measured response of model scale engine speed n_e on a step change in speed setting $n_{e,set}$ from 450 to 500 rpm (full scale equivalent engine speed), without inertia correction. The simulations are based on the non-linear mathematical description given in Chapter 2. The environmental conditions are given in Table 2.1. This Figure is based on the data in *exp_220.mat*, stored in the measurement data repository (Huijgens, 2020).

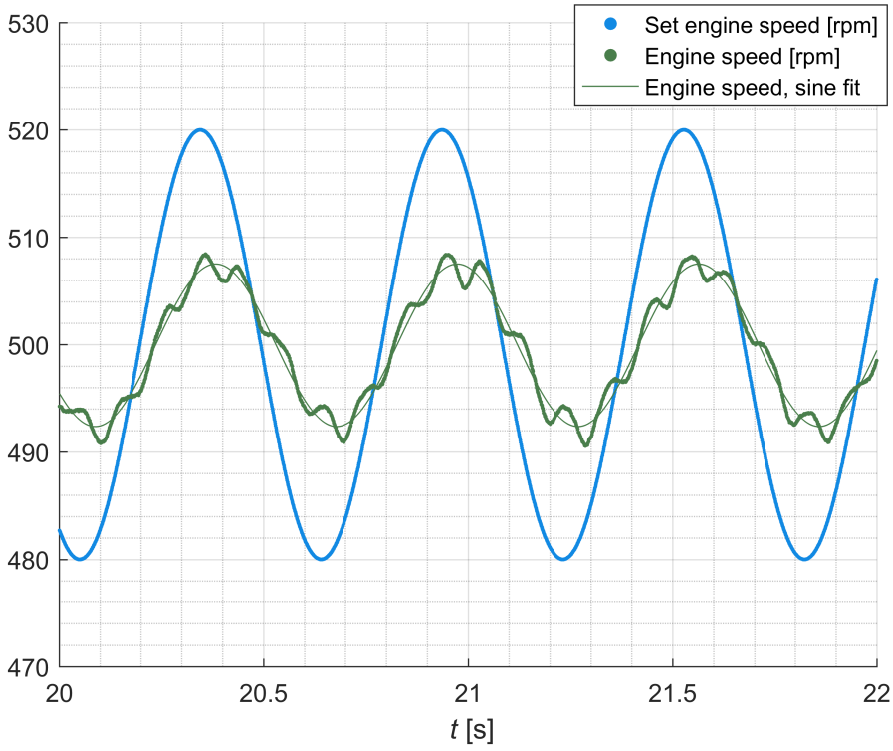


Figure 6.10: Time trace of closed loop response of engine speed ω on set engine speed ω_{set}, without inertia correction. The speed setting oscillates with a frequency of 10.63 rad/s, or 1.692 Hz, and an amplitude of 20 rpm around an equilibrium of 500 rpm, expressed in full scale equivalent engine speed. This Figure is based on the data in *exp_218.mat*, stored in the measurement data repository (Huijgens, 2020).

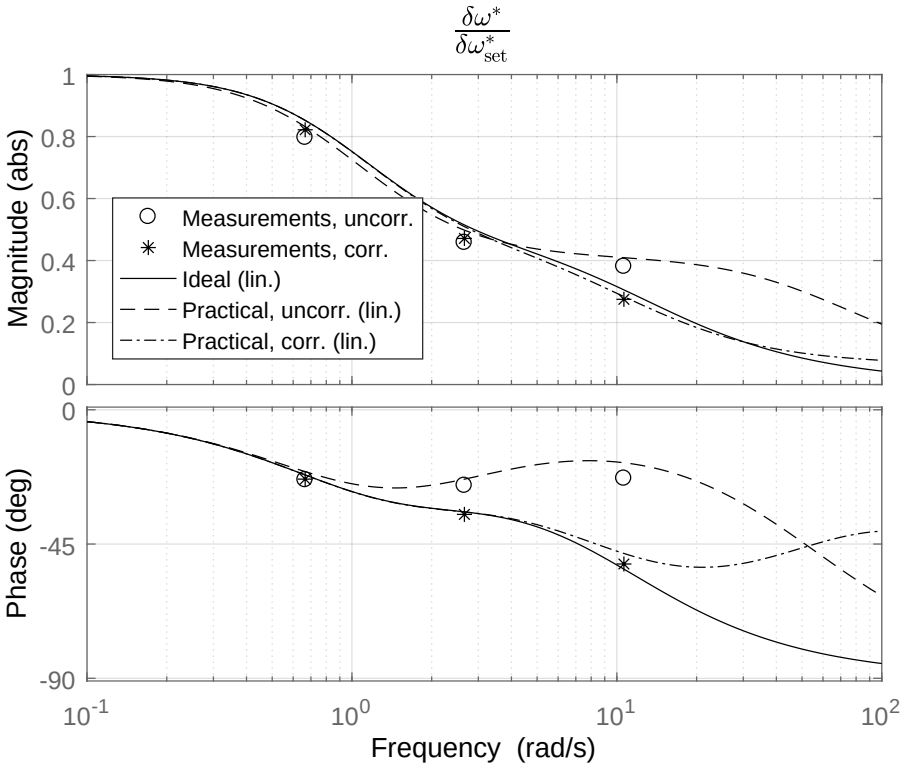


Figure 6.11: Simulated and measured closed loop response of shaft speed on set speed. Measurements with and without inertia correction are shown, while linear simulations are shown for the ideal scale model, practical scale model without inertia correction and practical scale model with inertia correction. The corresponding transfer function is given in Eq. (B.1). Linear predicts align well with measurements on the uncorrected scale model. Moreover, based on the requirements given in Eq. (2.33), one can conclude that shaft dynamics are accurately emulated in the complete relevant frequency range if the proposed corrections are applied. This Figure is based on the data in *exp_216.mat, exp_217.mat, exp_218.mat* (without inertia correction) and *exp_212.mat, exp_213.mat, exp_214.mat* (with inertia correction), stored in the measurement data repository (Huijgens, 2020).

Yet, shaft speed is not the only variable of interest. As another important parameter of engine and machinery load, the response of simulated drive torque is evaluated. As can be seen in Fig. 6.12, predictions by linear descriptions differ from measurements by only small amounts in the relevant frequency range, again confirming that the linear descriptions are valid representations of physical reality. Fig. 6.15 shows the response of simulated engine torque on a step change in speed setting, indicating that simulations correspond with measurements also for step responses.

Taking into account the dynamic distortions by the electric loop, it can be concluded that the non-linear and linear descriptions of the open loop and closed loop systems are valid representations of the practical scale model. At the same time, the ideal scale model is essentially equal to the practical scale model, although with different mechanical parameters and equilibrium values, and without an electric drive. As such, the mathematical descriptions of the practical and ideal scale models can be used to assess the dynamic similarity of HIL experiments and thus, the performance of the proposed corrections for scale effects. This is done in Section 6.5, paying particular attention to the performance of the inertia correction algorithm.

6.5 Validation of the Numerical Inertia Correction

In Section 6.4, it was proven that the mathematical descriptions of the ideal and practical scale models are valid representations of physical reality. Based on these descriptions, the inertia correction algorithm proposed in Chapter 4 can now be validated. This Section contains a comparison between the simulated dynamics of the ideal and corrected scale models, and HIL measurements with the numerical inertia correction applied. As such, the mathematical description of the corrected scale model can be validated, while also verifying that the numerical inertia correction indeed restores dynamic similarity in the relevant frequency range.

In analogy with the approach in Section 6.4.2, the corrected open loop response of shaft speed on torque is analysed first, followed by an analysis of corrected closed loop response. After a detailed analysis of response on torque and speed setting in Section 6.5.1, the dynamic response of engine speed and torque on propeller load fluctuations is evaluated in Section 6.5.2. As such, the response of torque and speed on all disturbance inputs is validated, proving that the HIL setup can be used to accurately emulate shaft dynamics.

6.5.1 Response on Speed Setting and Drive Torque

Open Loop Response

As was the case with the uncorrected scale model, open loop response of the corrected scale model is evaluated first. Eq. (4.23) presented a linear description of the response of shaft speed ω on drive torque M_d, including the inertia correction. To validate this linear description, the response of the scale model with inertia correction was measured in the towing tank and compared to linear simulations. Open loop response is measured in bollard pull conditions at the equilibrium conditions given in Table 6.2. Drive torque is varied with an amplitude of 0.5 Nm around an equilibrium torque of 4 Nm. The resulting measurements and simulations are compared in Fig. 6.8.

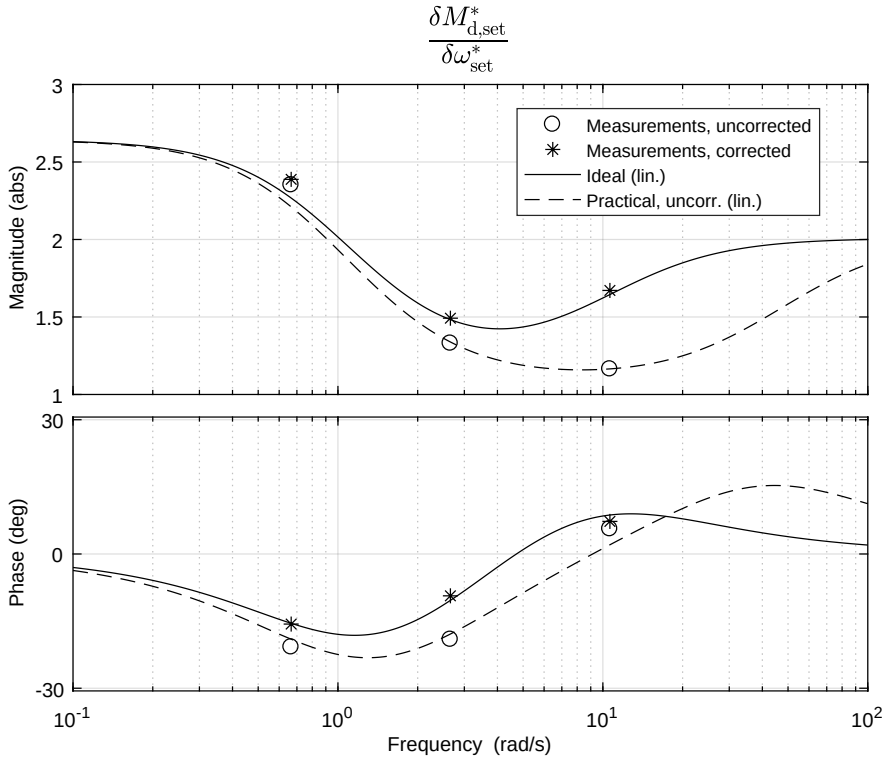


Figure 6.12: Simulated and measured closed loop response of drive torque on set speed. Measurements with and without inertia correction are shown, while linear simulations are shown for the ideal scale model and practical scale model without inertia correction. The corresponding transfer function is given in Eq. (B.2). Here, too, linear simulations are confirmed by measurements. While serving as a validation of the linear descriptions, this Bode diagram also indicates that the proposed corrections indeed result in dynamic similarity with the ideal scale model. This Figure is based on the data in *exp_216.mat, exp_217.mat, exp_218.mat* (without inertia correction) and *exp_212.mat, exp_213.mat, exp_214.mat* (with inertia correction), stored in the measurement data repository (Huijgens, 2020).

Measurements are conducted at the same frequencies as for the uncorrected scale model. Fig. 6.8 shows similar errors with and without inertia correction. At 10.63 and 21.26 rad/s, the phase error betweens the predicted behaviour – *Practical, corr. (lin.)* in the Bode diagram – and the measurements equal 12 and 22 degrees, respectively. These values are similar to the 8 and 20 degree phase errors for the uncorrected scale model. As was the case for the uncorrected scale model, these errors can be attributed to the electric loop and, to a lesser extent, inaccuracies in the estimated added inertia. Interestingly, the phase error introduced by the electric loop seems to compensate for the phase error introduced by the inertia correction. Although these two effects on themselves are undesirable, it may be useful to note this interaction for future implementations of the inertia correction algorithm.

It can be concluded that the open loop response of the HIL setup is similar to the ideal scale model, and that the mathematical description of the corrected scale model is valid. With this in mind, the closed loop response with inertia correction is evaluated.

Closed Loop Response

The dynamic behaviour of the corrected closed shaft speed loop can be predicted using the non-linear and linear descriptions given in Chapter 2. First, non-linear simulations and measurements of closed loop step response are visually compared. As can be seen in Fig. 6.13, there is a good correspondence between non-linear simulations of the ideal engine speed and HIL measurements with inertia correction.

Figs. 6.14 and 6.15 zoom in on shaft speed and engine torque response of the uncorrected and corrected scale models during the first half second after the step change in speed setting. While the time trace shows that the electric loop causes a delay of several milliseconds, it can be concluded that the inertia correction has an effect already after several milliseconds.

As was the case with the uncorrected scale model, additional experiments are conducted to obtain a more quantitative validation of the inertia correction. Again, measurements are conducted at the conditions described in Table 6.1, with sinusoidal variations of set engine speed with an amplitude of 20 rpm around an equilibrium of 500 rpm, expressed in full scale equivalent engine speed. Fig. 6.16 shows a time trace of measured response on the same sinusoidal speed settings as in Fig. 6.10, this time with inertia correction. Comparing these two Figures, the fluctuations in measured shaft speed are considerably smaller if the inertia correction is applied. Fig. 6.17 shows the same effect on the operating ellipses. Whereas the influence of inertia and thus, the inertia correction is rather limited at low frequencies, the shape, orientation and size of the ellipse may change considerably as frequencies increase. Here, too, small vibrations can be seen with a frequency equal to the shaft speed. As was mentioned earlier on in this Chapter, these vibrations are likely caused by a minor eccentricity of the QT sensor.

Fig. 6.11 shows the closed loop response of shaft speed on set speed with and without inertia correction at frequencies of 0.67, 2.66 and 10.63 rad/s. Comparing the simulated response of the ideal scale model with HIL measurements with inertia correction, one can conclude that at all three frequencies, the errors of gain and phase remain within the criteria given in Eq. (2.33). As is the case for the uncorrected

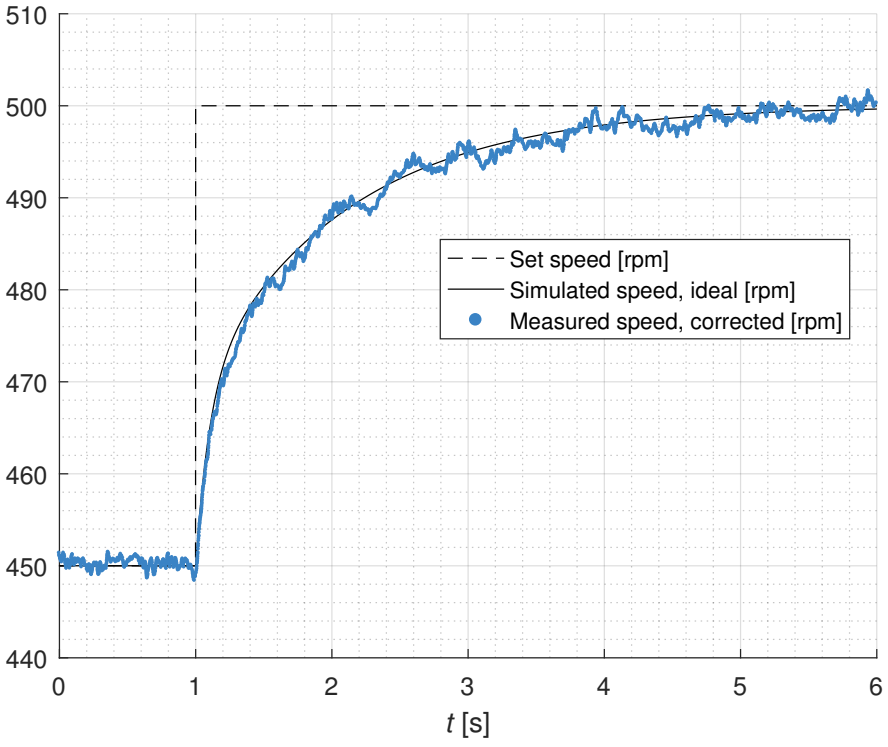


Figure 6.13: Simulated and measured response of model scale engine speed n_e on a step change in speed setting $n_{e,set}$ from 450 to 500 rpm (full scale equivalent speed). During the HIL experiment, the numerical inertia correction is applied to obtain correct shaft speed response. The simulations are based on the non-linear mathematical description given in Chapter 2. The environmental conditions are given in Table 2.1. As was the case for the uncorrected response, a good correspondence between simulations and measurements is observed. This Figure is based on the data in *exp_219.mat*, stored in the measurement data repository (Huijgens, 2020).

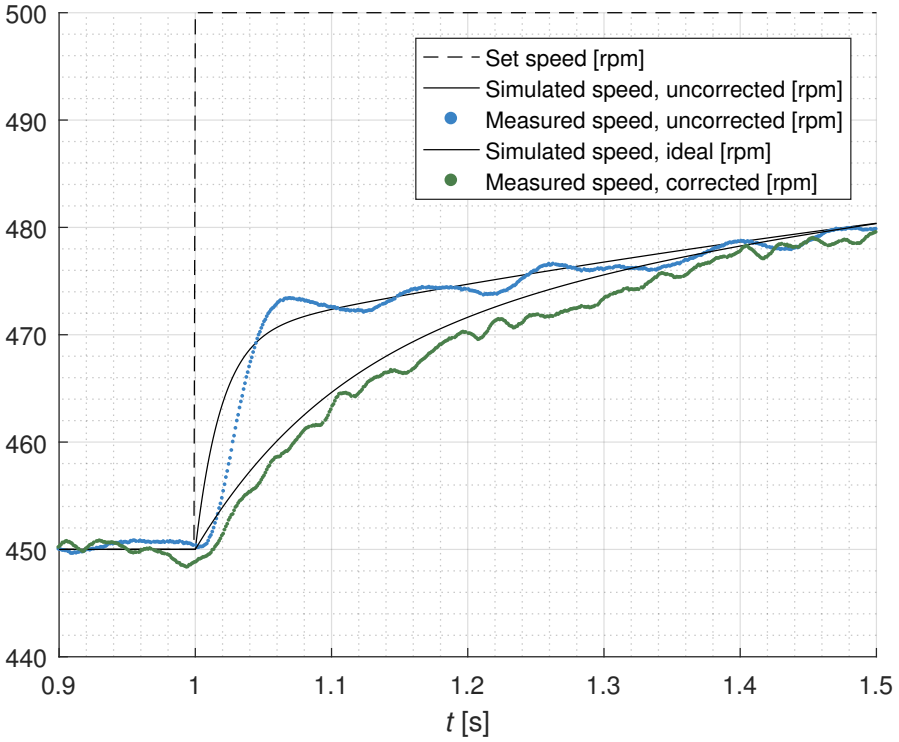


Figure 6.14: Close-up of the combined time traces shown in Figs. 6.9 and 6.13. The slow response of the electric loop results in a lagging response of shaft speed in the first milliseconds after a step change in speed setting. Apart from this short lag, the HIL experiments show a clear difference between uncorrected and corrected response. This Figure is based on the data in *exp_220.mat* (without inertia correction) and *exp_219.mat* (with inertia correction), stored in the measurement data repository (Huijgens, 2020).

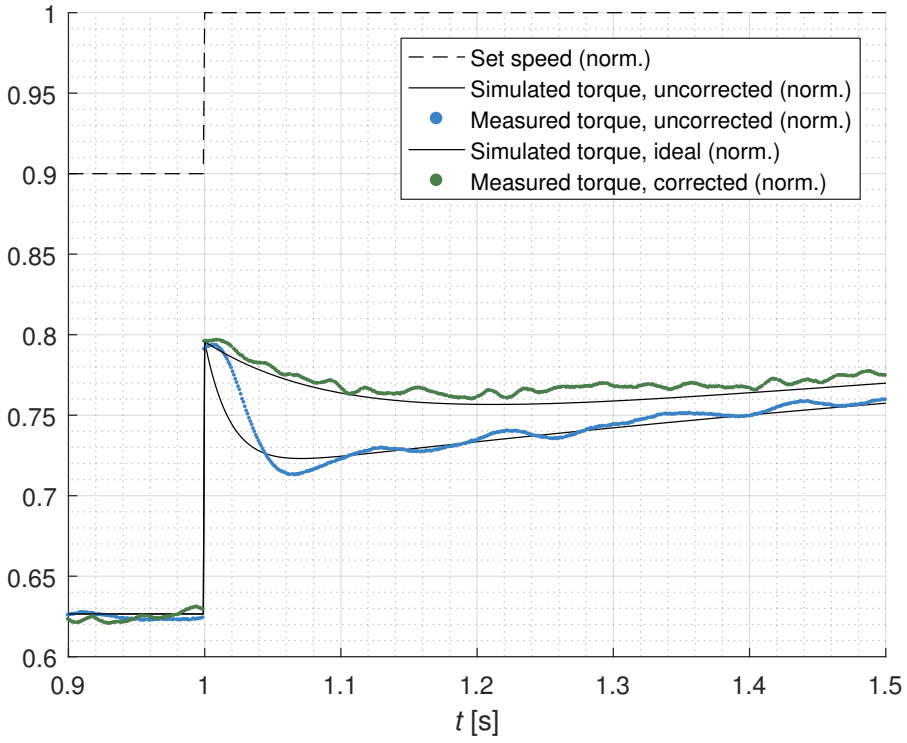


Figure 6.15: Normalised engine torque response on a step change in speed setting, during the simulations and HIL experiments also shown in Fig. 6.14. Speed and torque are normalised with respect to their nominal values. As is the case with shaft speed in Fig. 6.14, the engine torque behaves as expected. This Figure is based on the data in *exp_220.mat* (without inertia correction) and *exp_219.mat* (with inertia correction), stored in the measurement data repository (Huijgens, 2020).

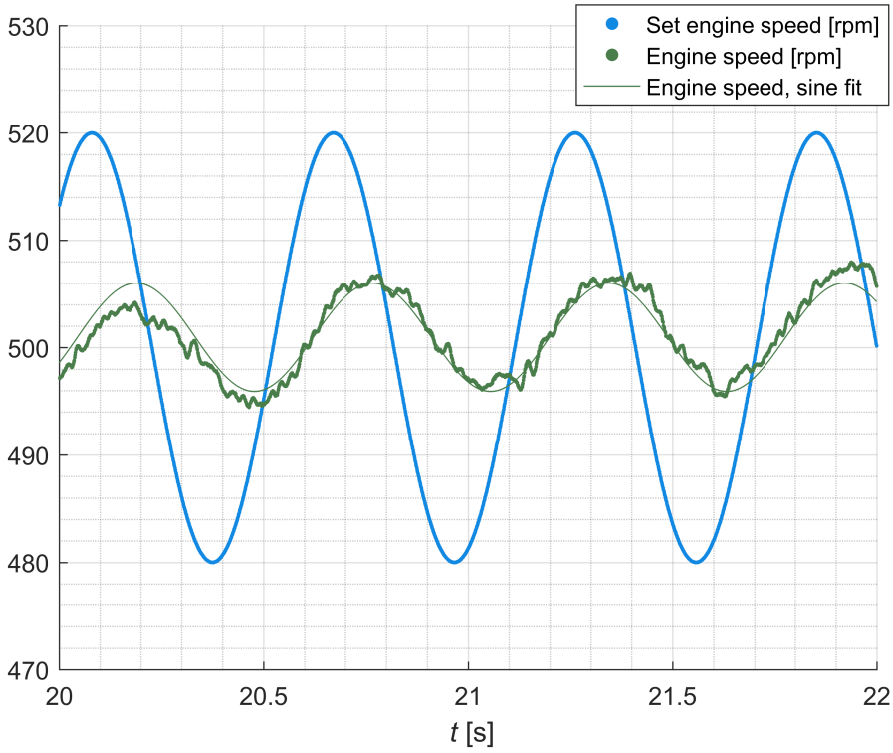


Figure 6.16: Time trace of closed loop response of engine speed ω on set engine speed ω_{set}, with inertia correction. The speed setting oscillates with a frequency of 10.63 rad/s, or 1.692 Hz, and an amplitude of 20 rpm around an equilibrium of 500 rpm, expressed in full scale equivalent engine speed. The amplitude of the shaft speed oscillations is considerably smaller than in the case without inertia correction shown in Fig. 6.10. This is due to the (virtually) larger moment of inertia of the propulsion system. This Figure is based on the data in *exp_214.mat*, stored in the measurement data repository (Huijgens, 2020).

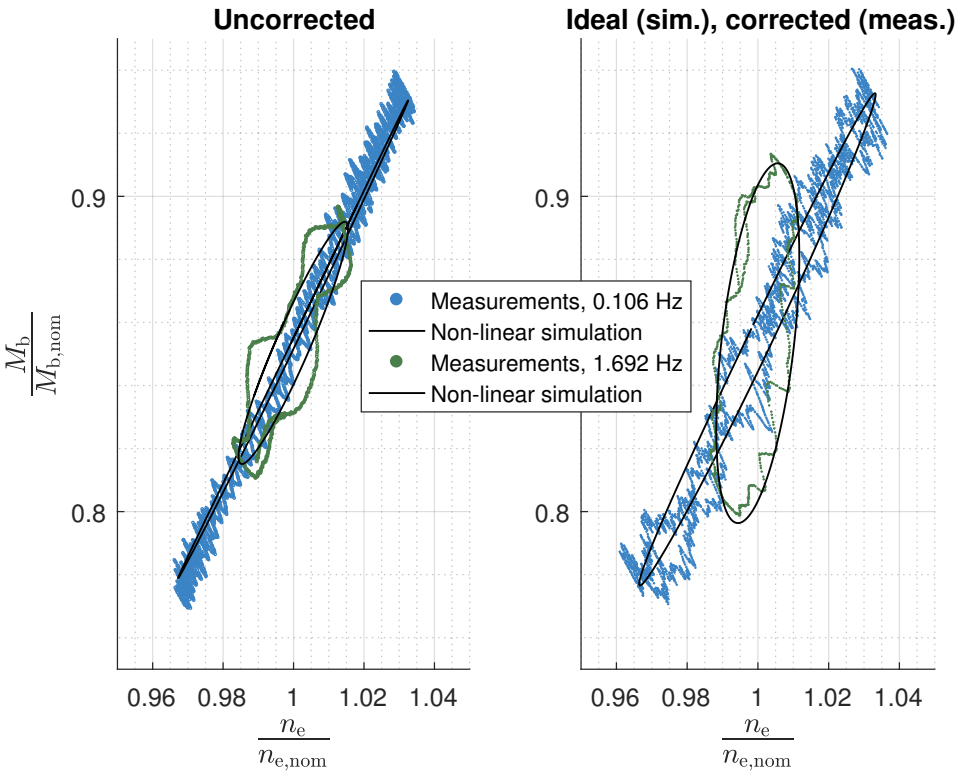


Figure 6.17: Operating ellipses containing normalised engine torque and speed during HIL experiments, with and without numerical inertia correction. The speed setting was varied with two different frequencies. For comparison, simulated operating ellipses of the ideal and practical uncorrected scale model are shown as well. These plots are based on the data in *exp_216.mat, exp_218.mat* (without inertia correction) and *exp_212.mat, exp_214.mat* (with inertia correction), stored in the measurement data repository (Huijgens, 2020).

Table 6.6: Parameters of different regular wave fields during HIL experiments. The fluctuations of normalised propeller advance speed δv_a^* are calculated based on a equilibrium advance speed of 1.73 m/s and a propeller hub immersion depth of 0.418 m.

Wave index	A_w [m]	ω_p [rad/s]	ω_E [rad/s]	δv_a^*
Bft 4	0.043	5	9.4	0.042
Bft 5 low	0.066	4.3	7.5	0.075
Bft 5 mid	0.099	3.7	6.1	0.119
Bft 5 high	0.140	3.3	5.2	0.167
Bft 6	0.186	2.9	4.4	0.218

scale model, the phase error at 10.63 rad/s is considerably smaller for the closed loop response than for the open loop response, shown in Fig. 6.8. In addition to this, Fig. 6.12 shows that simulated drive torque is accurately corrected, too. At all three considered frequencies, the measured response of drive torque corresponds well to linear simulations of the ideal scale model.

In conclusion, the measurements and simulations in this Section show that the response of the corrected scale model satisfies the requirements laid out in Eq. (2.33). Consequently, it can be concluded that the HIL setup with the proposed corrections for scale effects can be used to accurate emulate shaft dynamics in the relevant frequency range.

6.5.2 Response to Waves

In the previous Sections, the response to varying speed setting was investigated. Another common source of propulsion system dynamics are variations of propeller advance speed caused by waves and ship motions. Considering this, the response to varying advance speed is analysed, too. The analysis in this Section is limited to closed loop response with numerical inertia correction.

Section 6.3.1 introduced the considered model scale environment, which represents an ocean with fully developed wind waves. Table 6.4 introduced five wind wave fields according to the Pierson-Moskowitz spectrum, corresponding to five different wind speeds. As was indicated earlier in this Chapter, regular waves are considered rather than complete wave spectra as this greatly simplifies the analysis. Based on the modal frequencies and significant wave heights given in Table 6.4, five regular wave fields are generated during experiments. The parameters of the wave fields during HIL experiments are given in Table 6.6. From here on, these five wave fields are referred to with their corresponding Bft numbers shown in Table 6.6.

To analyse the closed loop response on waves, HIL measurements are compared to linear and non-linear simulations. As an example, Fig. 6.18 shows a part of a HIL experiment in wave type Bft 5 high. The time trace shows the wave height measured near the propeller as well as the normalised torque and speed of the simulated diesel engine. In the simulations, wave motions are modelled as uniform fluctuations of advance speed across the propeller disk, calculated at the location of the propeller hub. These fluctuations are in phase with the water level; their amplitude can be

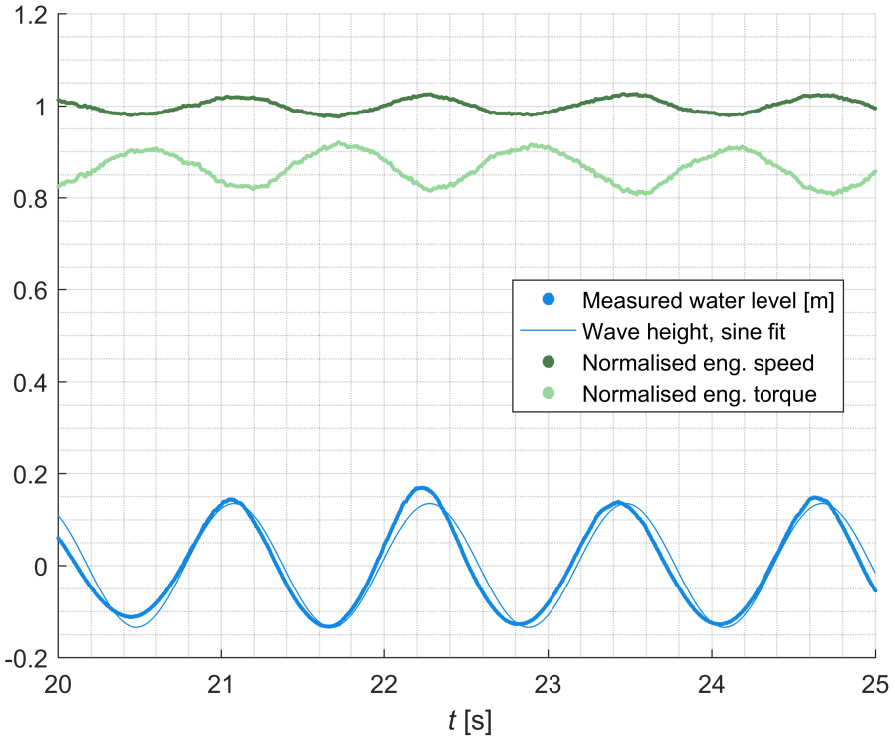


Figure 6.18: Time trace of closed loop response of engine speed and torque in wave type Bft 5 high, with numerical inertia correction. This Figure is based on the data in *exp_238.mat*, stored in the measurement data repository (Huijgens, 2020).

Table 6.7: Observed differences between measured and simulated phase angles, following from Figs. 6.19 and 6.20. In addition to the observed differences, the right column shows the expected differences based on a 0.07 m rearward offset of the wave probe.

Wave index	Observed $\varphi_{\mathrm{m-sim}}$ [deg.]		Expected $\varphi_{\mathrm{m-sim}}$ [deg.]
	$\delta\omega^*/\delta v_{\mathrm{a}}^*$	$\delta M_{\mathrm{d,set}}^*/\delta v_{\mathrm{a}}^*$	
Bft 4	22.0	16.2	22.1
Bft 5 low	19.2	14.3	15.7
Bft 5 mid	13.5	15.1	11.5
Bft 5 high	6.0	10.5	8.8
Bft 6	7.0	8.8	6.8

calculated as shown in Eq. (6.4). The propeller hub immersion depth h equals 0.418 m for the experiments described in this Section, avoiding propeller ventilation and other surface interaction effects at this stage.

$$A_{\mathrm{v}} = A_{\mathrm{w}} \cdot \omega_{\mathrm{p}} \cdot \exp\left(\frac{\omega_{\mathrm{p}}^2 \cdot h}{g}\right) \tag{6.4}$$

The theory supporting Eq. (6.4) is explained by, among others, Molland (2008). Wave heights are measured with a wave probe located close to the propeller. The wave probe essentially consists of two submerged electric wires with a known resistance; by measuring the voltage potential across these wires, the water level can be determined.

Dividing the advance speed fluctuations obtained from Eq. (6.4) by the equilibrium advance speed of 1.73 m/s, one obtains the amplitude of the normalised advance speed fluctuations, or δv_{a}^*. Based on these estimated fluctuations, Figs. 6.19 and 6.20 compare linear simulations of speed and torque to HIL measurements in Bode diagrams. In the shown measurements, the numerical inertia correction is applied, so measured gains and phases should ideally coincide with those of the ideal scale model. Whereas this seems to be indeed the case for the gains, the simulated and measured phases seem somewhat different.

Closer inspection of Figs. 6.19 and 6.20 reveals that the phase errors are approximately the same for speed and torque, and increase with frequency. This indicates that the water level was probably not measured exactly at the point of propeller inflow: a rearward offset of the wave probe would cause wave peaks and thus, advance speed peaks to be measured slightly later than their moment of arrival at the propeller. This would in turn result in a phase error in positive direction. Indeed, all phase errors seem to correspond to a rearward offset of the wave probe of approximately 0.07 m, as Table 6.7 shows. At the same time, the image in Appendix C suggests that such an offset may indeed have been present during the described HIL experiments. In the course of days, the wave probe had to be remounted several times, likely resulting in an imprecise mounting on the day the measurements were taken.

The correspondence between simulations and measurements can be further verified by comparing operating ellipses of the simulated engine. Fig. 6.21 shows simulated and measured operating ellipses resulting from wave types Bft 4, Bft 5 mid and Bft

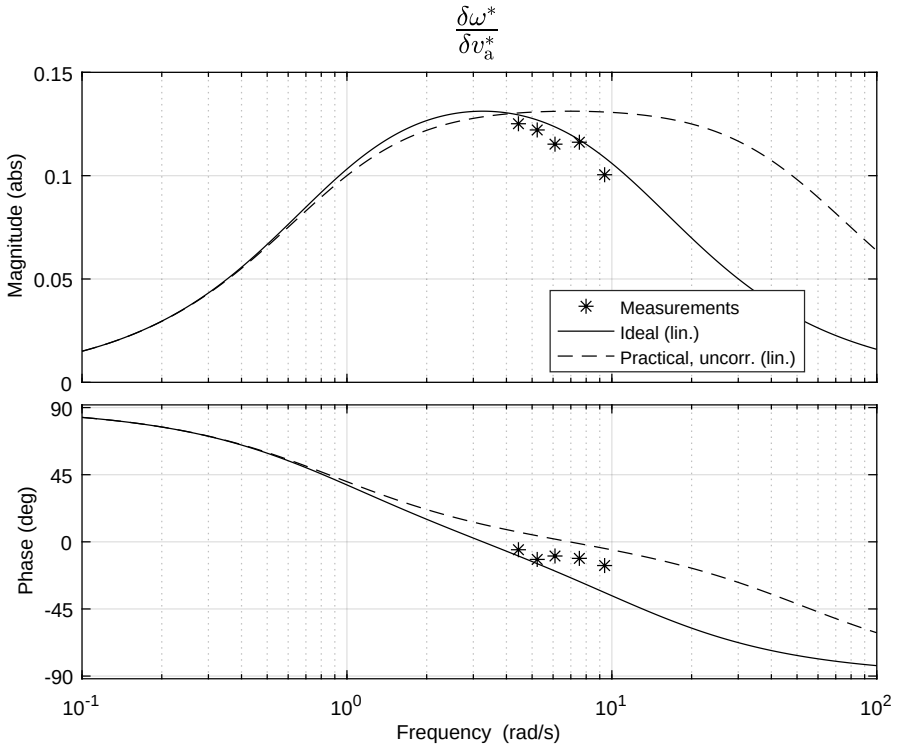


Figure 6.19: Linear simulations and HIL measurements of closed loop response of shaft speed on waves, with numerical inertia correction. The corresponding transfer function is given in Eq. (B.3). One can observe a frequency-dependent difference between simulated and measured phase. This difference is likely caused by an accidental rearward offset of the wave probe. This Figure is based on the data in *exp_234.mat*, *exp_235.mat*, *exp_236.mat*, *exp_237.mat* and *exp_238.mat*, stored in the measurement data repository (Huijgens, 2020).

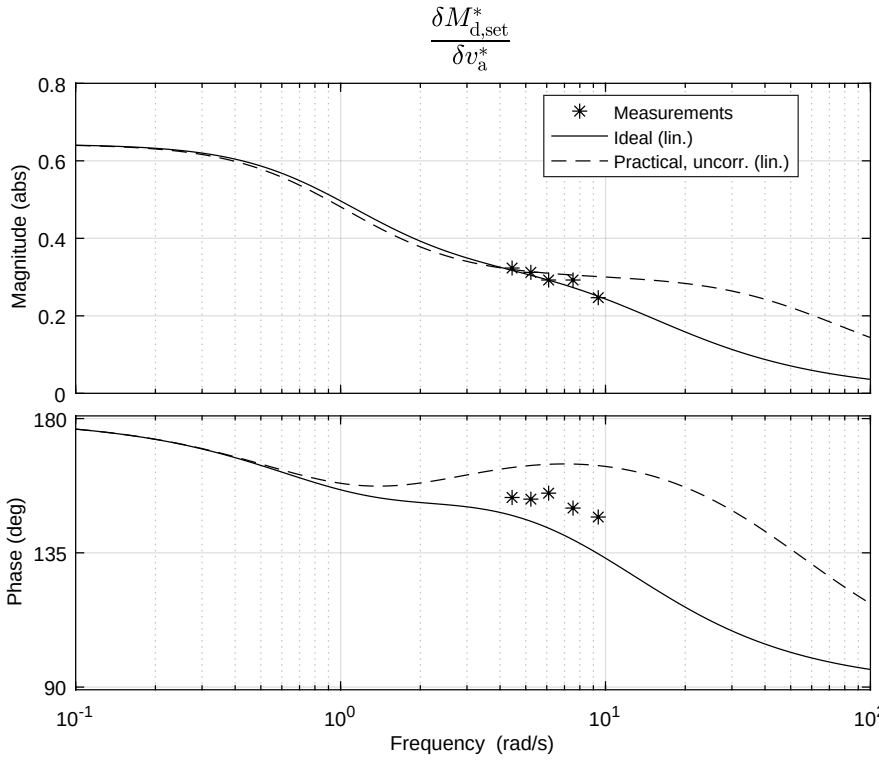


Figure 6.20: Linear simulations and HIL measurements of closed loop response of simulated engine torque on waves, with numerical inertia correction. The corresponding transfer function is given in Eq. (B.4). One can observe a frequency-dependent difference between simulated and measured phase. This difference is likely caused by an accidental rearward offset of the wave probe. This Figure is based on the data in *exp_234.mat, exp_235.mat, exp_236.mat, exp_237.mat* and *exp_238.mat*, stored in the measurement data repository (Huijgens, 2020).

6. Although this diagram is not subjected to a detailed, quantitative analysis, it does reaffirm that the HIL setup can indeed be used to accurately emulate the dynamic interaction between propeller and machinery in waves.

6.6 Conclusion

The aim in this Chapter was to validate the mathematical descriptions of shaft speed, and to subsequently validate the numerical inertia correction based on these mathematical descriptions. First, however, attention was paid to the full scale and model scale environments in Section 6.3, and how these environments define the relevant frequency. For the analyses in this Chapter, an ocean with fully developed wind waves was considered as described by the Pierson-Moskowitz wave spectrum. By explaining how the energy present in the waves is related to the encounter frequency, it was shown how the decay of the energy present in the waves sets an upper limit to the relevant frequency range.

Following the introduction of the model scale environment, the mathematical descriptions and numerical inertia correction were validated. Regarding the validation of the mathematical descriptions in Section 6.4, two conclusions were drawn. First, the electric loop responds considerably slower than expected. At the same time, the mathematical description is in line with literature. Thus, the electric loop likely contains or depends on an unidentified dynamic system with one or more relatively large time constants. As another possibility, the current control loop in the motor drive may contain unidentified discrete effects. Further investigation of the response of the electric loop and surrounding equipment and supply rails could shed more light on this phenomenon. Second, it can be concluded that the measured and simulated response of the uncorrected scale model correspond well, despite the unexpected response of the electric loop. This allows to conclude that the mathematical description of the shaft speed loop is an valid representation of physical reality.

Knowing that the practical and ideal shaft speed loops can be simulated accurately, the numerical inertia correction was validated by comparing measurements with inertia correction to simulations of the ideal scale model. From the analysis in Section 6.5, one can conclude that the dynamic response of shaft speed and torque indeed corresponds to the ideal scale model. This conclusion holds for response on varying speed setting as well as for response on waves.

In summary, the HIL open water setup can accurately emulate the dynamic behaviour of the considered ship propulsion system. Furthermore, it can be concluded that the mathematical descriptions, analyses and solutions in Chapters 2 through 5 provide accurate and practically applicable guidelines for such HIL experiments with ship propulsion systems.

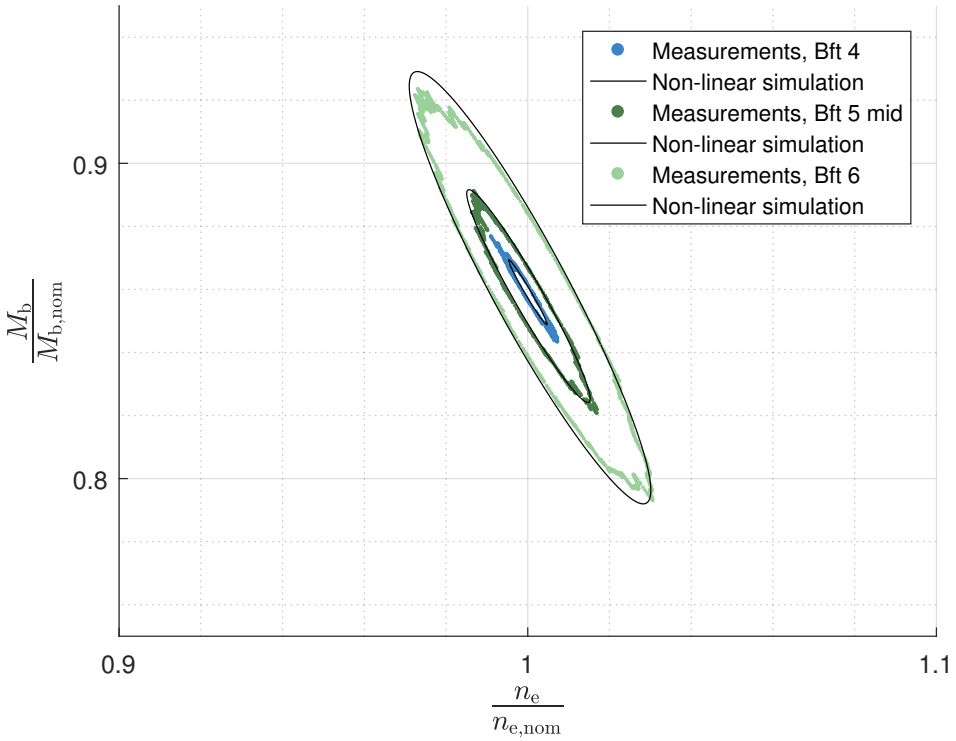


Figure 6.21: Normalised engine torque and speed during HIL experiments with numerical inertia correction and non-linear simulations of the ideal scale model. Operating ellipses are shown for wave types Bft 4, Bft 5 mid and Bft 6. The equilibrium values of the simulated ellipses are increased by approximately 4% in order to coincide with the measured equilibrium points. This Figure is based on the data in *exp_234.mat, exp_235.mat* and *exp_236.mat*, stored in the measurement data repository (Huijgens, 2020).

Chapter 7

Case Study: Propeller Ventilation

The analysis in Chapter 6 assumed relatively simple environments. Experiments were conducted in calm water and regular waves, mostly avoiding complex hydrodynamic phenomena. Although this facilitated the validation of hypotheses formulated in this dissertation, the added value of the HIL open water experiment can be better illustrated in a more complex case. Pinpointing the added value of HIL experiments compared to traditional experiments allows to answer the first research sub question, which was formulated as follows:

– What is the added value of HIL when evaluating ship propulsion systems?

Examples of complex cases are experiments on the interaction between waves and more advanced simulation models for propulsion machinery, or experiments in which the propeller pitch is varied in real time. Other interesting examples are experiments with propeller ventilation, investigating the response of the propulsion machinery on the sudden changes in propeller load associated with ventilation events. Considering the recent research in this area by MARIN, propeller ventilation is selected to demonstrate the added value of HIL here. This Chapter contains experiments on the interaction between a ventilating propeller and the propulsion machinery introduced in Chapter 2.

As a detailed study on propeller ventilation falls outside the scope of this dissertation, the aspects of hydrodynamics and multiphase flow behind ventilation receive only limited attention here. Instead, Section 7.1 contains a visual comparison of propeller thrust during traditional and HIL open water experiments. Although this comparison does not uncover and explain the mechanisms behind the dynamic behaviour of propeller torque and thrust, it does demonstrate the added value of HIL.

Elaborating on this in an independent but linked experiment, Section 7.2 contains a comparison of shaft dynamics with and without inertia correction, pinpointing the added value of the corrections proposed in this dissertation. Specifically, it is shown that the dynamic performance of the propeller is not necessarily a measure for the dynamic load of the propulsion machinery, and that inertia plays an important role in this respect.

Table 7.1: Conditions during the HIL experiments with propeller ventilation described in Sections 7.1 and 7.2. These conditions are similar to the experiments described in Table 6.1, with the main differences being a considerably smaller propeller immersion depth h and a smaller carriage speed. As a result, the propeller pierces the surface in wave troughs. Note that equilibrium values are applicable for calm water conditions.

	Symbol	Unit	Measured
Eq. propeller torque	$M_{\text{prop,hydro,0}}$	[Nm]	4.7
Eq. propeller thrust	$T_{\text{prop,0}}$	[N]	102.4
Eq. propeller speed	$n_{\text{s,0}}$	[rpm]	605
Propeller advance speed	v_{a}	[m/s]	1.37
Propeller immersion	h	[m]	0.218
Wave peak frequency	ω_{p}	[rad/s]	3.3
Wave encounter frequency	ω_{E}	[rad/s]	5.2

7.1 HIL Experiments on Propeller Ventilation

Propeller ventilation has been the subject of hydrodynamic research for decades. Yet, as it constitutes a highly complex phenomenon, there are no definitive models describing its effect on dynamic propeller performance. As is the case with other hydrodynamic phenomena, early efforts based on first principles and experiments in the model basin have been supplemented by approaches based on CFD and other numerical methods in the course of decades. For example, Swales et al. (1974) investigated the ventilation of hydrofoils, describing the mechanisms governing ventilation around lift-generating bodies. In a more quantitative approach, Wang et al. (1989) approximated thrust of ventilating propellers based on regression of open water measurements. More recent research efforts on this topic were reported by, among others, Koushan (2007), Califano (2010) and Kozlowska et al. (2020).

Most research on propeller ventilation concentrated on the hydrodynamic aspects, neglecting dynamic interaction with the propulsion system as it is present in full scale reality. At the same time, simulations and measurements in this dissertation suggest that this interaction potentially plays an important role for dynamic phenomena such as ventilation events. To further investigate the relevance of the propulsion system, experiments with propeller ventilation and an emulated diesel-mechanical propulsion system are conducted. Although a quantitative analysis is not made here, these measurements allow to draw conclusions regarding the added value of HIL for ventilation experiments.

A first series of experiments with propeller ventilation is conducted with and without emulated diesel-mechanical propulsion system. During these experiments, the propeller is moved through a wave train, and the propeller immersion is limited such that the propeller pierces the surface in the troughs of the largest waves. The wave height is varied to allow thrust to break down and recover over a prolonged period of time. Conditions during these experiments are given in Table 7.1.

Fig. 7.1 shows propeller thrust measured under such conditions with and without the emulated ship propulsion system. The propeller hub immersion is set to 0.218 m,

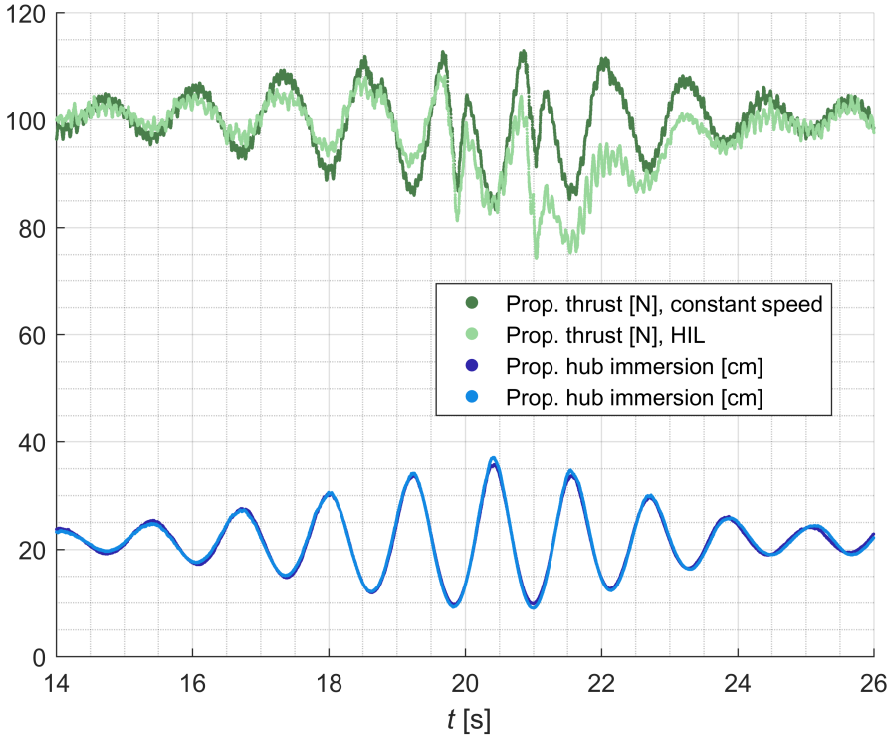


Figure 7.1: Time trace of measured propeller thrust, with constant propeller speed (*constant speed*) and with the emulated diesel-mechanical propulsion system as introduced in Chapter 2 (*HIL*). Measured thrust is filtered by a low-pass filter with a time constant of 0.0159 s. The conditions during these experiments are given in Table 7.1. This Figure is based on the data in *exp_251.mat* (constant speed) and *exp_250.mat* (HIL), stored in the measurement data repository (Huijgens, 2020).

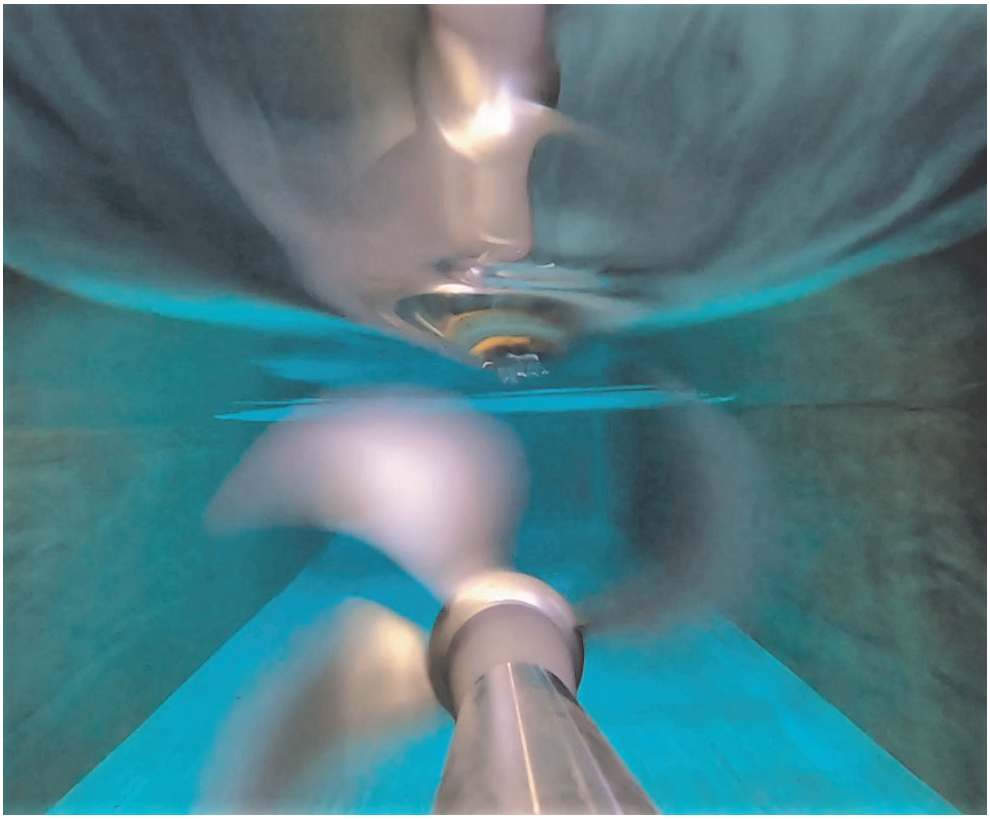


Figure 7.2: Looking forward from behind the propeller, shortly before ventilation inception. The image was taken during experiments under the same conditions as in Fig. 7.1. As can be seen, the free surface is locally deformed prior to ventilation events; ventilation vortices were not observed.

compared to 0.418 m in Chapter 6, triggering propeller ventilation in wave troughs. The 12 second trace can be roughly divided into three phases. In the first phase, wave heights are too small to cause ventilation. 0:18.5 marks the approximate beginning of the second phase, in which the propeller starts drawing air. As Fig. 7.2 shows, no vortices occur, while the free surface above the propeller clearly deforms prior to ventilation events. This type of ventilation is referred to as condition III by Kozlowska et al. (2009), and occurs only in case of limited propeller submergence. After the first ventilation inception, some air remains entrained between the propeller blades for the duration of the second phase; in other words, the propeller does not completely recover from ventilation in between wave troughs until the third phase. In the third phase, which starts from approximately 0:23, wave heights have decreased again and entrained air has mostly disappeared.

Experiments at constant propeller speed and HIL experiments both show considerable effects of ventilation on propeller thrust. Between 0:18.5 and 0:23, every wave trough triggers propeller ventilation, resulting in an immediate thrust breakdown in

both cases. However, the subsequent thrust recovery is considerably different. The amplitude of thrust fluctuations is considerably larger in the case with HIL emulation. In addition, whereas thrust seems to largely recover after each wave in the experiment with constant speed, the HIL experiment shows a more complex, time dependent loss of thrust. With HIL, thrust recovery takes multiple seconds (at model scale), with a minimum thrust approximately 10% lower than during constant speed experiments.

This allows to conclude that propulsion plant dynamics indeed have a profound impact on thrust loss during ventilation events and thus, in rough seas. This was noted before, as some past research on ventilation did take into account certain aspects of propulsion system dynamics. For example, Smogeli (2006) investigated ventilation while also considering, to some extent, dynamic properties of the propulsion drive and control system. Noting scale effects on moment of inertia, Smogeli (2006) also considered an inertia correction. However, no such correction was eventually applied, as it was concluded that the influence of inertia on torque and thrust response is negligible. This is an interesting observation as it seems to contradict simulations and measurements in this dissertation. As such, this case presents a good occasion to pinpoint the added value of the corrections proposed in this dissertation. In Section 7.2, the influence of the inertia correction on the emulated dynamics is investigated in particular in a second series of HIL experiments with propeller ventilation.

7.2 Added Value of the Inertia Correction

To demonstrate the added value of the proposed corrections for HIL open water tests, experiments are conducted in the conditions given by Table 7.1 with and without inertia correction. The measurements shown in Fig. 7.3 indicate that in such an environment, the influence of moment of inertia on propeller torque and thrust is negligible: the propeller torque and thrust traces of the corrected and uncorrected case largely overlap. This seems to confirm the observations by Smogeli (2006).

Interestingly, however, this is not the case for engine speed and engine torque, as is shown in Fig. 7.4. During each ventilation event, shaft speed and thus, engine speed rapidly increases as the load collapses. At this point, the difference in moment of inertia becomes apparent. As can be seen in Fig. 7.4, shaft response is more sluggish if the inertia correction is applied – note that the correction implies a virtual increase of moment of inertia in this case. Upon measuring the increasing shaft speed error, the shaft speed governor reduces the fuel rack setting and thus, engine torque. As such, the sluggish response of shaft speed propagates to the response of simulated engine torque. Interestingly, however, this sluggishness does not have a significant effect on propeller torque and thrust. The exact mechanisms behind this different behaviour is a topic for future research. However, one can expect that the differences between prime mover dynamics and dynamic propeller performance are related to the reduced hydrodynamic load on the propeller during ventilation events.

Figs. 7.3 and 7.4 show that the engine responds entirely different on its environment than does the propeller. The response of propeller torque and thrust appears to be mostly independent of shaft speed and therefore, parameters such as moment of inertia. The response of the propulsion machinery, on the other hand, is considerably affected by distorted inertia. In the case shown in Fig. 7.4, peaks in engine torque are approximately 30% smaller if the inertia correction is applied, while speed peaks

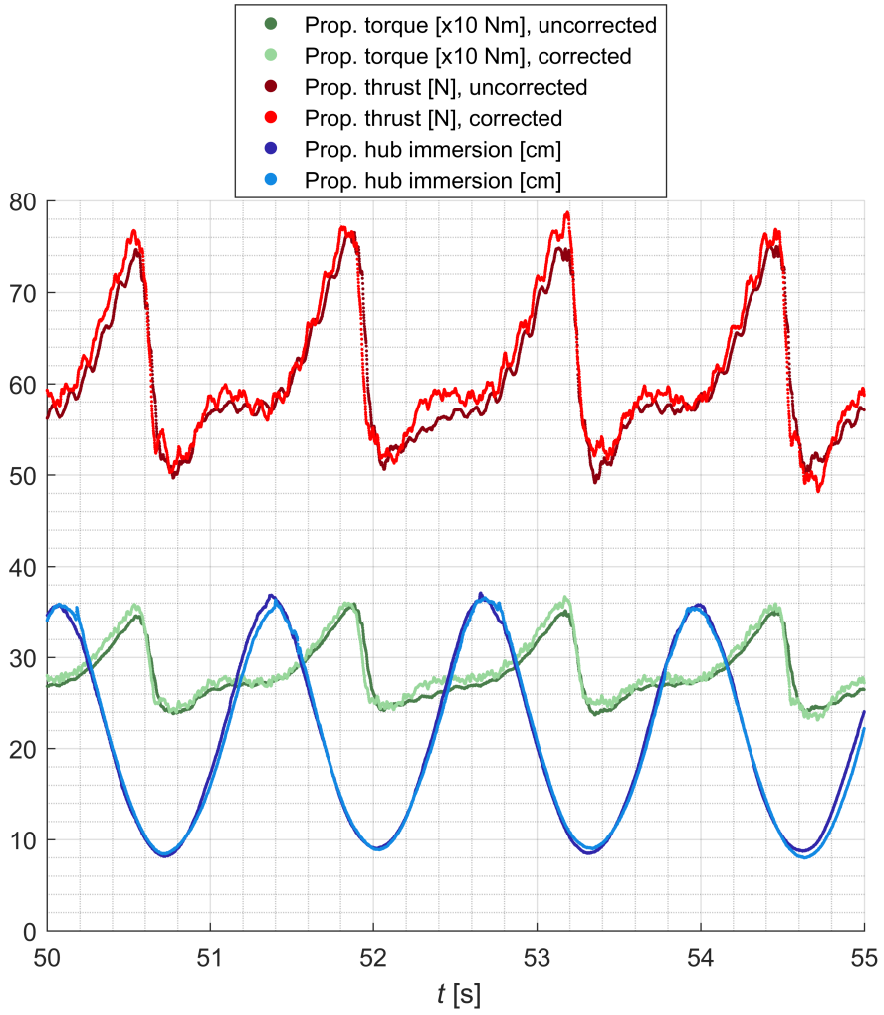


Figure 7.3: Time trace of measured propeller torque and thrust during HIL experiments with an emulated diesel-mechanical propulsion system, with and without numerical inertia correction. Measured torque and thrust are filtered by a low-pass filter with a time constant of 0.0159 s. The equilibrium immersion depth of the propeller hub equals 0.218 m. In this case, the influence of moment of inertia on propeller torque and thrust is negligible. The conditions during these experiments are given in Table 7.1. This Figure is based on the data in *exp_245.mat* (without inertia correction) and *exp_242.mat* (with inertia correction), stored in the measurement data repository (Huijgens, 2020).

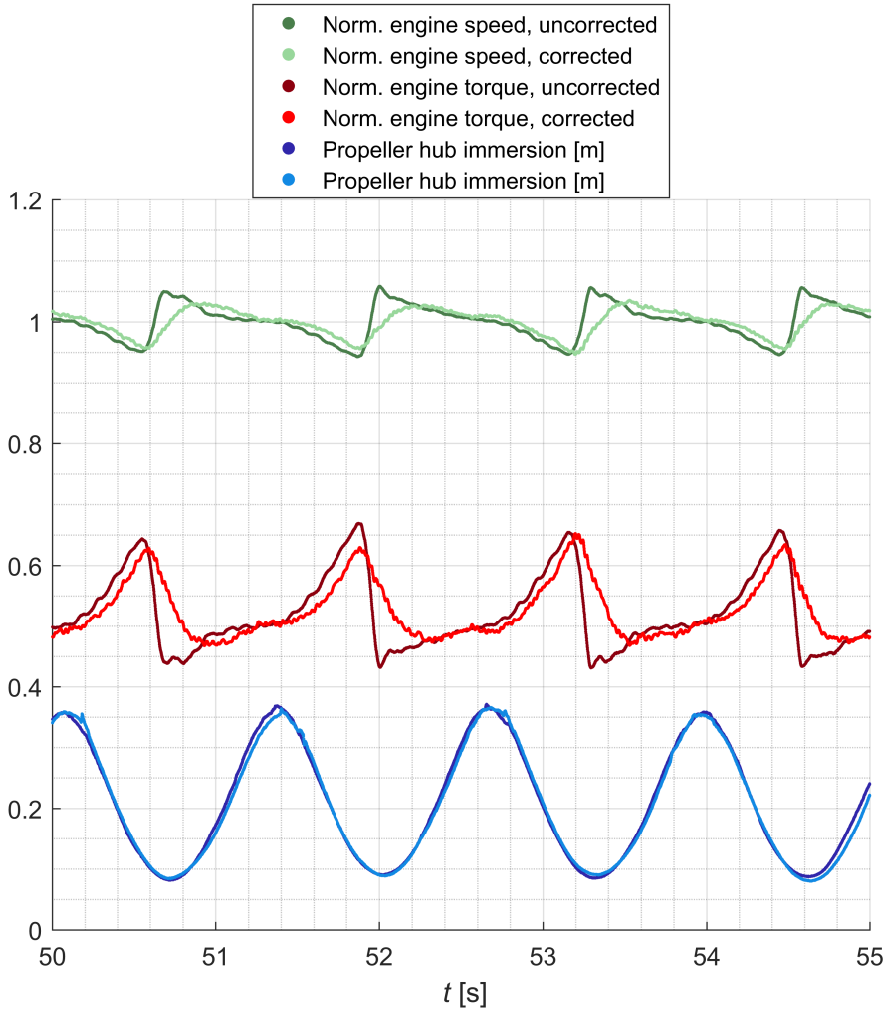


Figure 7.4: Time trace of engine torque and speed with an emulated diesel-mechanical propulsion system, with and without numerical inertia correction. Torque and speed are normalised with respect to their nominal values. The equilibrium immersion depth of the propeller hub equals 0.218 m. Contrary to propeller torque and thrust, the response of engine torque and speed on ventilation is considerably influenced by the moment of inertia. This Figure is based on the data in *exp_245.mat* (without inertia correction) and *exp_242.mat* (with inertia correction), stored in the measurement data repository (Huijgens, 2020).

are approximately 20% smaller. Moreover, the behaviour between peaks is entirely different. Considering this, failing to correct for the moment of inertia likely results in incorrect estimation of dynamic loads on the propulsion machinery and thus, the performance and wear of such machinery at full scale. This in turn may lead to overpowered or, worse, dangerously underpowered ships.

This Section allows to conclude that the performance of the propeller in complex, dynamic environments can be analysed in HIL experiments without the proposed friction and inertia correction. Although this interaction was not systematically investigated here, for instance by varying the frequency of disturbances, this observation is in line with past research. On the other hand, the interaction between the moment of inertia and the dynamic behaviour of the propulsion machinery is more complicated. When evaluating the dynamic load and thus, wear and tear of machinery, the corrections introduced in this dissertation must be applied in order to obtain accurate predictions.

7.3 Conclusion

Section 7.1 demonstrated the added value of hardware in the loop in open water experiments by comparing HIL open water experiments with a ventilating propeller to similar measurements with a traditional open water experiment. These measurements showed that breakdown and recovery of propeller torque and thrust occur considerably different if the propulsion machinery is emulated. During the HIL experiment, thrust drops to a level 10% lower than during the experiment at constant speed. In addition, propeller torque and thrust take longer to recover from ventilation events in the HIL experiment. This difference likely also depends on variables such as the wave encounter frequency and properties of the emulated propulsion system. If these are changed, the difference in predicted thrust loss may become smaller or larger; this dependency was not investigated in detail here.

Following this, Section 7.2 investigated the effect of inertia and, more specifically, the effect of the inertia correction on shaft dynamics during propeller ventilation events. Interestingly, the inertia of the emulated propulsion system does not seem to be relevant for the dynamic behaviour of propeller torque and thrust. It must be noted that the influence of governor settings and other properties of the propulsion system on propeller performance were not investigated; these may still have an important influence. In any case, the moment of inertia did have a profound impact on shaft speed and load of the simulated diesel engine. The mechanisms behind the different behaviour of propeller and machinery were not investigated here and are subject for future research. Yet, it can be concluded that when investigating the dynamic load of the propulsion machinery, moment of inertia and likely, other properties of the propulsion system are highly relevant. Thus, to investigate these dynamics in open water experiments, a HIL setup with the corrections proposed in this dissertation is required.

Chapter 8

Conclusions and Recommendations

The first Chapter in this dissertation introduced the potential of hardware in the loop to emulate the complex interaction between ship propulsion systems and dynamic environments such as rough seas. At the same time, it was recognised that HIL experiments in the model basin are subject to scale effects. These scale effects could distort the emulated dynamic behaviour to an extent that HIL experiments do not correspond to full scale reality. As the starting point for a detailed exploration of the potential and limitations of HIL in the model basin, the following research question was formulated:

To what extent can hardware in the loop techniques be used to emulate ship propulsion system dynamics at model scale?

This question encompasses too many aspects to be answered at once. Therefore, five sub questions were formulated; these questions will be recapitulated and answered in Section 8.1. The chronology of these sub questions was not maintained throughout the dissertation. Yet, as sub questions may follow from previous sub questions, this chronology is adhered to when formulating conclusions.

In addition to answering the research sub questions, the simulations and measurements in this dissertation yielded numerous other insights relevant for HIL experiments in the model basin. Based on these additional insights, conclusions are drawn in Section 8.2. Following these conclusions, recommendations are formulated in Section 8.3 regarding future HIL experiments in the model basin and regarding future research in general.

8.1 Answers to Research Questions

The main research question was broken down into five sub questions. The first sub question was formulated as follows:

1. What is the added value of HIL when evaluating ship propulsion systems?

This question is far easier to ask than to answer. In fact, a complete answer to this question requires detailed analysis and comparison of traditional and HIL experiments. As a result, this question could be answered only in Chapter 7, in which open water experiments with propeller ventilation were analysed. To demonstrate the added value of HIL, the experiments in the same environment were conducted with and without emulated ship propulsion system. In Fig. 7.1, propeller thrust was compared, showing a considerably greater thrust breakdown due to propeller ventilation if HIL is applied. During the HIL experiment, the minimum thrust was approximately 10% lower than during the experiment with constant propeller speed, while it took longer for thrust to recover from ventilation events. As such, it could be demonstrated that HIL has a clear added value when predicting dynamic propeller performance and machinery load in complex, dynamic environments.

Elaborating on experiments with propeller ventilation, Section 7.2 demonstrated the added value of the numerical inertia correction. The moment of inertia of the propulsion system seemed not to be relevant for the dynamic torque and thrust of the propeller in ventilating conditions, as was also concluded by Smogeli (2006). For shaft dynamics and machinery load, however, the moment of inertia does play an important role. As could be seen in Fig. 7.4, peaks in simulated engine brake torque decreased by approximately 30%, while peaks in shaft speed decreased by approximately 20% if a correction for moment of inertia is applied. In addition, the dynamic behaviour of engine torque and speed around their respective peak values was entirely different. This demonstrated that the proposed numerical inertia correction is crucial for correct emulation of propulsion system dynamics from propeller to prime mover. It is expected that application of HIL in other experiments, such as with more advanced machinery simulations or in different environments, would further demonstrate the added value of the proposed corrections for scale effects. This expectation forms the basis of one of the recommendations in Section 8.3.

This first research sub question was of a rather abstract nature. The second sub question was more concrete:

2. Which components are present in the scale model's propulsion system?

The answer to this question was given in Chapter 2, in which the components of the ideal scale model – the full scale propulsion system, downsized without any scale effects – and the components of the practical scale model – the HIL setup – are identified. The third sub question elaborated on the second question:

3. What are the dynamic properties of these components?

The analysis in Chapter 2 provided an answer to this question, too. In addition to listing the components of the ideal and practical scale models, Chapter 2 introduced mathematical descriptions of the static and dynamic behaviour of these components. The mathematical descriptions of individual components were then combined to obtain descriptions of the complete ideal and practical scale models. In the final Sections of Chapter 2, these mathematical descriptions were used to demonstrate distortions

of shaft dynamics by scale effects acting on different components and subsystems. The electric motor drive and moment of inertia of the propulsion system were identified as the most important potential sources of distortions of shaft dynamics. These observations give rise to the next sub question:

4. Which measures can be taken to avoid distortion of shaft dynamics by these components?

Solutions to the expected dynamic distortions were formulated in Chapters 3 through 5. First, distortions by the electric drive of the HIL setup were investigated in detail in Chapter 3. The mathematical descriptions derived in Chapter 2 were used to derive minimum controller settings in order to avoid distortions by the electric drive during HIL open water experiments. Next, dynamic distortions by scale effects on moment of inertia were analysed in Chapter 4, and a numerical correction for incorrect inertia was introduced. Finally, a compensation for friction torque was introduced in Chapter 5. With this, all anticipated distortions were addressed in theory. As a next step, this theory was to be put in practice as was implied by the fifth sub question.

5. How can these measures be applied in dynamic open water experiments?

In addition to introducing a compensation for friction torque, Chapter 5 described the HIL setup used for the experiments reported in this dissertation, as well as the practical preparations necessary to conduct these experiments. Following this, it was demonstrated in Chapter 6 that the mathematical descriptions derived in Chapter 2 are indeed valid representations of physical reality. Moreover, it was shown that the proposed corrections perform as predicted, and that the described HIL open water setup can accurately emulate shaft dynamics of ship propulsion systems.

Based on the answers to these sub questions, the main research question, which was recapitulated early on in this Chapter, can be answered. In essence, this answer forms a condensed conclusion of this dissertation.

By combining a state-of-the-art open water setup, a towing tank, a commercially available simulation computer and the correction algorithms introduced in this dissertation, hardware in the loop techniques allow to accurately emulate the interaction between ship propulsion systems and realistic, dynamic environments as they occur at sea, up to a frequency at which this interaction becomes negligible for the test case considered in this dissertation. For other test cases in which disturbances with higher frequencies may be relevant, the frequency limit for accurate emulation is set by the dynamic response of the electric propulsion drive and the performance of the inertia correction. The latter in turn depends on the properties of the shaft speed encoder and the simulation computer.

As was indicated earlier, the measurements and simulations in this dissertation provided more insights than those formulated in the answers in this Section. These additional insights are summarised in Section 8.2.

8.2 Additional Conclusions

8.2.1 Validity of the Mathematical Descriptions

The first additional conclusions and remarks pertain to the accuracy of the mathematical models introduced in Chapter 2. Although it was concluded in Chapter 6 that these descriptions were valid in general, there were conspicuous differences between simulations and HIL measurements in some cases. Most notably, the response of the electric loop was not as expected, as became apparent in Section 6.4.1. During measurements, current responded much slower on a change in current set point than simulations predicted. Since the mathematical description of the electric loop is in line with past literature, it was concluded that the cause for this unexpected dynamic response is likely located inside the motor drive or the supply rail. This observation shows that, contrary to what is often assumed, the electrodynamics inside the motor drive may not always be negligible.

As the available time for experiments in the towing tank was limited, the unexpected current response could not be investigated in full detail. However, measurements of shaft dynamics indicated that the slow response of current did not render the envisioned HIL experiments impossible. In Section 6.4.2, it was shown that distortions of shaft dynamics by current response were limited in the relevant frequency range, and that the response of the uncorrected shaft speed loop corresponded well with simulations. However, even when accounting for the distortions by current response, minor differences between simulations and measurements still remained. Fig. 6.8 showed the open loop response of shaft speed on drive torque, indicating a difference of several degrees between simulations and measurements on top of the phase error introduced by the slow current response. This difference may have been the result of an inaccurate estimation of entrained moment of inertia I_{H2O}. As of yet, no definitive estimation methods for this inertia component exist, and the prediction model by Burrill and Robson (1962) used here may have resulted in an underestimated added inertia.

However, for the closed loop response of shaft speed on speed setting, most of these errors vanished. If a speed control loop is introduced, the dynamics introduced by the PI feedback controller become dominant, overshadowing the errors introduced by the electric drive and added inertia. Thus, even with these unexpected distortions, the HIL open water experiments with closed shaft speed loop still meet the requirements outlined in Section 2.6.3.

8.2.2 Performance of the Proposed Solutions for Dynamic Distortions

In Chapter 2, three important causes for distortions of shaft dynamics were identified: the dynamic behaviour of the electric drive, scale effects on moment of inertia and scale effects on friction torque. These issues were addressed in Chapters 3 through 5, resulting in tuning guidance for the motor drive and realtime corrections for shaft friction and moment of inertia. The practical application of the friction torque correction received attention in Chapter 5, while the performance of the inertia correction was evaluated in Chapter 6. In both cases, it could be concluded that the corrections are sufficiently accurate in practice.

However, the tuning guidance derived in Chapter 3 could not be validated. As was indicated in Section 8.2.1, the measured response of motor current was considerably slower than predicted by the mathematical descriptions. As these descriptions also served as the basis for the tuning guidance, this guidance could not be validated with measurements. Still, this guidance is considered as valid, as the mathematical descriptions it is based on are in line with past literature.

8.2.3 Scalability of the HIL Propulsion Drive

In Section 4.4.3, it was shown that the numerical inertia correction is accurate up to a frequency of 13 rad/s, assuming the parameters of the considered HIL setup. This is sufficient for accurate emulation of the interaction between engine, propeller and the considered model scale environment, as was shown in Section 6.3. However, for experiments at smaller time scales – which means that the scale factor for time is larger –, this frequency limit could become an issue.

Free sailing model experiments, for example, are often equipped with relatively small propellers. If Froude scaling is maintained, this means that the scale factor for time increases. Ideally, the loop frequency should be increased proportionally with the time scale in order to maintain accuracy; in practice, this may not be possible for the reasons explained in this dissertation. Even greater challenges may arise when applying HIL during experiments in the cavitation tunnel. Such experiments are generally conducted at small geometric scales and high Reynolds numbers, implying scale factors for time several times larger than during the HIL experiments in this dissertation.

Yet, this does not necessarily mean the application of HIL is infeasible for free sailing model experiments, or even for cavitation tests. This can be illustrated by recapitulating the mechanisms behind the frequency limit of the HIL experiments described in this dissertation. The limit of 13 rad/s is largely due to the low setting of filter update weight a_0, which is set at 0.01. This means that each update of measured speed only accounts for 1% of the filtered speed. There are two reasons for this heavy filtering: measurement noise in the shaft speed signal, and instability of the inertia correction algorithm caused by the slow response of the electric drive. Both the measurement noise and the instability of the correction algorithm can be likely be avoided by carefully checking and choosing components such as shaft speed encoders and electric drives.

The encoder used to measure shaft speed emits 7200 pulses per rotation. By plotting these pulses in a scope, it was found that the space between the pulses varies slightly. As a result, the shaft speed measurement signal contains a repetitive noise pattern. Especially when calculating the discrete derivative, this presents an issue, as numerical differentiation considerably magnifies the noise level. Here, noise was reduced to acceptable levels by IIR filtering. However, a more elegant solution would be to install an encoder with exactly evenly spaced pulses. This would result in a smoother shaft speed signal, requiring less filtering.

The instability of the correction algorithm, on the other hand, results from the combined dynamics of the electric drive and the numerical inertia correction. Both the electric drive and inertia correction introduce considerable phase delays already at frequencies below 30 rad/s. At the same time, the inertia correction amplifies

the physical acceleration torque. If this torque amplification exceeds 1 while the combined phase delay of the electric drive and inertia correction equals 180 degrees, the inertia correction loop becomes unstable. This instability can be avoided by reducing a_0; however, as was indicated before, this also reduces the frequency range of similarity. Alternatively, this instability could be solved on a more fundamental level by identifying and eliminating the cause of the unexpectedly slow current response and thus, phase delay introduced by the electric drive. Instability of the inertia correction algorithm would then occur at higher frequencies, allowing for a higher filter update weight and thus, a larger similarity range.

In conclusion, HIL experiments likely allow emulation of shaft dynamics at higher frequencies than demonstrated in this dissertation. By selecting an encoder with exactly evenly spaced pulses and by paying close attention to the response of the electric loop, the required degree of shaft speed signal filtering can likely be reduced considerably. As such, the proposed HIL techniques can likely also be applied during experiments at considerably smaller time scales.

8.3 Recommendations

The conclusions in Sections 8.1 and 8.2 serve as a basis for the recommendations formulated in this final Section. The recommendations in Section 8.3.1 are related to the specific HIL setup used in this research project, while Section 8.3.2 contains general recommendations for future research.

8.3.1 Regarding the HIL Setup

In some respects, the experiments reported in Chapters 5 and 6 showed different results than simulations based on the mathematical descriptions given in Chapter 2. Measurements of equilibrium propeller torque were approximately four percent higher than simulations, while measurements on motor winding current showed considerably slower current response than simulations.

The higher equilibrium propeller torque was not entirely unexpected, as the simulations did not account for viscous scale effects. However, viscous scale effects were likely not the only reason for the relatively high measured torque. As was indicated in Chapter 5, the high measured torque may also be the result of small deformations of the torque and thrust sensor, although other causes could not be excluded. In any case, an increase in torque of this magnitude only has a negligible effect on emulated shaft dynamics, as was shown in Section 2.5.4. Still, a better understanding of the measured equilibrium conditions would add to the value of HIL open water experiments. A more detailed analysis of torque and thrust measurements by TU Delft's open water setup is therefore recommended.

Contrary to this limited increase in measured equilibrium torque, the slow response of motor winding current is highly relevant for dynamic open water experiments. Although measurements in Section 6.4.2 indicated that this slow response only has a marginal effect on closed loop shaft dynamics, the phase delay introduced by the electric loop ultimately means that heavy filtering is required to avoid unstable behaviour of the numerical inertia correction. By identifying the cause of the slow current response, the required degree of filtering could be reduced. This would in turn allow for

a larger frequency range in which shaft dynamics can be accurately emulated. Thus, a second recommendation is to conduct a detailed investigation into the dynamics of the electric drive and power supply with the aim of solving the issue of slow motor winding current response.

Another possible improvement of the HIL setup pertains to the shaft speed encoder. The pulse width of the currently installed encoder shows slight variations, resulting in a noisy shaft speed signal. This noise increases the required degree of filtering and as such reduces the maximum frequency at which HIL experiments can accurately emulate shaft dynamics. A third recommendation is thus to investigate the possibilities to install a shaft speed encoder with an exactly constant pulse width.

8.3.2 Further Research

A first recommendation for further research follows from the observations made in Chapter 7. It was found that the moment of inertia did not have a significant influence of the dynamic behaviour of propeller torque and thrust. However, there was a clear effect on shaft speed and engine load. A detailed analysis of this observation falls outside the scope of this dissertation and was thus not performed. It is recommended that this observation receives further attention in future research projects: a better understanding of the underlying physical mechanisms may improve insight into dynamic engine loads in ventilation events and other complex environments.

The above, rather concrete recommendation can be supplemented by more general recommendations regarding the application of HIL techniques in the model basin. By combining simulated dynamics with physical hydrodynamics, hardware in the loop techniques open up new directions of research in the model basin. First, HIL could be applied in the intersection of marine engineering and hydrodynamics, expanding the insight into the complex interaction between environment, propeller and machinery. As examples of this direction of research, the following applications can be thought of:

1. interaction between propulsion machinery and complex propeller loads due to ventilation events, cavitation, propeller-hull interaction, oblique propeller inflow and ship motions;

2. performance of novel propulsion technologies in realistic, dynamic environments and during load steps;

3. effect of advanced propulsion control strategies and estimators on propulsion system performance;

4. manoeuvring and course keeping capabilities using HIL experiments with free sailing models.

In the first two suggested research directions, HIL techniques could be used to increase insight into the performance of propulsion technologies using, for example, wind assistance and fuel cell technology. As such, HIL could accelerate the acceptance and application of such technologies in the maritime industry. As an example of the third proposed research direction, HIL could be used to demonstrate adaptive propeller pitch control based on measured incoming waves, with the aim of avoiding

peaks in propeller and machinery load. Recently, the marine engineering section at the TU Delft developed a controllable pitch propeller of which the blade pitch can be changed in realtime. Thus, the TU Delft possesses the tools to demonstrate such advanced control strategies already on the relatively short term. As an example of the fourth direction, HIL could be introduced in free sailing ship models, allowing to assess the performance of the ship from hull to prime mover during, for example, manoeuvring. It must be noted that during free sailing model experiments, forces acting on the scale model hull are subject to viscous scale effects. In order to obtain correctly scaled static and dynamic behaviour also when introducing a model scale hull, these scale effects require detailed attention. The research project initiated by Tanizawa et al. (2013a) may serve as an inspiration in this respect.

HIL could also be used for research in fundamental hydrodynamics. Using the dynamic capabilities of the HIL setup, phenomena such as entrained inertia could be systematically analysed. However, rather than to provide an exhaustive list of the possible future applications of HIL in the model basin, a conclusive recommendation is formulated:

Introducing hardware in the loop into traditional experiments in the ship model basin adds a new layer of information to such experiments. At the same time, HIL requires a relatively limited additional investment. Considering the increasing need for new technologies in the maritime industry and the uncertainties regarding the performance of these technologies in complex, dynamic environments, HIL can likely accelerate the development and uptake of these technologies within the maritime industry. It is therefore recommended to apply HIL in all future model basin experiments with dynamic environments.

Appendix A

Linearised Response of Ideal and Practical Scale Models

In Chapter 2, attention was paid to dynamic distortions of shaft speed response $\delta\omega^*/\delta\omega^*_{\text{set}}$. It was stated that in essence, the gain and phase of $\delta\omega^*/\delta\omega^*_{\text{set}}$ must be the same for the ideal and the practical scale model in the relevant frequency range. However, in addition to $\delta\omega^*$ and $\delta\omega^*_{\text{set}}$, Figs. 2.7 and 2.8 show other signals that are relevant when evaluating the behaviour of ship and machinery. On the input side, advance speed δv^*_{a} also causes response, while drive torque $\delta M^*_{\text{d,set}}$ is an important indicator of engine load. Note that in the HIL setup, the simulated drive torque is represented by $\delta M^*_{\text{d,set}}$ rather than δM^*_{d}. $\delta M^*_{\text{d,set}}$ is simulated and recorded inside the simulation computer, while δM^*_{d} cannot be directly measured and recorded. In order to demonstrate that the response of $\delta\omega^*/\delta\omega^*_{\text{set}}$ provides full insight into dynamic similarity of the HIL setup, it is verified that the transfer functions corresponding to all inputs and outputs are indeed similar, and that the influence of scale effects on the corresponding Bode diagrams is the same.

Eqs. A.1 through A.4 give transfer functions of the four combinations of shaft speed $\delta\omega^*$, simulated drive torque $\delta M^*_{\text{d,set}}$, set speed $\delta\omega^*_{\text{set}}$ and advance speed δv^*_{a}. Functions C_ω, C_{i}, S^*_1, S^*_2, Q^*_{u} and Q^*_ω are written out in Sections 2.3.1 and 2.3.2. Parameters for simulations in this Appendix were given in Tables 2.5 and 2.6. Transfer functions are given for the ideal and practical scale model.

The gain and phase of these transfer functions is determined by the locations of poles and zeros, which are the values of s for which the denominators and numerators are zero, respectively. Scale effects on shaft dynamics cause these poles and zeros to move, thus distorting gain and phase. One can see that the denominators of all four ideal transfer functions are exactly the same, while the numerators are varying combinations of the same terms. The same applies for the practical transfer functions. This indicates that, while these transfer functions are not entirely the same, they do have the same frequency-dependencies, and scale effects will cause similar distortions for all responses. To illustrate this, the Bode diagrams of these transfer functions are compared in Figs. A.1 through A.4.

For each response, three cases are shown: the response of the ideal scale model and the response of two practical scale model with the same parameters and an ad-

ditional, electric propulsion system, with varying current controller settings. Apart from the additional electric drive, the practical scale models have the same composition, parameters and equilibrium values as the ideal scale model. One of the practical scale models has current controller settings as recommended in Chapter 3. The other practical scale model has $K^*_{\mathrm{p,i}}$ and $K^*_{\mathrm{i,i}}$ both set to 0.1; in Chapter 2, it was shown that these settings introduce considerable dynamic distortions of shaft dynamics. These cases allow to compare trends in dynamic distortions due to improper current controller tuning. Similar analyses were conducted for scale effects on moment of inertia and equilibrium torque. These analyses resulted in the same conclusions, and are not included here for reasons of brevity.

Figs. A.1 through A.4 show that, if the current controller is tuned as recommended, dynamic distortions are negligible in the responsive frequency range for all transfer functions. Moreover, if $K^*_{\mathrm{p,i}}$ and $K^*_{\mathrm{i,i}}$ are set to 0.1, distortions of gain and phase in the responsive frequency range occur at the same frequencies. This indicates that $\delta\omega^*/\delta\omega^*_{\mathrm{set}}$ is indeed representative for the other transfer functions.

$$\left.\frac{\delta\omega^*(s)}{\delta\omega^*_{\mathrm{set}}(s)}\right|_{\mathrm{ideal}} = \frac{C_\omega(s)\cdot S^*_1(s)}{1+C_\omega(s)\cdot S^*_1(s)} \tag{A.1a}$$

$$\left.\frac{\delta\omega^*(s)}{\delta\omega^*_{\mathrm{set}}(s)}\right|_{\mathrm{practical}} = \frac{C_\omega(s)\cdot S^*_1(s)\cdot \frac{C_{\mathrm{i}}(s)\cdot Q^*_{\mathrm{u}}(s)}{1+C_{\mathrm{i}}(s)\cdot Q^*_{\mathrm{u}}(s)}}{1+\left(C_\omega(s)\cdot C_{\mathrm{i}}(s)\cdot Q^*_{\mathrm{u}}(s)-Q^*_\omega(s)\right)\cdot\frac{S^*_1(s)}{1+C_{\mathrm{i}}(s)\cdot Q^*_{\mathrm{u}}(s)}} \tag{A.1b}$$

$$\left.\frac{\delta M^*_{\mathrm{d,set}}(s)}{\delta\omega^*_{\mathrm{set}}(s)}\right|_{\mathrm{ideal}} = \frac{C_\omega(s)}{1+C_\omega(s)\cdot S^*_1(s)} \tag{A.2a}$$

$$\left.\frac{\delta M^*_{\mathrm{d,set}}(s)}{\delta\omega^*_{\mathrm{set}}(s)}\right|_{\mathrm{practical}} = \frac{C_\omega(s)\cdot\left(1-\frac{Q^*_\omega(s)\cdot S^*_1(s)}{1+C_{\mathrm{i}}(s)\cdot Q^*_{\mathrm{u}}(s)}\right)}{1+\left(C_\omega(s)\cdot C_{\mathrm{i}}(s)\cdot Q^*_{\mathrm{u}}(s)-Q^*_\omega(s)\right)\cdot\frac{S^*_1(s)}{1+C_{\mathrm{i}}(s)\cdot Q^*_{\mathrm{u}}(s)}} \tag{A.2b}$$

$$\left.\frac{\delta\omega^*(s)}{\delta v^*_{\mathrm{a}}(s)}\right|_{\mathrm{ideal}} = \frac{S^*_2(s)}{1+C_\omega(s)\cdot S^*_1(s)} \tag{A.3a}$$

$$\left.\frac{\delta\omega^*(s)}{\delta v^*_{\mathrm{a}}(s)}\right|_{\mathrm{practical}} = \frac{S^*_2(s)}{1+\left(C_\omega(s)\cdot C_{\mathrm{i}}(s)\cdot Q^*_{\mathrm{u}}(s)-Q^*_\omega(s)\right)\cdot\frac{S^*_1(s)}{1+C_{\mathrm{i}}(s)\cdot Q^*_{\mathrm{u}}(s)}} \tag{A.3b}$$

$$\left.\frac{\delta M^*_{\mathrm{d,set}}(s)}{\delta v^*_{\mathrm{a}}(s)}\right|_{\mathrm{ideal}} = \frac{-C_\omega(s)\cdot S^*_2(s)}{1+C_\omega(s)\cdot S^*_1(s)} \tag{A.4a}$$

$$\left.\frac{\delta M^*_{\mathrm{d,set}}(s)}{\delta v^*_{\mathrm{a}}(s)}\right|_{\mathrm{practical}} = \frac{-C_\omega(s)\cdot S^*_2(s)}{1+\left(C_\omega(s)\cdot C_{\mathrm{i}}(s)\cdot Q^*_{\mathrm{u}}(s)-Q^*_\omega(s)\right)\cdot\frac{S^*_1(s)}{1+C_{\mathrm{i}}(s)\cdot Q^*_{\mathrm{u}}(s)}} \tag{A.4b}$$

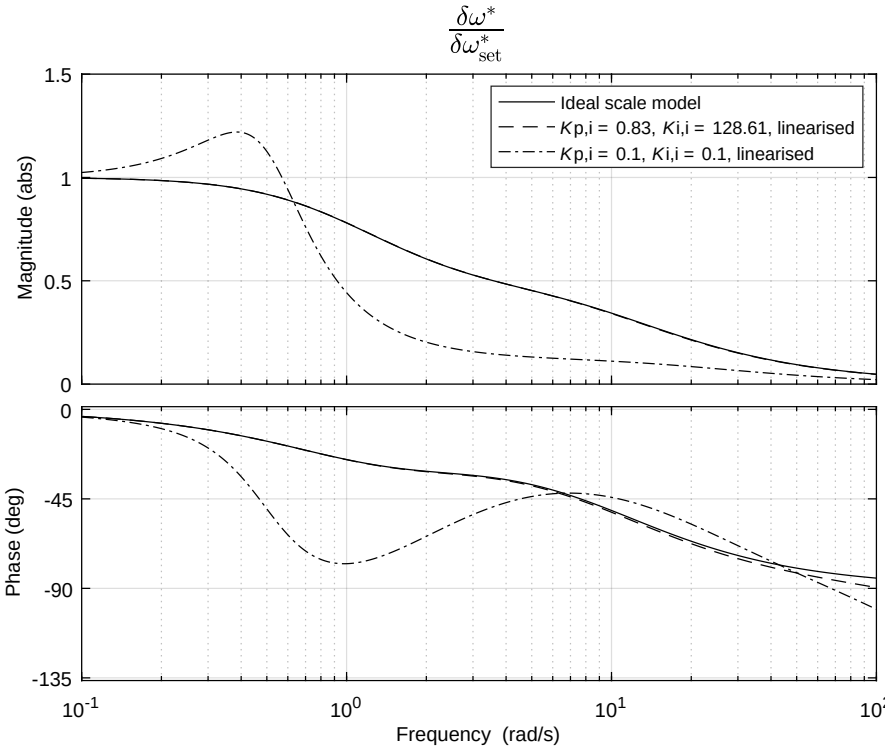


Figure A.1: Bode diagram of response of shaft speed $\delta\omega^*$ on set speed $\delta\omega^*_{\text{set}}$. Response is shown of the ideal scale model and practical scale models with varying current controller settings.

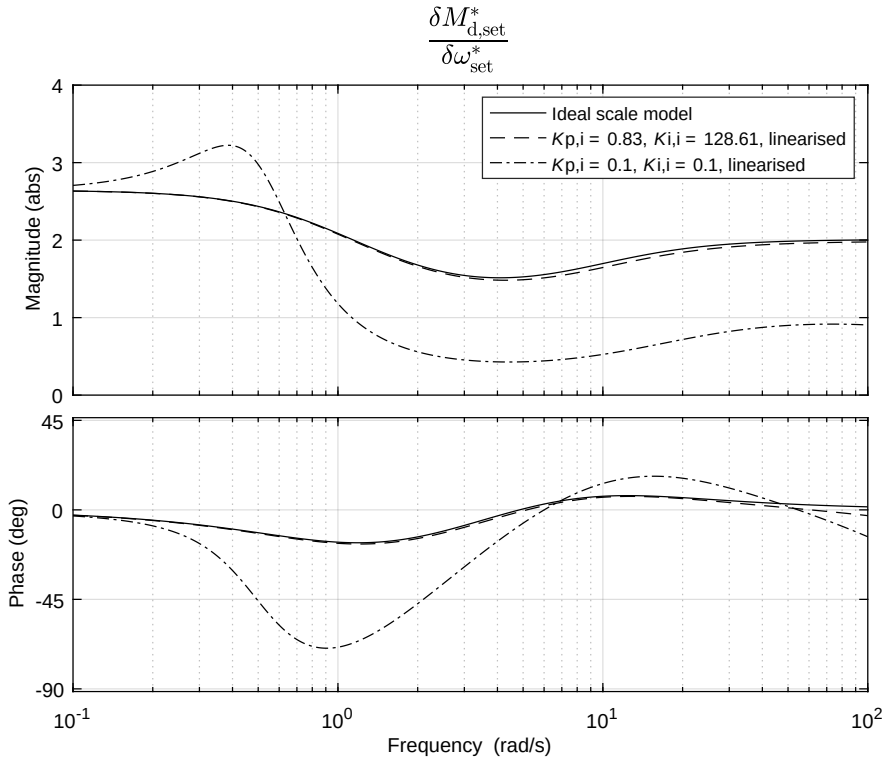


Figure A.2: Bode diagram of response of drive torque $\delta M^*_{\mathrm{d,set}}$ on set speed $\delta \omega^*_{\mathrm{set}}$. Response is shown of the ideal scale model and practical scale models with varying current controller settings.

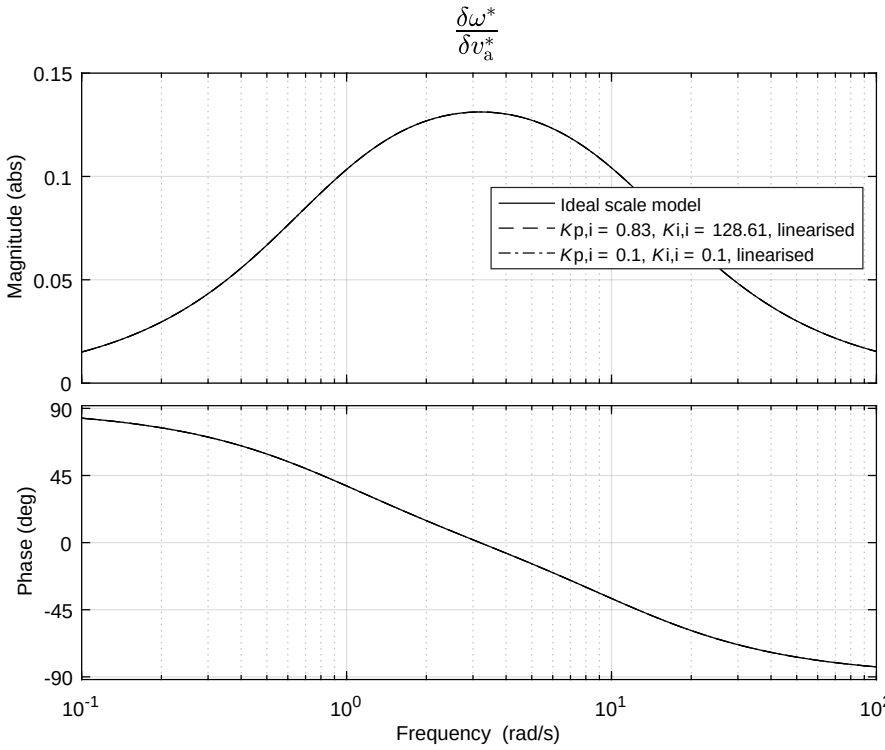


Figure A.3: Bode diagram of response of shaft speed $\delta\omega^*$ on advance speed δv_a^*. Response is shown of the ideal scale model and practical scale models with varying current controller settings.

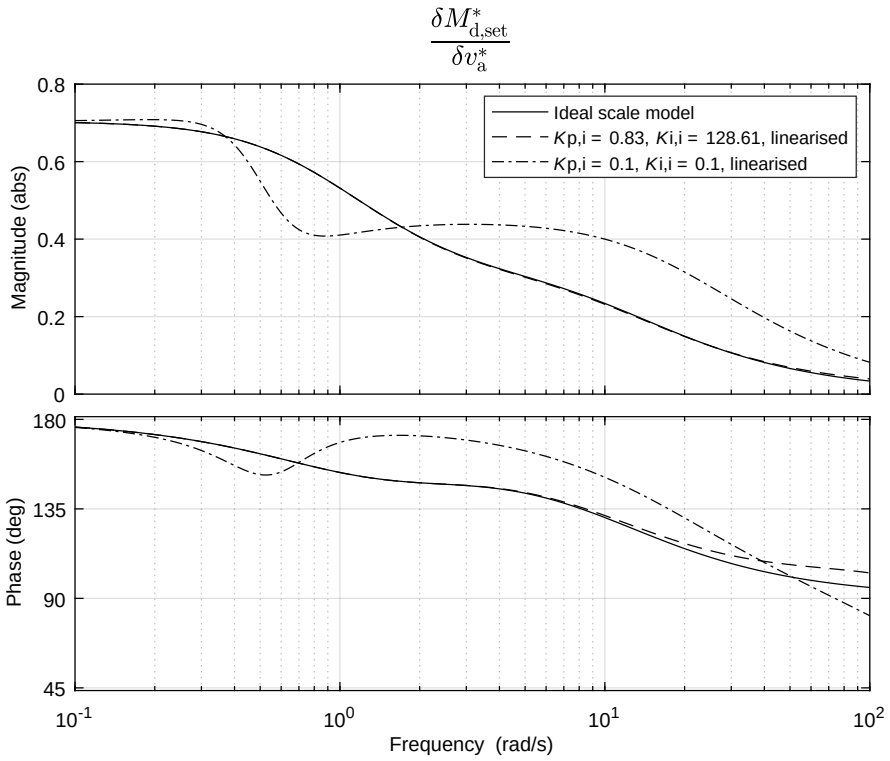


Figure A.4: Bode diagram of response of drive torque $\delta M^*_{\mathrm{d,set}}$ on advance speed δv^*_{a}. Response is shown of the ideal scale model and practical scale models with varying current controller settings.

Appendix B

Linearised Closed Loop Including Diesel Engine

In the analyses before Chapter 6, the influence of the diesel engine model on shaft dynamics was neglected in linear descriptions for reasons of simplicity. However, the non-linear model described in Section 2.2.1 does include a diesel engine model, and this model is also used for the HIL experiments reported in this dissertation. Thus, to be able to compare linear simulations and HIL measurements, linear descriptions models including the engine model must be derived, too. This Appendix introduces the block diagram and linear descriptions including the fuel rack map described in Section 2.2.1.

In the fuel rack map representing the diesel engine, torque is calculated from a given fuel rack setting and engine speed. The relation between fuel rack setting, speed and torque is mathematically expressed by Eq. (2.3) and visualised in Fig. 2.3. Fig. B.1 shows how this relation can be introduced into the block diagram of the ideal propulsion system, shown in Fig. 2.7. Functions C_ω, S_1^* and S_2^* are written out in Section 2.3.1 for the ideal and uncorrected practical scale model. When considering the practical scale model with numerical inertia correction, function S_1^* is described by Eq. (4.23) in Section 4.4.2.

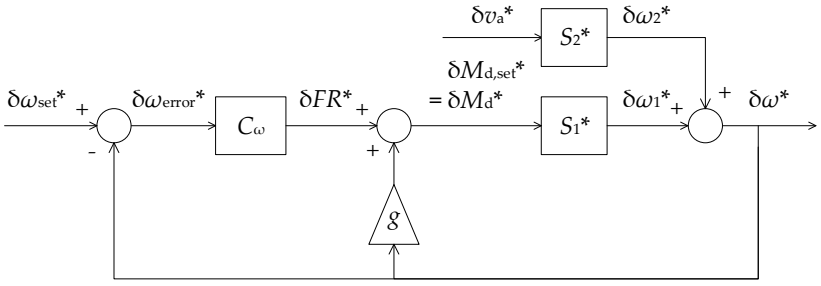


Figure B.1: Graphical representation of the linearised ideal scale model, including the diesel engine model introduced in Section 2.2.1.

From the block diagram in Fig. B.1, the four transfer functions given in Eqs. (B.1) through (B.4) can be derived. These extended linear descriptions are used in Chapter 6 to compare linear simulations and HIL measurements. As this comparison is made after the dynamic behaviour of the electric loop has been investigated, no further attention is paid to the electric loop here.

$$\frac{\delta\omega^*(s)}{\delta\omega^*_{\mathrm{set}}(s)} = \frac{C_\omega(s)\cdot S_1^*(s)}{1+\big(C_\omega(s)-g\big)\cdot S_1^*(s)} \tag{B.1}$$

$$\frac{\delta M^*_{\mathrm{d,set}}(s)}{\delta\omega^*_{\mathrm{set}}(s)} = \frac{C_\omega(s)}{1+\big(C_\omega(s)-g\big)\cdot S_1^*(s)} \tag{B.2}$$

$$\frac{\delta\omega^*(s)}{\delta v^*_{\mathrm{a}}(s)} = \frac{S_2^*(s)}{1+\big(C_\omega(s)-g\big)\cdot S_1^*(s)} \tag{B.3}$$

$$\frac{\delta M^*_{\mathrm{d,set}}(s)}{\delta v^*_{\mathrm{a}}(s)} = \frac{\big(-C_\omega(s)+g\big)\cdot S_2^*(s)}{1+\big(C_\omega(s)-g\big)\cdot S_1^*(s)} \tag{B.4}$$

Appendix C

Location of the Wave Probe During Experiments

Fig. C.1 shows the probe used to measure wave heights during experiments reported in this dissertation. The measured water level is a function of the voltage differential across the electric wire. Although the perspective of the image does not allow to accurately determine the location of the wave probe relative to the propeller, Fig. C.1 suggests that the water level may have been measured several centimetres to the rear of the propeller during experiments. This may have been caused by repeated remounting of the wave probe in the course of days. Measurements reported in Section 6.5.2 are consistent with a rearward offset of approximately 0.07 m.

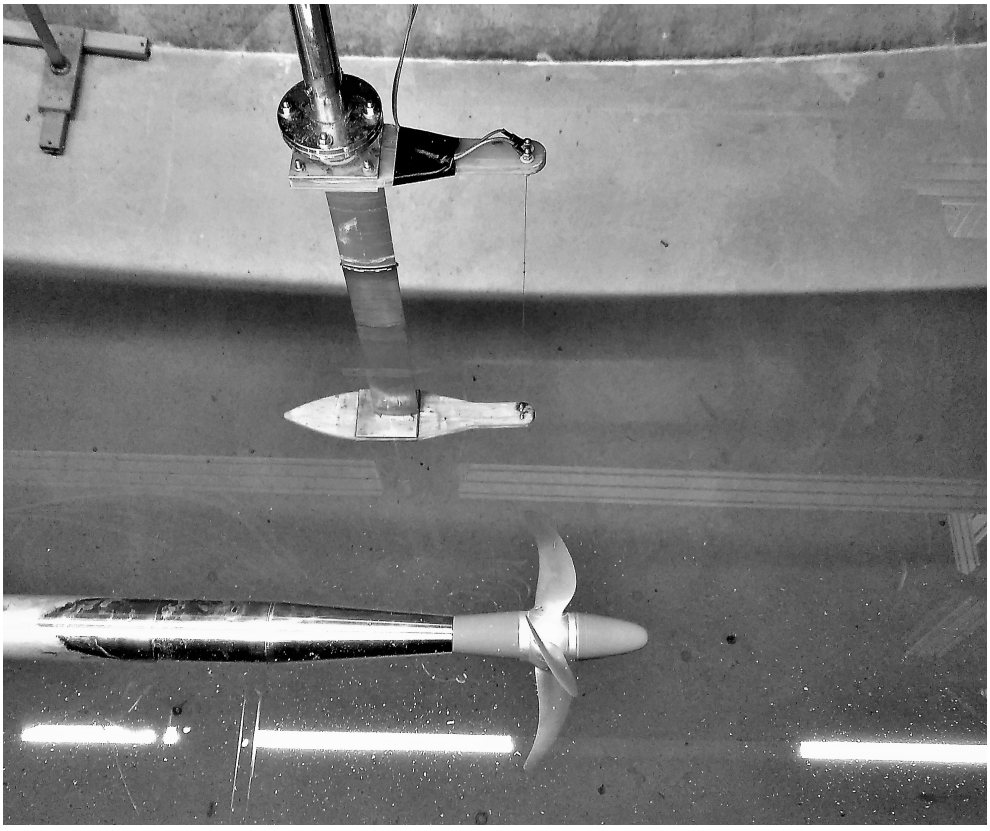


Figure C.1: Probe used to measure wave heights during experiments reported in this dissertation. The water level is measured by the electric wire at the front of the device.

Acronyms and Abbreviations

AC	Alternating current
Bft	Beaufort
CAN	Controller area network
CFD	Computational fluid dynamics
DC	Direct current
EEDI	Energy efficiency design index
EMF	Electromotive force
Eng.	Engine
Eq.	Equilibrium
FS	Full scale
HIL	Hardware in the loop
IIR	Infinite impulse response
IMO	International Maritime Organisation
Int.	Integral
I/O	Input/output
ITTC	International Towing Tank Conference
Max.	Maximum
Mech.	Mechanical
Min.	Minimum
MS	Model scale
NAB	Nickel-aluminium-bronze alloy
Nom.	Nominal
PDO	Process data object
PI	Proportional and integral (controller)
PMSM	Permanent magnet synchronous machine
Ppr	Pulses per rotation
Prop.	Propeller
PTO	Power take-off
PWM	Pulse width modulation
SDO	Service data object
STANAG	NATO standardization agreement
SWATH	Small waterline area twin hull

Nomenclature

Notation

A		Amplitude
a_0		IIR filter coefficient
b		Propeller torque derivative
c		Polynomial regression constant
D	[m]	Propeller diameter
e		Regression polynomial power
F_{n}		Froude number
FR		Fuel rack setting
G		Gain
g	[m/s^2]	Gravity constant
g		Fuel rack torque slope
$H_{1/3}$	[m]	Significant wave height
h	[m]	Propeller hub immersion
I	[kgm^2]	Moment of inertia
i	[A]	Current
i_{gb}		Gearbox reduction ratio
J		Propeller advance ratio
k_{e}	[Vs/rad]	Motor back EMF constant
K_{i}	[s^{-1}]	Integrator gain
K_{p}		Static gain
K_{Q}		Propeller torque constant
K_{T}		Propeller thrust constant
k_{t}	[Nm/A]	Motor torque constant
L	[m]	Length
L	[H]	Inductance
M	[Nm]	Torque
n	[rpm]	Shaft speed
n		Step index
P/D		Propeller pitch/diameter ratio
R	[Ω]	Electric resistance
R_{n}		Reynolds number
S	[m^{2}s/rad]	Spectral density of wave variance
s	[rad/s]	Pole frequency
t	[s]	Time

U_{10}	[m/s]	Wind speed 10 m above the surface
u	[V]	Voltage
v	[m/s]	Speed
W_{n}		Weber number
w		Wake fraction
x		Arbitrary input
y		Arbitrary output
z	[rad/s]	Zero frequency
z		Location in the z plane
η		Efficiency
φ	[deg.]	Phase angle
λ		Geometric scale factor
P		Density scale factor
τ	[s]	Time constant
μ	[rad]	Ship's course relative to incoming waves
ν	[m^2/s]	Kinematic viscosity
ρ	[$\mathrm{kg/m}^3$]	Density
σ		Standard deviation
ω	[rad/s]	Shaft speed
ω	[rad/s]	Wave frequency
ζ	[m]	Wave height

Subscripts

0	Equilibrium
1	Shaft speed component
2	Advance speed component
a	Advance
b	Brake
c	Correction
calc	Calculation
d	Drive
E	Encounter
e	Engine
est	Estimated
f	Filtered
fr	Friction
FS	Full scale
H2O	Entrained water
hydro	Hydrodynamic load
i	Current
id	Ideal scale model
l	Load
M	Torque
m	Measured
max	Maximum

mech	Propulsion motor and shaft
MS	Model scale
n	Pole index
net	Drive minus load
nom	Nominal
osc	Oscillation
prop	Propeller
p	Practical scale model
p	Wave peak
set	Setting
sim	Simulated
r	Relative rotative
s	Shaft
s	Ship
ss	Steady state
tot	Total
v	Advance speed
w	Wave
Δ	Discrete derivative
ω	Shaft speed

Superscripts

*	Normalised
=	Standardised controller setting

References

Altosole, M., Figari, M., Bagnasco, A., and Maffioletti, L. Design and test of the propulsion control of the aircraft carrier "Cavour" using real-time hardware in the loop simulation. In *Proceedings of the European simulation interoperability workshop (EURO SIW) 2007*, pages 67–74, Genoa, Italy, 2007.

Armaoglu, E., Eggers, R., Quadvlieg, F., and Coevorden, P. v. On the manoeuvrability of naval surface ships with respect to a new STANAG. In *Proceedings of the RINA warship 2010 conference*, London, UK, 2010.

Balmer, L. *Signals and Systems*. Prentice Hall, London, 1998. ISBN 0134956729.

Bassam, A. M., Phillips, A. B., Turnock, S. R., and Wilson, P. A. Experimental testing and simulations of an autonomous, self-propulsion and self-measuring tanker ship model. *Ocean Engineering*, 186, 2019. doi: https://doi.org/10.1016/j.oceaneng.2019.05.047.

Bertram, V. *Practical ship hydrodynamics*. Butterworth-Heinemann, Oxford, 1999. ISBN 9781483299716.

Bondarenko, O. and Kashiwagi, M. Dynamic behavior of ship propulsion plant in actual seas. *Journal of the Japan Institute of Marine Engineering*, 45:76–80, 2010. doi: https://doi.org/10.5988/jime.45.1012.

Brackley, M. and Pollock, C. Analysis and reduction of acoustic noise from a brushless DC drive. *IEEE transactions on industry applications*, 36(3):772–777, 2000.

Brown, M., Sanchez-Caja, A., Adalid, J. G., Black, S., Sobrino, M. P., Duerr, P., Schroeder, S., and Saisto, I. Improving propeller efficiency through tip loading. In *Proceedings of the 30th symposium on naval hydrodynamics*, Hobart, Australia, 2014.

Burrill, L. C. and Robson, W. Virtual Mass and Moment of Inertia of Propellers. *Trans. North East Coast Institution of Engineers and Shipbuilders*, 78, 1962.

Califano, A. *Dynamic loads on marine propellers due to intermittent ventilation*. Norwegian University of Science and Technology, 2010. ISBN 9788247125052.

Calleya, J., Pawling, R., and Greig, A. Ship impact model for technical assessment and selectionof Carbon dioxide Reducing Technologies (CRTs). *Ocean*

Engineering, 97:82–89, 2015. doi: http://dx.doi.org/10.1016/j.oceaneng.2014.12.014.

Campora, U. and Figari, M. Numerical simulation of ship propulsion transients and full-scale validation. *Proceedings of the Institution of Mechanical Engineers, Part M: Journal of Engineering for the Maritime Environment*, 217:41–52, 2003. doi: https://doi.org/10.1243/147509003321623130.

Carrica, P. M., Kerkvliet, M., Quadvlieg, F. H. H. A., Pontarelli, M., and Martin, J. E. CFD simulations and experiments of a maneuvering generic submarine and prognosis for simulation of near surface operation. In *Proceedings of the 31st symposium on naval hydrodynamics*, Monterey, USA, 2016.

Dallinga, R. P., Huijsmans, R. H. M., and Graham, R. Development of design tools for the prediction of SWATH motions. In *Proceedings of the seventeeth symposium on naval hydrodynamics*, The Hague, the Netherlands, 1988.

Dang, J., Van den Boom, H. J. J., and Ligtelijn, J. T. The Wageningen C- and D-series propellers. In *Proceedings of the 12th international conference on fast sea transportation (FAST)*, 2013.

Dorn, H. and McClellan, J. E. *Science and technology in world history: an introduction*. John Hopkins University Press, Baltimore, 1999. ISBN 0801858690.

Ferreiro, L. D. *Ships and science: the birth of naval architecture in the scientific revolution, 1600-1800*. MIT press, Cambridge, 2007. ISBN 9780262062596.

Geertsma, R. D., Negenborn, R. R., Visser, K., Loonstijn, M. A., and Hopman, J. J. Pitch control for ships with diesel mechanical and hybrid propulsion: Modelling, validation and performance quantification. *Applied Energy*, 206:1609–1631, 2017. doi: https://doi.org/10.1016/j.apenergy.2017.09.103.

Helma, S. An extrapolation method suitable for scaling of propellers of any design. In *Proceedings of the fourth international symposium on marine propulsors (SMP'15)*, Austin, USA, 2015.

Holtrop, J. and Mennen, G. G. J. An approximate power prediction method. *International Shipbuilding Progress*, 29(335):166–170, 1982.

Hooft, J. P. On the critical speed range of ships in restricted waterways. *International Shipbuilding Progress*, 16(177):145–154, 1969.

Hooft, J. P. and Nienhuis, U. The prediction of the ship's maneuverability in the design stage. *Transactions of the Society of Naval Architects and Marine Engineers*, 102:419–445, 1994.

Huijgens, L. J. G. Replication Data for: hardware in the loop emulation of ship propulsion systems at model scale, 2020. URL `https://doi.org/10.34894/ORXL9Y`.

Huijgens, L. J. G., Vrijdag, A., and Hopman, J. J. Propeller-engine interaction in a dynamic model scale environment. In *Proceedings of the 28th international ocean and polar engineering conference (ISOPE)*, Sapporo, Japan, 2018.

Huijgens, L. J. G., Vrijdag, A., and Hopman, J. J. Hardware in the loop experiments with ship propulsion systems in the towing tank: scale effects, corrections and demonstration. *Journal paper under review with Ocean Engineering*, 2021a.

Huijgens, L. J. G., Vrijdag, A., and Hopman, J. J. Hardware in the loop experiments on the interaction between a diesel-mechanical propulsion system and a ventilating propeller. *Journal paper in preparation*, 2021b.

Hunt, S. and Zondervan, G. J. D. Use of CFD in the optimisation of a naval support ship. In *Proceedings of the 2007 international conference on control, automation and systems (ICCAS)*, Seoul, Korea, 2007.

ITTC. Recommended procedures and guidelines: resistance test, 7.5-02-02-01. Technical report, 2011.

ITTC. Recommended procedures and guidelines: open water test, 7.5-02-03-02.1. Technical report, 2014a.

ITTC. Recommended procedures and guidelines: 1978 ITTC performance prediction method, 7.5-02-03-01.4. Technical report, 2014b.

Johansen, T. A., Fossen, T. I., and Vik, B. Hardware-in-the-loop testing of DP systems. In *Proceedings of the 2005 dynamic positioning conference*, Houston, USA, 2005.

Kim, Y. C., Kim, K. S., Kim, J., Kim, Y., Park, I. R., and Jang, Y. H. Analysis of added resistance and seakeeping responses in head sea conditions for low-speed full ships using URANS approach. *International Journal of Naval Architecture and Ocean Engineering*, 9:641–654, 2017. doi: http://dx.doi.org/10.1016/j.ijnaoe.2017.03.001.

Kitagawa, Y., Tanizawa, K., and Tsukada, Y. Development of an experimental methodology for self-propulsion test with a marine diesel engine simulator, third report: Auxiliary thruster system. In *Proceedings of the 24th international ocean and polar engineering conference (ISOPE)*, Busan, Korea, 2014.

Kitagawa, Y., Tanizawa, K., and Tsukada, Y. Development of an experimental methodology for self-propulsion test with a marine diesel engine simulator, fourth report: Direct measurement of actual ship speed in waves by model tests. In *Proceedings of the 25th international ocean and polar engineering conference (ISOPE)*, Kona, USA, 2015.

Kitagawa, Y., Bondarenko, O., Tsukada, Y., Fukuda, T., and Tanizawa, K. An application of the tank test with a model ship for design of ship propulsion plant system. *Marine Engineering*, 53(3):355–361, 2018. doi: https://doi.org/10.5988/jime.53.355.

Kollmorgen. S700 instruction manual. Technical report, 2015.

Kollmorgen. CAN-bus: fieldbus interface for S300 / S700. Technical report, 2016.

Koushan, K. Dynamics of propeller blade and duct loading on ventilated thrusters in dynamic positioning mode. In *Proceedings of the 2007 Dynamic Positioning Conference*, Houston, USA, 2007.

Kozlowska, A. M., Steen, S., and Koushan, K. Classification of different type of propeller ventilation and ventilation inception mechanism. In *Proceedings of the first international symposium on marine propulsors (SMP'09)*, Trondheim, Norway, 2009.

Kozlowska, A. M., Dalheim, Ø. Ø., Savio, L., and Steen, S. Time domain modeling of propeller forces due to ventilation in static and dynamic conditions. *Journal of Marine Science and Engineering*, 8(31), 2020. doi: https://doi.org/10.3390/jmse8010031.

Krasilnikov, V., Sileo, L., and Juong, T. Investigation into the influence of Reynolds number on open water characteristics of pod propulsors. In *Proceedings of the fourth international symposium on marine propulsors (SMP'15)*, Austin, USA, 2015.

Krasilnikov, V. I. Self-propulsion RaNS computations with a single-screw container ship. In *Proceedings of the third international symposium on marine propulsors (SMP'13)*, pages 430–438, Launceston, Australia, 2013.

Krüger, S. and Abels, W. Hydrodynamic damping and added mass of modern screw propellers. In *Proceedings of the 36th international conference on ocean and arctic engineering (OMAE)*, Trondheim, Norway, 2017.

Kuiper, G. *The Wageningen propeller series*. MARIN, 1992. ISBN 9789090072470.

Larsson, L., Raven, H. C., and Paulling, J. R. *Ship resistance and flow*. Society of Naval Architects and Marine Engineers, 2010. ISBN 9780939773763.

Lewis, F. M. and Auslaender, J. M. Virtual inertia of propellers. *Journal of Ship Research*, 3(4), 1960.

Li, H., Steurer, M., Shi, K. L., Woodruff, S., and Zhang, D. Development of a unified design, test, and research platform for wind energy systems based on hardware-in-the-loop real-time simulation. *IEEE Transactions on Industrial Electronics*, 53(4):1144–1151, 2006. doi: https://doi.org/10.1109/TIE.2006.878319.

Louzis, K., Ventikos, N., Koimtzoglou, A., and Eliopoulou, E. Statistics for marine accidents in adverse weather conditions. In *Proceedings of the second international conference on maritime technology and engineering (MARTECH)*, Lisbon, Portugal, 2014.

Martelli, M. and Figari, M. Real-time model-based design for CODLAG propulsion control strategies. *Ocean Engineering*, 141:265–276, 2017. doi: https://doi.org/10.1016/j.oceaneng.2017.06.029.

Martinez-Alvarado, R., Ruiz-Sanchez, F. J., Sanchez-Orta, A., and Garcia-Salazar, O. Dynamic response of BLDC thruster for small scale quadrotors under aerodynamic load torque. In *Proceedings of the 2014 IEEE international autumn meeting on power, electronics and computing (ROPEC)*, Ixtapa, Mexico, 2014.

Molland, A. F. *The maritime engineering reference book*. Butterworth-Heinemann, London, 2008. ISBN 9780750689878.

Molland, A. F., Turnock, S. R., and Hudson, D. A. *Ship resistance and propulsion: practical estimation of ship propulsive power*. Cambridge University Press, New York, 2011. ISBN 9780521760522.

Nounou, K., Charpentier, J. F., Marouani, K., Benbouzid, M., and Kheloui, A. Emulation of an electric naval propulsion system based on a multiphase machine under healthy and faulty operating conditions. *IEEE Transactions on Vehicular Technology*, 67(8):6895–6905, 2018.

Papanikolaou, A., Zaraphonitis, G., Bitner-Gregersen, E. M., Shigunov, V., el Moctar, O., Guedes Soares, C., Reddy, D. N., and Sprenger, F. Minimum propulsion and steering requirements for efficient and safe operation (SHOPERA). In *Proceedings of the 37th motorship propulsion and emissions conference*, Hamburg, Germany, 2015.

Pfitsch, D., Gordon, B., Rice, J., and Cubbage, S. Development and deployment of autonomous scale submarine models for hydrodynamic testing of U.S. navy submarine maneuvering characteristics. In *Proceedings of the OCEANS 2016 MTS/IEEE conference*, Monterey, USA, 2016. doi: https://dx.doi.org/10.1109/OCEANS.2016.7761068.

Pierson, W. J. and Moskowitz, L. A. Proposed spectral form for fully developed wind seas based on the similarity theory of S. A. Kitaigorodskii. *Journal of Geophysical Research*, 69:5181–5190, 1964.

Roach, A. Model boats in the context of maritime history and archaeology. *International Journal of Nautical Archaeology*, 37(2):313–334, 2008. doi: http://dx.doi.org/10.1111/j.1095-9270.2007.00177.x.

Roinila, T., Messo, T., Luhtala, R., Scharrenberg, R., de Jong, E., Fabian, A., and Sun, Y. Hardware-in-the-Loop methods for real-time frequency-response measurements of on-board power distribution systems. *IEEE Transactions on Industrial Electronics*, 66(7):5769–5777, 2019. doi: https://dx.doi.org/10.1109/TIE.2018.2860543.

Schreiber, V., Savitski, D., Augsburg, K., and Shyr, C. Hardware-in-the-loop testing of hydraulic brake systems with ESP and EPB control. In *Proceedings of EuroBrake 2016*, Milan, Italy, 2016.

Schulten, P. J. M. *The interaction between diesel engines, ship and propellers during manoeuvring*. Delft University Press, 2005. ISBN 9789040725791.

Schwanecke, H. Gedanken zur Frage der hydrodynamischen Schwingungserregung des Propellers und der Wellenleitung. In *Jahrbuch Schiffbautechnische Gesellschaft*, pages 252–280. 1963.

Shiba, H. Air-drawing of Marine Propellers. Technical report, Transportation Technical Research Institute, Japan, 1953.

Shigunov, V., Moctar, O., Papanikolaou, A., Potthoff, R., and Liu, S. International benchmark study on numerical simulation methods for prediction of manoeuvrability of ships in waves. *Ocean Engineering*, 165:365–385, 2018. doi: https://doi.org/10.1016/j.oceaneng.2018.07.031.

Skjetne, R. and Egeland, O. Hardware-in-the-loop testing of marine control systems. *Modeling, Identification and Control*, 27(4):239–258, 2006.

Smitt, L. W. Steering and manoeuvring of ships: full scale and model scale tests. *European Shipbuilding*, 20(1):8–17, 1971.

Smogeli, Ø. N. *Control of marine propellers: from normal to extreme conditions.* Norwegian University of Science and Technology, 2006. ISBN 8247181487.

Stapersma, D. and Vrijdag, A. Linearisation of a ship propulsion model. *Ocean Engineering*, 142:441–457, 2017. doi: https://doi.org/10.1016/j.oceaneng.2017.07.014.

Suzuki, R., Tsukada, Y., and Ueno, M. Estimation of full-scale ship manoeuvring motions from free-running model test with consideration of the operational limit of an engine. *Ocean Engineering*, 172:697–711, 2019. doi: https://doi.org/10.1016/j.oceaneng.2018.12.044.

Swales, P. D., Wright, A. J., McGregor, R. C., and Rothblum, R. The mechanism of ventilation inception on surface piercing foils. *Journal of Mechanical Engineering Science*, 16(1):18–24, 1974.

Tanizawa, K., Kitagawa, Y., Hirata, K., and Fukazawa, M. Development of an experimental methodology for self-propulsion test with a marine diesel engine simulator, the second report - propeller pitch control. In *Proceedings of the 23rd international offshore and polar engineering conference (ISOPE)*, Anchorage, USA, 2013a.

Tanizawa, K., Kitagawa, Y., Takimoto, T., and Tsukada, Y. Development of an experimental methodology for self-propulsion test with a marine diesel engine simulator. *International Journal of Offshore and Polar Engineering*, 23(3): 197–204, 2013b.

Tillig, F., Ringsberg, J. W., Mao, W., and Ramne, B. Analysis of uncertainties in the prediction of ships' fuel consumption – from early design to operation conditions. *Ships and Offshore Structures*, 13(1):13–24, 2018. doi: https://doi.org/10.1080/17445302.2018.1425519.

Ueland, E. S., Skjetne, R., and Vilsen, S. A. Force actuated real-time hybrid model testing of a moored vessel: a case study investigating force errors. *IFAC-PapersOnLine*, 51(29):74–79, 2018. doi: https://doi.org/10.1016/j.ifacol.2018.09.472. 11th IFAC Conference on Control Applications in Marine Systems, Robotics, and Vehicles.

Ueno, M. and Tsukada, Y. Rudder effectiveness and speed correction for scale model ship testing. *Ocean Engineering*, 109:495–506, 2015. doi: http://dx.doi.org/10.1016/j.oceaneng.2015.09.041.

Ueno, M., Tsukada, Y., and Kitagawa, Y. Rudder effectiveness correction for scale model ship testing. *Ocean Engineering*, 92:267–284, 2014. doi: https://dx.doi.org/10.1016/j.oceaneng.2014.10.006.

Ueno, M., Suzuki, R., and Tsukada, Y. Estimation of stopping ability of full-scale ship using free-running model. *Ocean Engineering*, 130:260–273, 2017. doi: https://doi.org/10.1016/j.oceaneng.2016.12.001.

Ueno, M., Suzuki, R., and Tsukada, Y. Model ship control and estimation of full-scale propeller torque in wind and waves. In *IFAC-PapersOnLine*, volume 51, pages 201–206, 2018. doi: https://doi.org/10.1016/j.ifacol.2018.09.493.

van Biert, L., Godjevac, M., Visser, K., and Aravind, P. V. A review of fuel cell systems for maritime applications. *Journal of Power Sources*, 327:345–364, 2016.

Vrijdag, A. Potential of hardware-in-the-loop simulation in the towing tank. In *Proceedings of the OCEANS 2016 MTS/IEEE conference*, Monterey, USA, 2016. doi: https://dx.doi.org/10.1109/OCEANS.2016.7761060.

Vrijdag, A. and Stapersma, D. Extension and application of a linearised ship propulsion system model. *Ocean Engineering*, 143:50–65, 2017. doi: https://doi.org/10.1016/j.oceaneng.2017.07.023.

Wang, G., Jia, D., Cao, M., and Sheng, Z. Propeller air ventilation and performance of ventilated propeller. In *Proceedings of the fourth international symposium on practical design of ships and mobil units (PRADS)*, Varna, Bulgaria, 1989.

Wang, X. and Walters, K. Computational analysis of marine-propeller performance using transition-sensitive turbulence modeling. *Journal of Fluids Engineering*, 134 (7):1–10, 2012. doi: https://dx.doi.org/10.1115/1.4005729.

White, F. M. *Fluid mechanics*. McGraw-Hill, Boston, US, 1998. ISBN 9780073529349.

Acknowledgements

Success is often claimed to be the result of hard work, natural aptitude and, inevitably, good luck. It is my firm belief, however, that the importance of a supportive environment is often underestimated. On the largest scale, this environment is defined by society, and if this dissertation is a success, it is not least because of the society in which I was born and raised. A society with accessible education, health care and social services is a prerequisite for civilisation and wealth, which in turn are prerequisites for progress and science.

Society has provided me with more than two decades of excellent education, with this PhD thesis as an important milestone. The past four years have contributed significantly to my personal development, and for a large part, this is due to the guidance by Arthur Vrijdag. Our countless exchanges of ideas have shaped this dissertation (including the cover) as well as my view on what it takes to be a scientist. I also owe thanks to my promotor Hans Hopman, not only for his trust and support. I am convinced that his style of leadership is instrumental for the relaxed yet professional atmosphere in the SDPO section. In addition, I would like to thank Jenny Coenen, who recognised my curiosity and inclination towards research during my Master thesis project, and invited me to start a doctoral research.

There are some colleagues which I would particularly like to thank for the discussions on serious and completely trivial matters. Reinier, Pascal, Jennifer, Daan, Harsh, Lindert, Marc and Ali: thanks for the good company. Thermodynamics, attacks by bears and parasites, career counselling: wise words were only a few office doors away. I will miss our fruitful but often also entirely pointless discussions. Writing these words in my home office, I also want to thank my former office mates. Chris, Kai and Faisal: thanks for the support on theoretical and practical matters, and for the philosophical discussions. And of course, for the friendly atmosphere throughout the years. I owe a special thanks to Chris for sharing his neat LaTeX dissertation template. Rinze, Peter (de Vos), Klaas and Milinko also deserve an honourable mention here, always there to introduce some wisdom into sometimes random attempts towards results. By the way, Rinze, thanks again for convincing me to join the navy hackathon. In several ways, those three days were among the most instructive of my entire PhD. In addition, I would not fail to mention the secretaries. Dineke, Anouk, Monique, Patty, Pauline and Gracia: thank you for keeping everything running smoothly in the department and for organising the Christmas dinners and department beach days. It was always something to look forward to; I hope that this tradition will be continued for many years to come.

During the experimental campaign, I have relied heavily on the expertise of the

towing tank team. Cornel, Peter (Poot), Frits, Pascal, Hans (van der Hek), Wick, Jennifer: without your support, patience and dexterity, the HIL project would have taken many months longer. With my research now nearing its end, it is great to see talented people like Ronald Roberti continuing with the HIL setup. To those who are interested in the future development of HIL in the towing tank, I suggest to keep an eye up for his graduation thesis. I want to extend my special thanks to Cornel for his efforts in the complex acquisition process of the open water setup. At MARIN, I owe my gratitude to Jan de Boer and his team of experts for designing and manufacturing a world class open water setup, and to Tom van Terwisga for his advice and for making available MARIN's C4-40 propeller.

Before my studies at the TU Delft, I followed the Bachelor track for merchant navy officers at the nautical school in Vlissingen. There, I was introduced in the wonderful world of control engineering, thermodynamics and marine engineering in general. These subjects were mostly given by Arie de Groot. I remember that not all students were particularly fond of these subjects, but still, Arie tried to make us see the beauty of the theory behind the practice. At least in my case, he succeeded, and I would like to thank him for that.

My parents deserve an honourable mention here, too. Although my intermittent motivation at secondary school may have caused them some despair at times, they have always been supportive when it came to education. To them, I owe a considerable part of my personal development. I would also like to thank Mathie and Tiny for their hospitality and conviviality all the times Nieke and I showed up in the North, and my room mates Niels, Jelle and Rick, for the easygoing atmosphere at home the past four years.

Last but not least, I want to thank Nieke. My work would have completely consumed me if you were not there to distract me every now and then with a new discovery or an afternoon of work in the garden. Maar ik ben vooral trots en vereerd dat je het aandurft om mee te gaan in mijn wilde toekomstplannen. Waar we ook terecht komen, je bent er niet alleen.

Curriculum Vitae

Lode Huijgens was born on 5 December 1990 in Vlissingen, the Netherlands. After a few years, his parents moved to Belgium, where he attended primary and secondary school. He finished secondary school with a diploma in Latin and Physical Sciences from College O.-L.-V. ten Doorn in Eeklo, Belgium. In 2009, he moved back to Vlissingen to follow the merchant navy officer training at Maritiem Instituut de Ruyter. After finishing nautical college in 2013, he continued his studies at Delft University of Technology (TU Delft), specialising in marine engineering and ship production. During his studies, he worked part time as an engineer at the R&D department of Damen Schelde Naval Shipbuilding where he also completed his Bachelor and Master graduation projects.

Having obtained his MSc in Marine Technology in 2016, he remained with TU Delft to start a doctoral research. The research concentrated on performance prediction of ship propulsion systems in realistic, dynamic environments, combining the fields of marine engineering, simulation, mechatronics, electrodynamics and (hydro)mechanics. He was involved in the acquisition and commissioning of the experimental equipment which he would eventually use to demonstrate his findings.

While working at TU Delft, Lode assisted in teaching, grading and supervision of BSc and MSc projects. In 2017, he became a board member of the Benelux branch of the Institute of Marine Engineering, Science and Technology (IMarEST), assisting with organising meetings, managing online communication and providing technical support.

Publications

Huijgens, L. J. G., Vrijdag, A., and Hopman, J. J. Propeller-engine interaction in a dynamic model scale environment. In *Proceedings of the 28th international ocean and polar engineering conference (ISOPE)*, Sapporo, Japan, 2018

Huijgens, L. J. G., Vrijdag, A., and Hopman, J. J. Hardware in the loop experiments with ship propulsion systems in the towing tank: scale effects, corrections and demonstration. *Journal paper under review with Ocean Engineering*, 2021a

Huijgens, L. J. G., Vrijdag, A., and Hopman, J. J. Hardware in the loop experiments on the interaction between a diesel-mechanical propulsion system and a ventilating propeller. *Journal paper in preparation*, 2021b